On the Hydrothermal Characteristics of MHD Nanofluid Flow

A

THESIS SUBMITTED FOR THE DEGREE OF

DOCTOR OF PHILOSOPHY (SCIENCE)

TO THE

DEPARTMENT OF MATHEMATICS

JADAVPUR UNIVERSITY

BY

SUPRAKASH MAITY

DEPARTMENT OF MATHEMATICS

JADAVPUR UNIVERSITY

KOLKATA-700032

WEST BENGAL

INDIA

SEPTEMBER, 2024

Dedicated to my parents with love....

CERTIFICATE FROM THE SUPERVISOR

*This to certify that the thesis entitled "**On the Hydrothermal Characteristics of MHD Nanofluid Flow**" submitted by **Sri Suprakash Maity** who got his name registered on 18th August 2021 for the award of Ph.D. (Science) degree of Jadavpur University, is absolutely based upon his own work under the supervision of **Prof. Prabir Kumar Kundu**, Department of Mathematics, Jadavpur University, and that neither this thesis nor any part of it has been submitted for either any degree/ diploma or any other academic award anywhere before.*

P. K. Kundu 12.09.2024

(Signature of the Supervisor date with official seal)

Professor
DEPARTMENT OF MATHEMATICS
Jadavpur University
Kolkata - 700 032, West Bengal

Acknowledgement

Earning a PhD has always been my dream because it allows me to explore my passion for mathematics at the highest level. Achieving this goal would be the culmination of my academic aspirations and a stepping stone to making meaningful contributions to the field. This dream cannot be fulfilled without the supports and contributions of many people.

I would like to express my deepest gratitude to my supervisor, Prof (Dr) Prabir Kumar Kundu, Department of Mathematics, Jadavpur University for his precious guidance, support, and encouragement throughout the course of my PhD journey. His insights and expertise have been instrumental in shaping this research and bringing it to fruition. I am very much thankful to Dr. Nilankush Acharya for his immense support and guidance. Achieving this degree will never be possible without his support and help.

I am grateful to acknowledge Dr. Shib Sankar Giri for his effortless guidance and valuable suggestions. I express Special thanks to my lab mates and senior research scholars Raju, Subrata, Shewta, Bikash and Sayantan. Your camaraderie, intellectual discussions, and collaboration have made this journey both enjoyable and enriching.

I am thankful to the administrative staffs and Professors and non-teaching staffs of the Department of Mathematics, Jadavpur University for their efficient handling of the proceedings of my Ph.D. degree. I deeply appreciate their efforts and commitment to ensuring a smooth and successful process.

I am deeply grateful to my parents Mr Sukumar Maity and Mrs Pranati Maity, whose selfless inspiration guided me to explore new paths and pursue my own destiny. Their unwavering support and encouragement have been the foundation of this journey.

I would like to express my deepest gratitude to my wife, Piyasa for her unwavering support, patience, and understanding throughout this PhD work. Her love, encouragement, and belief in me have been my constant source of strength and motivation.

I would like to express my heartfelt gratitude to my daughter, Shreejoyi and my sister, Supravita for their endless love, and joy throughout this journey. Their smiles and laughter have been a constant source of inspiration and motivation.

I would like to express my special thanks to, father in law Late Basudeb Ghosh, mother in law Subhali Ghosh. Their encouragement and belief in my abilities have been instrumental in my success.

Date: 12.09.2024

Suprakash Maity

Suprakash Maity

ABSTRACT

Title: On the Hydrothermal Characteristics of MHD Nanofluid Flow

Index No.: 85/21/Maths./27
Submitted by: Suprakash Maity

Improvement in technology requires more energy efficient tools to give more efficiency. Nanofluid and hybrid nanofluid are more efficient due to their high thermal conductivity. In this research we have analyzed various models for nanofluid and hybrid nanofluid flow. First Chapter explores the basics of nanofluid. Nanofluid preparation technique, its stability, applications are also discussed. The main fundamental governing equations are presented in this chapter. Various significant parameters which are responsible for heat and mass transfer are also mentioned. The entropy generation investigation of hybrid nanofluidic transport over an unsteady spinning disk are considered in Chapter 2. The magnetic influence, velocity slips, and thermal radiative effects are included within the flow. Chapter 3 explores a novel conviction of hybrid nanofluid with an enhanced model under inclined magnetic field along with its thermo physical properties. Active and passive control implementation on the nanofluid flow over a stretching cylinder is explored in Chapter 4. Chapter 5 reveals the consequences of steady and unsteady nanofluid flow over a bidirectional stretching sheet. The steady flow of hybrid nanofluid is considered over a rotating disk under magnetic field in Chapter 6. In Chapter 7 we investigated the second order slip effect under multiple convective conditions. Nanofluid flow is taken over a permeable stretching cylinder. We investigated the Casson nanofluid flow over a curved stretching sheet in Chapter 8. In Chapter 9 we investigated the effects of actively and passively controlled nanofluid flow over a wedge. Multiple slippery consequences along a stretching cylinder is considered in Chapter 10. The nanofluid flow on a curved stretching surface under magnetic influence is considered in Chapter 11. Some future research scopes along this direction and a general conclusion on the problems considered in the thesis are also included.

Suprakash Maity

Full Signature of the Candidate
Date: 12.09.2024

P. K. Kundu.

Signature with Seal of the Supervisor
Date: 12.09.2024

Professor
DEPARTMENT OF MATHEMATICS
Jadavpur University
Kolkata - 700 032, West Bengal

CONTENTS

PREFACE

Improvement in technology requires more energy efficient tools to give more efficiency. Traditional liquid like water, kerosene, ethylene glycol are incapable to collect high level efficiency due to their low thermal conductivity. Magnetohydrodynamics (MHDs) is the study of any electrically conducting fluid flow under magnetic field. Owing to the flow of an electrically conducting nanofluid under a magnetic field, electric current is prompted in the system and it again has its own magnetic field. Induced current reacted to the magnetic field and create electromagnetic force which disturb the motion of fluid. The system of equations of MHD consists of Ohm's law of electric current, Gauss's law, Faraday's law and Ampere's law. MHD generator, power plant, nuclear reactor, solar wind flow, blood flow sensor are some important application of MHD flow. Computational astrophysics is also blessed with MHDs. Magnetic behavior of plasmas infusion reactor also studied by the concepts of MHD flow.

In this thesis we have analyzed various models for nanofluid and hybrid nanofluid flow. Different important parameters are introduced to stimulate the system. Numerical outcomes are on the basis of heat and mass transfer and represented by several graphs and tables. Other hydrothermal features are also explored.

First chapter explores the basics of nanofluids. Nanofluid preparation technique, its stability, applications are also discussed. The main fundamental governing equations are presented in this chapter. Various significant parameters which are responsible for heat and mass transfer are also properly mentioned in this chapter. Lastly the total MHD flow details are also discussed in this chapter. The entropy generation investigation of hybrid nanofluidic transport over an unsteady spinning disk are considered in chapter 2. The magnetic influence, velocity slips, and thermal radiative effects are included within the flow. Entropy generation-related figures are depicted for diverse parameters and parametric effects on Bejan number are also analyzed. Chapter 3 explores a novel conviction of hybrid nanofluid with an enhanced model under inclined magnetic field along with its thermo physical properties. Surface slip and permeable texture of the sheet reveal excellent points of the flow. Active and passive control implementation on the nanofluid flow over a stretching cylinder is explored in chapter 4. Realistic velocity slip and thermal jump properties are discussed. Appearance of external heat source and magnetic influence is also introduced.

Results are compared considering with slip and without slip conditions, whereas the concentration profile is described under active and passive control condition. Chapter 5 reveals the consequences of steady and unsteady nanofluid flow over a bidirectional stretching sheet. A magnetic field is working in the normal direction. The Brownian motion together with thermophoresis are taken into consideration. Moreover, chemical reaction within the nano ingredients also attracts novel corner in this study. Differential transformation method (DTM) is used to solve the set of ODEs. The steady flow of hybrid nanofluid is considered over a rotating disk under magnetic field in chapter 6. The nanoparticles titanium oxide (TiO_2) and ferrous ($CoFe_2O_4$) are used with its physical properties and water is considered as host liquid. The foremost purpose of this communication is that how hydrothermal integrity varies for hybrid nanofluid over a spinning disk in presence of magnetic orientation. A comparison of linear and nonlinear thermal radiation for the above mentioned parameters are taken and efficiency of nonlinear radiation is established. In Chapter 7 we investigates the second order slip effect under multiple convective conditions. Nanofluid flow is taken over a permeable stretching cylinder. Suction and injection of nanofluid together with Brownian motion and thermophoresis is also incorporated in this study. We investigate the Casson nanofluid flow over a sheet which is curved and stretching in nature in chapter 8. Radiation, slip provisions and magnetic field of uniform rate are also included in this study. Moreover, chemical reaction of higher order within the Nano ingredients also play an important role in flow system. Chapter 9 investigates the effects of actively and passively controlled nanofluid flow over a wedge. Comparison is done for various wedge angle parameters. Magnetic field is employed in normal to the flow direction. Velocity slip effect and external heat source is also included into the system. Multiple slippery consequences along a stretching cylinder is considered in chapter 10. Brownian migration along with thermophoresis effect are applied together with an external heat source. Magnetic influence is considered perpendicular to the axis of cylinder. All the results obtained are compared under no slip and with slip provisions. Chapter 11 explores the nanofluid flow on a curved stretching surface under magnetic influence. Realistic velocity slip together with convective boundary condition are included. The system is also blessed with radiation and higher order chemical reaction. Active and passive control of nanoparticles are considered and under both boundary conditions the flow analysis is compared.

CHAPTER 1

Introduction

Now a days technology has improved so much that produces more efficient tools than previous era. Improvement in technology requires more energy efficient tools to give more efficiency. Traditional liquid like water, kerosene, ethylene glycol are incapable to collect high level efficiency due to their low thermal conductivity. Refrigerators, nuclear reactors, heat exchangers, polymer coating industries, electronic devices are emerging area of application of heat transmission. Computers are most used engineering tool in the current era which has micro level chip setup. Cooling technique is most important for this type of advanced technical gadgets. In this chapter nanofluid is introduced properly with its various phenomena and several thermo physical properties. The vast area of application of nanofluid is also covered.

1.1 Nanofluid

A large number of industrial process, nuclear reactor, and solar equipment involve heat transfer mechanism. Thermal cooling and heating process is very useful in these sectors. Base fluids with low thermal conductivity is incapable to meet up with the huge thermal transmission of fluids. Traditional heat transmission fluids like water, mineral oil, ethylene glycol are taken as coolant of this heat transfer mechanism. Many more theoretical and experimental investigations are done to get a new fluid which can capable to meet our demand. Then micrometer and millimeter sized particles with good thermal conductivity is mixed with base fluid and used as a coolant. The main problem of these types of fluid is that the particles are settled down very fast in the liquids which leads to an unstable fluid. After that nanometer sized particles called nanoparticles are taken and mixed with base fluid to get a new fluid known as “nanofluid”. These particles has better stability than millimeter sized particles and surface area also increased which leads to more effective thermal transportation. The aspect ratio i.e. surface area and volume proportion of nanoparticles are 1000 times more than millimeter sized particles.

Choi [1] first introduced the term “nanofluid” to create a stable and highly conducting fluid with advance heat transmission features. Various metal particles and metal oxides are experimentally used to create nanofluid with better thermal profile. The ultimate aim of nanofluid

is to improve its thermal properties at the smallest possible concentration specifically less than 5% of volume.

1.2 Synthesis of Nanofluid:

Synthesis of nanofluid is very important for its application. Perfectly prepared nanofluid give optimized heat transport rate. Schematic representation of the process is given in Figure 1.1 So superior quality of preparation phase gives higher application quality. To prepare the nanofluid we have to take care that the nanofluid is free from any agglomeration and chemical alternation. Besides that it is also very important that prepared nanofluid is free from clogging. Generally two types of techniques are used to prepare nanofluid.

- Single step method
- Two step method
- **Single step method**:

In this method nanoparticles are manufactured and disseminate into the base liquid concurrently. In this process agglomeration of nanoparticles are avoided. Nanoparticles are vaporized directly into the base fluid. Agglomeration of nanoparticles are avoided by continuous circulation of base fluid. This process cannot produce nanofluid in large scale. The stability of this nanofluid is also not up to the mark. The synthesize cost of this method is comparatively high.

- **Two step method:**

In two step technique at first nano sized material is produced by common industrial method after that it is mixed with base fluid by homogenization or magnetic agitation or any other method. It is less expensive as the construction of nano sized particle is already in industrial practice. But a crucial problem in two step method is aggregation of nanoparticles after few hours. Due to this instability several advanced technique including one step method also used to synthesis nanofluid.

Different types of base fluid and nanoparticles are used to form nanofluid. To improve the stability of nanofluid generally surfactant is mixed with it externally. A list of base fluid nanoparticles and surfactant are given in Table 1.1.

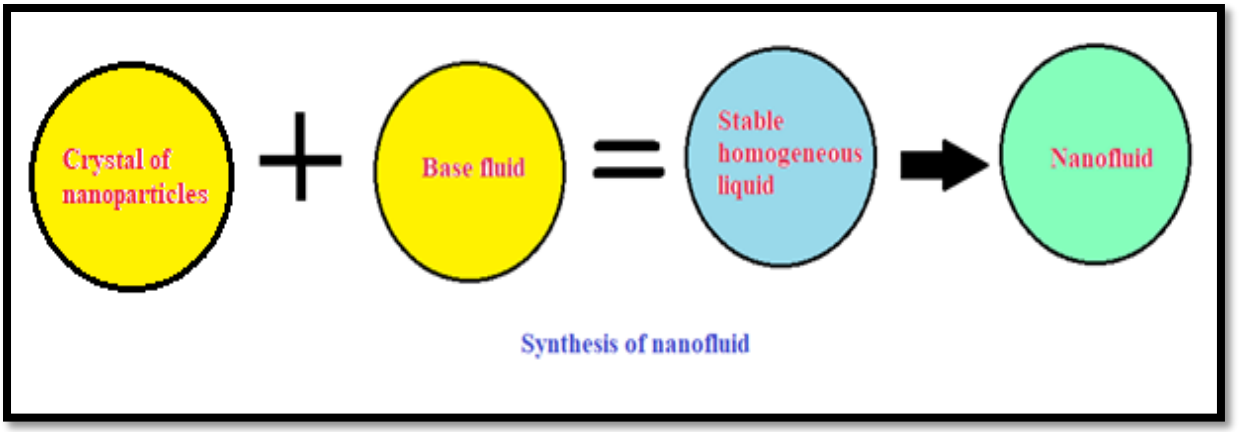

Figure 1.1 Process of synthesis of nanofluid

Table 1.1: List of base fluids, nanoparticles and surfactant

Base fluid	**Nanoparticles**	**Surfactant**
Water, oil, Ethylene glycol, kerosene etc.	Metallic nanoparticles (Cu, Al, Fe, Ag) Non-metallic nanoparticles (Aluminium oxide, copper oxide) Carbon nanotubes	NADDBS, CTAB, SDS, Laurite salt

1.3 Stability of Nanofluid

Foremost intension of nanofluid is to improve thermal phenomena. The main limitation of usage of nanofluid in realistic situation is its stability. Important application of nanofluid take place where it goes through high level heating and cooling procedure. In this process the nanoparticles run inside the fluid and naturally their collision rate get increased. Collection of randomly collided nanoparticles is the main barrier. Thus it is a challenge to the researcher and engineer to maintain a stable dispersion of nanoparticles inside the nanofluid.

Van der Waals attraction force of strength 0.4-4.0 kJ/mole take place when distance between the particles is 0.3-0.6 nm. If there is lack of repulsion force, the dispersed molecules will collected themselves and its leads to instabilization.

To increase the stability [2] of nanofluids surfactant is added to it in proper measurement. Surfactants has such a chemical property that can change the surface and other characteristics to the colloidal solution. For this reason the stability of the nanofluid changed. But we have to choose a proper surfactant to prepare a stable nanofluid. Different types of techniques are available to measure the stability of nanofluid. The widely used techniques are as follows:

- Sedimentation technique – in this technique external force is employed to the nanofluid and sedimentation of nanoparticles are found in base fluid. A stable nanofluid will give constant concentration of nanoparticles with time.
- Zeta potential-in this technique [3] measurement of electric potential difference is calculated. This process is served by ZSN device. [4] Zeta potential value lies between 40 mV to 60 mV is considered as stable nanofluid, whereas below this value is unstable and above this value is super stable nanofluid.
- Many other methods like light scattering method [5]**,** spectral analysis method [6], and centrifugation method [7] are applied to calculate the stability of nanofluid.

Now the main point of concern is how to improve stabilization. There are two methods namely electrostatic stabilization and steric stabilization.

- Electrostatic stabilization- in this process colloidal particles are charged negatively and take place at the surface. They attract the positive ions but double layers of negative electric charge produce repulsive force which is the main preventive force of agglomeration.
- Steric stabilization- in this process nanoparticles are surrounded by sterically bulky substances. Various surfactants perform this function. They create a steric blockage which threaten the nanoparticles to agglomerate.

The Figure 1.2 gives a schematic representation of both types stabilization.

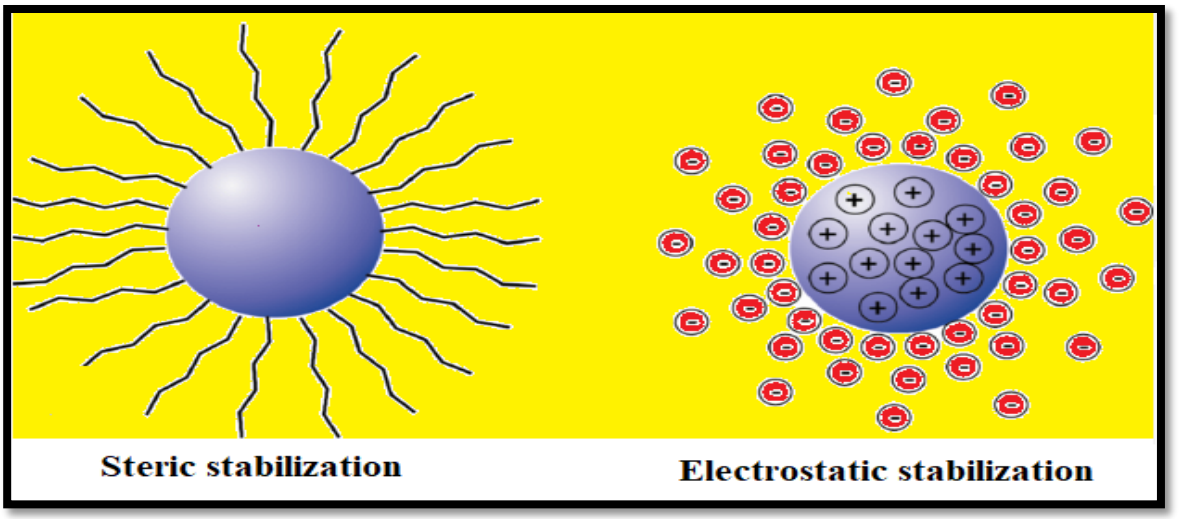

Figure 1.2 Schematic representation of stabilization

1.4 Boundary layers

Boundary layers are categorized into three forms

(i)Velocity boundary layer

(ii)Thermal boundary layer

(iii) Concentration boundary layer

(i) Velocity boundary layer:

Boundary layer theory is very important to study the features of nanofluid flow or MHD flow. Navier and Stokes had established the equations of motion of a viscous fluid. The stream property is not clearly described this equation. Ludwig Prandtl [8] has taken a fluid with very small viscosity and describe its motion. He found near the surface of flow area the viscosity plays a vital role. As the fluid proceed through the stationary body, the molecules which are just next to the body hang on to it and furnish zero velocity. This phenomena is known as “No slip conditions”. The velocity of the molecules above the surface is reduced due to collision with previously sticking molecules. This process affects one after another layers. So there is a variation of velocity with respect to distance from the surface. After a certain distance the velocity will not vary with respect to distance and it is called free stream velocity. This thin layer above the surface in which velocity

changed to free stream velocity from zero is called boundary layer. Length of this layer is known as boundary layer thickness.

Boundary layer is divided into two sections, they are viscous region and inviscid region. It is also classified into two systems depending on the value of Reynolds number, they are Laminar and Turbulent. For lower Reynolds number the boundary layer is laminar i.e. the stream wise velocity changed uniformly. When Reynolds number is higher, the boundary layers experienced unsteady swirling flow and creates turbulence.

(ii) Thermal boundary layer:

Let us consider a surface with temperature $T_{surface}$ and a free stream fluid of temperature T_{∞} flow over the surface. Surface temperature is higher than stream temperature. In this circumstances when the fluid come in contact of the warmer surface the adjacent layer temperature of fluid will become $T_{surface}$. The consequent layers of the fluid also turn down away from a definite height and the fluid temperature tends to T_{∞}. In this way there is a temperature gradient and where the temperature changed to 99% of T_{∞}, it is called thermal boundary layer thickness. Consequent layers are called Thermal boundary layer.

(iii) Concentration boundary layer

When two different fluid of variety of concentration flow one over another or a fluid flow over a surface, concentration boundary layer formed. The process is very similar to the thermal and velocity boundary layer. We consider the distance of the certain point where the deviation in concentration of surface and liquid or both liquid is 99% of the free stream is called concentration layer thickness.

1.5 Heat transfer

Heat transfer is a process of transmission of thermal energy from high temperature object to low temperature object until it possess an equilibrium. Generally it occurs by three different ways namely **Conduction**, **Convection** and **Radiation**.

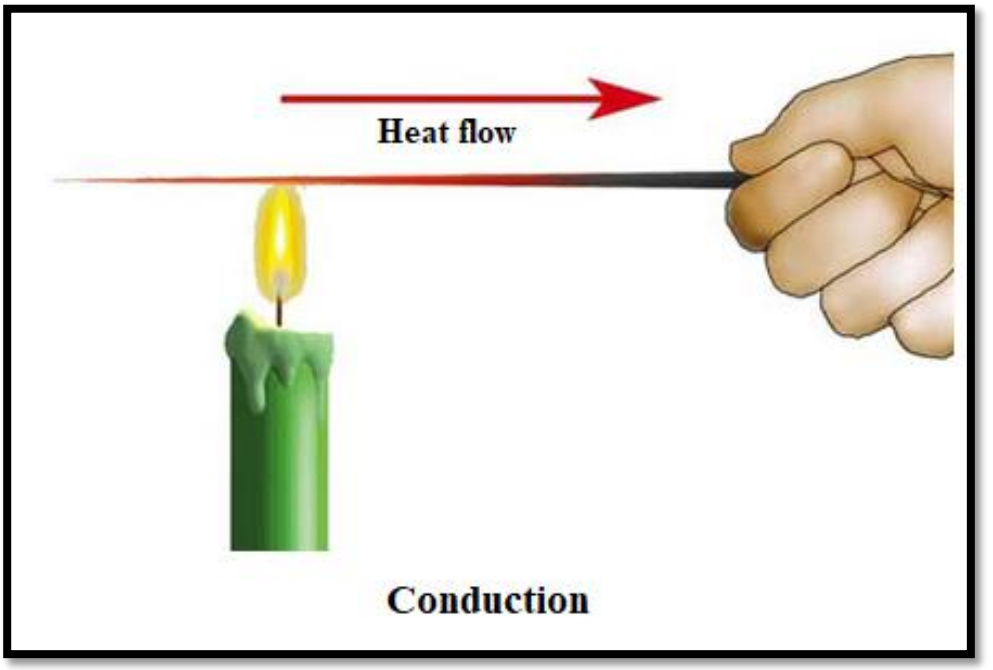

Figure 1.3 Heat conduction process

- **Conduction:**

In this procedure thermal energy is transmitted to its nearest molecules. Generally heat conduction is direct contact method of transmission. Generally this type of transmission occurred due to transfer of energy between adjacent molecules. Solid, liquid and gas are three states; among them gas has large gap between particle whereas liquid has comparatively smaller gaps. But solid has lattice structure with high level bonding. Thermal energy transmitted from high temperature molecule to low temperature molecule and make them balanced with same energy level. Thermal conduction depends on area of the surface of heat transfer, thermal conductivity of the material and temperature difference of the surfaces. In Figure 1.3 it is shown symbolically. Heat conduction equation can be written as

$$Q_{conduction} = -\kappa A \nabla T , \qquad (1.1)$$

where Q denotes heat transfer rate, κ denotes thermal conductivity, A stands for area of the surface and ∇T signifies the temperature difference between two surfaces.

- **Convection**:

Convection process of heat transfer occurred by transmission of fluid molecules which consumes thermal energy. When lower part of a fluid absorbed heat then lower portion density is decreased. This lower dense fluid goes upward and higher dense fluid come to downward from upper portion to fill up the vacant space. This procedure repeatedly occur and circulation of fluid take place. Three types of convection are there (i) natural convection (ii) forced convection (iii) mixed convection.

Free convection take place due to buoyancy effect and density distribution of fluid. Forced convection take place due external forces like suction, pump which produce forces to flow the fluid and automatically the vacant space is filled up by higher density fluid. Mixed convection refers to forced convection in presence of free convection.

Convective heat transfer is controlled by Newton's law of cooling which can be stated as heat transfer is proportional to temperature difference of fluid from environment.

$$Q_{convection} = h_f A\left(T_w - T_\infty\right), \tag{1.2}$$

where Q denotes heat transport rate, h_f stands for convective heat transport co efficient, A is surface area, T_w temperature of fluid and T_∞ temperature far away from the fluid.

- **Radiation:**

This type of heat transmission occur without any contact between materials. Electromagnetic radiation is the key behind this phenomena. Radiative heat transportation has a vital role in thermal profile of nanofluids. The electromagnetic radiation is emitted by all the materials having temperature above absolute zero. The heat transfer is proportional to fourth power of absolute temperature of the material is given by Stefan – Boltzmann law. It is found that radiant heat energy emitted from black body from unit area is given by

$$E = \sigma T^4. \tag{1.3}$$

Total amount of radiation can be calculated by the formula

$$Q_{rad} = e\sigma A\left(T^4 - T_c^{\,4}\right), \tag{1.4}$$

where e designates emissivity of the object, A stands for heat radiating area, T and T_c represents temperature of radiator and temperature of surroundings. σ Stands for Stefan – Boltzmann constant.

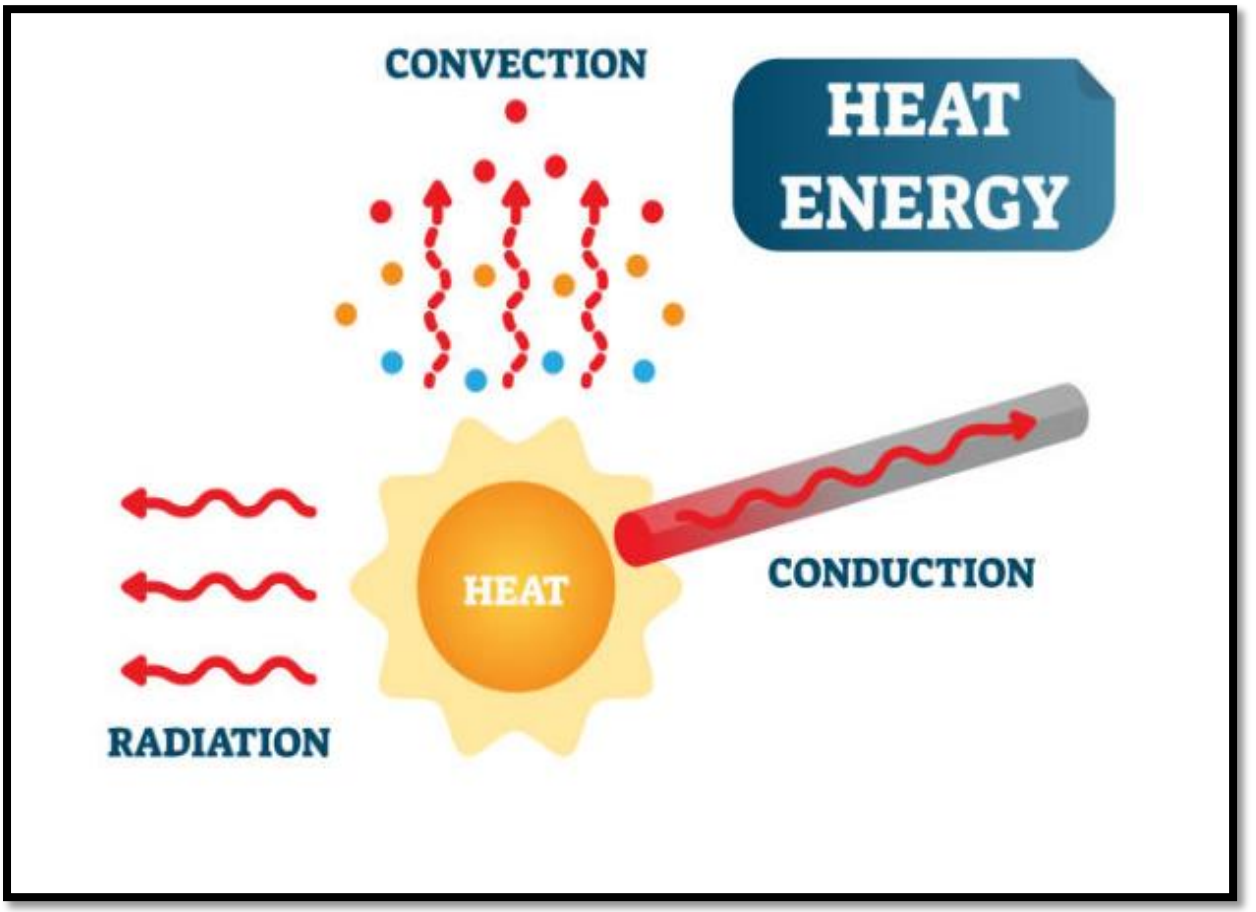

Figure 1.4 Heat radiation process

1.6 Mass transfer

In study of fluid dynamics mass transfer is very significant. In flow of nanofluid we should know about the mass transfer process. The main reason behind this is concentration gradient. Nanofluid flow occur from high concentrated region to low concentrated region and the process continue until the uniformity holds. This process is completed by diffusion and convection of fluid flow.

- **Diffusive mass transfer:**

The very first law which is related to the mass transfer is well known as Fick's first law of dispersion. Renowned inventor Adolf Fick [9] proposed it in 1855. Main proposal of this law is molar flux due to diffusion of a fluid in space is proportional to the concentration gradient. In Figure 1.5 diffusion process is shown with diagram.

$$\overrightarrow{J_x} = -D_m \nabla \phi \ , \qquad (1.5)$$

where $\overrightarrow{J_x}$ stands for molar flux, $\nabla \phi$ is concentration gradient and D_m represents proportionality constant which is also known as mass diffusion coefficient.

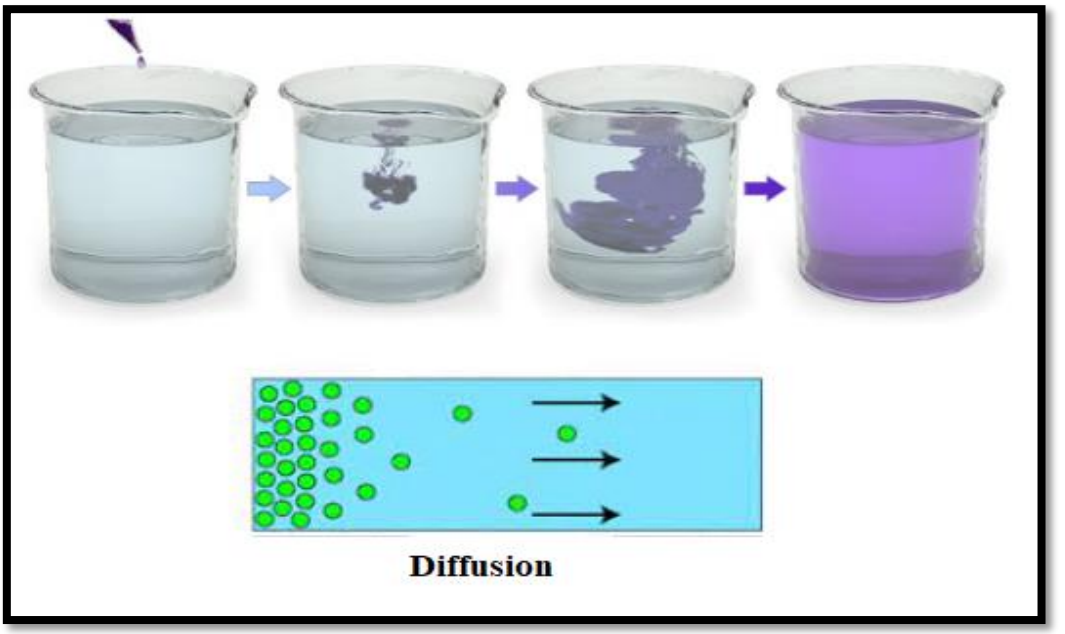

Figure 1.5 Diffusion process in a glass

- **Convective mass transfer:**

Mass transfer can also be occurred by convective process like heat transfer. It is the mixture of diffusion and advection. Diffusion is the process of random motion of molecules due to concentration gradient whereas advection is motion of molecules due to fluid velocity. Convective mass transportation can be described by Newton's law of cooling.

$$Q_m = h_m A(C_w - C_\infty)\,, \tag{1.6}$$

where Q_m stands for rate of heat transfer, h_m is mass transfer coefficient, A is area of heat transfer, C_w indicates surface concentration and C_∞ designates concentration away from the surface.

1.7 MHD flow

Magnetohydrodynamics is the study of any electrically conducting fluid flow under magnetic field. Owing to the flow of electrically conducting nanofluid under a magnetic field electric current is prompted in the system and it again has its own magnetic field. Induced current reacted to the magnetic field and create electromagnetic force which disturb the motion of fluid. The field MHD was invented by Swedish Nobel laureate Alfven [10]. The mathematical equations of MHD consists of Ohm's law of electric current, Gauss's law, Faraday's law and Ampere's law.

Let us consider electric field $\vec{E}(r,t)$ and magnetic field $\vec{B}(r,t)$ then the electromagnetic field controlled by Maxwell's equations [11] are:

$$\vec{\nabla}\cdot\vec{E} = \frac{\rho_e}{\varepsilon_0} \quad \text{(Gauss's law)}, \tag{1.7}$$

$$\vec{\nabla}\cdot\vec{B} = 0 \quad \text{(Gauss's law for magnetism)}, \tag{1.8}$$

$$\vec{\nabla}\times\vec{E} = -\frac{\partial\vec{B}}{\partial t} \quad \text{(Faraday's law)}, \tag{1.9}$$

$$\vec{\nabla}\times\vec{B} = \mu_0\vec{J} + \mu_0\varepsilon_0\frac{\partial\vec{E}}{\partial t} \quad \text{(Ampere's law)}, \tag{1.10}$$

where $\vec{J}(r,t)$ and ρ_e denote current density and charge density respectively. For static medium Ohm's law together with electrical conductivity σ expressed as

$$\vec{J} = \sigma\vec{E}\,. \tag{1.11}$$

But for electrically conducting fluid flow with velocity $\vec{u}$, the law is changed as

$$\vec{J} = \sigma\left(\vec{E} + \vec{u} \times \vec{B}\right). \tag{1.12}$$

Incorporating Maxwell's equations the output equations changed as follows

$$\frac{\partial \vec{B}}{\partial t} = \vec{\nabla} \times \left(\vec{u} \times \vec{B}\right) - \vec{\nabla} \times \left(\eta^* \vec{\nabla} \times \vec{B}\right), \tag{1.13}$$

where $\eta^* = \frac{1}{\mu_0 \sigma}$ designates magnetic diffusivity. For an ideal electrical conductor $\sigma \to \infty$, so $\eta^* \to 0$ and hence equation (1.13) reduced to

$$\frac{\partial \vec{B}}{\partial t} = \vec{\nabla} \times \left(\vec{u} \times \vec{B}\right) . \tag{1.14}$$

A unit volume fluid with magnetic field $\vec{B}(r,t)$ and current density $\vec{J}(r,t)$ encounter a MHD force called Lorentz force. Mathematical formula for Lorentz force is given by

$$\vec{F}_m = \vec{J} \times \vec{B} = \frac{1}{\mu_0}\left(\vec{\nabla} \times \vec{B}\right) \times \vec{B} . \tag{1.15}$$

If Maxwell's equations are incorporated with fluid dynamics to obtain MHD equations then the reduced equations are given as follows:

$$\frac{\partial \rho}{\partial t} + \vec{\nabla} \cdot \left(\rho \vec{u}\right) = 0 \ , \tag{1.16}$$

$$\rho\left(\frac{\partial \vec{u}}{\partial t} + \vec{u} \cdot \nabla \vec{u}\right) + \nabla \vec{p} - \rho g - \rho \nu \nabla^2 \vec{u} - \frac{1}{\mu_0}\left(\vec{\nabla} \times \vec{B}\right) \times \vec{B} = 0 \quad , \tag{1.17}$$

$$\frac{\partial \vec{p}}{\partial t} + \vec{u} \cdot \nabla \vec{p} + \gamma \vec{p} \nabla \cdot \vec{u} = 0 \ , \tag{1.18}$$

$$\frac{\partial \vec{B}}{\partial t} - \vec{\nabla} \times \left(\vec{u} \times \vec{B}\right) = 0 \ , \tag{1.19}$$

$$\vec{\nabla} \cdot \vec{B} = 0, \tag{1.20}$$

where $\vec{p}$ stands for pressure and γ denotes adiabatic index.

Application of MHD flow is largely distributed. MHD generator, power plant, nuclear reactor, solar wind flow, blood flow sensor are some important application of MHD flow. Computational astrophysics is also blessed with magnetohydrodynamics. Magnetic behavior of plasmas infusion reactor also studied by the concepts of MHD flow. Solar flares stellar and galactic eruptions can also be described by MHD flow equations.

1.8 Significant parameters of heat transfer

Nanofluids have higher thermal transportation property than ordinary fluid. Thermal features of nanofluids has noteworthy applications in science and engineering. Only particle mixing in base fluid may create nanofluids but it is not the only parameter which amplify the thermal behaviors. There are some key parameters which leads to amplified thermal properties of nanofluids. In the next subsections the parameters and their effectiveness are discussed.

- **Volume fraction of nanoparticles**

In the application of nanofluids thermal conductivity feature is most useful. Ordinary fluids which is found in nature have less thermal conductivity than any metal. Associating tiny metal particles into ordinary base fluids surely amplify thermal conductivity. Maxwell [12] addressed this amplification of thermal conductivity. Volume fraction of nanoparticles is thus one of the leading parameter to promoted thermal conductivity rate. Volume fraction ϕ can be defined as

$$\phi = \frac{\frac{4}{3}\pi r^3 N}{V} \quad , \tag{1.21}$$

here the particles are assumed as spherical in shape, N denotes the number of particles in volume V and r is the radius of the particles. When volume fraction is less than 5% then nanofluids become stable and give better thermal results.

- **Nanoparticle shape**

Thermal behavior of nanofluids is largely affected by the shapes of nanoparticles. Generally nanoparticles are of spherical and cylindrical shape. Cylindrical shaped [13] nanoparticles promises better thermal profile than spherical shape. Cylindrical shaped nanoparticles are

generally proposed by carbon nanotubes. Cylindrical shaped nanoparticles give better aspect ratio than spherical shaped nanoparticles which is the key reason behind its higher thermal profile.

- **Nanoparticle size**

Nanoparticle size is also a dominating feature for thermal profile. Smaller nanoparticle size produce more surface area which raises thermal conductivity. Heat conduction depends on surface area of nanoparticles and thus small sized nanoparticles produce better thermal output.

- **Brownian motion**

Brownian motion is movement of tiny particles which are submerged in fluid. Scottish botanist Robert Brown first study the fluctuation of particles. For example movement of dust particles in a room. Brownian motion generally increase the thermal conductivity of nanofluids. Brownian motion declines as the size of nanoparticles get increased. Brownian motion is a diffusive process and is computed by Stokes-Einstein formula with diffusive constant D_B is given by $D_B = \frac{Tk_B}{3\pi\mu_f d_p}$, where T designate Temperature, $k_B = \frac{R}{N_A}$ designates Boltzmann's constant, R stands for gas constant and $N_A = 6.022\times10^{23}$ stands for Avogadro's number, viscosity of the fluid is denoted by μ_f, particle radius is designated by $\frac{d_p}{2}$.

- **Thermophoresis**

Thermophoresis is also known as thermo- diffusion or Soret effect. It is actually the property of particle relocation in the opposite direction of temperature gradient. Generally nanoparticles move towards cooler region from warmer provinces due to temperature gradient inside the flow region. The force which accommodate the particles to relocate is called thermophoretic force.

$$\vec{j}_{s,T} = -\rho_s \phi V_T = -\rho_s D_T \frac{\nabla T}{T} \quad . \tag{1.22}$$

Thermophoretic flux is denoted by the above equation. The diffusion coefficient D_T for thermophoresis is given by McNab and Meisen [14]

$$D_T = \beta\phi\frac{\mu_f}{\rho_f} \quad , \tag{1.23}$$

where β is the proportionality factor.

- **Base fluid**

Base fluid selection is very important for thermal conductivity of nanofluid. Viscosity of base fluid affects the Brownian motion of nanoparticles which is predominant factor of thermal conductivity. Wang et al. [15] has taken copper and aluminium based nanoparticles in various base fluids like water, EG, vacuum pump oil and they got difference in thermal behavior for different base fluid.

- **pH value**

pH is one of the important key factor that influence thermal conductivity. Many result from investigation suggest that thermal conductivity decrease as the pH value get increased. Zhu et al. [16] explored that aluminium oxide based nanofluid gives almost 23% augmented value when pH is take 2.0 only but it reduced to 19% when pH value is taken 11.5. So by controlling pH value of nanofluid one can improve thermal behavior of nanofuid.

- **Surfactant**

Promoted thermal profile of nanofluid is very important for the researchers but to create highly conducted nanofluid one must keep in mind the stability of nanofluid. Nanoparticles get agglomerated and clustered after some time and become unstable. To overcome this situation surfactant is mixed with nanoparticles. Xia et al. [17] observed that in comparison of SDS and PVP surfactant over aluminium oxide based nanofuid PVP gives better control on stability.

- **Nanoparticle material**

Better thermal profile can be obtained by proper selection of nanoparticle material in the base fluid. Metallic nanoparticles give higher thermal conductivity than oxide nanoparticles. Only metallic based nanofluid preparation is very difficult so the job is done by oxidizing the particles. Recently carbon nanotube (CNT) based nanoparticles receive much more attention as this promise better thermal conductivity.

- **Electric field and Magnetic field**

Nanofluid flow is highly affected by electric and magnetic field as they are electrically and thermally conducted. Magnetohydrodynamics (MHD) flow is a specimen of nanofluid flow under

magnetic flux. From the laws of Electromagnetism it is evident that magnetic flux can creates electric current in a conducting fluid. It again creates a dragging force in the liquid which oppose the flow and it is known as Lorentz force. Lorentz force is given by

$$\vec{F} = q\left(\vec{E} + \vec{v} \times \vec{B}\right), \tag{1.24}$$

where q stands for charge of particles, $\vec{E}$ designates electric field, $\vec{v}$ is the velocity of the particles and $\vec{B}$ is magnetic field.

1.9 Thermophysical properties of nanofluid

Thermal profile of nanofluids also extensively depends on various thermophysical properties. Density(ρ), specific heat(ρc_p), Dynamic viscosity(μ), Thermal conductivity (κ) and electrical conductivity (σ) are most predominated properties. Without proper knowledge of this properties thermal behavior of nanofluid cannot be explained properly. Many more experiment is done to get some accurate output of this properties. The constant thermophysical properties for different base fluids is given in Table 1.2.

- **Density**

Density of nanofluid is measured by considering the suspended nanoparticles in the nanofluid. From the following formula one can observe that it is calculated by considering the density of both nanoparticles and base fluid.

$$\rho_{nf} = (1-\phi)\rho_f + \phi\rho_s, \tag{1.25}$$

where ρ_{nf}, ρ_f, ρ_s is designated as density of nanofluid, base fluid and nanoparticles respectively and ϕ is denoted as volume fraction.

Table 1.2 Thermo physical properties of base fluids and Nanoparticles [18, 19, and 20]

Material	$\rho(\text{kg/ m}^3)$	$C_p(\text{J/ kg K})$	$K(\text{W/ m K})$	$\beta\times10^{-5}(\text{K}^{-1})$
Pure Water	997.1	4179	0.613	21
Ethylene glycol	1114	2415	0.252	57
Engine oil (EO)	884	1909	0.145	70
Mineral Oil	920	1670	0.138	64
Silver (Ag)	10500	235	429	1.89
Copper (Cu)	8933	385	401	1.67
Aluminium	2701	902	237	2.31
Titanium Oxide(TiO2)	4250	686.2	8.9538	0.9
Alumina (Al2O3)	3970	765	40	0.85
Copper Oxide (CuO)	6510	540	18	0.85

- **Specific heat**

Specific heat capacity is a noteworthy thermophysical property which affects the thermal profile of nanofluid. The formula for specific heat is given by

$$(\rho C_p)_{nf} = (1-\phi)(\rho C_p)_f + \phi(\rho C_p)_s \qquad (1.26)$$

Subscripts nf, f and s stands for nanofluid, base fluid and nanoparticles respectively.

- **Dynamic viscosity**

Dynamic viscosity is also very promising features that control thermal profile of nanofluid. Einstein [21] gave an expression for making out the dynamic viscosity of dilute liquids that contain spherical particles. In the model, the interconnections between the particles are neglected. The expression is given as follows:

$$\mu_{nf} = (1 + 2.5\phi)\,\mu_f \,, \tag{1.27}$$

where the notations have their usual meanings. Brinkman [22] extended the above formula for relatively small volume fraction as follows:

$$\mu_{nf} = \frac{\mu_f}{(1-\phi)^{2.5}} \,. \tag{1.28}$$

- **Thermal conductivity**

Thermal conductivity is also an essential property for thermal transportation. The traditional model was given by Maxwell [12].

$$\frac{\kappa_{nf}}{\kappa_f} = \frac{(\kappa_s + 2\kappa_f) - 2\phi(\kappa_f - \kappa_s)}{(\kappa_s + 2\kappa_f) + \phi(\kappa_f - \kappa_s)} \,. \tag{1.29}$$

But the most effective thermal conductivity κ_{nf} of the nanofluid for arbitrary shaped nanoparticles according to Hamilton and Crosser [23] model is given by

$$\kappa_{nf} = \kappa_f \left[\frac{\kappa_s + (n-1)\kappa_f - (n-1)\phi(\kappa_f - \kappa_s)}{\kappa_s + (n-1)\kappa_f + \phi(\kappa_f - \kappa_s)} \right] , \tag{1.30}$$

where n is the empirical shape aspect for nanoparticles and is defined as $n = 3/\psi$ and ψ is the ratio of the sphericalness clarified as the ratio of the surface area of a sphere (with the same volume as the given particle) to the surface area of the particle. $n = 3$ Is taken for spherical shaped nanoparticles and in that case the Hamilton and Crosser model becomes identical to the Maxwell model. Also $n = 1.5$ for cylindrical (nanotube) shaped nanoparticles.

- **Electrical conductivity**

Electrical conductivity of nanofluid is given by

$$\frac{\sigma_{nf}}{\sigma_f} = 1 + \frac{3(\sigma - 1)\phi}{(\sigma + 2) - (\sigma - 1)\phi}, \quad \text{where } \sigma = \frac{\sigma_s}{\sigma_f}. \tag{1.31}$$

The subscripts are of usual meaning. It is also very important feature for thermal profile of nanofluid. As in MHD flow magnetic profile and electric profile are related together so it is noteworthy in calculating thermal transmission proficiency.

1.10 Continuum assumption of nanofluid

Nanofluids are prepared by mixing nanoparticles in a base fluid. So it is the point of argument is the rules of fluid dynamics is applicable for nanofluid? The answer is yes if it can be presumed as continuum. Under this assumption the fluid properties like pressure, temperature density are well defined. The value of Kundsen number is estimated to determine the nature of nanofluid. The formula for Kundsen number is given by

$$K_n = \frac{\lambda}{d_p} \quad , \tag{1.32}$$

where d_p is the diameter of nanoparticle and λ is the mean free path defined by

$$\lambda = \frac{RT}{\pi\sqrt{2}d_m N_A P} . \tag{1.33}$$

R is universal gas constant, T is the temperature, d_m is the molecular diameter of the base fluid, N_A is the Avogadro's constant and P is the pressure.

The value of Kundsen number declares whether the nanofluid act as continuum or not. When the Value of Kundsen number is below unity the continuum assumption is valid.

Table 1.3: Types of continuum medium for different values of K_n

K_n	**Continuum characteristics**
$0.0 < K_n < 0.01$	No slip region
$0.01 < K_n < 0.1$	Slip flow region
$0.1 < K_n < 10$	Transitional region
$K_n > 10$	Free molecular motion

1.11 General equations of nanofluid flow

In this section the governing equations of nanofluid flow is described. This equations are the key of the simulation process which are computed by MAPLE and MATLAB software. These equations are mainly continuity equation, momentum equations and energy equations.

Continuity Equation

The equation of continuity is instituted from conservation of mass. The equations can be written as follows:

$$\frac{\partial \rho_{nf}}{\partial t} + \nabla \cdot \left(\rho_{nf} \mathbf{v} \right) = 0 \ . \tag{1.34}$$

If steady and incompressible fluid is taken then it is changed to

$$\nabla \cdot \left(\rho_{nf} \mathbf{v} \right) = 0 \ . \tag{1.35}$$

Nanofluid flow with nanoparticles under Brownian migration and Thermophoresis it is as follows.

$$\frac{\partial \phi}{\partial t} + \mathbf{v} \cdot \nabla \phi = \nabla \cdot \left(D_B \nabla \phi + D_T \frac{\nabla T}{T} \right) \ . \tag{1.36}$$

Here D_B and D_T designate Brownian motion and Thermophoresis diffusive coefficients.

Momentum equations

The momentum equations are also known as Navier-Stoke's equations. The flow properties are also governed by this equations. For incompressible nanofluid flow the general momentum equations are given by

$$\rho_{nf} \left[\frac{\partial \mathbf{v}}{\partial t} + \left(\mathbf{v}.\nabla \right) \mathbf{v} \right] = -\nabla p + \mu_{nf} \nabla^2 \mathbf{v} + \rho_{nf} \mathbf{F} \ , \tag{1.37}$$

where $\mathbf{F}$ is other forces proceeding on the flow. p stands for pressure in the flow. Considering the forces due to gravity, thermal expansion and electric current density $\mathbf{J}$ under external magnetic field $\mathbf{B}$ the above equation changed to

$$\rho_{nf} \left[\frac{\partial \mathbf{v}}{\partial t} + \left(\mathbf{v}.\nabla \right) \mathbf{v} \right] = -\nabla p + \mu_{nf} \nabla^2 \mathbf{v} + \left(\rho \beta \right)_{nf} g \Delta T + \mathbf{J} \times \mathbf{B} \, , \tag{1.38}$$

where $\mathbf{v}$ is velocity, p is pressure, ρ_{nf} is density of the nanofluid, μ_{nf} is the dynamic viscosity of the nanofluid, g is force due to gravity and β_{nf} is thermal expansion coefficient of nanofluid.

Energy Equation

The first law of thermodynamics is the main idea behind the energy equations. The energy equations mainly control the temperature distribution inside the flow region. The energy equation for single phase flow model with an incompressible nanofluid is given by

$$\left(\rho C_p\right)_{nf}\left[\frac{\partial T}{\partial t}+\left(\mathbf{v}.\nabla\right)T\right]=\frac{\partial Q}{\partial t}+k_{nf}\nabla^2 T+\varphi \ . \qquad (1.39)$$

Here φ denotes the heat generation due to Joule heating and viscous dissipation. Q Is the external het source.

For Brownian motion and thermophoretic diffusion modelling the equation is given by

$$\left(\rho C_p\right)_{nf}\left[\frac{\partial T}{\partial t}+\left(\mathbf{v}.\nabla\right)T\right]=\frac{\partial Q}{\partial t}+k_{nf}\nabla^2 T+\left(\rho C_p\right)_s\left\{D_B\nabla\phi\cdot\nabla T+D_T\frac{\nabla T\cdot\nabla T}{T}\right\}. \qquad (1.40)$$

1.12 Applications of nanofluid

Continuously escalating research on nanofluids gives us lucrative heat transmission rate than ordinary fluids. It has vast applications on science and engineering field. Major field applications are described below.

- **Industrial cooling:**

Nanofluids used as a cooling appliance in various industries. Nano fluids save almost 1 trillion Btu of energy in the US industrial sector. Where as in the US electric production sector nanofluids save almost 10 to 30 trillion Btu energy [24, 25]. Closed loop cooling technique with nanofluid and nanotechnology based heat transfer of fluids that enhanced the thermal properties by 10-50 percent than ordinary fluids. This industrial grade coolants are used in many public usage based industries like food and beverage processing industries, oil and gas industries, chemical and plastic industries and many more.

- **Nuclear reactors:**

In this new era nuclear power is most useful power for generation of electricity. Nuclear power is also an important tool to determine the potential of any country. Interior water system and exterior water system are used in nuclear reactors. The exterior water system absorb the heat and electrical energy produced by the nuclear reactors. Interior water system is used as a coolant and also as a neutron moderator. Emergency shut down and removal of thermal energy is a big problem in the nuclear reactor which can be optimized by proper use of nanofluids as a coolant. [26, 27]

- **Automobile:**

Heavy duty engines which create high level thrusts are required to release thermal energy to function properly. Higher horsepower engine require higher cooling capacity to operate smoothly. Ethylene glycol based nanofluids are used as a coolant of engine [28, 29]. Tzeng et al. [30] mixed up cupper based oxides and aluminium based oxides into the engine transmission oil to enrich the cooling capacity and get desired result.

- **Space and defense sectors**:

Space and defense sector is most important for any nation. In space research limitation of volume and weight is prime factor. As a result a high capacity cooling technique is required to fulfill its engineering requirement keeping its limitation. Ordinary fluids hardly satisfy the above mentioned constraints, so we use high capacity nanofluids to overcome the problem. Rocket engine, jet engine, submarine engine are appropriate examples of system where nanofluids play a vital role. Many more military instruments and space instruments improved to its advanced features with the help of such efficient cooling capacity.

- **Electronic applications**:

Electronic engineering field is an area of application of nanofluid for its fast thermal dissipation properties. Several electronic instruments such as microchips, processors are blessed with nanofluid cooling technique. Notebook computers desktop laptops are designed with phase

changed liquid cooling heat pipes. Ma et al. [31] developed the system of oscillating heat pipes which has several applications on electronic gadgets [32]

- **Solar equipment**:

Solar energy is very much important for this new era as it is a very useful renewable energy source. Satellites, electronic gadgets are blessed with solar energy has a problem of high thermal energy absorption. This high thermal energy can damage the gadgets. Nanofluid cooling system solve the problem of thermal intensity in solar equipment. Liu et al. [33] used copper oxide based nanofluid in a compound parabolic concentrator and found high level thermal properties than ordinary base fluids like water.

- **Nanodrug delivery:**

Activity and proficiency of drug can be improved by colloidal distribution of nanoparticles. Gold particles exhibits nontoxic transports of drugs and also in gene - delivery applications. Sun et al. [34] noticed the application of nanographene oxide for drug delivery and cellular imaging. Several functional features of nanoparticles can amplify the effectiveness of drug in various way.

- **Nanocryosurgery**:

Nanocryosurgery is a technique of medical advantage using the freezing procedure to remove unwanted tissues. Yan and Liu [35] distinguish between conventional cryosurgery and nanocryosurgery. They found higher freezing rate in case of nanocryosurgery which is more effective than ordinary one.

- **Other applications**:

Above all applications are noteworthy besides that many more field of applications [36] are there for nanofluids. It has vast application in the area of fuel capacity enhancing, LED floodlight, vehicle brake fluid, coolant, microbial fuel, lubricants, food processing, energy storage, biomedical applications and many more.

1.13 Literature review

A fluid including particle of nanosized is called a nanofluid. Generally the metals, carbides, oxides are used to construct nanofluid with host fluids like oil, water, ethylene glycol, kerosene etc. The fully immersed ingredients are termed as nanoparticles. Nowadays, to gain effective heat transport features researchers incorporated different shaped nanoparticles, because variation of base medium, size and choice of particles influence the effective conductivity. Choi [1] first amplify the thermal influencing activity of fluids using nanoparticles. Crane [37] first discussed the flow over a stretching plate. Heat transfer on a stretching sheet having suction was considered by Gupta and Gupta [38]. Anderson et al. [39] considered an unsteady stretched surface to pass the flow. Nanofluid flow runs over stretching sheet having provisions of convective boundary layer was conceived by Makinde and Aziz [40]. Mabood et al. [41] explored the attributes of Brownian motion and thermophoresis when nanofluid passed over a revolving stretching sheet. They have also considered the effect of radiation and magnetic field. The analogous problem but with a slender stretching surface and slip effects was considered by Redddy et al. [42]. In the recent past some semi-analytical as well as numerical methods have been developed in the literature. They are used to get more precise approximate outcomes of the nonlinear governing equations. Differential transformation method (DTM) [43-46], variation parameter method (VPM) [47, 48]. Variational iteration method [49], adomian decomposition method (ADM) [50,51], homotopy perturbation method (HPM) [52], homotopy analysis method (HAM) [53,54], natural decomposition method [55] and many more methods give approximate solutions with higher accuracy. Thriveni and Mahanthesh [56] reported the nonlinear radiative and quadratic convective MHD Cu-Al_2O_3/H_2O hybrid nanoliquid stream within an annulus. The consequences suggest for skin friction nonlinear convection is most favorable. Mahanthesh et al. [57] addressed the magnetically influenced and dissipative Ag-MoS_2 hybrid nanofluid stream passing over the isothermal wedge. They noted that thermal increment and heat transfer are reduced for the magnetic field. Ahmadian et al.[58] numerically described Ag-MgO/water-based hybrid nanofluid stream through downward-upward moving wavy disk. Consequences convey the heat transmission enhancement of about 15% for the wavy surface as compared to flat ones. Tassaddiq et al. [59] disclosed the heat and mass transmission performance of SWCNT-MWCNT-Fe_3O_4 /water hybrid flow over the impermeable swirling disk. They showed that carbon nanotube and Fe_3O_4 based nanocomposite exhibits

effective heat transmission and thermal efficiency compared to single ferrite nanoparticles. Hayat et al. [60] discussed the entropy analysis of dissipative and radiative magnetohydrodynamic flow owing to a revolving disk. The consequence indicates the reduction in entropy for the magnetization.

Iiaz et al. [61] described the entropy analysis of chemically reactive radiative Sisko nanofluid stream over a swirling disk. The outcomes reveal the entropy enhancement for the magnetic presence. Zeeshan et al. [62] addressed the shape impact of nanosized particles on the entropy minimization of unsteady mixed convective nanoliquid flow through a revolving disk. They suggested the spherical-shaped nanoparticle to diminish the entropy. Nadeem et al. [63] investigated the radiative Darcy–Forchheimer nanofluid flow passing through a swirling disk assuming heat sink/source existence. They reported the entropy enhancement for magnetic and radiation parameters. Lubrication aspects of magneto nanofluid flow was considered by Ahmad et al. [64]. Oldroyd –B fluid MHD flow with cross diffusion was reported by Sandeep and Reddy [65]. Streamline study of micropolar liquid with carbon nanotube was investigated by Reddy and Kumar. [66] They have also introduced Cattaneo Christov feature in their study. Oldroyd – B fluid flow across a cone under the influence of Cattaneo Christov heat flux was investigated by Reddy [67]. Analysis of radiation enforcement over Brownian motion together with chemical reaction was discussed there. Chemical reaction played a vital role on concentration framework. This problem was considered by Khan et al. [68] for Carreau-Yasuda nanofluid. They have also considered nonlinear stretching foil accompanied by chemical reaction. Gireesha et al. [69] analyzed the nonlinear stretching flow in appearance of chemical reaction framework. Eid et al. [70] studied the chemically reacted Prandtl nanofluid. Escalation of concentration profile for chemically reacted nanofluid was spotted by them. Many geometric models like rotating disk, stretching sheet, circular disk and curved stretching sheet are very much used in fluid flow. Curved stretching surfaces are of significant interest for the researchers. Yasmin et al. [71] considered the micro polar flow guiding by stretching sheet of curved nature. They explored curvature radius lift up temperature profile besides that concentration lines also inflated. Importance of Stefan gusting and convective warmth shifting in nanofluid flow atop a curved sort of stretching sheet accompanied by reaction of chemical elements was investigated by Manjunatha et al. [72].

Nield and Kuznetsov [73] presented a hypothesis related to volume fragment of nanoparticle. They had controlled the properties of nanoparticle to organize the temperature at

boundary layer. Kuznetsov and Nield [74] also considered the problem with different aspect. Besides Brownian motion they [75, 76] included thermophoresis parameter as well to get more appropriate realistic approach. Presently it is presumed that there exist no normal flux at the superficial area not only that but also the nanonoparticle fraction value adjust accordingly. The supposition of constant nanoparticle concentration at the superficial area is considered as active control of the nanoparticles concentration. The same authors again studied the problems by considering a new setup boundary provisions for nanoparticles concentration at the surface of the plate which is more realistic, since it includes the effects of two parameters, Brownian motion and thermophoresis. Since then, models are presented in order to analyze active and passively controlled flow of nanoparticles. Actively and passively controlled nanofluid flow was analyzed by Halim et al. [77, 78]. Squeezed flow by active and passive control of nanofluid under thermal radiation was inspected by Atlas et al. [79]

At nanolevel no slip criteria is not properly effective. Velocity slip effect between the layers highly influence the nanofluid flow and its thermophysical phenomena. Change of pressure is also a reason behind the slip in the fluid flow. Navier [80] declares that component of tangential velocity of fluid at its surface is proportional to tangential stress. He also reported the appropriate boundary conditions. Stagnation point flow of nanoliquid along a convectively heated stretching surface was taken by Nandi et al. [81].They have taken partial slip and also investigated the outcomes numerically and statistically. Seth et al. [82] considered the exponential stretching sheet with partial slip effect. They found influence of slip parameter over velocity lines. Peristaltic flow of Prandtl nanofluid was taken by Hayat et al. [83]. They have incorporate inclined magnetic field and also slip effect. Upreti et al. [84] assessed the quantity of entropy generation in three dimensional flow. They have taken hybrid nanofluid with convective conditions and the heat lines are found to be very effective. Wu [85] reported the second order slip effect for randomly selected Kundsen number. Turkyilmazoglu [86] solved the flow equations analytically due to second order slip condition and found that it influence the heat and mass transfer. Mabood and Das [87] taken second order slip effect over a sheet expandable in single direction. They found that incorporation of melting effect together with second order slip, influence the flow characteristics. Fang et al. [88] investigate second order slip prototype through a shrinking sheet. They found the effect of two slip parameters in the flow characteristics, and observed that the effect of second order parameter is lesser than the first order.

Nanofluid flow through a wedge with suction and injection effect was studied by Watanabe [89]. Chamkha et al. [90] take vertical wedge immersed in a porous medium under radiation effect. Finite difference method was incorporated to solve Falkner Skan equation by Asaithambi [91]. Gorla et al. [92] extended the wedge problem considering mixed convection of nanofluid in porous medium. They considered vertical wedge to perform their investigation. Khan and Pop [93] investigated the effect of nanofluid flow over a moving wedge. Kandasamy et al. [94] considered Heimenz flow of Cu–water nanofluid over porous wedge. They also incorporated solar radiation in the system. Rahaman and Eltayeb [95] considered thermal jump and convective condition for a rarefied fluid flow through a wedge. Krishna and Chamkha [96] discussed the MHD flow under Hall effects between two parallel plates. Rahaman and Amira [97] looked into the fluctuating transport properties of nanofluid flow over a wedge. They also considered nonlinear slip and found locally similar solution of the system.

1.14 Thesis Layout

Some nanofluid models are explored in this thesis. The flow characteristics including hydrothermal features are discussed here. Various geometries are considered and different materials are mixed to create several nanofluids. The models are solved numerically and in for some cases analytically also. The results are discussed with proper graphs and tables. The models discussed in the thesis might have some applications in science and technology. Different flow models considered in the thesis are given in the following chapters. Chapter 2 illustrates the entropy generation investigation of hybrid nanofluidic transport over an unsteady spinning disk. The magnetic influence, velocity slips, and thermal radiative effects are included within the flow. Ferrous oxide (Fe_3O_4) and graphene oxide (GO) are employed as tiny nanoingredients, and water (H_2O) is the base medium. The dimensional leading equations are settled to dimensionless nonlinear ordinary differential equations (ODEs) by significant similarity transformations. Then classical RK-4 (Runge Kutta 4^{th} order) scheme with a shooting process has been initiated to execute the numerical simulation. The software MAPLE is employed to run the entire simulation with an indispensable accuracy rate. Several streamlines, graphs, and requisite tables are executed to divulge the parametric impact on the nanofluidic stream. Entropy generation-related figures are depicted for diverse parameters and parametric effects on Bejan number are also analyzed.

Moreover, corresponding physical consignment like the measure of the frictional hindrance, heat transport are calculated and reviewed.

Chapter 3 explores a novel conviction of hybrid nanosuspension with an enhanced model under inclined magnetic field along with its thermophysical properties. Surface slip plus permeable texture of the sheet reveal excellent points of the flow. The prime equations are changed to ODEs with the assistance of similarity transformation and subsequently solved numerically. A hybrid nanofluid with Ag and CuO nanoparticles as well as CuO for usual nanofluid with water as base fluid are taken to explore salient attribute and parameters. Several graphs, streamlines, contours are presented to convey the impact of inclined magnetism of hybrid condensed structure of the flow. Reduced frictional coefficient and heat transfer coefficient are calculated and reviewed.

Chapter 4 explores the active and passive control implementation on the nanofluid flow over a stretching cylinder. Realistic velocity slip and thermal jump properties are included. Appearance of external heat source and magnetic influence is also reckoned. Concentration and temperature profiles are modified due to integration of Brownian motion together with thermophoresis. Leading equations are transformed into ODEs by suitable similarity transformation and then solved by RK-4 shooting technique. Entire simulation is settled by MAPLE software with proper rate of accuracy and the outcomes are portrayed by graphs and tables. Results are compared considering both slip and without slip conditions, whereas the concentration profile is described under active and passive control conditions.

Chapter 5 reveals the consequences of steady and unsteady nanofluid flow over a bidirectional stretching sheet. A magnetic field is assumed to be working in the normal direction. The Brownian motion together with thermophoresis is taken into consideration. Moreover, chemical reaction within the nanoingredients also included in this study. The leading equations of the considered model are transferred to nonlinear ordinary differential equations (ODEs) by appropriate similarity transformation. Differential transformation method (DTM) is used to solve the set of ODEs. MAPLE software is used to solve this with the desired accuracy rate. Results are presented with graphs and tables. Corresponding physical quantities such as Nusselt number, skin friction and Sherwood number are exhibited. Excellent improvement in heat and mass transfer are observed, which can be visualized by tables.

In Chapter 6, the steady flow of an incompressible viscous electrically conducting hybrid nanofluid is considered over a rotating disk under magnetic field. The nanoparticles titanium oxide

(TiO_2) and ferrous ($CoFe_2O_4$) are used with its physical properties and water is considered as host liquid. The foremost purpose of this study is that how hydrothermal integrity varies for hybrid nanosuspension over a spinning disk in presence of magnetic orientation. Governing equations with boundary conditions are transformed by similarity transformations and then solved numerically with RK-4 method. A comparison of linear and nonlinear thermal radiation for the above mentioned parameters are considered and efficiency of nonlinear radiation is established. The same phenomena over nanofluid and hybrid nanofluid are also discussed.

In Chapter 7, the second order slip effect under multiple convective conditions are considered. Nanofluid flow is taken over a permeable stretching cylinder. Suction and injection of nanofluid together with Brownian motion and thermophoresis is also incorporated in this study. Transformation of leading partial differential equations is done with the help of appropriate similarity transformation. The nonlinear Ordinary differential equations (ODEs) are solved by Runge Kutta 4^{th} order (RK-4) method with shooting technique. MAPLE software is used to simulate the system with a degree of precision of 10^{-6}. Several graphs and tables are included to exhibit the findings in this investigation.

The Casson nanofluid flow over a sheet which is curved and stretching in nature is analyzed in chapter 8. Radiation and slip provisions are also taken into consideration. Magnetic field of uniform rate is assumed. Convective heat and mass transfer extract dominant conclusions from the system. The Brownian migration together with thermophoresis are also included into the flow structure. Moreover, chemical reaction of higher order within the nanoingredients also attracts an interest. Guiding equations furnished by the selected model are resettled to ODEs of nonlinear type by proper similarity transformation. We have worked on MAPLE software to work out this with the suitable accuracy rate. The numerical results thus obtained are discussed with the help of diagrams and tables. Corresponding physical quantities such as Nusselt number, skin friction and Sherwood number have been analyzed. Magnificent advancement in heat sifting is disposed by magnetic and Brownian motion specification. The graphs prescribed the effects of thermophoresis and slip parameter.

Chapter 9 investigates the effects of actively and passively controlled nanofluid flow over a wedge. Comparison is done for various wedge angle parameter. Magnetic field is employed in normal to the flow direction. Velocity slip effect and external heat source are considered into the system. Leading partial differential equations are converted to nonlinear ordinary differential

equations with the help of suitable similarity transformation. Runge Kutta -4 method with shooting technique is used to solve the system. MAPLE software is applied to simulate the whole system. The results are described by graphs and corresponding values of physical interest are tabulated properly.

In Chapter 10 we have investigated multiple slippery consequences along a stretching cylinder. Brownian migration along with thermophoresis are considered together with an external heat source. Magnetic influence is considered perpendicular to the axis of cylinder. Standard flow equations are transformed into Ordinary Differential Equations by proper similarity transformations. They are solved numerically by Runge Kutta scheme of 4^{th} order (shooting technique) method with the assistance of MAPLE software. Entire simulation is done with proper accuracy rate and finally portrayed by graphs and tables. Comparisons are made assuming no slip and with slip provisions.

Chapter 11 explores the nanofluid flow on curved stretching surface under magnetic influence. Realistic velocity slip together with convective boundary condition is imported. The system is also blessed with radiation and higher order chemical reaction. Active and passive control of nanoparticles are considered and under both boundary conditions the flow analysis is compared. Leading equations of the system is a set of partial differential equations which are transformed by similarity variables into a set of highly nonlinear ordinary differential equations (ODEs). The system is solved by Runge Kutta 4^{th} order method (RK-4) with shooting technique. The simulation is done by MAPLE-2021 software. Outcomes are portrayed in terms of several graphs and tables and comparison for different conditions are also included. Velocity lines are compared for suction and injection effect, but thermal and concentration profiles are compared under active and passive control of nanoparticles.

1.15 List of Published Papers

1. N. Acharya, S. Maity and P.K. Kundu, “Entropy generation optimization of unsteady radiative hybrid nanofluid flow over a slippery spinning disk”, Proceedings of the Institution of Mechanical Engineers, Part C, 236(11) (2022), 6007-6024.
2. N. Acharya, S. Maity and P.K. Kundu, “Influence of inclined magnetic field on the flow of condensed nanomaterial over a slippery surface: the hybrid visualization”, Applied Nanoscience, 10 (2019), 633-647.
3. S. Maity and P.K. Kundu, “Influence of active and passive control of nanoparticles for the magnetized nanofluid flow over a slippery stretching cylinder”, International Journal of Modern Physics B, 37(19) (2023), 2350184.
4. N. Acharya, S. Maity and P.K. Kundu, “Differential transformed approach of unsteady chemically reactive nanofluid flow over a bidirectional stretched surface in presence of magnetic field”, Heat Transfer, 49(6) (2020), 3917-3942.
5. N. Acharya, S. Maity and P.K. Kundu, “Framing the hydrothermal features of magnetized TiO2–CoFe2O4 water-based steady hybrid nanofluid flow over a radiative revolving disk”, Multidiscipline Modeling in Materials and Structures, 16(4) (2019), 765-790.
6. S. Maity and P.K. Kundu, “Influence of second order slip and multiple convective conditions on magnetized Nanofluid flow over a permeable stretching cylinder”, International Journal of Modern Physics B, 37(30) (2023), 2350270.
7. S. Maity and P.K. Kundu, “Magnetically driven chemically reactive Casson nanofluid flow over curved surface with thermal radiation”, Heat Transfer, 51(6) (2022), 4882-4905.
8. S. Maity and P.K. Kundu, “Active and passive control of nanoparticles under the influence of magnetized nanofluid flow over a convectively heated slippery wedge”, Journal of Nanofluids, 12 (2023), 2273-2284.
9. S. Maity and P.K. Kundu, “Influence of multiple slips on magnetically driven nanofluid flow over an externally heated stretching cylinder”, Heat Transfer, 52(2) (2023), 1395-1412.
10. S. Maity and P.K. Kundu, “Magnetically driven nanofluid flow over a slippery bended Surface under thermal radiation and higher order chemical reaction”, Modern Physics Letters B, (2024), 2450131.

CHAPTER 2

Entropy Generation Optimization of Unsteady Radiative Hybrid Nanofluid Flow over a Slippery Spinning Disk*

2.1 Introduction

In this chapter, an unsteady, thermally radiative magnetized water-based hybrid nanoliquid with graphene and ferrous oxide over a revolving slippery disk is investigated. The nonlinear leading equations after reducing to ODEs by proper similarity transformation, RK-4 shooting technique is introduced to unravel the system and the simulation is done via MAPLE-2018 software. The hydrothermal consequences, entropy, Bejan numbers are plotted and deliberated for various parameters. The heat trasnsfer and frictional effects are also calculated which will perform to advance the engineering apparatus. All the outcomes are described graphically and comparison is done over nanofluid and hybrid nanofluid. Graphene nanofluids exhibit enhanced thermal conductivity, specific heat capacitance and improved heat transfer rate. There are least possibility of erosion, corrosion, thermal and chemical stability [98-99]. The impressive application of graphene nanoparticles is assured in microbial fuel cells, solar cells, biomedical applications, tissue engineering, cancer therapy, drug delivery, biosensing, etc. The graphene nanoparticle proves to be the best medium for gene and drug delivery applications because of its ultrahigh surface area. Magnetic nanosized particles seem to be most efficient owing to their biomedical functions. Thus, the mixture of graphene and Fe_3O_4 water-based hybrid nanofluid will probably improve the biotechnological functions of cancer therapy, drug delivery, and related issues. As per the authors' knowledge, no study till now has been reported that provides information on the above mentioned issues.

***This chapter is based on the paper published in: Proceedings of the Institution of Mechanical Engineers Part C (SAGE), 222 (2016), 42-37, (SCI).**

2.2 Mathematical formulation

2.2.1 Governing equations

A viscous laminar unsteady incompressible hybrid nanofluid flow is assumed over a single free to move disk with angular velocity speed $\frac{\Omega}{1-\lambda t}$ about the z-axis, where $1-\lambda t>0$ and the dimension of λ is Sec^{-1}. A time-dependent magnetic strength $B=\frac{B_0}{\sqrt{1-\lambda t}}$ is applied perpendicular to the disc. The spinning disk is set down at $z=0$ and the fluid is outspread over $z\geq 0$. The disk surface consumes an invariable temperature T_w while T_∞ is the free streamlet temperature. We also assumed that there is no chemical reaction between the nanoparticles, absence of thermal jump, joule heating is also considered. Under these circumstances, the equations which lead the system are noted below following [100-102, 62]:

$$\frac{\partial u}{\partial r}+\frac{u}{r}+\frac{\partial w}{\partial z}=0 \tag{2.1}$$

$$\rho_{hnf}\left(\frac{\partial u}{\partial t}+u\frac{\partial u}{\partial r}-\frac{v^2}{r}+w\frac{\partial u}{\partial z}\right)+\frac{\partial p}{\partial r}=\mu_{hnf}\left(\frac{\partial^2 u}{\partial r^2}+\frac{1}{r}\frac{\partial u}{\partial r}-\frac{u}{r^2}+\frac{\partial^2 u}{\partial z^2}\right)-\sigma_{hnf}B^2u \tag{2.2}$$

$$\rho_{hnf}\left(\frac{\partial v}{\partial t}+u\frac{\partial v}{\partial r}+\frac{uv}{r}+w\frac{\partial v}{\partial z}\right)=\mu_{hnf}\left(\frac{\partial^2 v}{\partial r^2}+\frac{1}{r}\frac{\partial v}{\partial r}-\frac{v}{r^2}+\frac{\partial^2 v}{\partial z^2}\right)-\sigma_{hnf}B^2v \tag{2.3}$$

$$\rho_{hnf}\left(\frac{\partial w}{\partial t}+u\frac{\partial w}{\partial r}+w\frac{\partial w}{\partial z}\right)+\frac{\partial p}{\partial z}=\mu_{hnf}\left(\frac{\partial^2 w}{\partial r^2}+\frac{1}{r}\frac{\partial w}{\partial r}+\frac{\partial^2 w}{\partial z^2}\right) \tag{2.4}$$

$$\left(\rho C_p\right)_{hnf}\left(\frac{\partial T}{\partial t}+u\frac{\partial T}{\partial r}+w\frac{\partial T}{\partial z}\right)=\kappa_{hnf}\left(\frac{\partial^2 T}{\partial r^2}+\frac{1}{r}\frac{\partial T}{\partial r}+\frac{\partial^2 T}{\partial z^2}\right)-\frac{\partial q_r}{\partial z} \tag{2.5}$$

Where, the simplification of radiative heat flux q_r can be done by Rosseland approximation $q_r=-\frac{4\sigma^*}{3\kappa^*}\frac{\partial T^4}{\partial z}$ and the Taylor series expansion of T^4 about T_∞ ignoring higher-order terms we get $T^4\approx 4TT_\infty^3-3T_\infty^3$ [103,104].

2.2.2 Thermophysical properties

In the simulation, water is taken as the base fluid. Graphene and Ferrous oxide are taken as nanoparticles to make the hybrid nanosuspension, whereas only graphene oxide is introduced to simulate the mono nanofluid. Thermophysical details are listed in Table 2.1. The results for mono nanofluid are gained by replacing the second particle concentration value (ϕ_2) as zero. This investigation is executed for both hybrid and mono nanofluid. The comparison is also given in this work. The thermophysical models of Takabi et al. [105] and Chamkha et al. [106] in Table 2.2 are used to exhibit the hydrothermal interactions smoothly. The thermophysical properties for mono nanofluid are given by Oztop and Abu-Nada [107], Maxwell [11].

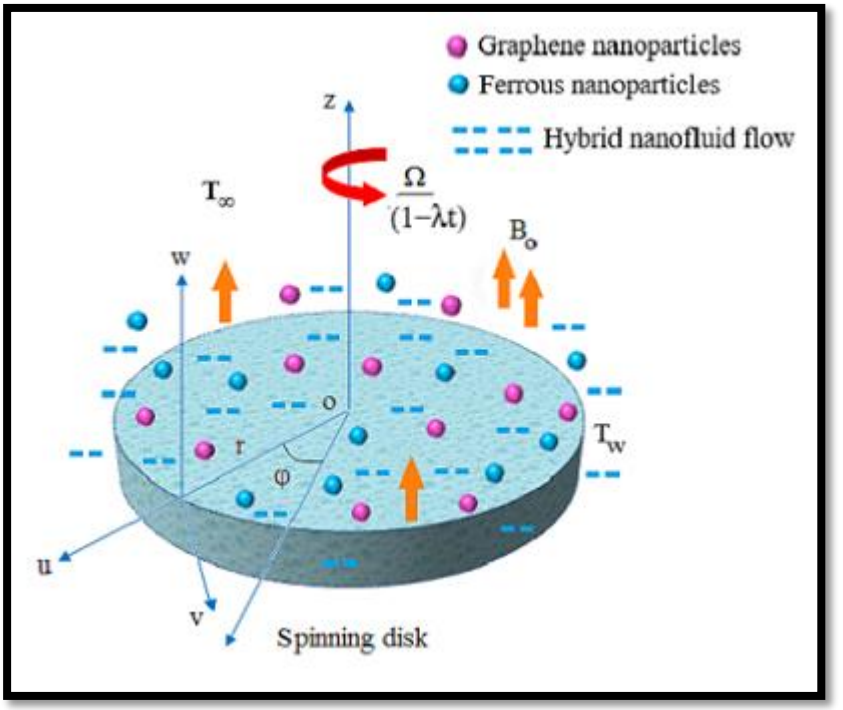

Figure 2.1 Schematic of the hybrid nanofluidic transport

Table 2.1: Thermophysical properties of base fluid and nanoparticles [99, 108]

Physical properties	**Water**	**Graphene oxide**	Fe_3O_4
C_p **(J/Kg K)**	4180	2100	670
ρ **(Kg/m^3)**	997	2250	5180
κ **(W/mK)**	0.6071	2500	9.7
σ $(\Omega m)^{-1}$	0.005	10^7	25000

2.2.3 Boundary conditions

The suitable boundary restrictions are as follows:

$$\left.\begin{aligned} u = \frac{\alpha\Omega r}{1-\lambda t} + L\frac{\partial u}{\partial z},\ v = \frac{\Omega r}{1-\lambda t} + L\frac{\partial v}{\partial z},\ w = 0,\ T = T_w \ \ at\ z = 0, \\ and \\ u \to 0, v \to 0, T \to T_\infty \qquad at\ z \to \infty. \end{aligned}\right\} \tag{2.6}$$

Where α denotes the stretching factor and $L = L'\sqrt{1-\lambda t}$.

2.2.4 Similarity transformation

To translate the system of equation dimensionless we have to use the following conversion [62] where η is the similarity variable.

$$\left.\begin{aligned} \eta = \sqrt{\frac{\Omega}{\nu_f(1-\lambda t)}}z,\ \ u = \frac{r\Omega}{1-\lambda t}f(\eta),\ v = \frac{r\Omega}{1-\lambda t}g(\eta), \\ w = \sqrt{\frac{\nu_f\Omega}{(1-\lambda t)}}h(\eta),\ \theta(\eta) = \frac{T-T_\infty}{T_w-T_\infty},\ \overline{p} = -\frac{\mu_f\Omega}{1-\lambda t}P(\eta). \end{aligned}\right\} \tag{2.7}$$

Table 2.2: Thermophysical models of hybrid nanofluid and mono nanofluid [121, 124, and 126]

Properties	**Nanofluid** $(Graphene/water)$
Density	$\rho_{nf}=(1-\phi)\rho_f+\phi\rho_s$
Heat capacity	$(\rho C_p)_{nf}=(1-\phi)(\rho C_p)_f+\phi(\rho C_p)_s$
Viscosity	$\mu_{nf}=\dfrac{\mu_f}{(1-\phi)^{2.5}}$
Thermal conductivity	$\dfrac{\kappa_{nf}}{\kappa_f}=\dfrac{\kappa_s+2\kappa_f-2\phi(\kappa_f-\kappa_s)}{\kappa_s+2\kappa_f+\phi(\kappa_f-\kappa_s)}$
Electrical conductivity	$\dfrac{\sigma_{nf}}{\sigma_f}=1+\dfrac{3(\sigma-1)\phi}{(\sigma+2)-(\sigma-1)\phi}, where\ \sigma=\dfrac{\sigma_s}{\sigma_f}$
Properties	**Hybrid Nanofluid** $(Fe_3O_4\ and\ Graphene/water)$
Density	$\rho_{hnf}=(1-\phi_1-\phi_2)\rho_f+\phi_1\rho_1+\phi_2\rho_2$
Heat capacity	$(\rho C_p)_{hnf}=(1-\phi_1-\phi_2)(\rho C_p)_f+\phi_1(\rho C_p)_1+\phi_2(\rho C_p)_2$
Viscosity	$\mu_{hnf}=\dfrac{\mu_f}{(1-\phi_1-\phi_2)^{2.5}}$
Thermal conductivity	$\dfrac{\kappa_{hnf}}{\kappa_f}=\left\{\dfrac{\kappa_1\phi_1+\kappa_2\phi_2}{\phi_1+\phi_2}+2\kappa_f+2(\kappa_1\phi_1+\kappa_2\phi_2)-2(\phi_1+\phi_2)\kappa_f\right\}\times\left\{\dfrac{\kappa_1\phi_1+\kappa_2\phi_2}{\phi_1+\phi_2}+2\kappa_f-2(\kappa_1\phi_1+\kappa_2\phi_2)+(\phi_1+\phi_2)\kappa_f\right\}^{-1}$
Electrical conductivity	$\dfrac{\sigma_{hnf}}{\sigma_f}=1+\dfrac{3\left(\dfrac{\phi_1\sigma_1+\phi_2\sigma_2}{\sigma_f}\right)-3(\phi_1+\phi_2)}{2+\left\{\dfrac{\phi_1\sigma_1+\phi_2\sigma_2}{(\phi_1+\phi_2)\sigma_f}\right\}-\left\{\dfrac{\phi_1\sigma_1+\phi_2\sigma_2}{\sigma_f}-(\phi_1+\phi_2)\right\}}$

2.2.5 Dimensionless appearance

After applying the transformation given in equation (2.7) to the equations (2.1)-(2.5), we get the following dimensionless form:

$$2f + h' = 0 \tag{2.8}$$

$$f'' - \frac{A_1}{A_4}\left\{ f^2 - g^2 + hf' + S\left(f + \frac{\eta}{2} f' \right) \right\} - \frac{A_5}{A_4} Mf = 0 \tag{2.9}$$

$$g'' - \frac{A_1}{A_4}\left\{ 2fg + hg' + S\left(g + \frac{\eta}{2} g' \right) \right\} - \frac{A_5}{A_4} Mg = 0 \tag{2.10}$$

$$A_1\left\{ hh' + \frac{S}{2}\left(h + \eta h' \right) \right\} = -P' + A_4 h'' \tag{2.11}$$

$$\frac{1}{\Pr}\left(1 + \frac{4N}{3A_3} \right)\theta'' - \frac{A_2}{A_3}\left(h\theta' + S\frac{\eta}{2}\theta' \right) = 0 \tag{2.12}$$

Where, $A_1 = \frac{\rho_{hnf}}{\rho_f}, A_2 = \frac{(\rho C_p)_{hnf}}{(\rho C_p)_f}, A_3 = \frac{\kappa_{hnf}}{\kappa_f}, A_4 = \frac{\mu_{hnf}}{\mu_f}, A_5 = \frac{\sigma_{hnf}}{\sigma_f}$

The boundary conditions in equation (2.6) are also converted through the similarity transformation as in (2.7). The reduced boundary conditions are given by:

$$\left.\begin{array}{c} f(0) = \alpha + L_s\, f'(0),\ g(0) = 1 + L_s\, g'(0),\ h(0) = 0,\ \theta(0) = 1 \\ f(\infty) = 0,\ g(\infty) = 0,\ \theta(\infty) = 0 \end{array}\right\} \tag{2.13}$$

Some parameters are noted as local parameters, but it is still convincing to study the flow dynamics because such an approach preserves mass and momentum equations [109,110].

2.2.6 Physical quantities

The quantities of engineering attention are mainly the frictional coefficient and Nusselt number which are given in equation (2.14):

$$\left.\begin{array}{c} C_f = \dfrac{\sqrt{\tau_{wr}^2 + \tau_{w\varphi}^2}}{\rho_{hnf}\left(\dfrac{r\Omega_v}{1-\lambda t} \right)^2},\ Nu = \dfrac{rq_w}{\kappa_f\left(T_w - T_\infty \right)} \end{array}\right\} \tag{2.14}$$

Where, $$\tau_{wr}=\mu_{hnf}\left(\frac{\partial u}{\partial z}+\frac{\partial w}{\partial r}\right)_{z=0},\tau_{w\varphi}=\mu_{hnf}\left(\frac{\partial v}{\partial z}+\frac{1}{r}\frac{\partial w}{\partial \varphi}\right)_{z=0},\ q_w=-\kappa_{hnf}\left(\frac{\partial T}{\partial z}\right)_{z=0}+q_r\big|_{z=0}\Bigg\}$$

(2.15)

Converting them into dimensionless form after registering the similarity transformation, we get the reduced skin frictional coefficient and Nusselt number. The results are as follows:

$$C_{fr}=\sqrt{\mathrm{Re}_z}C_f=\left\{\frac{\left(1-\phi_1-\phi_2\right)^{-2.5}}{\left(1-\phi_1-\phi_2\right)+\phi_1\left(\frac{\rho_1}{\rho_f}\right)+\phi_2\left(\frac{\rho_2}{\rho_f}\right)}\right\}\sqrt{f'^2(0)+g'^2(0)} \tag{2.16}$$

$$Nu_r=\mathrm{Re}_z^{-\frac{1}{2}}Nu=-\frac{\kappa_{hnf}}{\kappa_f}\left(1+\frac{4N}{3A_3}\right)\theta'(0) \tag{2.17}$$

2.2.7 Entropy generation and Bejan number

The volumetric local entropy generation rate inside any thermal device considering the magnetic field and axial symmetry is noted as follows [111, 60]:

$$\dot{S}'''_{Gen}=\frac{\sigma_{hnf}B^2}{T_w}(u^2+v^2)+\frac{\mu_{hnf}}{T_w}\left\{\begin{bmatrix}2\left\{\left(\frac{\partial u}{\partial r}\right)^2+\frac{u^2}{r^2}+\left(\frac{\partial w}{\partial z}\right)^2\right\}\\+\left(\frac{\partial v}{\partial z}\right)^2+\left(\frac{\partial u}{\partial z}\right)^2\\+\left\{r\frac{\partial}{\partial r}\left(\frac{v}{r}\right)\right\}^2\end{bmatrix}+\frac{\kappa_f}{T_w^2}\left(\frac{\partial T}{\partial z}\right)^2\left(\frac{\kappa_{hnf}}{\kappa_f}+\frac{16\sigma^*T_\infty^3}{3\kappa^*\kappa_f}\right)\right\} \tag{2.18}$$

Where the leading part $\frac{\sigma_{hnf}B^2}{T_w}(u^2+v^2)$ is known as irreversibility caused by Joule dissipation. This is produced by the electrically conducting liquid undergoing the magnetic field, thus inducing the electric currents that flow within the liquid, The second term $\frac{\mu_{hnf}}{T_w}\left[2\left\{\left(\frac{\partial u}{\partial r}\right)^2+\frac{u^2}{r^2}+\left(\frac{\partial w}{\partial z}\right)^2\right\}+\left(\frac{\partial v}{\partial z}\right)^2+\left(\frac{\partial u}{\partial z}\right)^2+\left\{r\frac{\partial}{\partial r}\left(\frac{v}{r}\right)\right\}^2\right]$ corresponds to fluid's frictional irreversibility that is the outcome of friction originated due to rotation and intermolecular

activities, the last one $\frac{\kappa_f}{T_w^2}\left(\frac{\partial T}{\partial z}\right)^2\left(\frac{\kappa_{hnf}}{\kappa_f}+\frac{16\sigma^* T_\infty^3}{3\kappa^*\kappa_f}\right)$ known as thermal irreversibility term which marks the entropy generation owing to heat transmission that accommodates the entropy through heat transport because of axial conduction from the revolving disk. The entropy generation correlates the dimensionless entropy production rate, which defines the ratio between the real entropy production rate and characteristic entropy production rate. The conversion in the equation (2.7) is employed to make local entropy generation dimensionless as in (2.18) and in this way, the entropy generation becomes [111, 60]:

$$N_G=\varepsilon\left(A_3+\frac{4N}{3}\right)\theta'^2+Br\left[\frac{A_4}{\mathrm{Re}}\left(4f^2+2h'^2\right)+\bar{r}^2\left\{A_4\left(f'^2+g'^2\right)+A_5M\left(f^2+g^2\right)\right\}\right] \tag{2.19}$$

Where $N_G=\frac{\dot{S}'''_{Gen}}{\frac{\kappa_f\Omega\Delta T}{(1-\lambda t)\nu_f T_w}}$. The meaning of all the symbols and terms in equation (2.19) is as follows. $\varepsilon=\frac{\Delta T}{T_w}$ is the dimensionless reduced temperature difference, $Br=\frac{\mu_f\Omega^2R^2}{(1-\lambda t)^2\kappa_f\Delta T}$ is the rotational Brinkman number, which stands for the ratio of continuous heat conduction from the disk top to the viscous heat created by shear, $\mathrm{Re}=\frac{\Omega R^2}{(1-\lambda t)\nu_f}$ is the rotational Reynolds number, $\bar{r}=\frac{r}{R}$ is the nondimensional radial coordinate.

The Bejan number (Be) relates the entropy due to heat transport to the entire entropy generation in a ratio format. Be is analyzed to acquire a more detailed view of entropy within the system. The quantity Be can be mathematically expressed as [111, 60]:

$$Be=\frac{1}{1+N_T} \tag{2.20}$$

Where $$N_T=\frac{Br\left[\frac{A_4}{\mathrm{Re}}\left(4f^2+2h'^2\right)+\bar{r}^2\left\{A_4\left(f'^2+g'^2\right)+A_5M\left(f^2+g^2\right)\right\}\right]}{\varepsilon\left(A_3+\frac{4N}{3}\right)\theta'^2} \tag{2.21}$$

Be Ranges between $0.0 \le Be \le 1.0$. The joule dissipative factor and frictional effect dominance over entropy for $Be = 0.0$. When $Be = 0.5$ then irreversibility caused by joule heating and liquid friction becomes equal with heat transport irreversibility. Again, heat transport seems to dominate the entropy for $Be = 1.0$.

The nondimensional volumetric entropy and average Bejan number are mathematically defined [111, 60]:

$$N_{G,av} = \frac{1}{\forall}\int_0^m\int_0^1 2\pi\bar{r}N_G d\bar{r}d\eta \tag{2.22}$$

$$Be_{av} = \frac{1}{\forall}\int_0^m\int_0^1 2\pi\bar{r}Bed\bar{r}d\eta \tag{2.23}$$

Where $\forall$ defines the considered volume. We considered a large finite region to estimate the volumetric entropy for both thermal and velocity boundary layers. Consequently, the integration range lies within $0 \le \bar{r} \le 1$ and $0 \le \eta \le m$ treating m as sufficiently large.

2.3 Numerical procedure

2.3.1 Numerical method

The leading multi-order nonlinear equations (2.8)–(2.12) are correlated with the boundary norms (2.13). These equations are solved using RK-4 based shooting technique. Firstly, the foremost equations are renewed into 1st-order ODEs and then the RK-4 scheme with shooting technique has been implemented to do the integration step by step. The requisite variables are renewed as:

$$\begin{pmatrix} f \\ f' \\ g \\ g' \\ h \\ \theta \\ \theta' \end{pmatrix} = \begin{pmatrix} z_1 \\ z_1' = z_2 \\ z_3 \\ z_3' = z_4 \\ z_5 \\ z_6 \\ z_6' = z_7 \end{pmatrix} \tag{2.24}$$

Thus, the modeled problem is renovated as:

$$\begin{pmatrix} z_1' \\ z_2' \\ z_3' \\ z_4' \\ z_5' \\ z_6' \\ z_7' \end{pmatrix} = \begin{pmatrix} z_2 \\ \frac{A_1}{A_4}\left\{ z_1^{\,2} - z_3^{\,2} + z_5 z_2 + S\left(z_1 + \frac{\eta}{2} z_2 \right) \right\} + \frac{A_5}{A_4} M z_1 \\ z_4 \\ \frac{A_1}{A_4}\left\{ 2 z_1 z_3 + z_5 z_4 + S\left(z_3 + \frac{\eta}{2} z_4 \right) \right\} - \frac{A_5}{A_4} M z_3 \\ -2 z_1 \\ z_7 \\ \frac{\frac{A_2}{A_3}\left(z_5 z_7 + S \frac{\eta}{2} z_7 \right)}{\frac{1}{\Pr}\left(1 + \frac{4N}{3A_3} \right)} \end{pmatrix} \tag{2.25}$$

$$\begin{pmatrix} z_1(0) \\ z_2(0) \\ z_3(0) \\ z_4(0) \\ z_5(0) \\ z_6(0) \\ z_7(0) \end{pmatrix} = \begin{pmatrix} \alpha + L_s\, z_2(0) \\ \beta_1 \\ 1 + L_s\, z_4(0) \\ \beta_2 \\ 0 \\ 1 \\ \beta_3 \end{pmatrix} \tag{2.26}$$

Then the three unknowns $\beta_1, \beta_2,$ *and* β_3 are guessed and the entire numerical simulation was executed by MAPLE-18 until $f(\infty) = 0,\ g(\infty) = 0,\ \theta(\infty) = 0$ is attained. Also, the asymptotic boundary condition i.e., at $\eta \to \infty$ are substituted by $\eta = \eta_\infty$. The inner iterative procedure is performed having a convergence limit 10^{-6} in all cases. Thus, the entire solution is obtained.

2.3.2 Testing of code

To access the validity of our model, we have extracted the values of $f'(0)$ *and* $g'(0)$ for various unsteadiness and stretching parameters. We have acquired such numeric outcomes

assuming the unsteady viscous flow over the spinning disk and the magnetic field, velocity slip was ignored. We then enlisted those values in Table 2.3 and compared them with Fang and Tao [112]. It explores a decent agreement with the previous investigation.

Table 2.3: Comparison of results with previous literature

	$\alpha = 0.0$				$\alpha = 2.0$			
	$f'(0)$		$g'(0)$		$f'(0)$		$g'(0)$	
	Fang and Tao [112]	Present work	Fang and Tao [112]	Present work	Fang and Tao [112]	Present work	Fang and Tao [112]	Present work
$S = -0.1$	0.5308	0.530774	-0.5789	-.578976	-3.1178	-3.117812	-2.0530	-2.05298
$S = -0.2$	0.5515	0.551551	-0.5416	-.541561	-3.0784	-3.078445	-2.0373	-2.03735
$S = -0.5$	0.6143	0.614332	-0.4284	-.428396	-2.9601	-2.960913	-1.9901	-1.99006
$S = -1.0$	0.7198	0.719812	-0.2366	-.236627	-2.7622	-2.762257	-1.9111	-1.91097

2.4 Results and discussion

This section addresses the consequences of the flow parameters on both hybrid and ordinary nanofluid hydrothermal behavior. Requisite streamlines, graphs, and tables have been shown to disclose the same. Numeric outputs of frictional factor and heat transference are estimated and reviewed. Bejan numbers and entropy generations have also been analyzed. The parametric values that we have presumed to simulate the complete investigation are $\alpha = 0.5,\ M = 0.5,\ L_S = 0.5,\ N = 2.0,\ \phi_1 = 0.02,\ \phi_1 = 0.02, \Pr = 6.2$ unless specified.

2.4.1 Effect of magnetic parameter (M)

Figure 2.2 discloses that radial velocity declines for both nanoliquids. The same reduction is perceived for tangential velocity in Figure 2.3 This reduction is owing to the Lorentz force which

is a retardative force that resists the smooth transit of the liquids. Near the vicinity i.e. within $0.0 \le \eta \le 2.0$ maximum effect is noted. The radial velocity explores a comparatively high deviation in velocity near the surface. Also, hybrid nanoliquid exhibits a low-velocity profile compared to mono nanofluid. Extra nanoparticles within the hybrid nanoliquid make it slightly denser compared to the usual nanofluid and create frictional force inside the fluid which forbids the velocity to increase highly. The magnetic field also produces a viscous barrier which creates a frictional force between molecules and surface, which is also another reason for velocity reduction. A reverse outcome is noticed for the axial velocity in Figure 2.4. Both nanofluids gain increasing velocity near the surface and the effect is huge. Hybrid nanofluid seems to acquire comparatively high velocity than the usual one. Figure 2.6-2.9 depicts the streamline variation for the magnetic effect. We observe that the stream function values decrease as we enhance the magnetic effect. This is because of the Lorentz effect. For the lower magnetic effect, the streamline is observed to stretch more effortlessly in the horizontal direction. Figure 2.10-2.13 portrays the three-dimensional streamlines. It is obvious from Figures 2.10-2.13 that the streamlines tend to be spiral-shaped near the vicinity, but those streamlines tend to be parallel to the rotational axis. The radial, axial, tangential velocity components exist instantaneously near the disk surface. The radial component causes the outward radial deflection, while the tangential component provides the circumferential deflection. These two consecutive deflections make the streamline spiral-shaped. The more we enhance the magnetic strength, the liquid shows more propensity to be parallel with the revolving axis. Table 2.4 predicts that skin friction decreases for the magnetic parameter. Hybrid nanofluids depict reduction at the rate of 0.0930795, while usual nanofluid delivers the rate as 0.082569. Numerically, a higher frictional effect is provided by hybrid nanofluid due to the existence of double tiny ingredients. Figure 2.5 enlightens that temperature amplifies for the magnetic parameter which agrees with Mahanthesh et al. [113]. The maximum effect is noted within $1.0 \le \eta \le 3.0$. The resistive Lorentz force generates friction with the surface and nanoparticles. The prolongation of this frictional hindrance translates the frictional heat into thermal energy. Hybrid nanofluid explores a higher thermal profile because hybrid nanofluid contains double nanosized particles which intensify its thermal conductivity. Consequently, improved heat transference is detected for hybrid nanofluid in Table 2.5, and heat transference boosts for magnetic effect. Comparatively, mono nanofluid reveals a low heat transport feature at the rate of 0.3664755 than hybrid nanofluid with the rate of 0.555949.

Figure 2.14 illustrates the enrichment in entropy generation for the magnetic effect. Since the magnetic effect contributes to the augmentation of frictional effect and thermal profile, hence entropy increases. Hybrid nanofluid explores improved heat transport and thermal conductivity compared to mono nanofluid. Thus, hybrid nanofluid conveys low entropy compared to mono nanofluid. The deviation between two nanofluids is quite impressive. Thus, to minimize the entropy, hybrid nanofluid is undoubtedly the most feasible medium as compared to the usual one and the magnetic field should be reduced. This fallout is of engineering interest for nuclear-MHD-spinning disk propulsion. The Bejan number in Figure 2.15 depicts the reduction for both fluids. Initially $(0.0 \le \eta \le 0.5)$, we detect a slight increase, but after then the decrease is seen. Hybrid nanofluid reveals a high effect close to the surface, but such effect becomes the opposite after $\eta > 1.0$. Since we observe that $0.0 \le Be \le 1.0$ then the frictional effect becomes dominant in the entropy. Figure 2.16 illustrates the contribution of each factor on the entropy for different magnetic values.

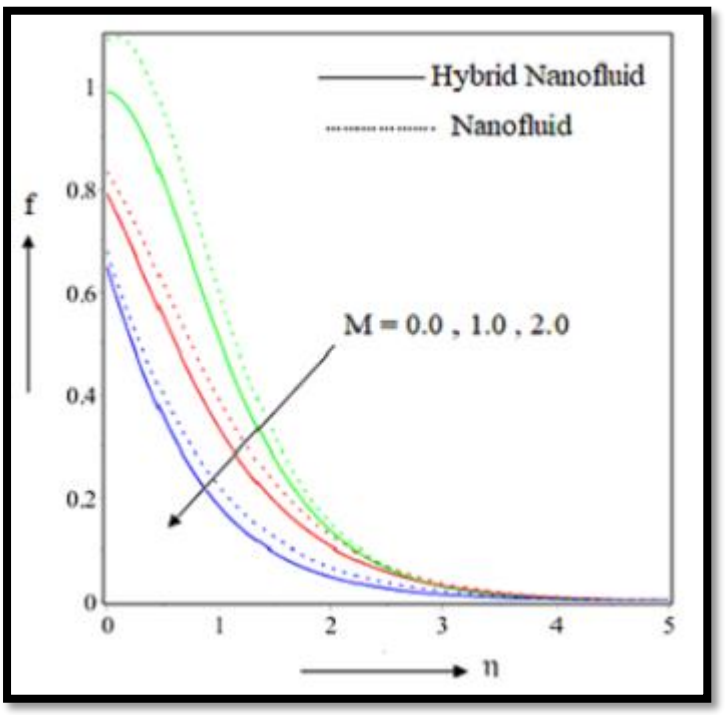

Figure 2.2: Effect of magnetic parameter on radial velocity

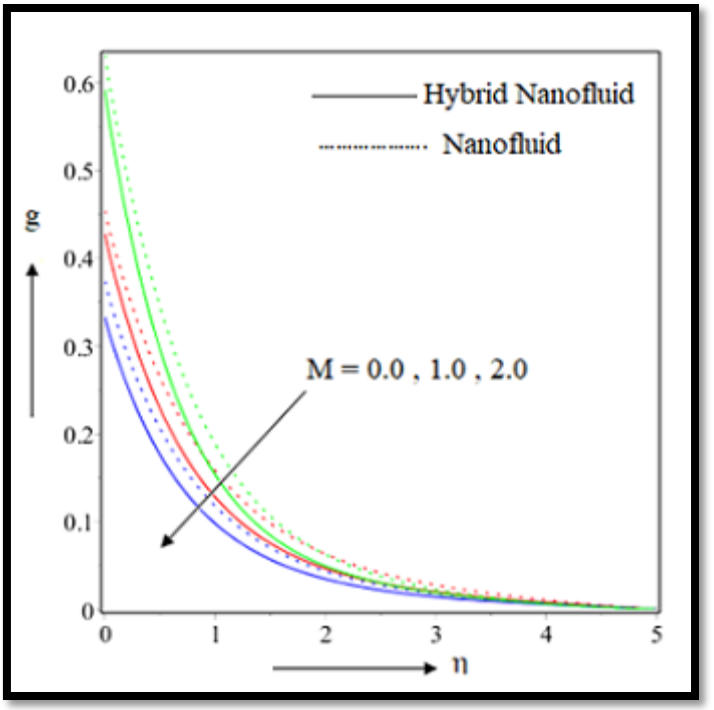

Figure 2.3: Effect of magnetic parameter on tangential velocity

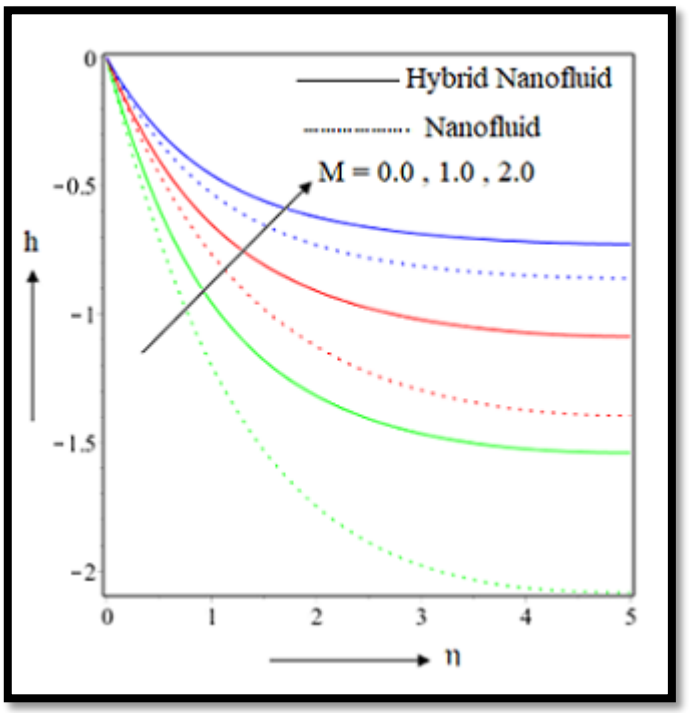

Figure 2.4: Effect of magnetic parameter on axial velocity

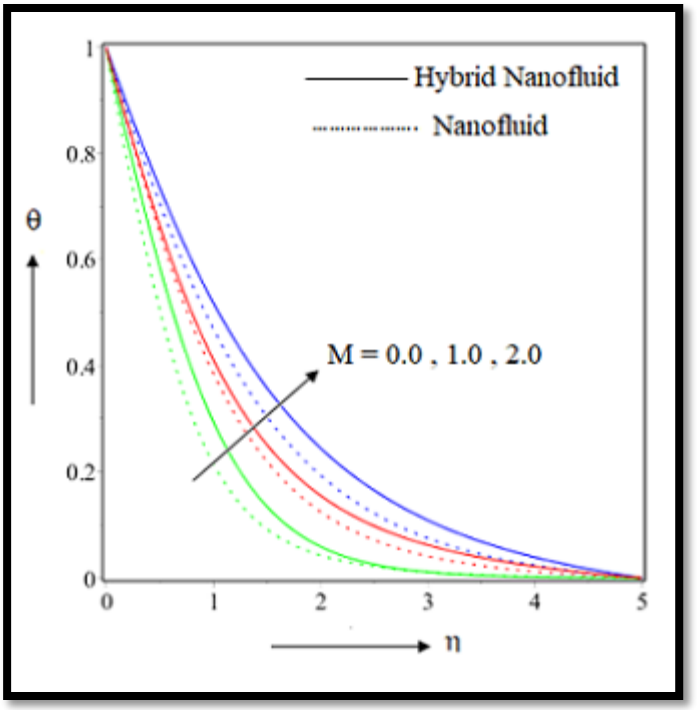

Figure 2.5: Effect of magnetic parameter on temperature

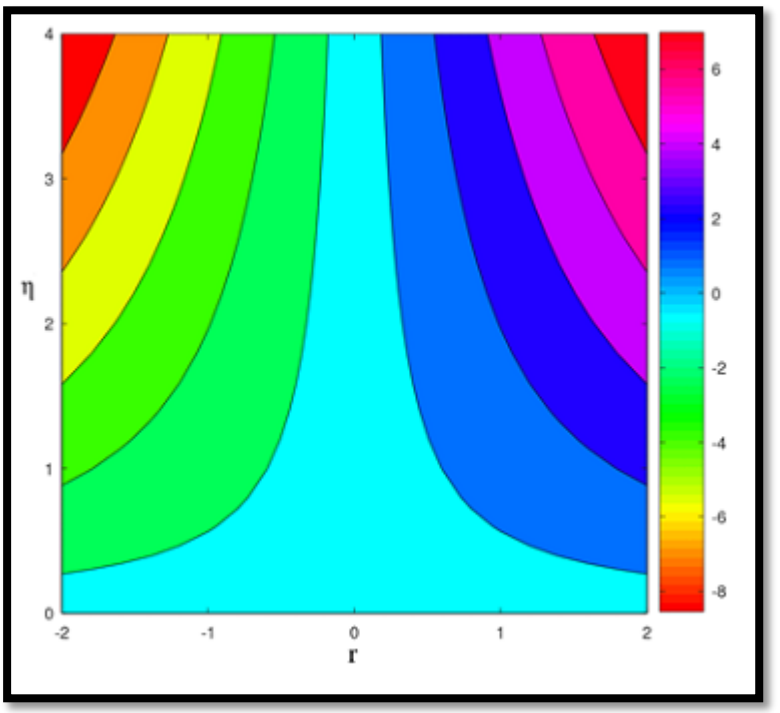

Figure 2.6: Streamlines pattern for $M = 0.0$

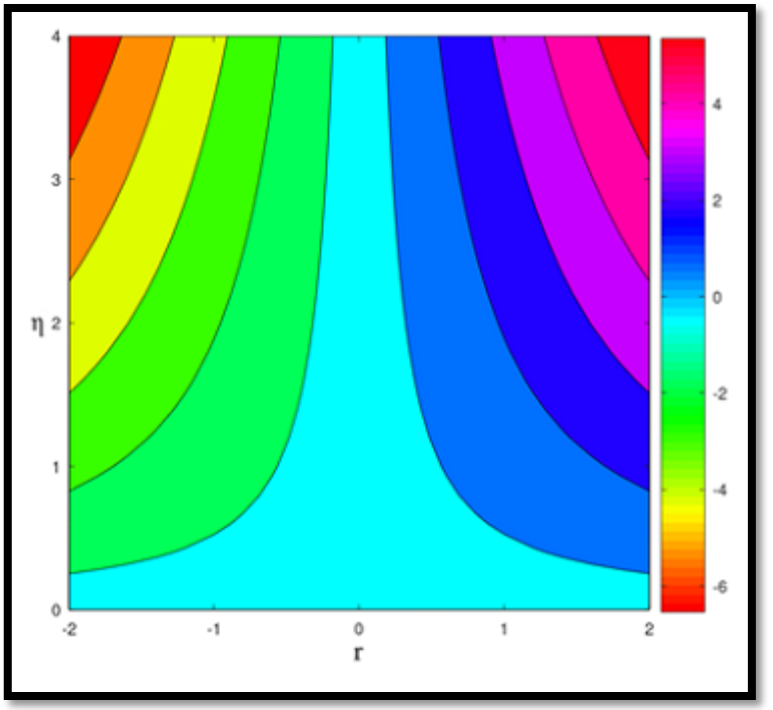

Figure 2.7: Streamlines pattern for $M = 0.5$

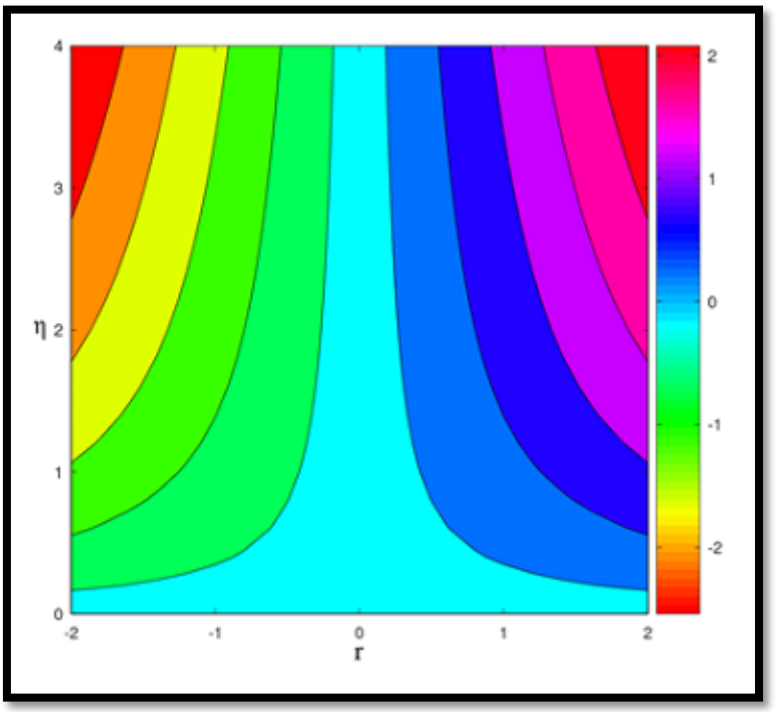

Figure 2.8: Streamlines pattern for $M = 1.0$

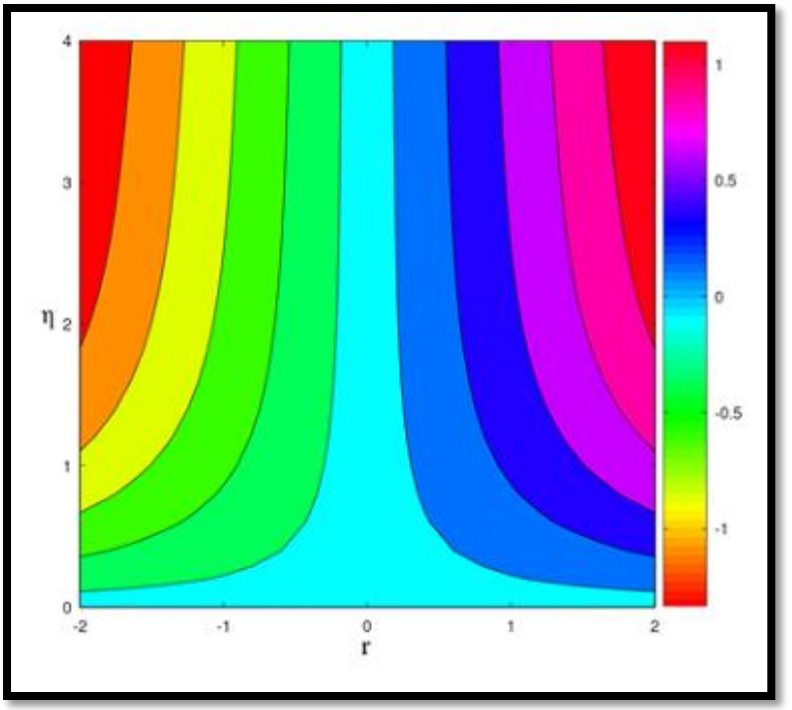

Figure 2.9: Streamlines pattern for $M = 1.5$

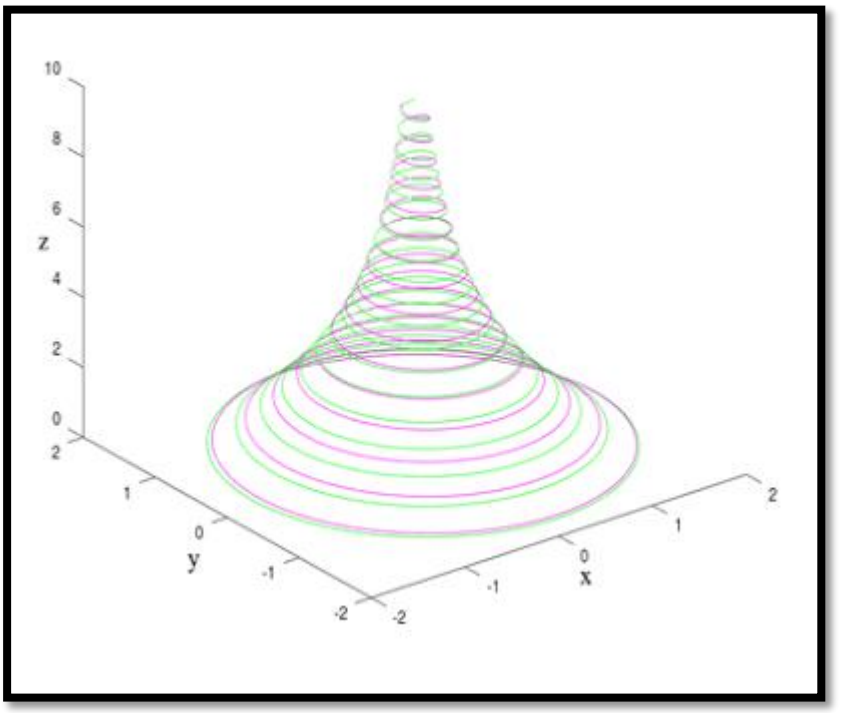

Figure 2.10: Three-dimensional streamlines pattern for $M = 0.0$

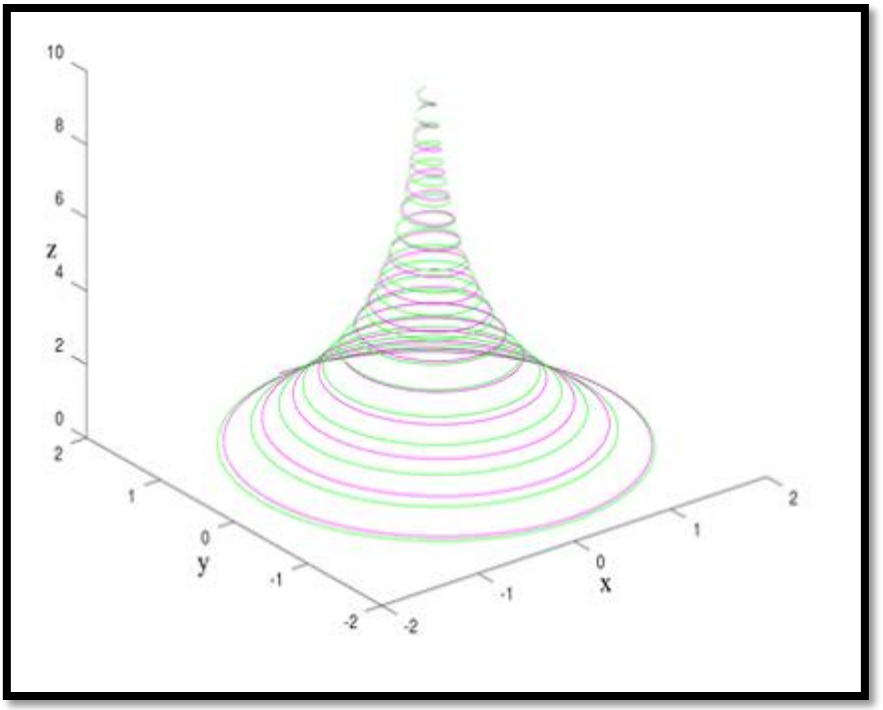

Figure 2.11: Three-dimensional streamlines pattern for $M = 0.5$

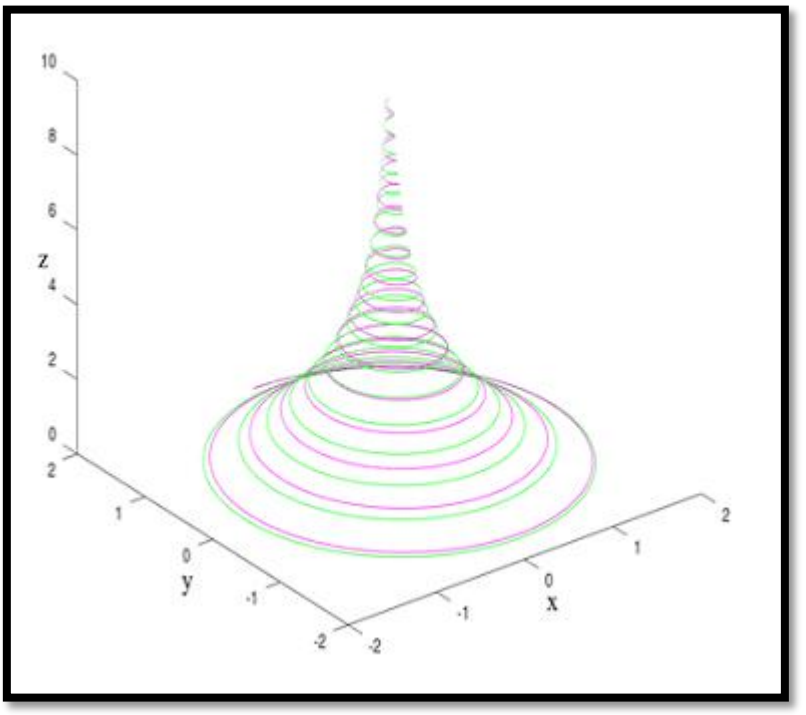

Figure 2.12: Three-dimensional streamlines pattern for $M = 1.0$

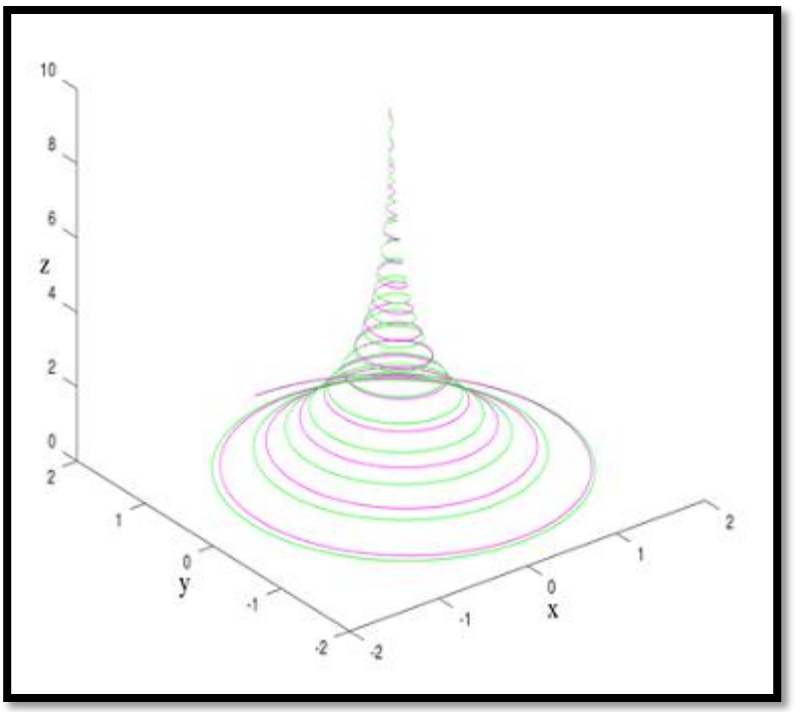

Figure 2.13: Three-dimensional streamlines pattern for $M = 1.5$

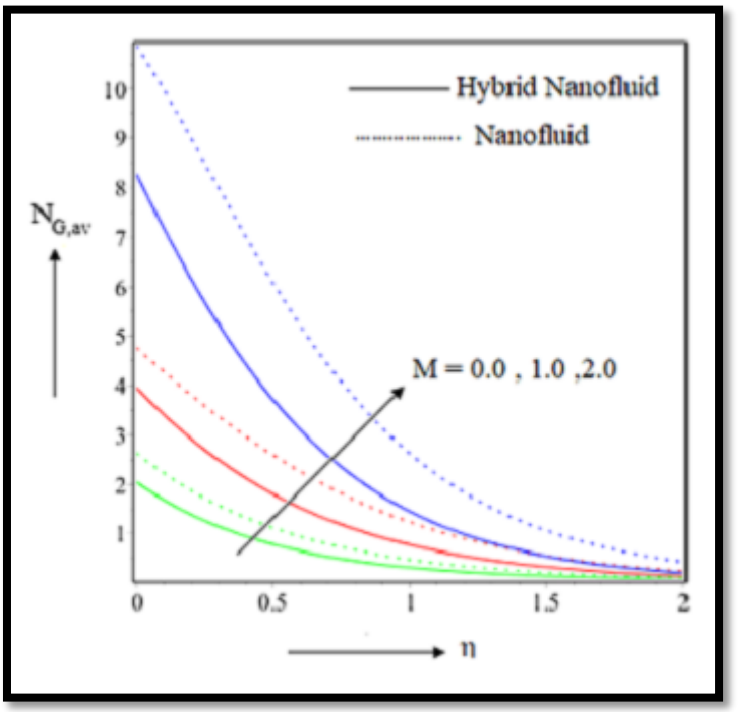

Figure 2.14: Effect of magnetic parameter on entropy generation

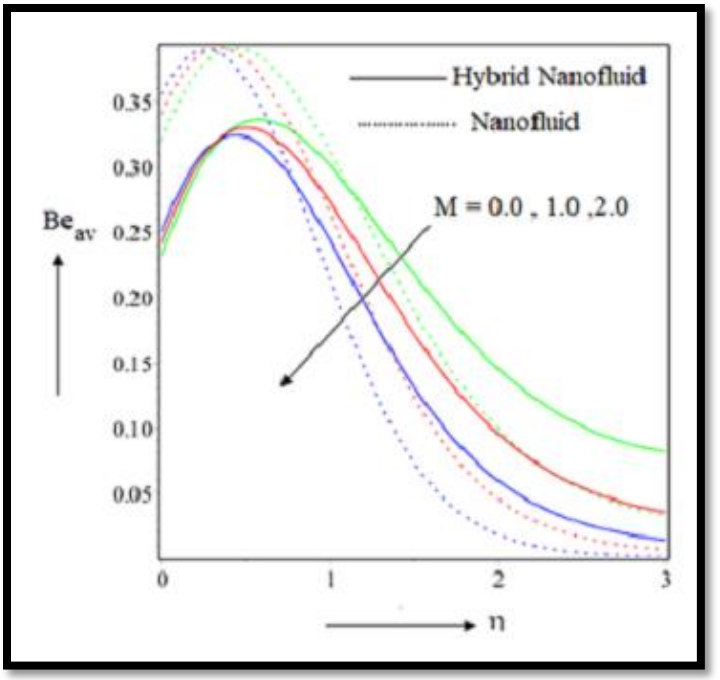

Figure 2.15: Effect of Magnetic parameter on Bejan number

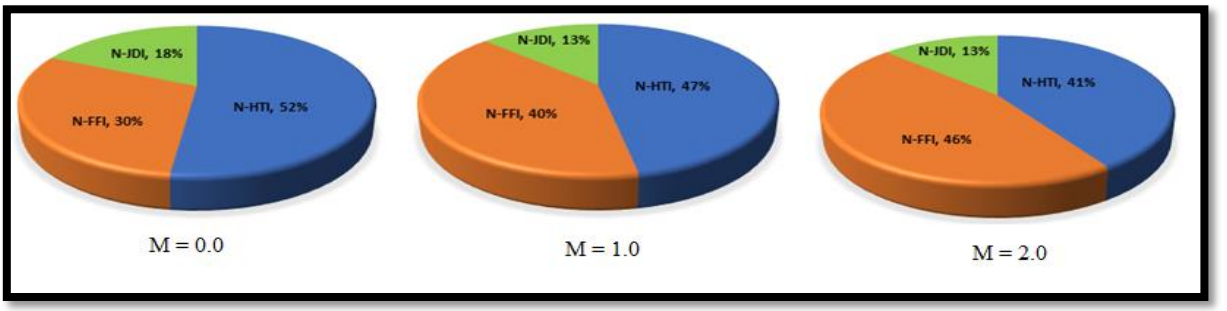

Figure 2.16: Contribution of heat transfer irreversibility (HTI), fluid friction irreversibility (FFI), and joule dissipation irreversibility (JDI) in the average entropy generation for different magnetic parameter values

2.4.2 Effect of slip parameter (L_s)

Figures 2.17-2.19 delineate the velocity trajectory for the slip parameter. The radial velocity in Figure 2.17 demonstrates a dual scenario. The velocity declines inside the region $0.0 \le \eta \le 1.5$, while the opposite is traced after $\eta > 1.5$. Physically, the reduction in velocity near the disk surface will be compensated by the enhanced velocity distribution to conserve the mass flow rate. Mono nanofluid acquires high velocity than hybrid nanofluid. Besides, tangential

velocity in Figure 2.18 diminishes smoothly. The reverse is accurate for axial velocity in Figure 2.19. Figure 2.21-2.24 portrays the streamlines for the slip parameters. The frictional coefficient in Table 2.4 reduces for both fluids. But hybrid nanofluid provides the maximum drag on the surface. The reduction rate is 0.368996 for hybrid nanofluid and 0.325655 for mono nanofluid. The temperature in Figure 2.20 swells for the slip parameter. A slip-less surface conveys the minimum thermal impact. As usual, a hybrid nanofluid explores the maximum thermal outcomes. Both fluids disclose the decrease in heat transfer in Table 2.5. Hybrid nanofluid comparatively fosters heat transmission. The reduction rate is 0.837099 for the usual nanofluid and it is 0.64583 for hybrid nanofluid.

Entropy drops off for the slip parameter in Figure 2.25. The reduction is high near the disk surface. Most interestingly, entropy reduction is high when $L_s = 1.5$. Hybrid nanofluid decays the entropy. Thus, to minimize the entropy and related irreversibility, one should go with hybrid nanofluid and slippery surfaces. This might have useful applications in the rotor-stator system. Bejan number escalates in Figure 2.26 for both fluids but mostly for hybrid nanofluid. It detects that heat transport irreversibility plays a predominant role in entropy generation. Figure 2.27 exemplifies the impact of each factor on the entropy for different slip values.

2.4.3 Effect of unsteadiness parameter (S)

Figures 2.28 and 2.29 disclose the same dual outcome as it was in Figures 2.17 and 2.18. Compared to the previous, here the effect is slightly lower. Here, we receive the dual nature for tangential velocity also, but in the case of slip parameter, such outcome was very minor. Axial velocity in Figure 2.30 increases smoothly. But hybrid nanofluid assures high velocity than the usual one. Skin friction reduces in Table 2.4, but hybrid nanoliquid provides the maximum impact. The temperature in Figure 2.31 escalates for unsteady parameters and as expected hybrid nanofluid displays the maximum. Table 2.5 confirms the heat transfer amplification at the rate of 0.801066 for hybrid nanofluids.

Entropy generation declines in Figure 2.32 for unsteady parameters and close to the disk surface such outcomes are distinct. The major impacts are marked within $0.0 \le \eta \le 1.5$. Hybrid nanofluid, being an enhanced heat transport medium exhibits low entropy as compared with the mono nanofluid. Also, higher parametric values of unsteadiness diminish the related entropy inside

the system. Thus, to minimize the entropy, hybrid nanofluid along with high unsteady value is most effective when compared to mono nanofluid. The Bejan number extracts a dual feature in Figure 2.33. Near the surface, it shows a reducing tendency. But slight away from the disk surface, it reveals an opposite trend and this trend is clear and distinct. Though initially, the usual nanofluid shows slightly high Bejan values, ultimately hybrid nanofluid dominates the most.

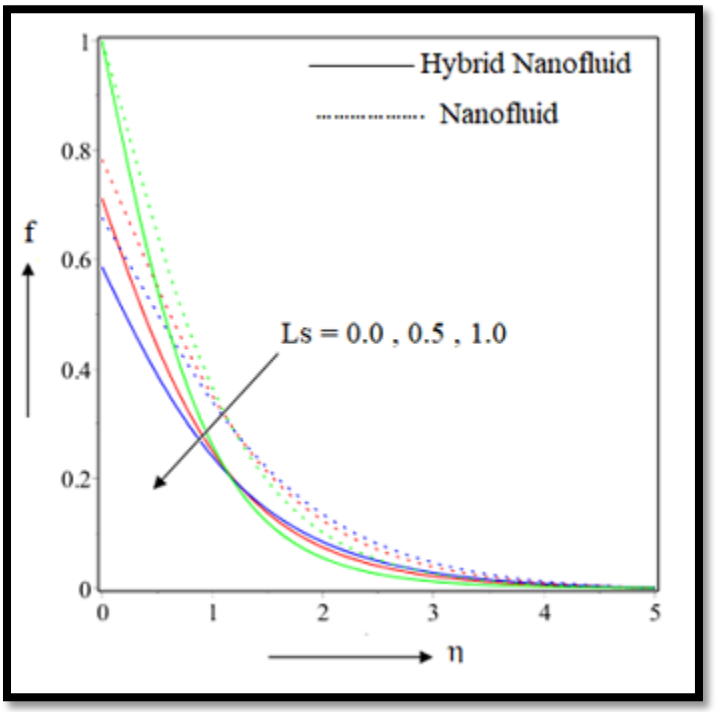

Figure 2.17: Effect of magnetic parameter on radial velocity

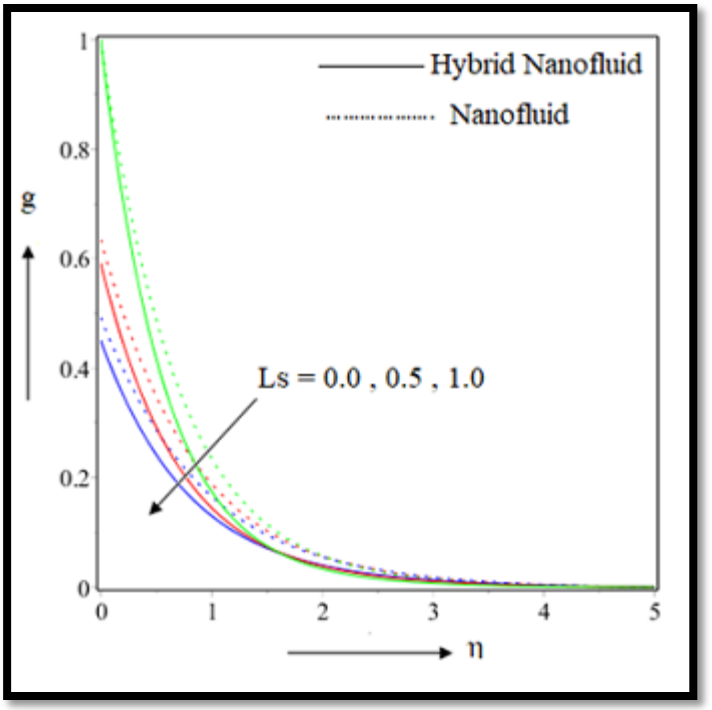

Figure 2.18: Effect of magnetic parameter on tangential velocity

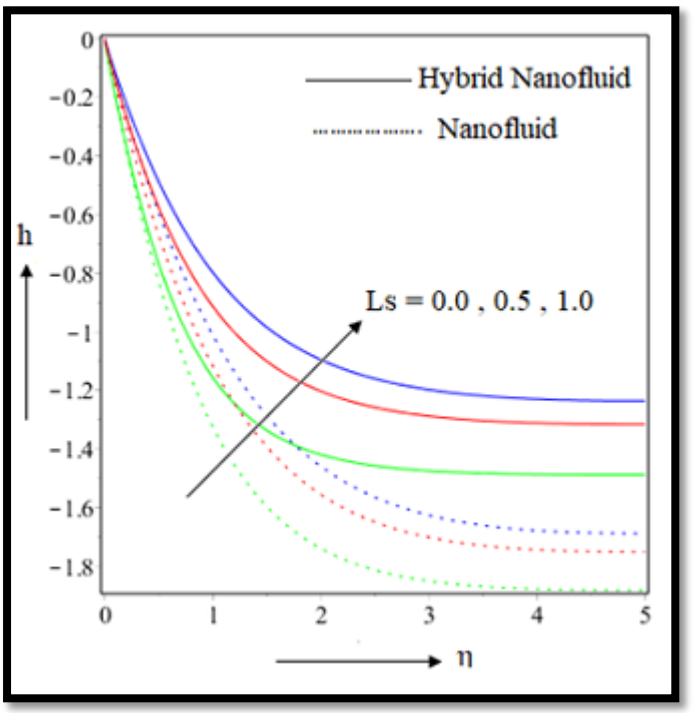

Figure 2.19: Effect of magnetic parameter on axial velocity

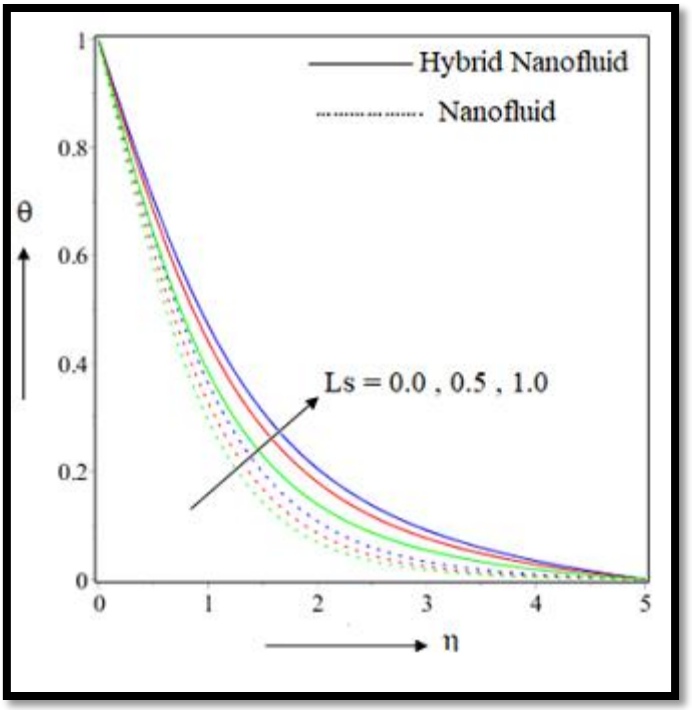

Figure 2.20: Effect of magnetic parameter on temperature

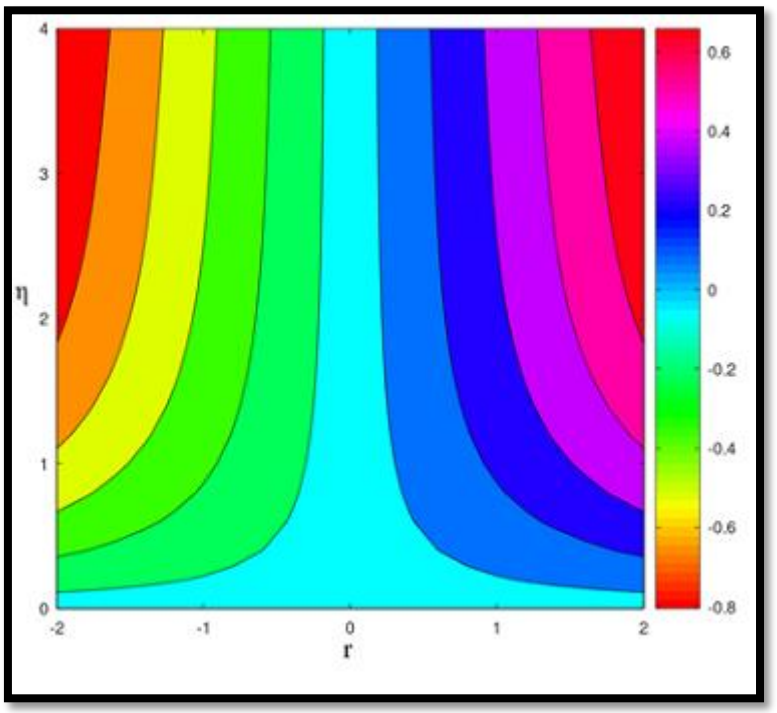

Figure 2.21: Streamlines pattern for $L_s = 0.0$

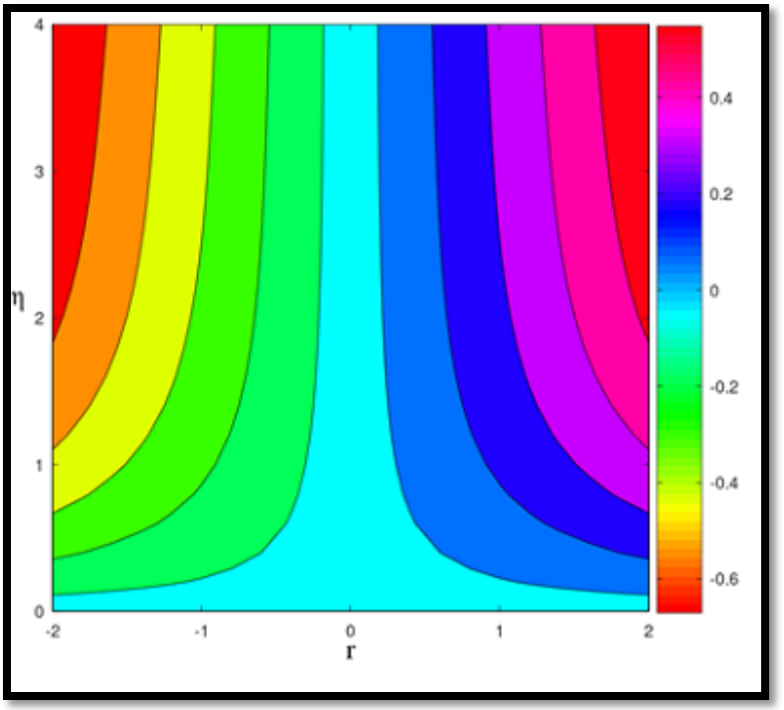

Figure 2.22: Streamlines pattern for $L_s = 0.5$

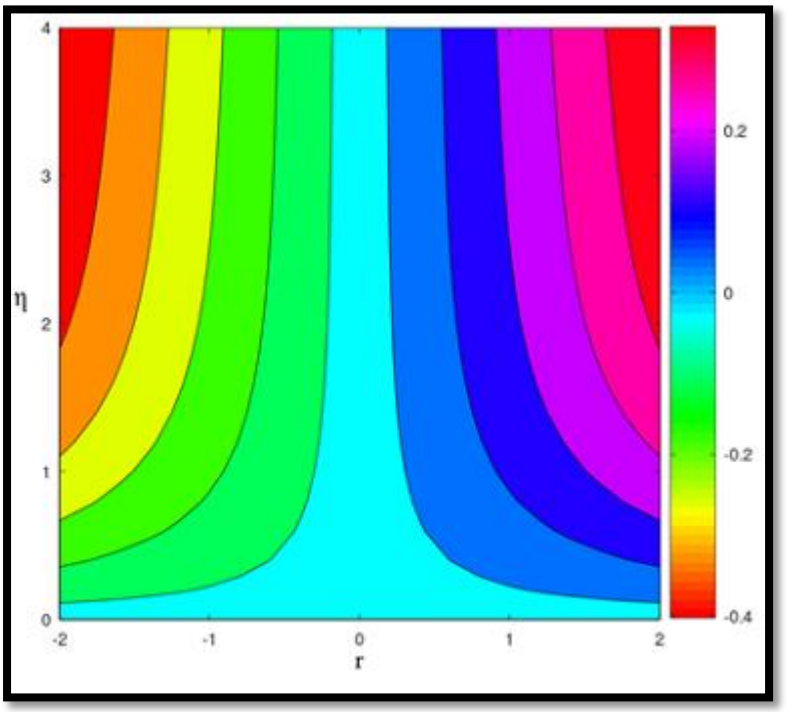

Figure 2.23: Streamlines pattern for $L_s = 1.0$

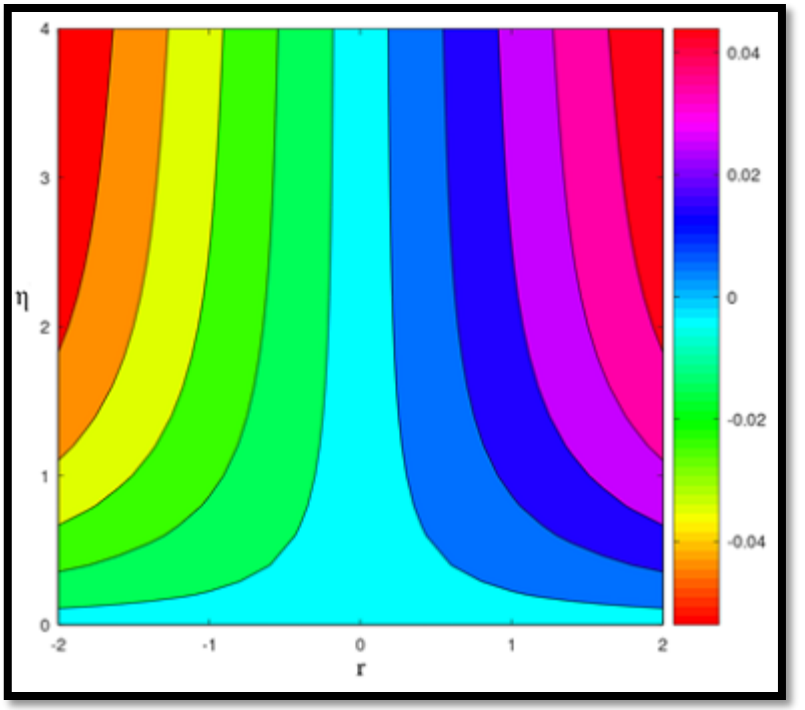

Figure 2.24: Streamlines pattern for $L_s = 1.5$

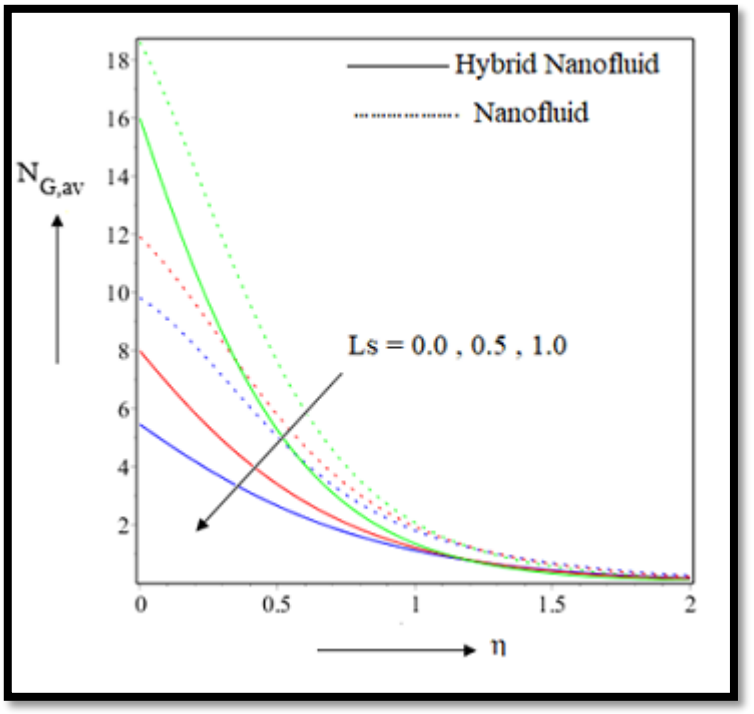

Figure 2.25: Effect of slip parameter on entropy generation

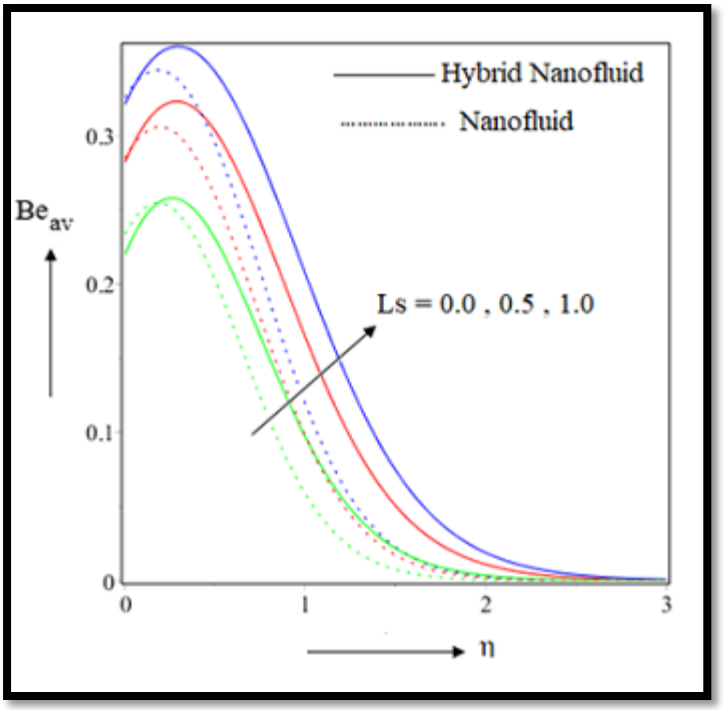

Figure 2.26: Effect of slip parameter on Bejan number

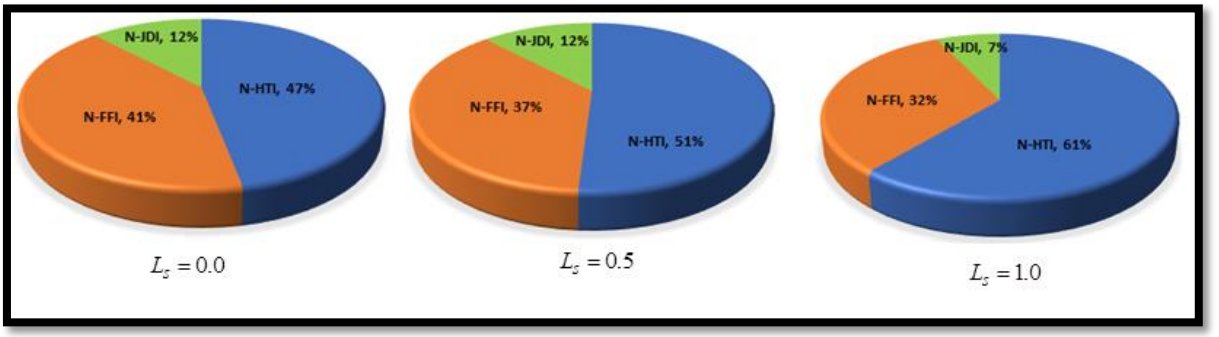

Figure 2.27: Contribution of heat transfer irreversibility (HTI), fluid friction irreversibility (FFI), and joule dissipation irreversibility (JDI) in the average entropy generation for different slip parameter values

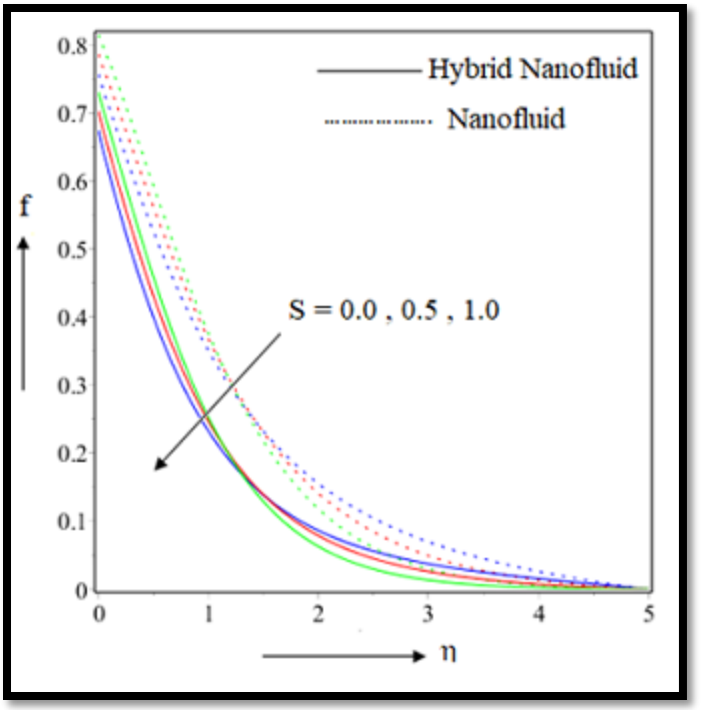

Figure 2.28: Effect of unsteady parameter on radial velocity

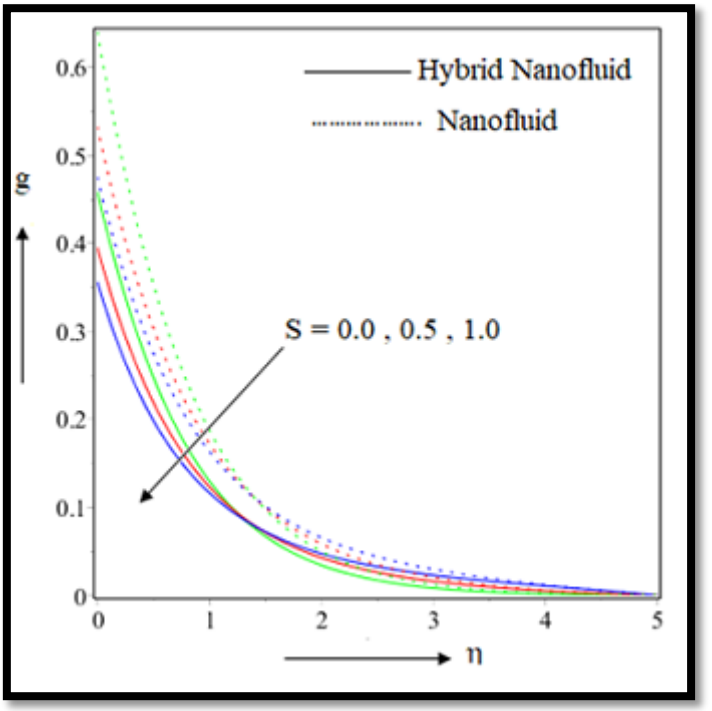

Figure 2.29: Effect of unsteady parameter on tangential velocity

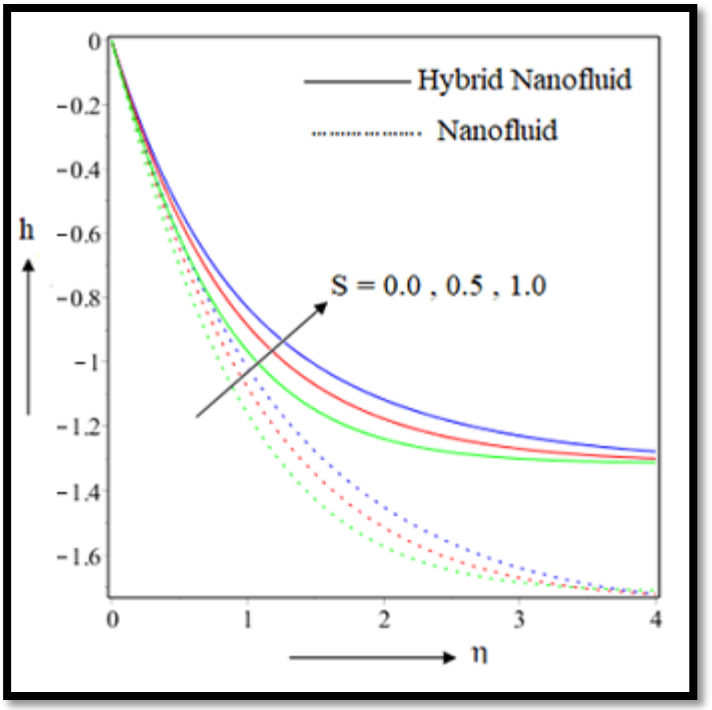

Figure 2.30: Effect of unsteady parameter on axial velocity

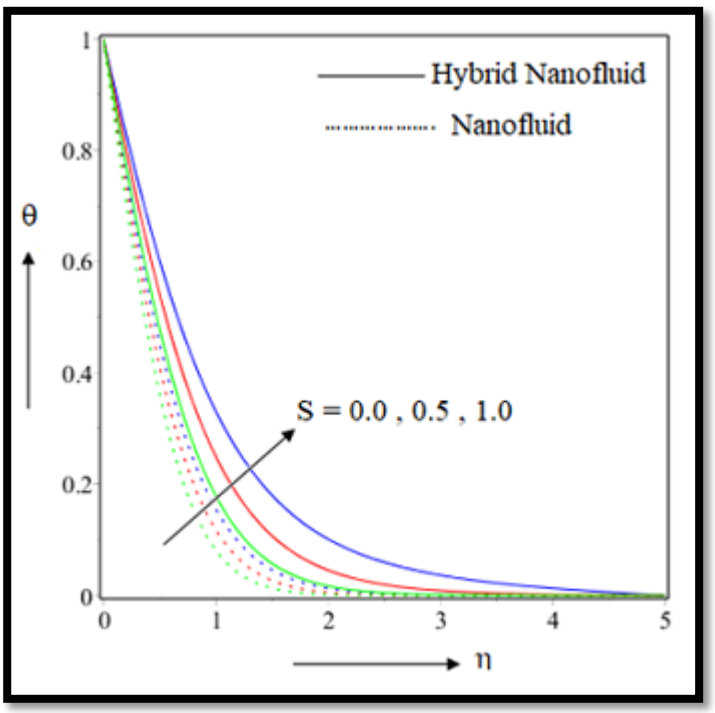

Figure 2.31: Effect of unsteady parameter on temperature

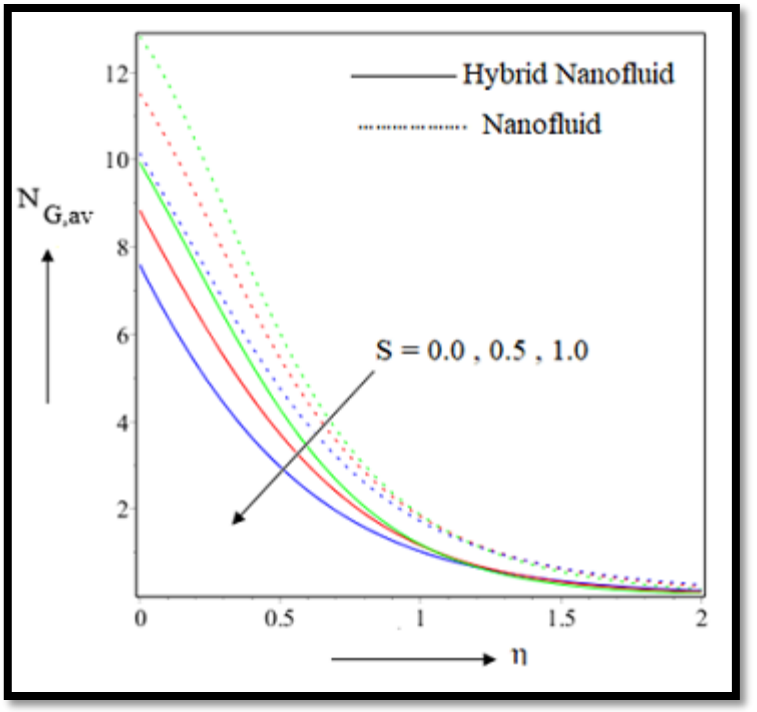

Figure 2.32: Effect of unsteady parameter on entropy generation

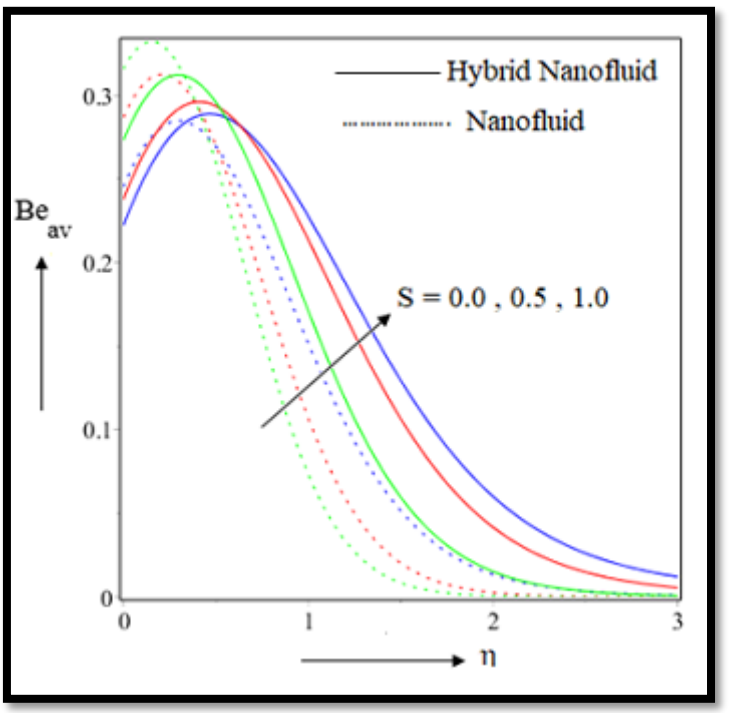

Figure 2.33: Effect of unsteady parameter on Bejan number

2.4.4 Effect of radiation parameter (N)

Figure 2.34 describes that the temperature escalates for the radiation parameter. One can detect a clear and high intensification in the thermal profile when the radiation value is increased. High radiative values inject high radiative energy inside the fluid system. This extra radiative energy aids the tiny nanoparticles to migrate faster from one region to another. Such frequent motion of the tiny particles causes more friction with the other particles. Continuation of such frictional heat eventually enhances temperature. Hybrid nanofluid explores an elevated thermal picture than usual nanofluid. The presence of double tiny particles makes them more suitable to avail this high temperature. Table 2.5 extracts reduction in heat transference for radiation. The reduction rate is 1.048766 for hybrid nanofluid and 1.389546 for usual nanofluid. Hybrid nanofluid as expected confirms to reveal high heat transport than mono nanofluid. Entropy generation drops off for high radiation in Figure 2.35. It gets lesser in the case of hybrid nanofluid. Close to the disk surface, it takes its highest value and gradually it merges to zero asymptotically. Figure 2.37 explains the influence of each factor on the entropy for different radiation parameters. Bejan number portrays the dual scenario in Figure 2.36. Inside $0.0 \le \eta \le 1.5$ it declines, but the same amplifies effectively afterward. Usual nanofluid depicts low Bejan profile than hybrid nanofluid.

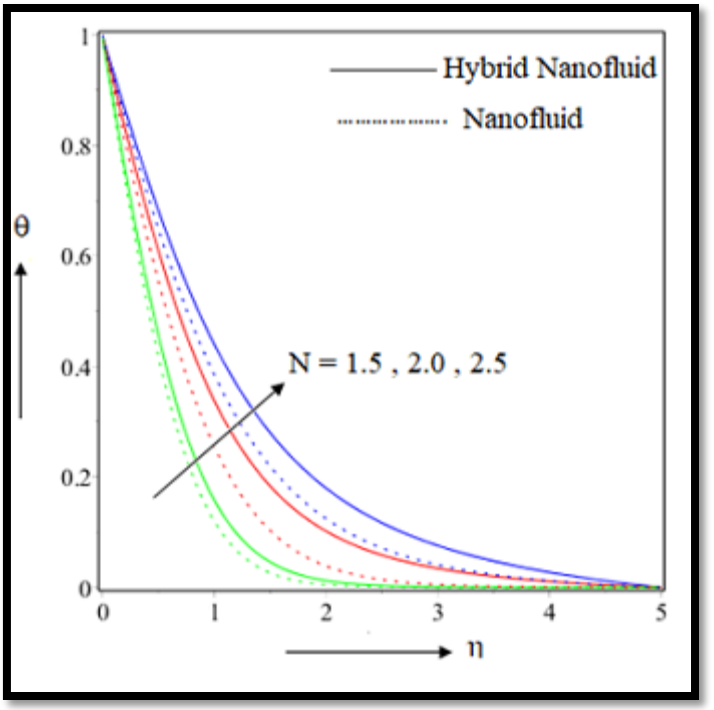

Figure 2.34: Effect of radiation parameter on temperature

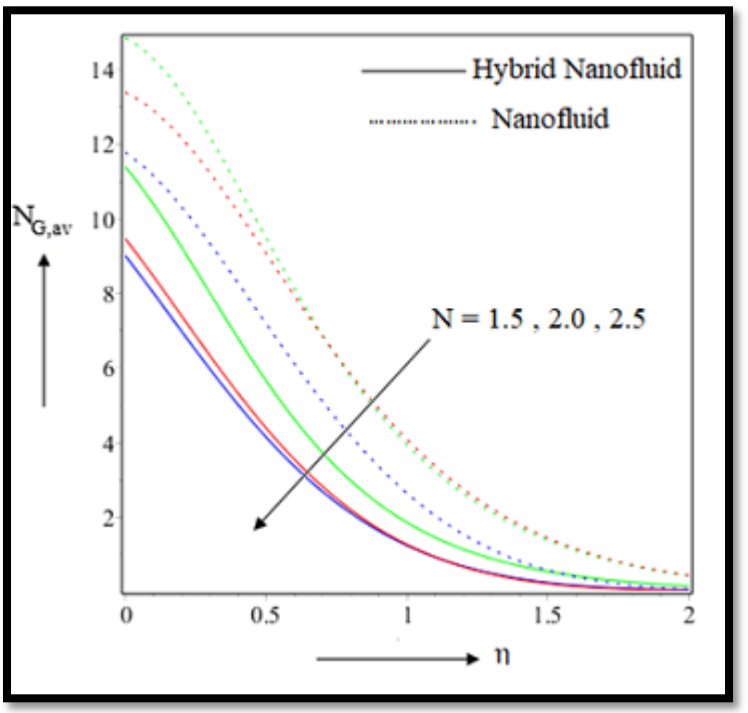

Figure 2.35: Effect of radiation parameter on entropy generation

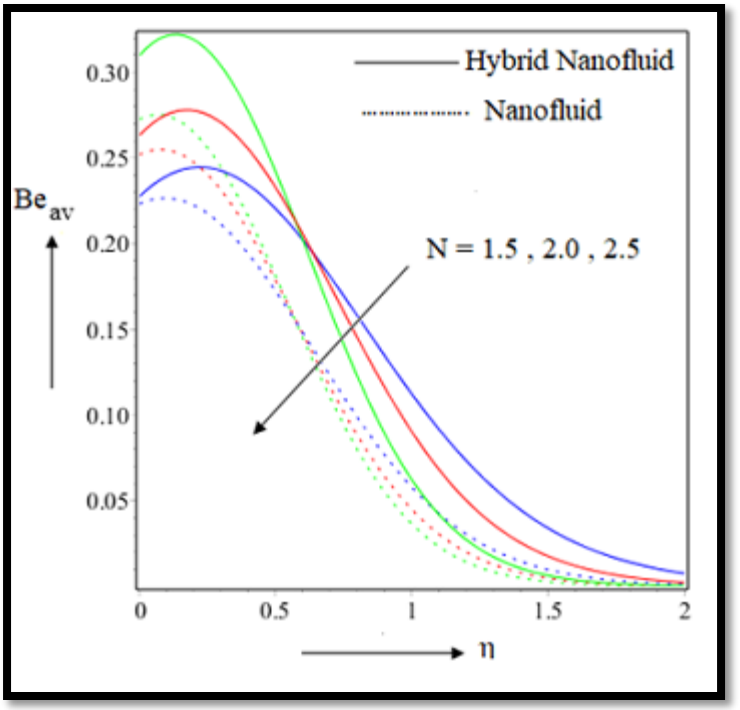

Figure 2.36: Effect of radiation parameter on Bejan number

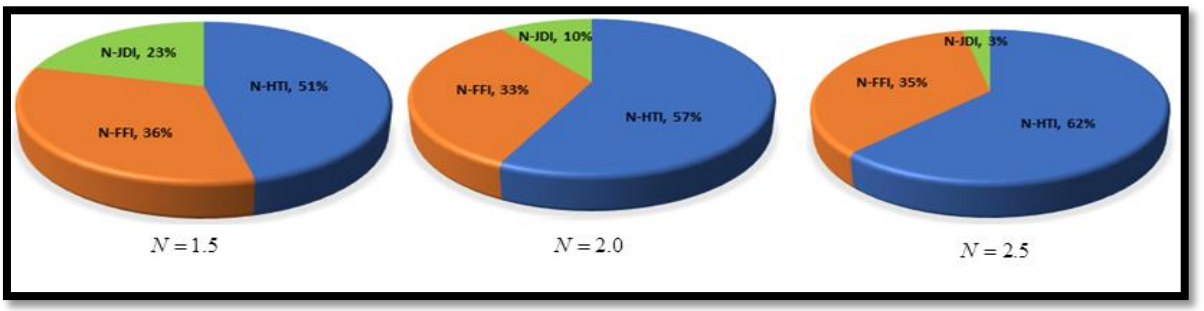

Figure 2.37: Contribution of heat transfer irreversibility (HTI), fluid friction irreversibility (FFI), and joule dissipation irreversibility (JDI) in the average entropy generation for different radiation parameter values

2.4.5 Effect of nanoparticle volume fraction (ϕ_1) and Brinkman number (Br)

The addition of extra tiny particles within the fluid generally increases the resulting thermal conductivity of the liquid. So, it is hoped that a high-volume fraction of tiny particles will enhance the thermal profile. The same is noticed in Figure 2.38. Usual nanofluids only carry single tiny ingredients, thus exhibiting low temperature compared to hybrid nanofluid. The outcomes are

minor and only distinct outcomes are received inside $1.0 \le \eta \le 3.0$. Heat transfer ultimately seems to increase for nanoparticle volume fraction in Table 2.5 and the usual nanofluid reveals the least. The increase rate is 4.01685 for the usual nanofluid, but it is 6.7557 for hybrid nanofluid. A high-volume fraction increases the heat transference, so the related entropy decreases for both fluids in Figure 2.39. Hence, hybrid nanofluid and a small increase in nanoparticle volume fraction will reduce the entropy effectively. Figure 2.41 explains the impact of each factor on the entropy for different radiation parameters. Bejan number demonstrates in Figure 2.40 the same profile as it was in Figure 2.36. Entropy generation amplifies for the Brinkman number in Figure 2.42, while the Bejan number depicts the opposite in Figure 2.43.

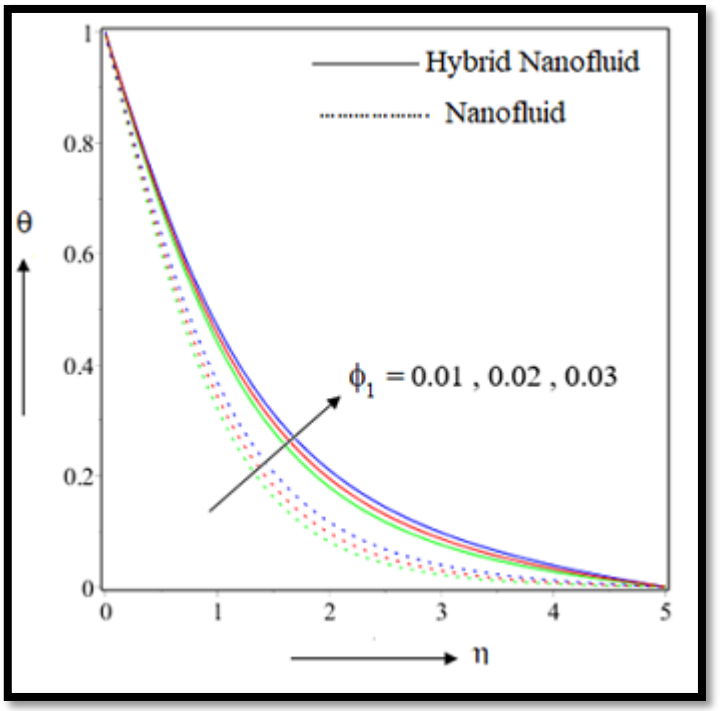

Figure 2.38: Effect of nanoparticle volume fraction on temperature

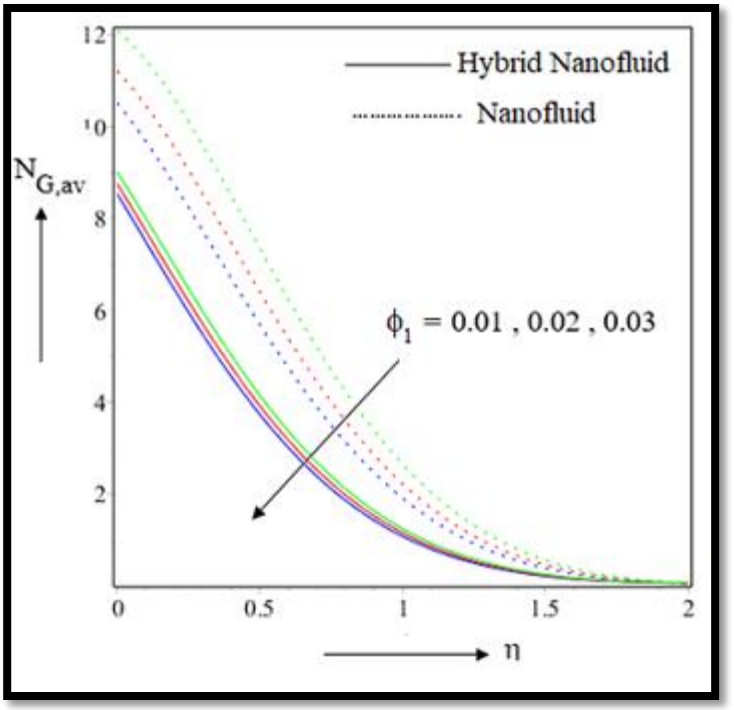

Figure 2.39: Effect of nanoparticle volume fraction on entropy generation

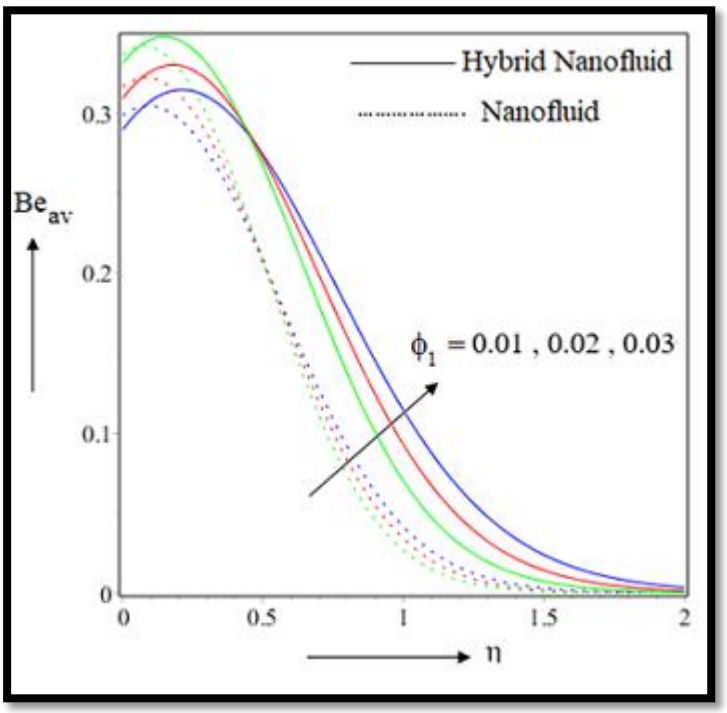

Figure 2.40: Effect of nanoparticle volume fraction on Bejan number

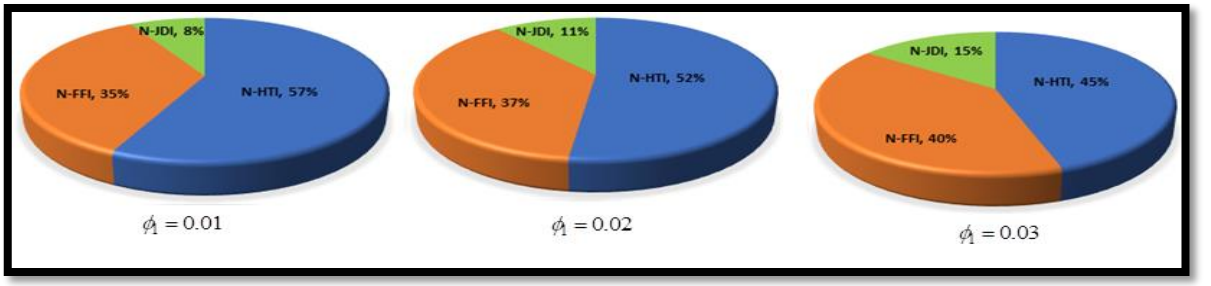

Figure 2.41: Contribution of heat transfer irreversibility (HTI), fluid friction irreversibility (FFI), and joule dissipation irreversibility (JDI) in the average entropy generation for different volume fraction parameter values

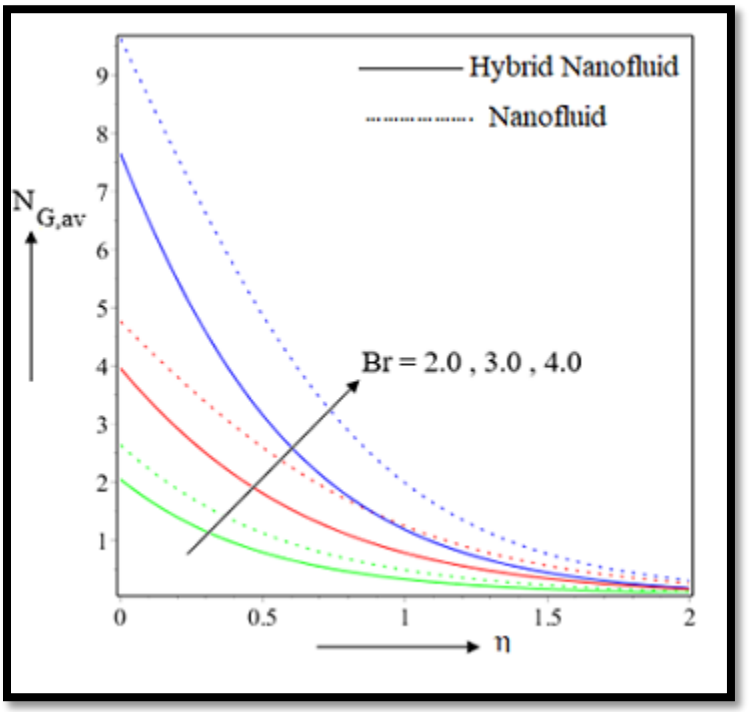

Figure 2.42: Effect of Brinkman number on entropy generation

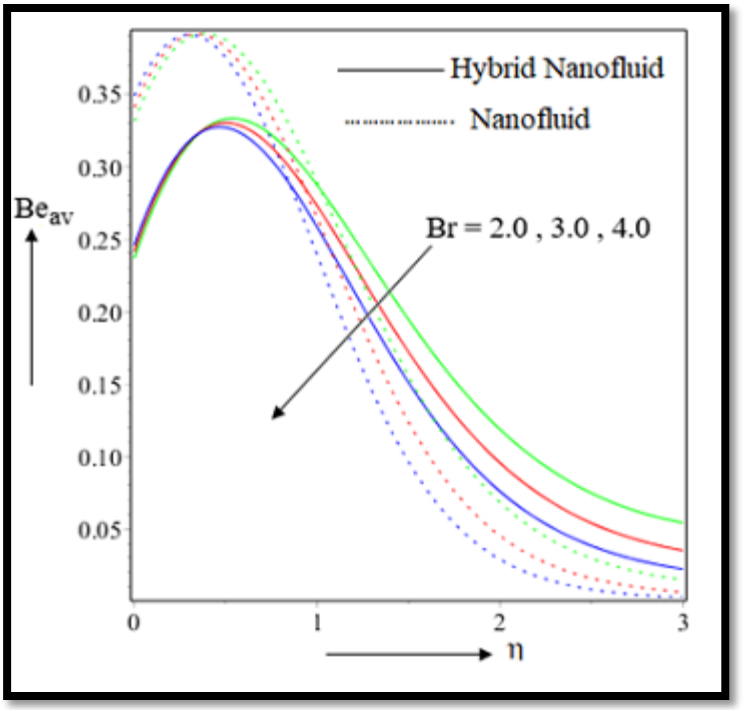

Figure 2.43: Effect of Brinkman number on Bejan number

2.5 Conclusions

This investigation discloses the entropy analysis of magnetized hybrid nanofluid passing over a revolving disk. Graphene and ferrous nanoparticles with host liquid water are treated as functioning liquid. The thermal radiation and velocity slips are given prime consideration to model the flow. The dimensionless leading equations are executed using the RK4 shooting technique. Various streamlines, graphs, tables are produced to extract the parametric consequence on the flow. Moreover, the entropy production and related Bejan number are also viewed graphically. The following outcomes are the important issues noted during the simulation:

- The radial velocity reduces for the magnetic parameter, but the slip and unsteadiness parameters exhibit the dual outcomes. The tangential velocity declines for magnetic and slips parameters, whereas unsteadiness reveals the dual impact. The axial velocity intensifies for every parameter. Hybrid nanofluid illustrates the low-velocity profile except for the case of axial velocity.
- Frictional effects seem to drop off for every parameter. Hybrid nanofluid conveys the highest value of skin friction.

- Temperature increases for every parameter. Heat transfer drops for radiation and slip parameter, while others render the opposite. Hybrid nanofluid conveys the maximum thermal impact and heat transport.
- The entropy enhances for the Brinkman number and magnetic parameter, while other parameters depict the opposite scenario. Hybrid nanofluid comparatively reduces the system entropy. Thus unsteady, slip, and radiation parameters can effectively decline the entropy and maximum optimization is possible for hybrid nanofluid.
- Magnetic and Brinkman numbers decline the Bejan numbers. The slip parameter portrays the opposite. The rest of the parameters illustrates the dual consequences.

Various combinations of nanoparticles, the hybrid base fluid, viscous dissipation, joule heating, and some novel geometry along with physically reliable conditions can be further introduced to extend the investigation.

Table 2.4: Effects of the parameters on skin friction

M	L_s	S	Cf_r	
			Hybrid nanofluid	Usual nanofluid
0.0	0.5	0.5	0.560996	0.426311
1.0			0.467203	0.382156
2.0			0.374837	0.261173
S_{lp}			-0.0930795	-0.082569
0.5	0.0		0.650812	0.553398
	0.5		0.392070	0.362166
	1.0		0.281816	0.227743
	S_{lp}		-0.368996	-0.325655
	0.5	0.0	0.412136	0.387732
		0.5	0.365491	0.326971
		1.0	0.292647	0.274391
		S_{lp}	-0.119489	-0.113341

Table 2.5: Effects of the parameters on heat transfer

M	N	L_s	S	ϕ_1	Nu_r	
					Hybrid nanofluid	Usual nanofluid
0.0	2.0	0.5	0.5	0.02	3.135029	3.094542
1.0					3.990335	3.745917
2.0					4.246927	3.827493
S_{lp}					0.555949	0.3664755
1.0	1.5				4.779901	4.835463
	2.0				4.670728	4.434850
	2.5				3.731135	3.445917
	S_{lp}				-1.048766	-1.389546
	2.0	0.0			4.556602	4.289946
		0.5			4.233214	3.731135
		1.0			3.910772	3.452847
		S_{lp}			-0.64583	-0.837099
		0.5	0.0		2.413126	2.351162
			0.5		2.876349	2.514335
			1.0		3.214732	2.875314
			S_{lp}		0.801606	0.524152
		0.5		0.01	4.291135	3.731354
				0.02	4.350421	3.762262
				0.03	4.426249	3.811691
				S_{lp}	6.7557	4.01685

CHAPTER 3

Influence of Inclined Magnetic Field on the Flow of Condensed Nanomaterial over a Slippery Surface: The Hybrid Visualization*

3.1 Introduction

In this chapter we have considered the impact of inclined magnetic strength on hybrid nanofluid flow. The flow is assumed to be flowed over permeable stretching surface. Surface slip mechanism is executed to explore the hidden features of the hybrid composite. The PDEs (Partial Differential Equations) are changed to ODEs (Ordinary Differential Equations) by similarity transformation and finally it is solved numerically. Various aspects and effects of parameters like change in angle, suction - injection etc. are discussed in this paper. It is well known that, unitary nanoliquid is required to cooling the nano-equipment or to amplify the heat transfer under different situations, and hybrid nanofluid provides the most fitted medium to improve the heat transmission. Their thermophysical characteristics are influenced under uniform magnetic orientation. To the author's knowledge, no problem considering the effect of inclined magnetic field without radiation on a hybrid nanofluid ($CuO - Ag / Water$) over a permeable stretching sheet having suction effect has been reported in the literature.

3.2 Mathematical formulation

3.2.1 Problem statement

Let us presume a viscous, incompressible and laminar steady electrically conducted nanoliquid flow over a stretched surface. The stretching surface is located along $x-axis$ and the

***This chapter is based on the paper published in: Applied Nanoscience, 10 (2019), 633-647, (SCIE).**

fluid runs in the province $y > 0$ as exhibited in Figure 3.1. The sheet is regarded as permeable in nature and its stretching speed is of the form $u_w = ax$. Magnetic field which is of uniform strength B_0 is applied at an inclined position of angle γ with the $x-axis$. Here we have utilized a special type of nanofluid i.e. hybrid nanofluid, which fundamentally allocates the composition of two dissimilar particles into base liquid. To frame our mathematical section, we have gone through few hypothesis that there is no chemical reaction between tiny particles and base solution, no temperature jump occurs between tiny nanosized particles and base fluid, viscous dissipation is waived. Also, nanoparticles and base liquid maintain thermal equilibrium. The magnetic field created due to induction is considered to be so small that it can be neglected compared to applied magnetic field. The equations which governed the flow can be prescribed using the order of magnitude analysis along with boundary layer approximations are following [114,115]

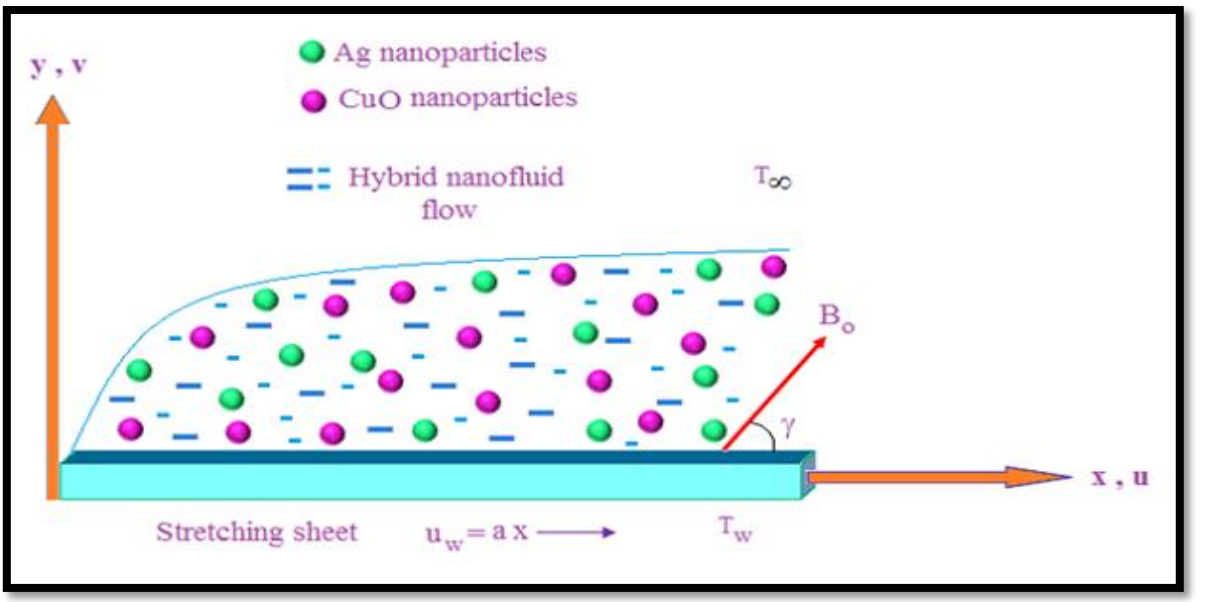

Figure 3.1: Schematic of the flow

$$\frac{\partial u}{\partial x}+\frac{\partial v}{\partial y}=0 \tag{3.1}$$

$$u\frac{\partial u}{\partial x}+v\frac{\partial u}{\partial y}=\frac{\mu_{hnf}}{\rho_{hnf}}\frac{\partial^2 u}{\partial y^2}-\frac{\sigma_{hnf}}{\rho_{hnf}}B_0^2 u\sin^2\gamma \tag{3.2}$$

$$u\frac{\partial T}{\partial x}+v\frac{\partial T}{\partial y}=\frac{k_{hnf}}{(\rho C_p)_{hnf}}\frac{\partial^2 T}{\partial y^2} \tag{3.3}$$

3.2.2 Thermophysical features

In this investigation, we preserve our study jointly for nanofluid and hybrid nanoliquid. We have picked two particles namely Ag and CuO for hybrid nanofluid and CuO for ordinary nanofluid. To acquire the hydrothermal features perfectly, we have assembled the upcoming equations using the thermophysical model for hybrid nanofluid as prescribed by Devi and Devi [116]. Those formulations are depicted in Table 3.1. Also thermophysical data of nanoparticles is enlisted in Table 3.2.

Table 3.1: Thermophysical properties of nanofluid and hybrid nanofluid

Properties	**Nanofluid (** CuO / *water* **)**
Density	$\rho_{nf}=(1-\phi)\rho_f+\phi\rho_s$
Heat capacity	$(\rho C_p)_{nf}=(1-\phi)(\rho C_p)_f+\phi(\rho C_p)_s$
Viscosity	$\mu_{nf}=\frac{\mu_f}{(1-\phi)^{2.5}}$
Thermal conductivity	$\frac{k_{nf}}{k_f}=\frac{k_s+(n-1)k_f-(n-1)\phi(k_f-k_s)}{k_s+(n-1)k_f+\phi(k_f-k_s)}$
Electrical conductivity	$\frac{\sigma_{nf}}{\sigma_f}=1+\frac{3(\sigma-1)\phi}{(\sigma+2)-(\sigma-1)\phi}$ *where* $\sigma=\frac{\sigma_s}{\sigma_f}$
Properties	**Hybrid Nanofluid(** $Ag-CuO$ / *water* **)**
Density	$\rho_{hnf}=\left\{(1-\phi_2)\left[(1-\phi_1)\rho_f+\phi_1\rho_{S_1}\right]\right\}+\phi_2\rho_{S_2}$
Heat capacity	$(\rho C_p)_{hnf}=\left\{(1-\phi_2)\left[(1-\phi_1)(\rho C_p)_f+\phi_1(\rho C_p)_{S_1}\right]\right\}+\phi_2(\rho C_p)_{S_2}$
Viscosity	$\mu_{hnf}=\frac{\mu_f}{(1-\phi_1)^{2.5}(1-\phi_2)^{2.5}}$

Thermal conductivity	$\frac{k_{hnf}}{k_{bf}} = \frac{k_{s_2} + (n-1)k_{bf} - (n-1)\phi_2(k_{bf} - k_{s_2})}{k_{s_2} + (n-1)k_{bf} + \phi_2(k_{bf} - k_{s_2})}$ $where \ \frac{k_{bf}}{k_f} = \frac{k_{s_1} + (n-1)k_f - (n-1)\phi_1(k_f - k_{s_1})}{k_{s_1} + (n-1)k_f + \phi_1(k_f - k_{s_1})}$
Electrical conductivity	$\frac{\sigma_{hnf}}{\sigma_{bf}} = \frac{\sigma_{s_2} + 2\sigma_{bf} - 2\phi_2(\sigma_{bf} - \sigma_{s_2})}{\sigma_{s_2} + 2\sigma_{bf} + \phi_2(\sigma_{bf} - \sigma_{s_2})}$ $where \ \frac{\sigma_{bf}}{\sigma_f} = \frac{\sigma_{s_1} + 2\sigma_f - 2\phi_1(\sigma_f - \sigma_{s_1})}{\sigma_{s_1} + 2\sigma_f + \phi_1(\sigma_f - \sigma_{s_1})}$

Table 3.2: Thermophysical properties of base fluid and nanoparticles

Physical properties	Water	CuO	Ag
C_p (J/Kg K)	4180	535.6	235
ρ (Kg/m^3)	997	6500	10500
κ (W/mK)	0.6071	20	429
σ (S/m)	5.5×10^{-6}	5.96×10^{7}	3.5×10^{6}

3.2.3 Boundary conditions

The indispensable boundary conditions for the present problem are:

$$\left.\begin{aligned} &u = u_w + l\frac{\partial u}{\partial y},\ v = v_w,\ T = T_w \ at\ y = 0 \\ &u \to 0, T \to T_\infty \ as\ y \to \infty \end{aligned}\right\} \qquad (3.4)$$

Where, l assigns the velocity slip factor.

3.2.4 Similarity transformation

Here, we executed similarity transformation to convert the leading PDEs (3.1)-(3.3) along with (3.4) into nonlinear ODEs. The requisite renovations are as follows:

$$\left.\begin{aligned} \eta = \sqrt{\frac{a}{\nu_f}}y,\ u = axf'(\eta),\ v = -\sqrt{\nu_f a}\, f(\eta) \\ \theta(\eta) = \frac{T - T_\infty}{T_w - T_\infty} \end{aligned}\right\} \tag{3.5}$$

Using the above set of similarity transformation as in (3.5) equations (3.1)-(3.3) along with (3.4) alter as:

$$f''' + \frac{A_1}{A_4}\left(ff'' - f'^2\right) - \frac{A_5}{A_4}Mf'\sin^2\gamma = 0 \tag{3.6}$$

$$\frac{1}{\Pr}\theta'' + \frac{A_2}{A_3}f\theta' = 0 \tag{3.7}$$

Where, the prime symbolizes the derivatives with respect to η and

$$A_1 = \frac{\rho_{hnf}}{\rho_f}, A_2 = \frac{(\rho C_p)_{hnf}}{(\rho C_p)_f}, A_3 = \frac{k_{hnf}}{k_f}, A_4 = \frac{\mu_{hnf}}{\mu_f}, A_5 = \frac{\sigma_{hnf}}{\sigma_f}$$

Similarly, boundary conditions renovate as:

$$\left.\begin{aligned} f = S,\ f' = 1 + Lf'',\ \theta = 1\ at\ \eta = 0 \\ f' \to 0,\ \theta \to 0\ as\ \eta \to \infty \end{aligned}\right\} \tag{3.8}$$

The non-dimensional factors of our analysis are:

Here, $S > 0$ designates suction, $S = 0$ corresponds to impermeable surface and $S < 0$ denotes injection through permeable texture.

3.2.5 Physical quantities

Physical quantities which are noteworthy for engineering purpose to design equipment at nanolevel, are skin friction and Nusselt number. They are mathematically framed as:

$$C_f = \frac{2\mu_{hnf}\left(\frac{\partial u}{\partial y}\right)_{y=0}}{\rho_{hnf} u_w^{\,2}},\ Nu = \frac{1}{\kappa_f\left(T_w - T_\infty\right)}\left(\kappa_{hnf}\frac{\partial T}{\partial y}\right)_{y=0}\Bigg\} \tag{3.9}$$

Implementing the similarity renovation as in (5), we acquired reduced skin friction and reduced Nusselt number from equation (9) respectively in the following away:

$$C_{fr} = \sqrt{\mathrm{Re}_x}\ .\ C_f = \left(\frac{\sqrt{2}\left(1-\phi_1\right)^{-2.5}.\left(1-\phi_2\right)^{-2.5}}{\left(1-\phi_2\right)\left\{\left(1-\phi_1\right)+\phi_1.\left(\frac{\rho_{s_1}}{\rho_f}\right)\right\}+\phi_2.\left(\frac{\rho_{s_2}}{\rho_f}\right)}\right) f''(0) \tag{3.10}$$

$$Nu_r = \frac{Nu}{\sqrt{\mathrm{Re}_x}} = -\frac{\kappa_{hnf}}{\kappa_f}\theta'(0) \tag{3.11}$$

3.3 Numerical procedure

3.3.1 Method of solution

The coordination of differential equations (3.6)-(3.7) together with boundary conditions (3.8) is difficult to solve analytically, hence it is solved numerically. A methodical systematic shooting technique in composition of RK-4 method is used to satisfy the asymptotic boundary condition and to acquire the desired solution. To complete this we first transform the leading nonlinear ODEs into an initial value problem. We do this by relabeling the variables in the subsequent way:

$$\left(f,\ f',\ f'',\ \theta,\ \theta'\right)^T = \left(z_1,\ z_1' = z_2,\ z_2' = z_3,\ z_4,\ z_4' = z_5\right)^T \tag{3.12}$$

On behalf of our numerical scheme, we obtain the system as:

$$\begin{pmatrix} z_1' \\ z_2' \\ z_3' \\ z_4' \\ z_5' \end{pmatrix} = \begin{pmatrix} z_2 \\ z_3 \\ z_4 \\ -\frac{A_1}{A_4}\left(z_1 z_3 - z_2^{\,2}\right) + \frac{A_5}{A_4} M z_2 \sin^2\gamma \\ z_5 \\ -\Pr\frac{A_2}{A_3} z_1 z_5 \end{pmatrix} \tag{3.13}$$

$$\begin{pmatrix} z_1(0) \\ z_2(0) \\ z_3(0) \\ z_4(0) \\ z_5(0) \end{pmatrix} = \begin{pmatrix} S \\ 1 + L\beta_1 \\ \beta_1 \\ 1 \\ \beta_2 \end{pmatrix} \tag{3.14}$$

Above illustrated systems (13-14) are required to solve. Inputs of unknowns S, β_1, β_2 firstly are presumed and whole numerical outcomes have been achieved using MAPLE-17 until $f' \to 0,\ \theta \to 0\ as\ \eta \to \infty$ are fulfilled. The boundary conditions at $\eta \to \infty$ are replaced by those at $\eta = \eta_\infty$. The process is repeated so that the converged result secures a tolerance limit of 10^{-6} level. The obtained numerical results are shown in a table and plotted graphically.

3.3.2 Code of verification

To assure the validity of our current model, we have compared the values of $\theta'(0)$ for diverse values of Pr and checked those values with Wang [117] in Table 3.3. To achieve this, in our simulative work, we select the numerical values of active parameters as $M = \gamma = \phi_1 = \phi_2 = L = S = 0.0$. We noticed that extracted outcomes are in good assurance with those as communicated by [117].

Table 3.3: Comparison of values of $\theta'(0)$ for various Pr

Pr	$\theta'(0)$	
	Wang [117]	Present
0.7	0.4539	0.453962
2.0	0.9114	0.911397
7.0	1.8954	1.895420
20.0	3.3539	3.353861

3.4 Results and discussion

This section is dedicated to explore the hydrothermal features owing to requisite factors on velocity and temperature profile. We have put on display such effects through pictures plus tables. To retain our parametric study, we have allocated the parametric values in our simulation as $\Pr = 6.2,\ L = 0.5,\ M = 0.5,\ S = 0.5,\ \phi_1 = 0.05,\ \phi_2 = 0.05$ unless otherwise given. The simulative features are obtained for diverse values of parameters.

3.4.1 Effect of Magnetic Parameter (M)

The consequence of magnetic parameter M over velocity $f'(\eta)$ and temperature $\theta(\eta)$ are portrayed through Figure 3.2 and 3.3. Figure 3.2 communicates a clear drop off for velocity inside the flow regime. Clear consequence is marked within $0.0 \le \eta \le 3.0$ (not precisely determined). Beyond that portion, the curve retains its asymptotic convergence. Actually, Lorentz force is created by this magnetic field due to the motion of an electrically conducted fluid and such force are blessed with retardation feature. That's why we encounter an opposing tendency in $f'(\eta)$. For both nanofluid and hybrid nanofluid as M boosts, the retardation strength increases. As a consequence, velocity also declines. Comparatively, hybrid nanosuspension acquires less magnitude in $f'(\eta)$ than that of usual nanosuspension. Table 3.4 explores reduction features in

Cf_r . Outcome is proper for nanosuspension. For hybrid nanoliquid it declines at 18.95%, but for usual nanoliquid it was 20.35%. Resistive features of the liquid with the surface texture, originates a friction at the molecular level. Continuation of such frictional effort aids to increase the temperature in Figure 3.3. Clear outcome has been perceived inside $0.0 \le \eta \le 2.0$ (not precisely determined). Hybrid suspension seizes maximum temperature than usual suspension. Physically, presence of double additive mixtures provides the fluid to acquire maximum temperature. In Table 3.5 heat transport drops off at 3.45% for hybrid nanoliquids, but ordinary nanosuspension illustrates 4.15%. Thus, slower reduction in heat transport is assured for hybrid nanofluid.

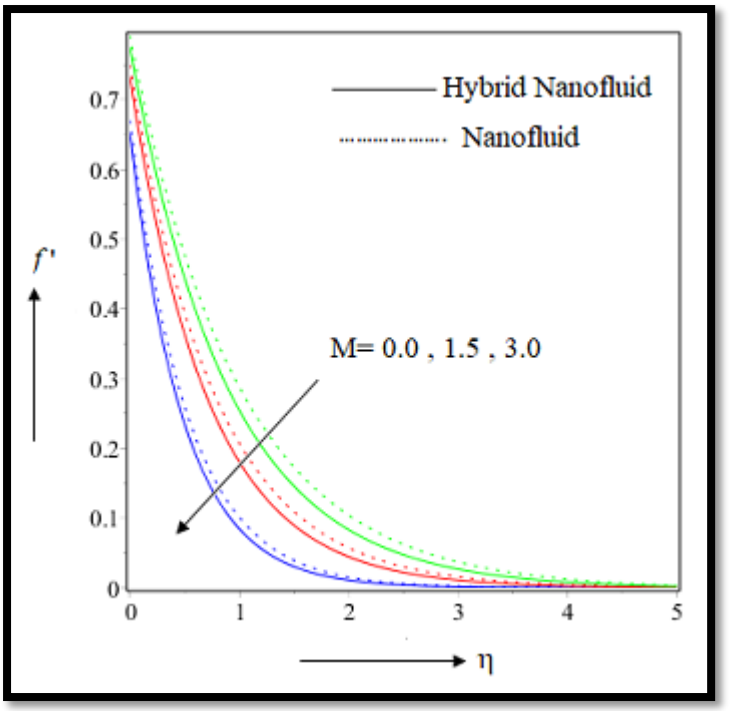

Figure 3.2: Effect of M on $f'(\eta)$

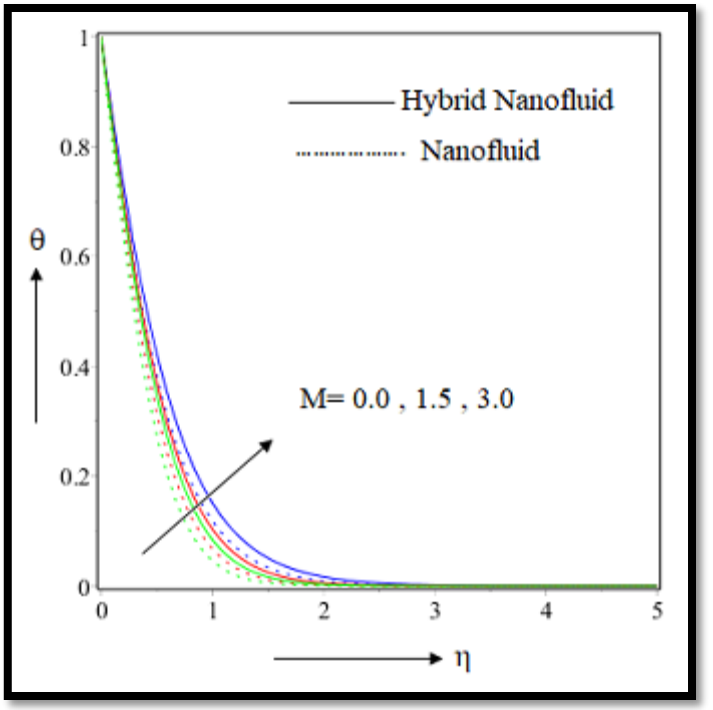

Figure 3.3: Effect of M on $\theta(\eta)$

3.4.2 Effect of Slip Parameter (L)

Outcome of slip factor L is depicted in Figure 3.4. Velocity is found to decline for both nanosolutions. Distinct features are perceived within $0.0 \le \eta \le 1.0$ (not precisely determined). That's why impressive impact is restored near the texture of the surface. Highest speed up is foreseen for no-slip condition. As soon as slip factor raises nanoliquid's velocity begins to drop off. Skin friction gets increased due to L. Comparatively, maximum impact is perceived for hybrid nanocomposite. The increment rate is 27.30% for hybrid nanofluid in Table 3.4, whereas usual suspension exhibits 25.37% increment. Physically, addition of double additives in hybrid liquids drags the texture mostly. Thus texture of sheet will be more drag affected for hybrid composite. Figure 3.16 depicts the contour plot of hybrid nanofluid Cf_r for M *and* L. Effect of L on the trajectory of temperature has been depicted in Figure 3.5. As the slip parameter increase the velocity gets decreased. But as the velocity lessens, the frictional hindrance swells and as an outcome heat produced. So temperature gets increased in this case. Hybrid nanocomposite acquires

utmost temperature in comparison with usual nanofluid. Heat transfer shrinks for L . Thus cooling procedure will be little bit slowed down for L .

3.4.3 Effect of Inclination angle of Magnetic Field (γ)

The impression of inclination angle γ on velocity and temperature are illustrated through Figure 3.6 and 3.7. This gives magnificent consequence on velocity distribution and temperature also. Effects are distinct and lucid in Figure 3.6. There is a trigonometric "sin" factor of magnetic strength is involved. As the angle enlarges in between $0^0 \to 90^0$ the magnetic strength gets increased and thus the $M \sin^2(\gamma)$ term in equation (3.6) aid the nanoliquid speed to reduce. Drag affect is decreased for the inclined magnetic orientation. Table 3.4 portrays 10.53% declination for hybrid nanocomposite and 11.26% reduction for usual nanoliquids. It is apparent that the temperature $\theta(\eta)$ will be improved for the augmentation in γ. Cause of this occurrence is same as in section 4.2. Table 3.5 explores that heat transport is provoked for elevated γ. Comparatively, effective and major heat transfer is assured for hybrid nanoliquids. Rate has been marked 5.85% where it is 4.17% for usual nanosolution. Thus, efficient cooling procedure can be maintained for γ. Contour plot of hybrid nanofluid Nu_r for L *and* γ is depicted in Figure 3.20.

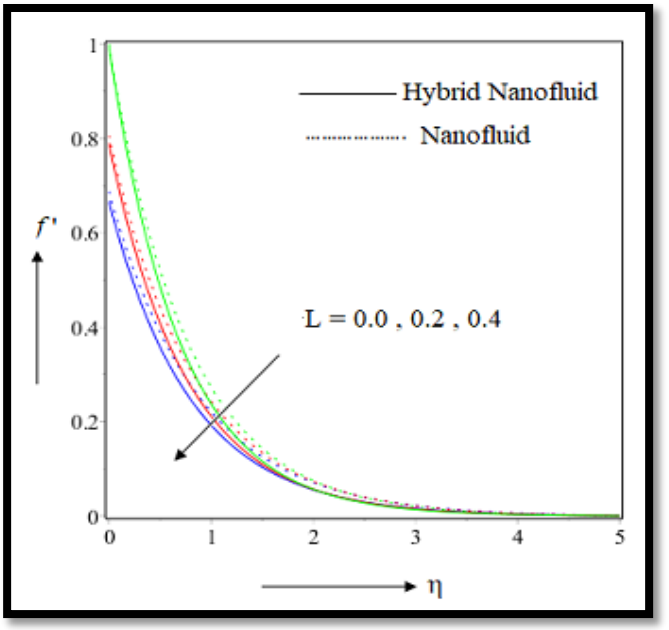

Figure 3.4: Effect of L on $f'(\eta)$

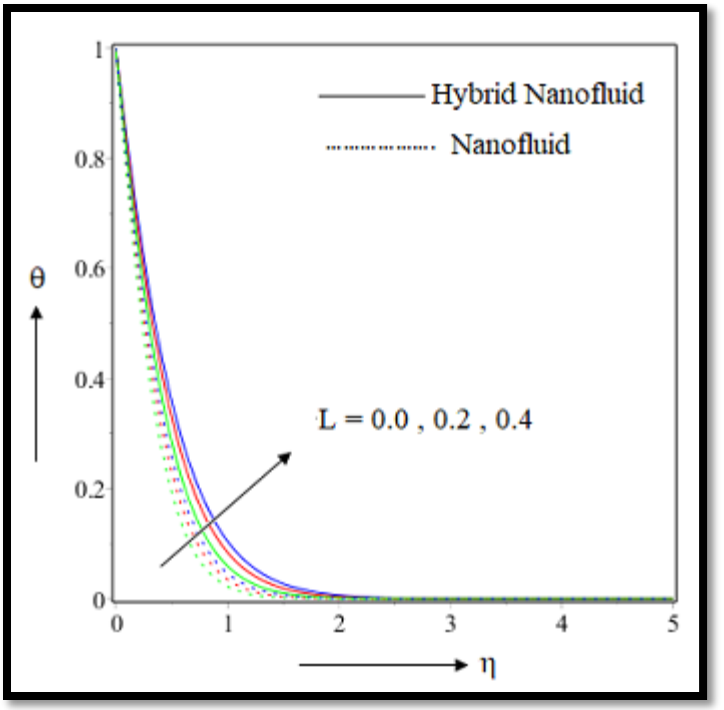

Figure 3.5: Effect of L on $\theta(\eta)$

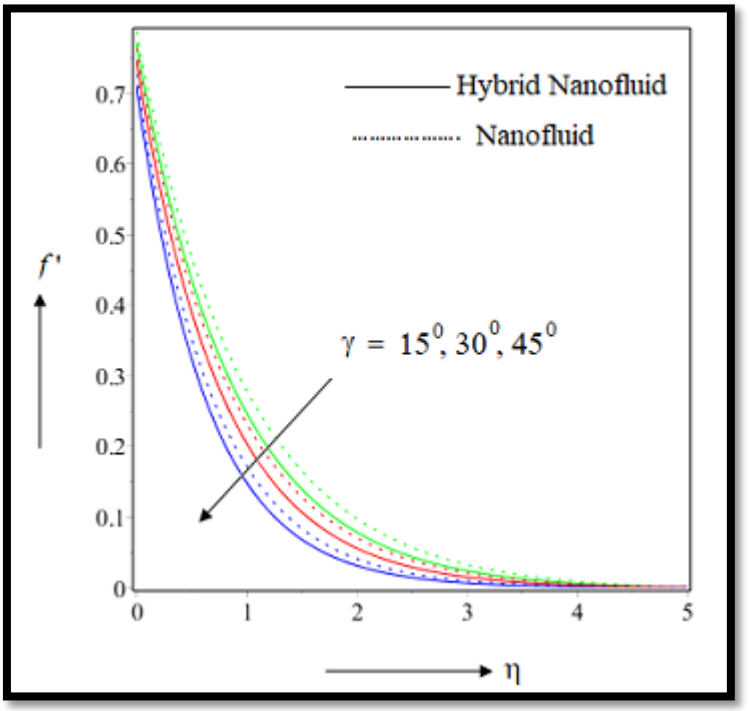

Figure 3.6: Effect of γ on $f'(\eta)$

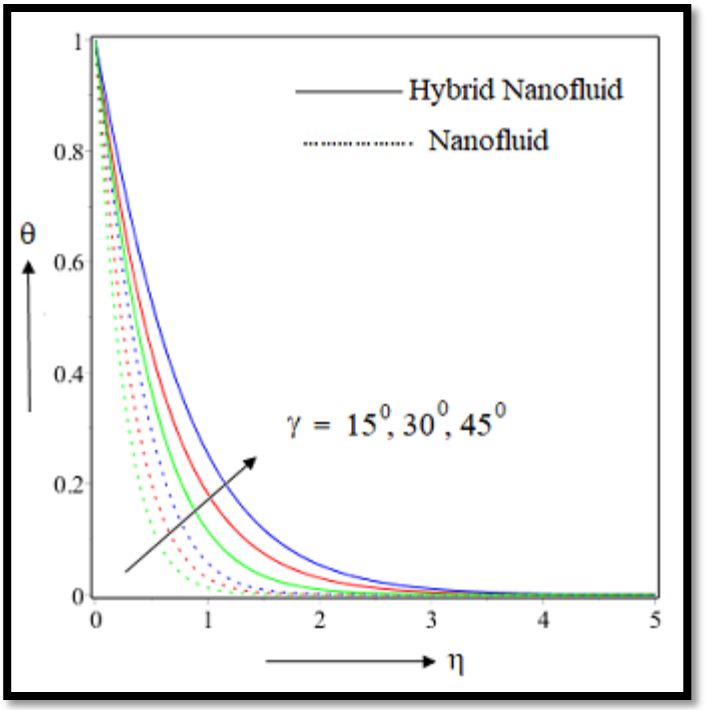

Figure 3.7: Effect of γ on $\theta(\eta)$

3.4.4 Effect of Suction/injection parameter (S)

Consequences of suction or injection parameter S on velocity and temperature are revealed in Figure 3.8 and Figure 3.9. Amplification of suction parameter $(S > 0.0)$ has the propensity to force the liquid into unoccupied spaces. So the velocity gets decreased in Figure 3.8 for both CuO-Water as well as $Ag - CuO / Water$ nanosolution. Maximum speed is observed for impermeable textured surface. Besides, for injection case $(S < 0.0)$ reverse outcome has been perceived. Now, impermeable character of the sheet succors the least profile. Usual nanosolution gets enhanced velocity profile in both injection and suction case. For injection, drag factor in Table 3.4 has found to escalate at 9.17% rate, where opposite outcome is traced for suction at the rate 10.16%. Thus, texture will be less affected for suction. Figure 3.18 expresses contour diagram of hybrid nanofluid's Cf_r for γ *and* S. Temperature also decreased for $(S > 0.0)$ through that permeable surface. Maximum temperature is assured for impermeable surface in Figure 3.9. But,

opposite outcome has been explored for $(S < 0.0)$. Impermeable surface is supposed to have minimum outcome for injection. Consequences are found distinct and clearly traceable. Hybrid nanocomposite acquires elevated outline as compared to ordinary nanosolution. Physically, inclusion of double tiny mixtures assists the hybrid nanoliquid to achieve enhanced temperature. Figure 3.10, 3.11 and 3.12 depict the features of streamline for suction, impermeable and injection cases respectively. Suction procedure leads the system to acquire 9.62% increment in heat transport. Injection mechanism assures reverse consequence. 41.68% reduction is marked for injection. Here, maximum cooling performance is provided by impermeable texture in Table 3.5. Pictorial appearance of contours for hybrid nanofluid Nu_r for S *and* M has been exhibited in Figure 3.21.

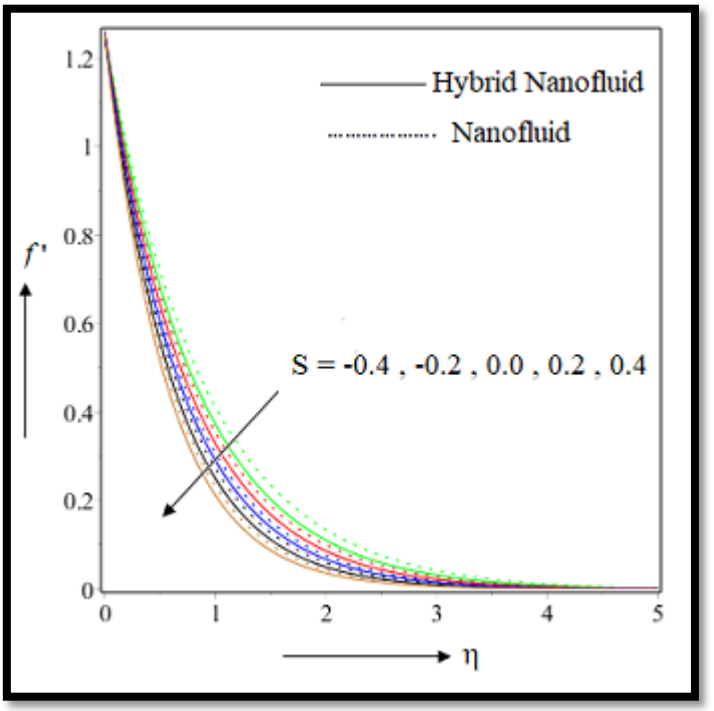

Figure 3.8: Effect of S on $f'(\eta)$

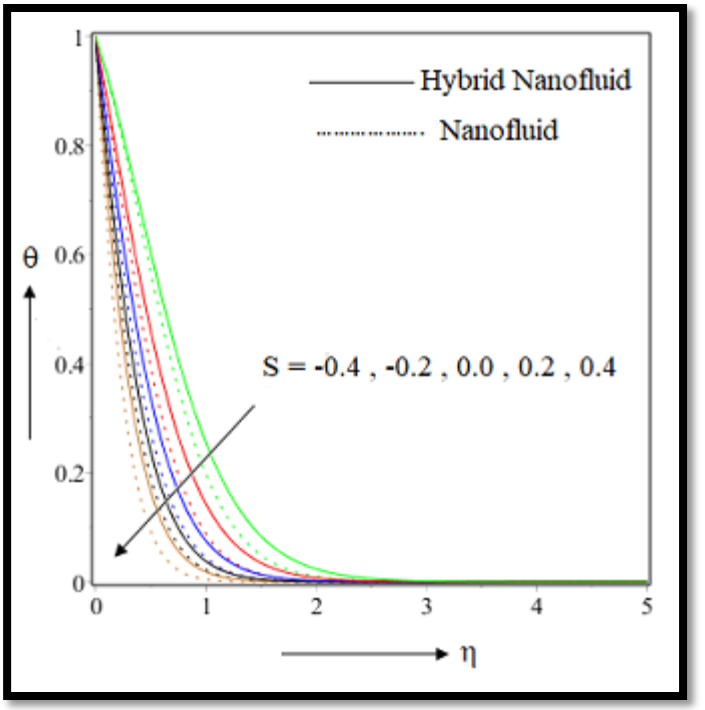

Figure 3.9: Effect of S on $\theta(\eta)$

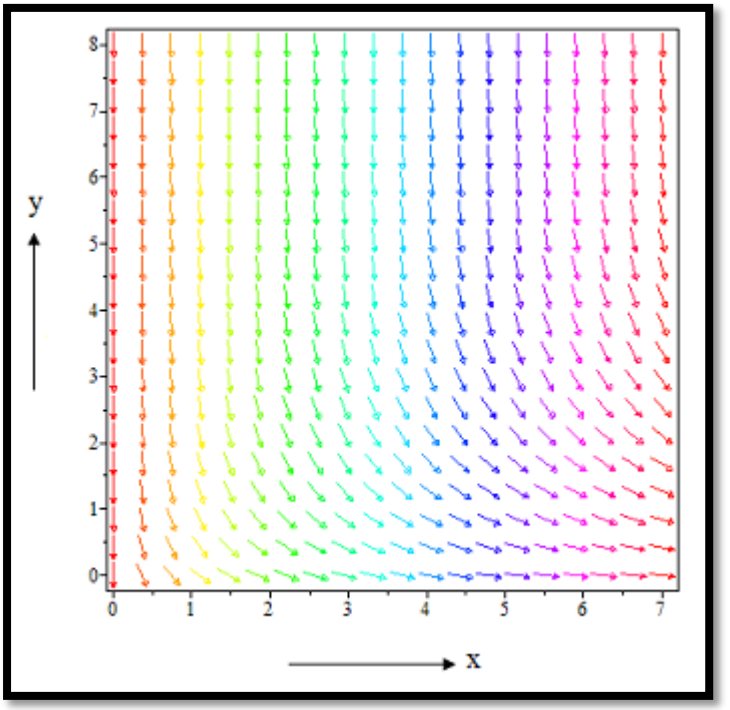

Figure 3.10: Streamlines features when S=0.2

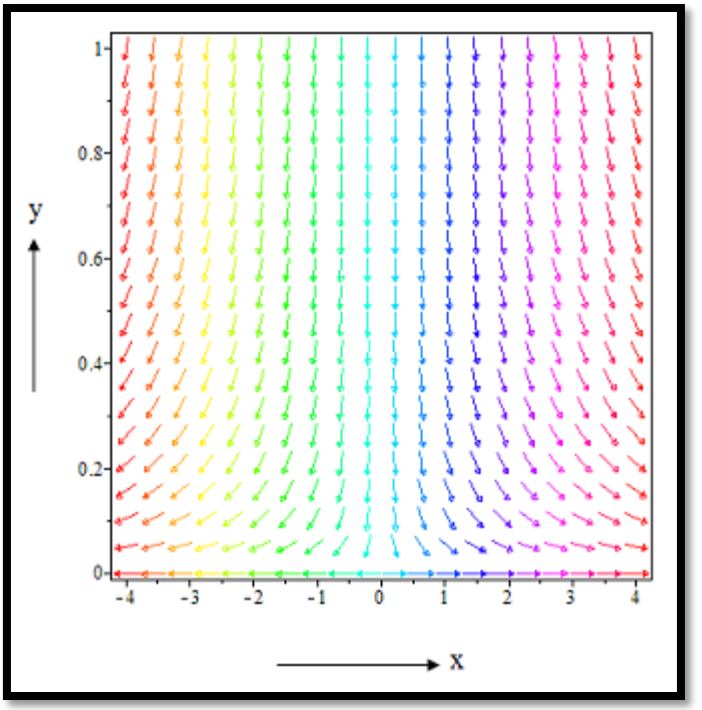

Figure 3.11: Streamlines features when S=0.0

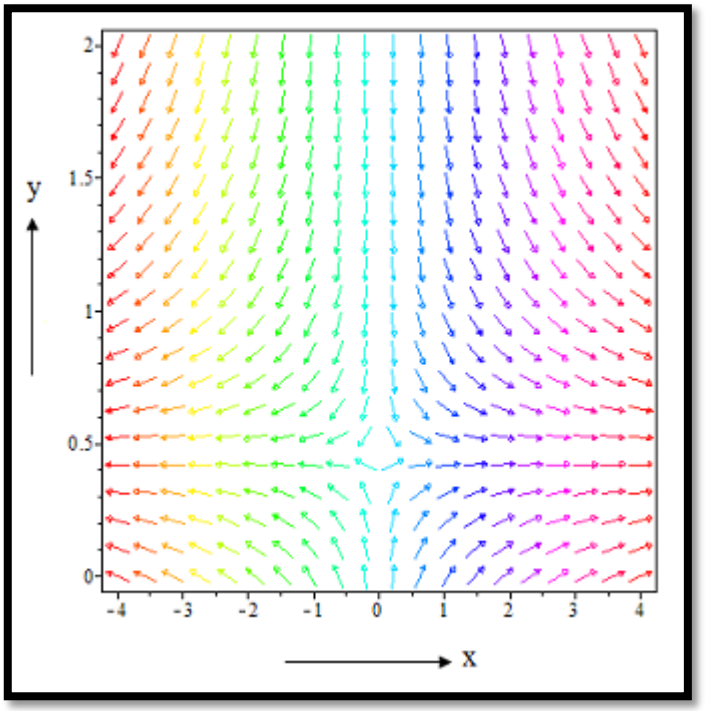

Figure 3.12: Streamlines features when S= - 0.2

3.4.5 Effect of nanoparticle volume fraction (ϕ_1, ϕ_2)

Figure 3.13 exhibits impact of volume fractions on velocity profile. For hybrid nanoliquids we varied the values of ϕ_2. But to simulate usual nanoliquids we altered those of ϕ_1. As the volume fraction boosts the dimensionless velocity profile also enlarges for both nano-composites. Ordinary nanofluid obtains high profile as compared to hybrid suspension. Thus at the vicinity fluid demonstrates less impact on velocity distribution. But, slight away from the surface effects started to flourish. Addition of tiny ingredients provides favorable intensification in Cf_r. Contour representation of skin friction is exemplified in Figure 3.17. Similarly, temperature distribution as in Figure 3.14 enhanced owing to raising volume fraction. Physically, adding more tiny ingredients into host liquid facilitates the nanoliquids to dissipate more energy as heat. Thus effective heat distribution also increased. At the proximity of sheet affects sound well enough. But, beyond $\eta > 1.0$ such effect is vanished. Again hybrid nanofluid attains elevated than usual one. Heat transfer is getting amplified due to addition of nanocomposites. It is quite justified because more inclusion of nanoparticles aids the nanosolution to achieve high heat transport rate. Figure 3.19 provides contour diagram of heat transfer due to M *and* ϕ_2.

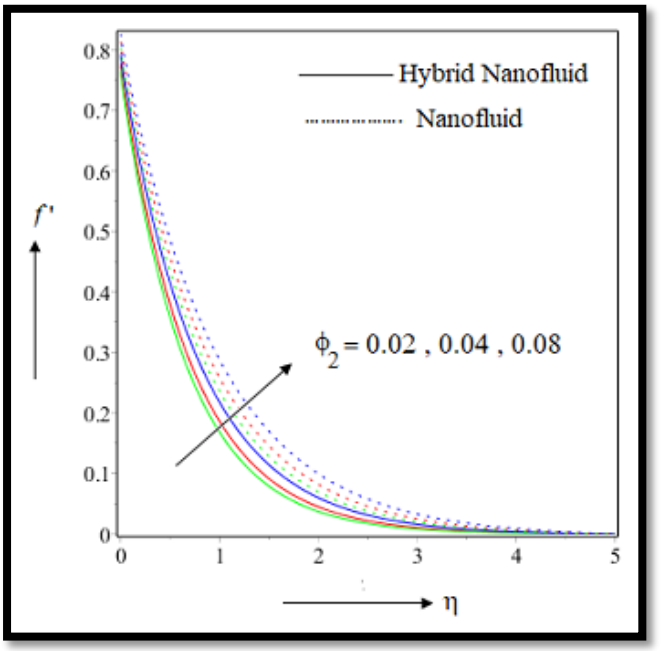

Figure 3.13: Effect of ϕ_2 on $f'(\eta)$

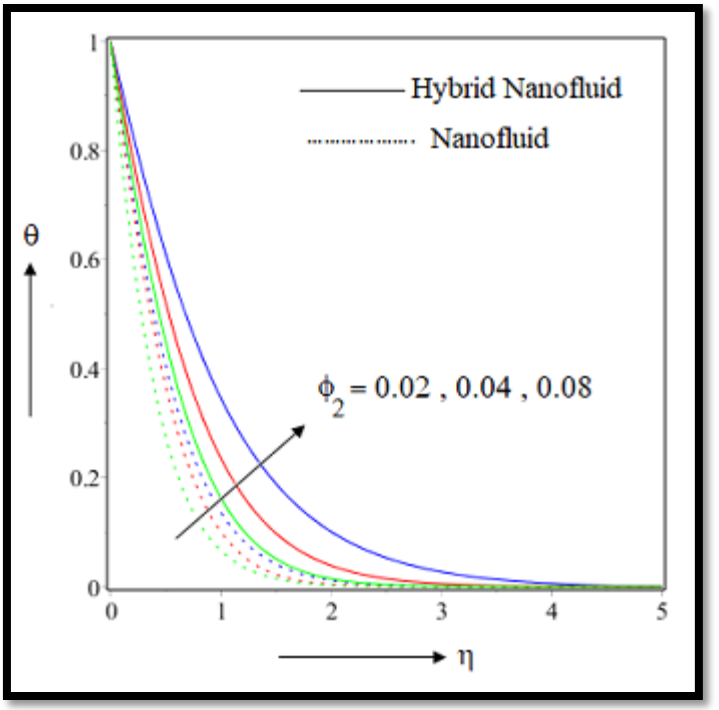

Figure 3.14: Effect of ϕ_2 on $\theta(\eta)$

3.4.6 Effect of Prandtl number (Pr)

Since, our velocity profile is free from Pr ; hence we can't detect any effect on velocity due to Pr . But, our dimensionless temperature in Figure 3.15 has been found to reduce as Pr goes high. Within $0.0 \le \eta \le 1.5$ (not precisely determined) outcome is perceived distinctly. Though hybrid liquid depicts comparatively high profile, but the deviation of temperature among hybrid and usual nanosuspension is high enough. Higher Pr values ensure maximum heat transport features as enlisted in Table 3.5.

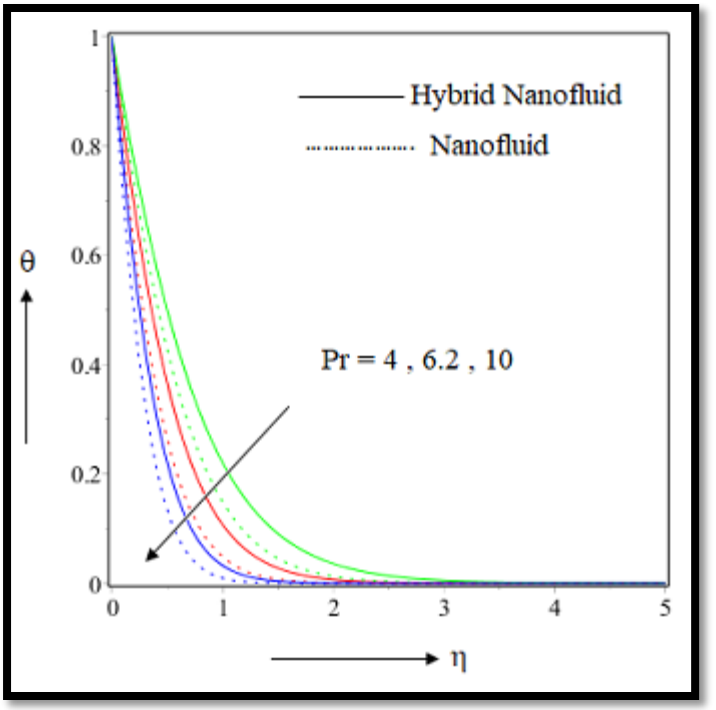

Figure 3.15: Effect of Pr on $\theta(\eta)$

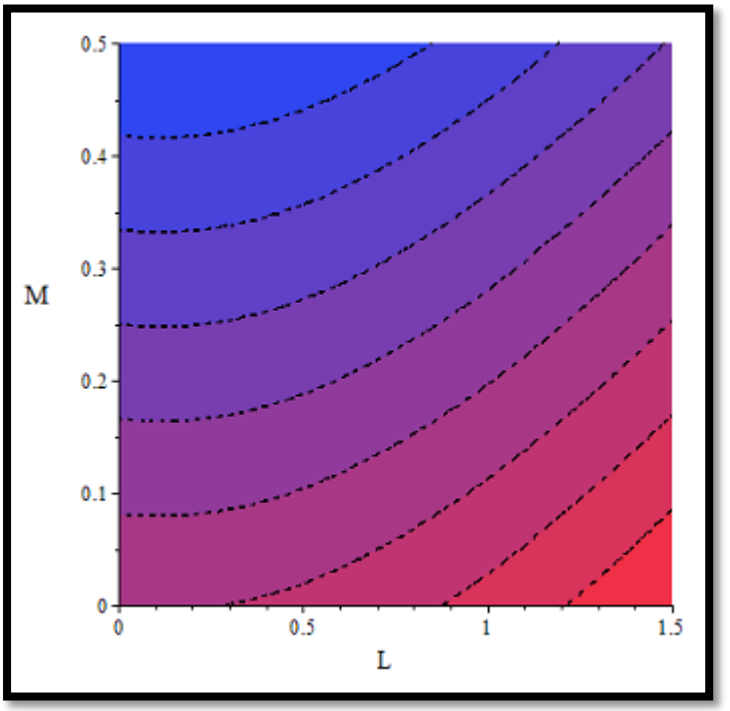

Figure 3.16: Contour plots of hybrid nanofluid Cf_r for M *and* L

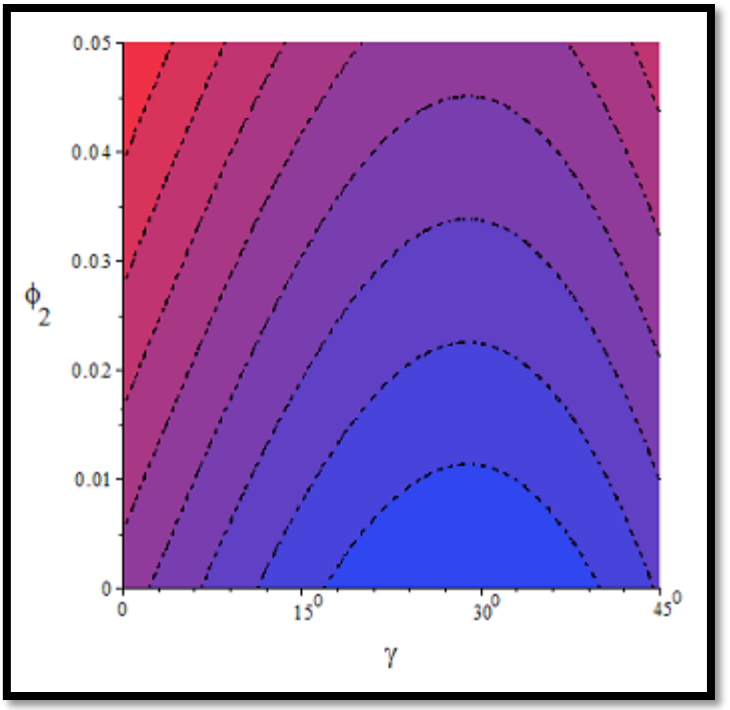

Figure 3.17: Contour plots of hybrid nanofluid Cf_r for γ *and* ϕ_2

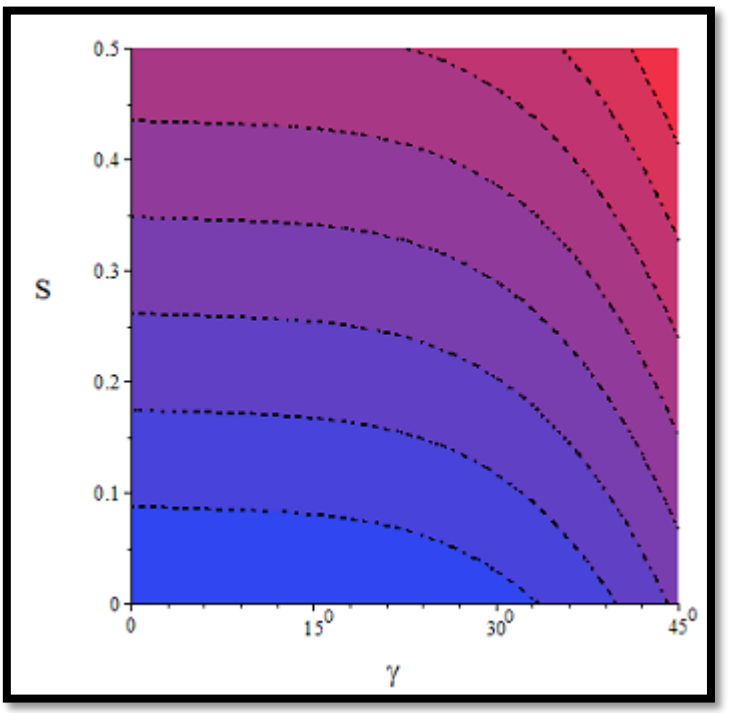

Figure 3.18: Contour plots of hybrid nanofluid Cf_r for γ *and* S

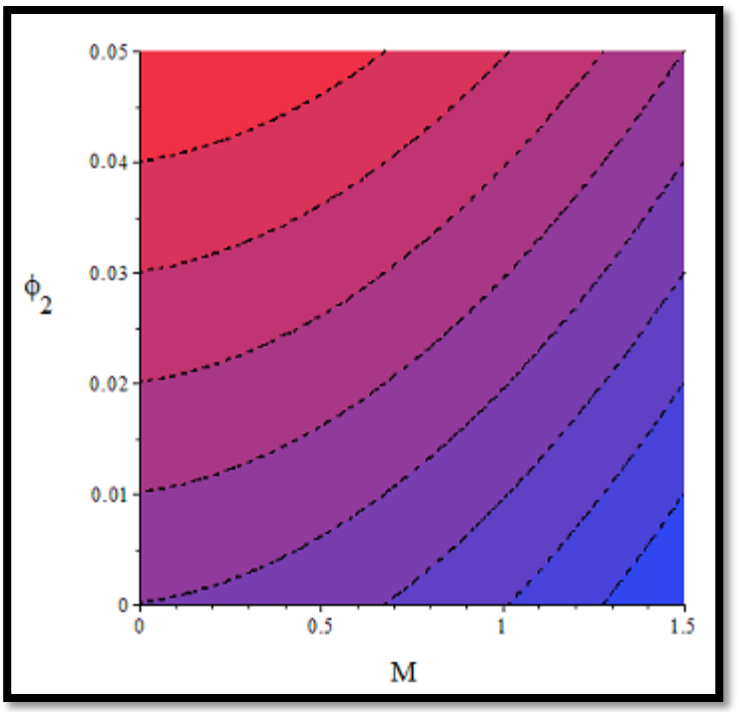

Figure 3.19: Contour plots of hybrid nanofluid Nu_r for M *and* ϕ_2

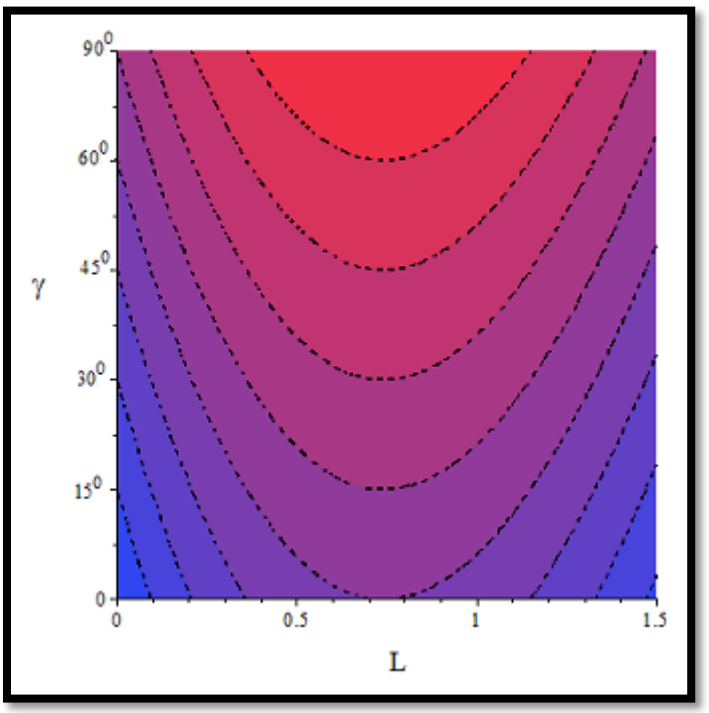

Figure 3.20: Contour plots of hybrid nanofluid Nu_r for L *and* γ

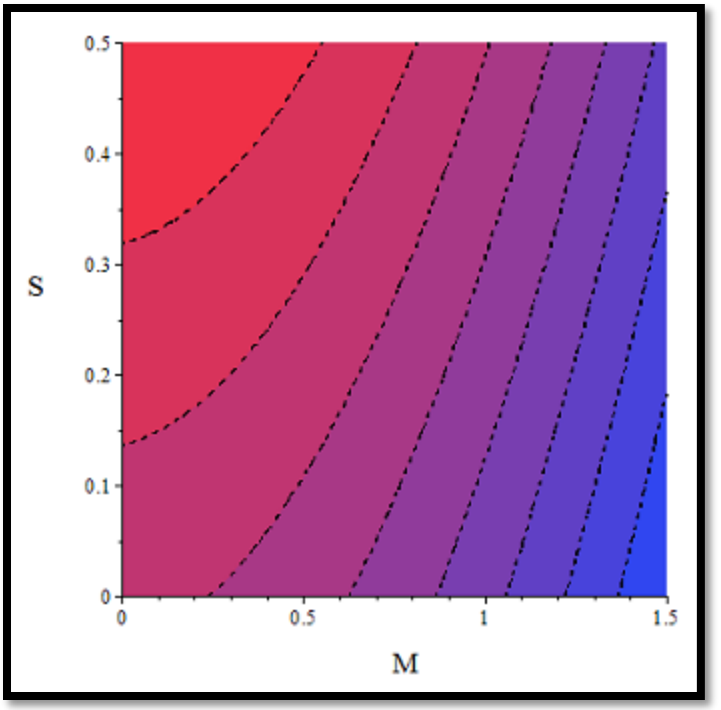

Figure 3.21: Contour plots of hybrid nanofluid Nu_r for S *and* M

3.5 Conclusions

In this chapter we have concentrated to describe the inclined magnetic effects on the hydrothermal features of two types of nanoliquid; hybrid and usual. The requisite flow has been passed over permeable stretched surface. Surface slip is also introduced. Leading equations are deformed from PDE to ODE by via well-known similarity renovation. Employing RK-4 procedure, we sketched out those ODEs numerically. Exhaustive features of inclined magnetic affect, surface slip, suction or injection, volume fraction are delineated through tables, graphs. Through our full examination some leading points succour our attention on the subsequent observations:

- Velocity acquires rising tendency for $S < 0.0$ *and* ϕ_2, but reverse upshot is assured owing to M, L, γ *and* $S > 0.0$.
- Usual nanosuspensions have always enhanced velocity profile than hybrid.

- Temperature gets intensified for $M, L, \gamma, S < 0.0$ *and* ϕ_2, whereas decreasing nature was marked for $\mathrm{Pr},\ S > 0.0$.
- Existence of double additives conveys amplifying thermal appearance for hybrid composites.
- Thermal transfer becomes effective for magnetic inclination and rate is decoded 5.85% for hybrid solution. Also, injection extracts maximum drop down in heat transport which was on average 41.68%.
- Hybrid nanofluid consumes maximum heat transfer capability compared usual nanoliquid.

Table 3.4: Effects of parameters on Cf_r for both nanofluids

M	γ	L	S	ϕ_2	Cf_r		CPU time
					hybrid nanofluid	*nanofluid*	
0.0	30^0	0.5	0.5	0.05	-1.350531	-1.190559	2.26 s
1.5					-1.606563	-1.432874	2.25 s
3.0					-2.087785	-1.886505	2.26 s
0.5	15^0				-1.371193	-1.212159	2.27 s
	30^0				-1.515682	-1.348704	2.18 s
	45^0				-1.738168	-1.558377	2.18 s
	15^0	0.0			-2.242303	-1.923860	2.17 s
		0.2			-1.630114	-1.435997	2.17 s
		0.4			-1.297694	-1.159280	2.18 s
		0.5	-0.4		-2.393350	-2.089991	2.19 s
			-0.2		-2.637914	-2.368753	2.19 s
			0.0		-2.883109	-2.629647	2.20 s
			0.2		-3.179158	-2.855917	2.18 s
			0.4		-3.502402	-3.153557	2.18 s
			0.5	0.02	-1.816123	-1.457692	2.27 s
				0.04	-1.733624	-1.382480	2.25 s
				0.08	-1.602861	-1.290178	2.25 s

Table 3.5: Effects of parameters on Nu_r for both nanofluids

M	γ	L	S	ϕ_2	Pr	Nu_r		CPU time
						hybrid nanofluid	*nanofluid*	
0.0	30^o	0.5	0.5	0.05	6.2	2.064331	1.828131	1.57 s
1.5						1.992989	1.752233	1.58 s
3.0						1.655440	1.588306	1.55 s
0.5	15^o					2.106254	1.654795	1.57 s
	30^o					2.215450	1.732874	1.71 s
	45^o					2.270334	1.828610	1.71 s
	15^o	0.0				1.545295	1.435461	1.70 s
		0.2				1.351229	1.328651	1.71 s
		0.4				1.223387	1.187994	1.72 s
		0.5	-0.4			0.610605	0.651107	1.70 s
			-0.2			1.047001	1.166779	1.67 s
			0.0			1.590383	1.789433	1.69 s
			0.2			1.743521	1.820027	1.68 s
			0.4			2.222163	2.353675	1.67 s
			0.5	0.02		1.876231	1.787690	1.71 s
				0.04		2.024536	1.864352	1.70 s
				0.08		2.134261	1.987690	1.72 s
					4.0	2.137192	2.014571	1.71 s
					6.2	2.216543	2.087653	1.76 s
					10.0	2.240761	2.164329	1.77 s

CHAPTER 4

Influence of active and passive control of nanoparticles for the magnetized nanofluid flow over a slippery stretching cylinder*

4.1 Introduction

In this chapter the investigation is done for the active passive controlled flow over a stretching cylinder assuming realistic velocity slip and temperature jump conditions. Passively controlled flow conditions are more realistic than that of actively controlled flow conditions. External heat source and perpendicular magnetic field to the axis of cylinder is considered in our model. PDEs are converted into ODEs by similarity transformations. The boundary conditions are also converted. The following results are derived from the outcomes of our investigation.

- The effects of several parameters on velocity profile for both velocity slip and no slip conditions.
- The effects of several parameters on frictional drag for both velocity slip and no slip conditions.
- The effects of several parameters on temperature profile for both active and passive control of nanoparticles.
- The effects of several parameters on heat transmission for both active and passive control of nanoparticles.
- The effects of several parameters on concentration profile for both active and passive control of nanoparticles.
- The effects of several parameters on mass transmission for both active and passive control of nanoparticles.

***This chapter is based on the paper published in: International Journal of Modern Physics B, 37(19) (2023), 2350184, (SCIE).**

4.2. Mathematical formulation:

4.2.1. Governing equations

A steady, laminar, incompressible nanofluid flow along a stretching cylinder with radius b is considered in this problem. r -Axis is measured along radial direction whereas z - axis is taken along axis of the cylinder. The system is described in Figure 1. $z=0$ Plane is the plane of symmetry for the nanofluid flow. Temperature and concentration at surface are respectively T_w and C_w but the ambient temperature and concentration are T_∞ and C_∞ . A magnetic influence B_0 is admitted in the radial direction. In our discussion (w,u) are taken as velocity components along (z,r) axes. Brownian migration and thermophoresis effect are employed in the flow. An external heat source Q is taken into account. Active and passive control of nanoparticle concentration registered in the system. The upshots of temperature jump and velocity slip provision also taken in our study. We have taken the estimate of magnetic Reynolds number so small such that upshots of induced magnetic influence become negligible. Hall effects Ohmic heating together with viscous dissipation is omitted in this inspection. Under these assumptions, the leading equations [118-120] are

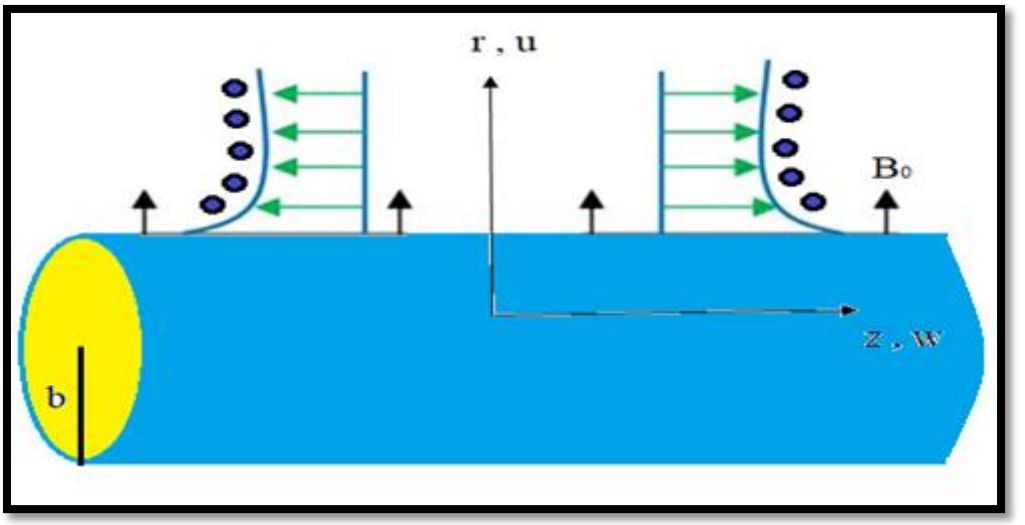

Figure 4.1: Physical geometry of the flow

$$\frac{\partial}{\partial z}(rw)+\frac{\partial}{\partial r}(ru)=0 \tag{4.1}$$

$$\rho_f\left(w\frac{\partial w}{\partial z}+u\frac{\partial w}{\partial r}\right)=\mu_f\left(\frac{\partial^2 w}{\partial z^2}+\frac{1}{r}\frac{\partial w}{\partial r}\right)-\sigma_f B_0^2 w \tag{4.2}$$

$$\rho_f\left(w\frac{\partial u}{\partial z}+u\frac{\partial u}{\partial r}\right)=-\frac{\partial p}{\partial r}+\mu_f\left(\frac{\partial^2 u}{\partial r^2}+\frac{1}{r}\frac{\partial u}{\partial r}-\frac{u}{r^2}\right) \tag{4.3}$$

$$\left(\rho C_p\right)_f\left(w\frac{\partial T}{\partial z}+u\frac{\partial T}{\partial r}\right)=\kappa_f\left(\frac{\partial^2 T}{\partial r^2}+\frac{1}{r}\frac{\partial T}{\partial r}\right)+Q\left(T-T_\infty\right)+\tau\left[D_B\frac{\partial C}{\partial r}\frac{\partial T}{\partial r}+\frac{D_T}{T_\infty}\left(\frac{\partial T}{\partial r}\right)^2\right] \tag{4.4}$$

$$\left(w\frac{\partial C}{\partial z}+u\frac{\partial C}{\partial r}\right)=D_B\left(\frac{1}{r}\frac{\partial}{\partial r}\left(r\frac{\partial C}{\partial r}\right)\right)+\frac{D_T}{T_\infty}\left(\frac{1}{r}\frac{\partial}{\partial r}\left(r\frac{\partial T}{\partial r}\right)\right) \tag{4.5}$$

Here, p is the pressure, ρ_f is fluid density, σ_f is electrical conductivity related to the fluid, T is temperature connected to the liquid. D_B, D_T Are referred to Brownian diffusion coefficient, thermophoresis coefficient. κ_f Refers to conductivity related to thermal attributes of the fluid. $\left(\rho C\right)_f$ Is the heat capacitance of fluid, $\tau=\frac{\left(\rho C\right)_p}{\left(\rho C\right)_f}$ illustrates the (Effective heat capacity of the fluid)/ (Heat capacity of the fluid).

4.2.2. Boundary conditions

The boundary provisions [118-120] for the above introduced model are given by the following equations:

$$u=0, w=w_w+L_{vel}\frac{\partial w}{\partial r}, T=T_w+L_{temp}\frac{\partial T}{\partial r}, \text{ at } r=b$$

$$\begin{cases} D_B\dfrac{\partial C}{\partial r}+\dfrac{D_T}{T_\infty}\dfrac{\partial T}{\partial r}=0, & \text{for passive control of } \phi \\ C=C_w, & \text{for active control of } \phi \end{cases} \text{, at } r=b \tag{2.6}$$

$$w \to 0, T \to T_\infty, C \to C_\infty \text{ at } r \to \infty \tag{2.7}$$

Where u and w are the velocity components along the r and z axes, respectively, and $w_w = 2az$ where a is a positive constant. L_{vel}, L_{temp}, are velocity , thermal slip factor respectively.

4.2.3. Similarity transformations

We convert the foremost flow equations (2.1-2.5) into system of ODEs by the following similarity variables as in [120]

$$\left.\begin{aligned} &u = -\frac{abf(\eta)}{\sqrt{\eta}}\ ,\ w = 2azf'(\eta)\ ,\ \theta(\eta) = \frac{T - T_\infty}{T_w - T_\infty}\ , \\ &\begin{cases} \phi(\eta) = \dfrac{C}{C_\infty} - 1\ , & \text{for passive control of } \phi \\ \phi(\eta) = \dfrac{C - C_\infty}{C_w - C_\infty}\ , & \text{for active control of } \phi \end{cases} \\ &\eta = \left(\frac{r}{b}\right)^2 \end{aligned}\right\} \tag{2.8}$$

After needed modernization equation (2.1) satisfies automatically. After dropping pressure Equation (2.2) to (2.5) changed as follows.

$$\eta f''' + f'' + \mathrm{Re}\left(ff'' - f'^2\right) - Mf' = 0 \tag{2.9}$$

$$\eta\theta'' + (1 + \mathrm{Re}\,\mathrm{Pr}\, f)\theta' + H\theta + \eta\left(Nb\theta'\phi' + Nt\theta'^2\right) = 0 \tag{2.10}$$

$$\eta\phi'' + \left(\frac{1}{2} + \mathrm{Re}\, Scf\right)\phi' + \frac{Nt}{Nb}\left(\frac{1}{2}\theta' + \eta\theta''\right) = 0 \tag{2.11}$$

Corresponding boundary equations are also changed as follows.

$$\left.\begin{aligned} &f(1) = 0,\ f'(1) = 1 + Lsvf''(1), \theta(1) = 1 + Lst\theta'(1) \\ &\begin{cases} Nb\phi'(1) + Nt\theta'(1) = 0\ , & \text{for passive control of } \phi \\ \phi(1) = 1\ , & \text{for active control of } \phi \end{cases} \end{aligned}\right\} \quad , \quad \text{at } r = b \tag{2.12}$$

$$f'(\infty)=0,\theta(\infty)=0,\phi(\infty)=0 \text{ at } r\to\infty \tag{2.13}$$

Where $\Pr=\frac{\nu_f}{\alpha_f}$ stands for Prandtl number , $\mathrm{Re}=\frac{ab^2}{2\nu_f}$, $Sc=\frac{\nu_f}{D_B}$, $H=\frac{Qb^2}{4\alpha_f}$, $M=\frac{\sigma_f {B_0}^2}{a\rho_f}$ designates Reynolds number , Schmidt number , external heat source parameter and magnetic parameter., $Nt=\frac{\tau D_T\left(T_w-T_\infty\right)}{T_\infty\nu_f}$ is thermophoresis parameter. Slip parameters for velocity, temperature depicted by $Lsv=\frac{2L_{vel}}{b}, Lst=\frac{2L_{temp}}{b}$

$$\begin{cases} Nb=\dfrac{\tau D_B C_\infty}{\nu_f}\ , & \text{for passive control of } \phi \\ Nb=\dfrac{\tau D_B\left(C_w-C_\infty\right)}{\nu_f}\ , & \text{for active control of } \phi \end{cases}$$

Is denoted as Brownian migration parameter.

4.2.4. Physical quantities

Appropriate physical quantities which are most useful for engineering applications are

$$\left.\begin{aligned} C_f&=\frac{2\tau_w}{\rho w_w^2} \text{ where } \tau_w=\mu_f\left(\frac{\partial w}{\partial r}\right)_{r=b} \\ Nu&=\frac{aq_w}{\kappa_f\left(T_w-T_\infty\right)} \text{ where } q_w=-\kappa_f\left(\frac{\partial T}{\partial r}\right)_{r=b} \\ Sh&=\frac{aq_m}{D_B\left(C_w-C_\infty\right)} \text{ where } q_m=-D_B\left(\frac{\partial C}{\partial r}\right)_{r=b} \end{aligned}\right\} \tag{2.14}$$

Here C_f denotes local skin friction Nu stands for local Nusselt number and Sh stands for local Sherwood number respectively. τ_w, q_w, q_m Designates surface shear stress, heat flux and mass flux respectively. Applying similarity variables, we came into the reduced parameters as

$$C_{f_r}=f''(1)$$

$$Nu_r = -\theta'(1)$$

$$Sh_r = \begin{cases} -\dfrac{\phi'(1)}{\phi(1)}, & \text{for passive control of } \phi \\ -\phi'(1), & \text{for active control of } \phi \end{cases} \tag{2.15}$$

4.3. Numerical procedure

4.3.1. Solution technique

The system of equations along with its boundary conditions are difficult to solve by any analytical method. In this case we have employed numerical structures to solve the framework. Rk-4 method with shooting technique is adopted to solve the required solution. The whole simulation is done by MAPLE – 2019 software. Outcomes of the inspection is described by graphs and tables in subsequent sections. Proper programme of the above problem leads us to a numerical outcomes up to 10^{-6} degree of exactness. The code is also validated by appropriate results.

4.3.2. Code verification

We validate our results and outcomes by comparing it with similar type of previous results. Wang [121] has taken the viscous fluid through expandable cylinder. The values of various parameters are adjusted as $M = 0, H = 0, Lsv = 0, Lst = 0$ to compare the result with previous outcomes. Brownian motion and thermophoresis also neglected in the comparison process In the following Table 4.1 we have analogized the values of $f''(1)$ for separate values of Reynolds number parameter and detected that it matched almost correctly. In the other Table 4.2 the values of $\theta'(1)$ is analogized for different values of Prandtl number taking the Reynolds number fixed to its value 1.

Table 4.1: Comparison of numerical outcomes of $f''(1)$ with previous studies

R	Wang [121]	Present Results
	$f''(1)$	$f''(1)$
0.1	-0.48181	-0.48182
1	-1.17776	-1.17775
2	-1.59390	-1.59391
5	-2.41745	-2.41745
10	-3.34445	-3.34447

Table 4.2: Comparison of numerical outcomes of $\theta'(1)$ with previous studies

Pr	Wang [121]	Present Results
	$\theta'(1)$	$\theta'(1)$
0.2	-0.2572	-0.25721
0.7	-0.5880	-0.58802
2	-1.0650	-1.06502
7	-2.0590	-2.05901
20	-3.5210	-3.52100

4.4. Results and discussion

The following sections contained the results and facts found in this inspection. The effect of various parameters are compared under active and passive control of nanoparticles. Magnetic parameter and Reynolds number are also compared und with slip and no slip conditions. Temperature slip parameter is analogized under active and passive control. Our main focus in this

research is to observe the difference between active control and passive control of nanoparticles. The basic value of the parameter throughout the simulation is takes as follows.

$$\left.\begin{array}{l} M = 1.0\ ,\ \mathrm{Re} = 1\ ,\ Sc = 5 \\ Nb = 0.5\ ,\ Nt = 0.5\ ,\ H = 0.5 \\ Lsv = 0.5\ ,\ Lst = 0.5\ ,\ \mathrm{Pr} = 8 \end{array}\right\}$$

4.4.1. Influence of Magnetic parameter M

The influence of magnetic parameter over nanofluid velocity, temperature and nanoparticle concentration is expressed in the Figures 4.2-4.4. In Figure 4.2 we observe that velocity profile decrease for higher magnetic parameter. The reason behind this is the resistive Lorentz force which is produced in the system. This force resist the velocity profile and the velocity get diminished. Similar effect is observed in presence and absence of velocity slip. Proper difference is observed for $1 \le \eta \le 5$. (Approximately determined) the drag force creates friction which generates more heat in the system and consequently temperature profile upraised. In Figure 4.3 the observance is portrayed graphically and prominent remark is observed in $1 \le \eta \le 5$ (approximately determined)

For both active and passive control temperature is increased but from table 3 we found that in case of active control reduced Nusselt number diminished by 4.15% whereas for passive control it is 6.16%. Higher value of Nusselt number also found in case of passive control condition. Giri et al. [122] found the similar result in their research. Figure 4.4 exhibits that concentration profile increase for active and passive control condition. Clear pictorial observance is in the interval $2 \le \eta \le 6$ (not accurately determined). It is noticed that 24.22% reduction in Sherwood number for active control condition in Table 4.5.

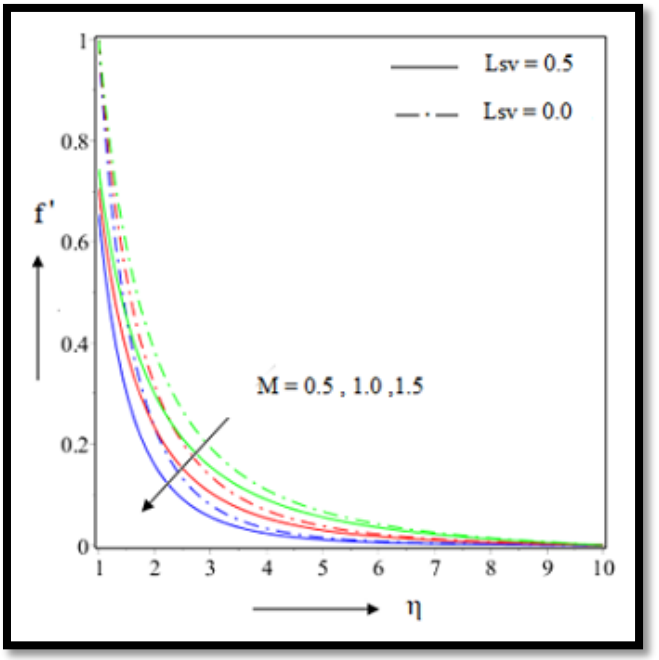

Figure 4.2: Effect of M on $f'(\eta)$.

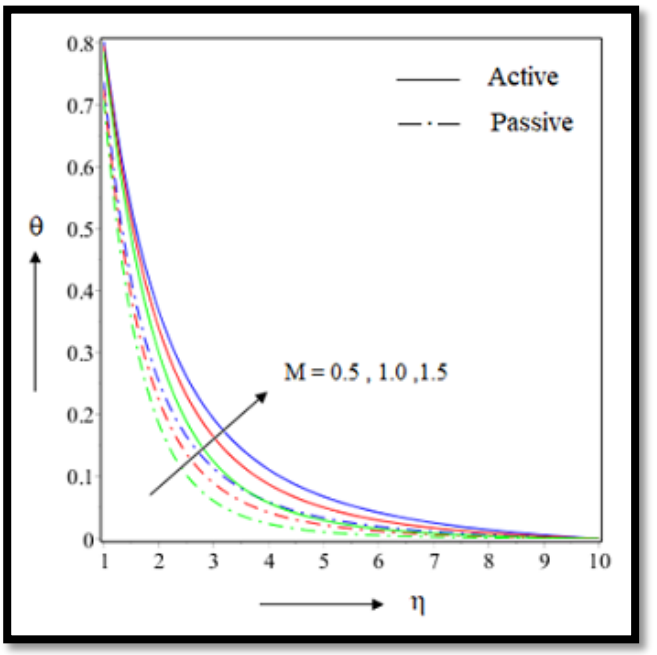

Figure 4.3: Effect of M on $\theta(\eta)$.

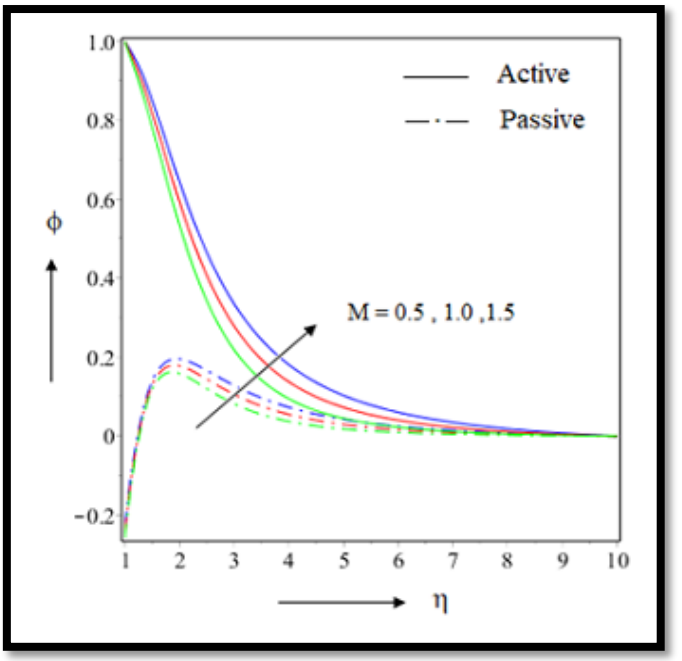

Figure 4.4: Effect of M on $\phi(\eta)$.

4.4.2. Influence of Reynolds number Re

Effect of Reynolds number over velocity temperature and concentration is portrayed in this section. Graphical presentation for the above mentioned profile with respect to similarity variable are given Figures 4.5-4.7. We inspect that velocity profile detained due to higher value of Reynolds number. Increment in Reynolds number yield more turbulent force in the system and the velocity get diminished. In presence of velocity slip magnitude of velocity profile decreased. From Table 4.3 we get approximately 16% change in skin friction co efficient happened for slip condition whereas for no slip condition it jumps to 18% approximately. Prominent overview observed in the interval $1 \le \eta \le 6$ (not accurately determined). Temperature profile and nanoparticle concentration is also detained for higher value of Reynolds number. Figure 4.6 and 4.7 describe the result graphically. Passive control condition gives more detained magnitude of temperature profile. Prominent observation is achieved in the interval $1 \le \eta \le 6$ (not accurately determined). Nusselt number increased by 14.5% for active control and 20.77% for passive control condition. Concentration profile is also reduced for higher value of Reynolds number. The prominent view is in the interval $1 \le \eta \le 6$ (not accurately determined) beyond that it converges asymptotically.

Mass transfer quantity can be obtained from Table 4.5 which is 48.83% for active control condition and 10.1% for passive control condition. Higher magnitude of Sherwood number is observed in case of passive control condition.

4.4.3. Influence of Prandtl number Pr

Prandtl number's effect over temperature and concentration is discussed in this portion. Figure 4.8 and 4.9 portrayed the graphical representation of the above mentioned scheme with respect to similar variable. In Figure 4.8 we observe temperature has been curtailed when Pr grown for both the active control and passive control cases. The larger Prandtl fluids implies lower thermal diffusivities and the smaller Pr implies maximum thermal diffusivities. Also, temperature profile is greater in active control compared to passive control. Clear observance occur in the interval $2 \leq \eta \leq 6$ (not accurately determined). In Table 4.4 we see that the reduced Nusselt number decreased by 23.81% in active control and 12.90% in passive control.

In Figure 4.9 we see the concentration ϕ diminished when Pr getting higher in active control and also in passive control. The fraction of nanoparticle volume appears to be sensitive with Pr parameter value. The clear observation is in the range $2 \leq \eta \leq 5$ (not accurately determined). In active control Sherwood number decreased by 25.01% but in case of passive control it deviated by 4.31% only.

4.4.4. Influence of Heat source parameter H

How the heat source parameter H affected the temperature is discussed in this section. The graph in Figure 4.10 shows the impression of the heat source parameter H over nanofluid temperature. In both the instances of active control and passive control temperate is increased. Here temperature profile is greater in active control compared to passive control. From table 4.5 we can see that for active control mass transfer quantity is increased by 9.14% but interestingly for passive control it is increased by only 6.60%. In Figure 4.10 the observance is portrayed graphically and noticeable outcome is observed in $1 \leq \eta \leq 8$ (Not accurately determined). After this interval the graph converges asymptotically.

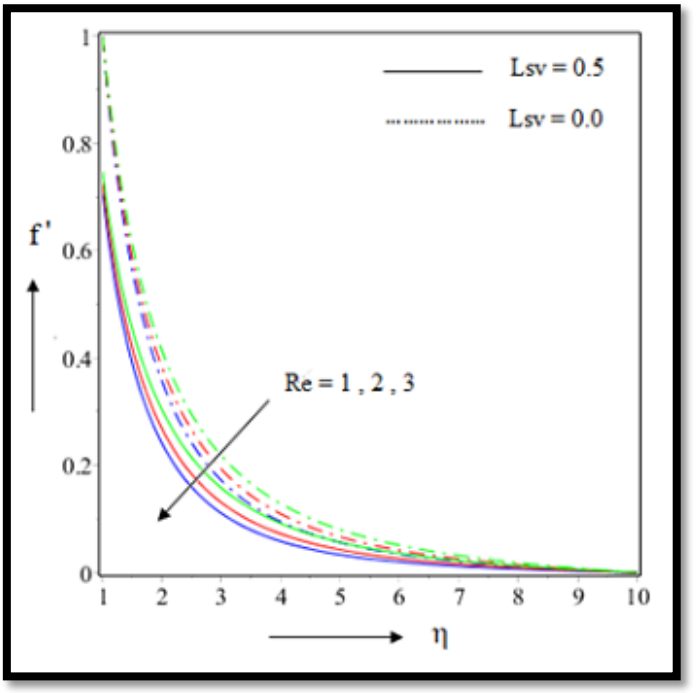

Figure 4.5: Effect of Re on $f'(\eta)$.

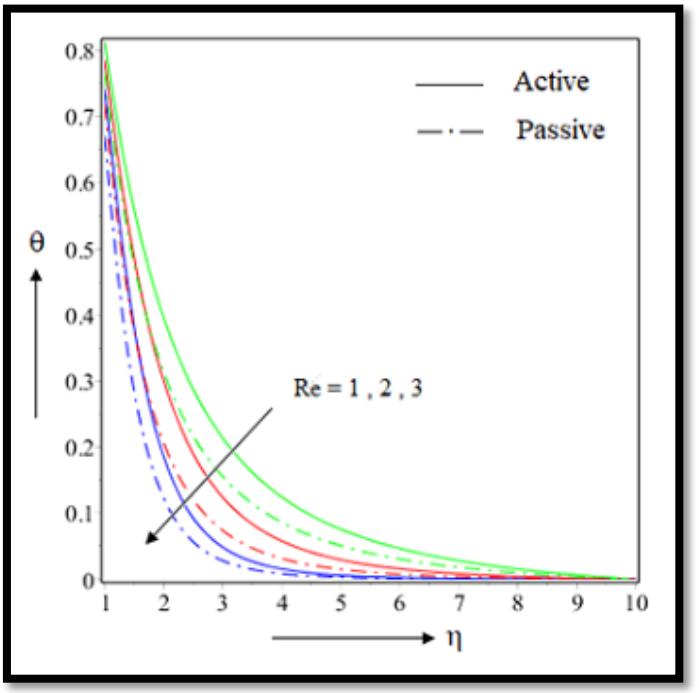

Figure 4.6: Effect of Re on $\theta(\eta)$.

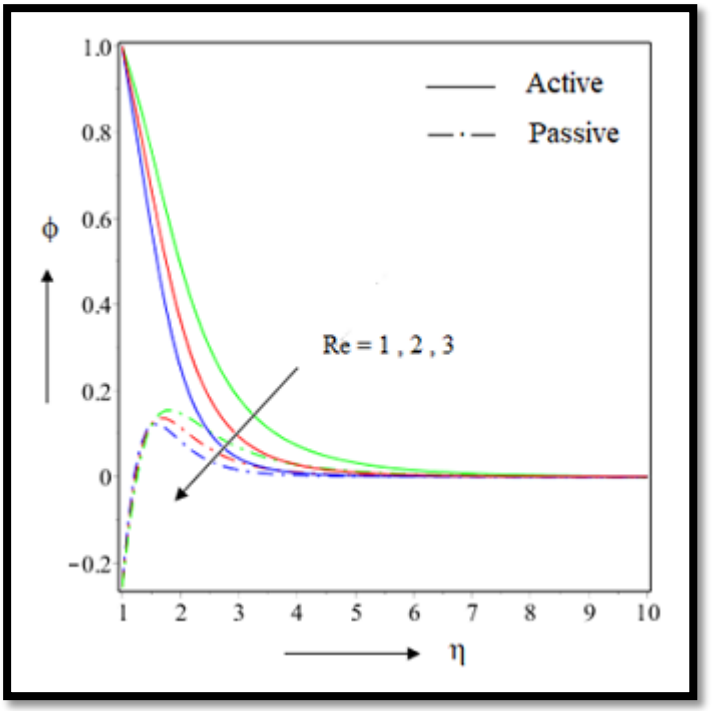

Figure 4.7: Effect of $\mathbf{Re}$ on $\phi(\eta)$.

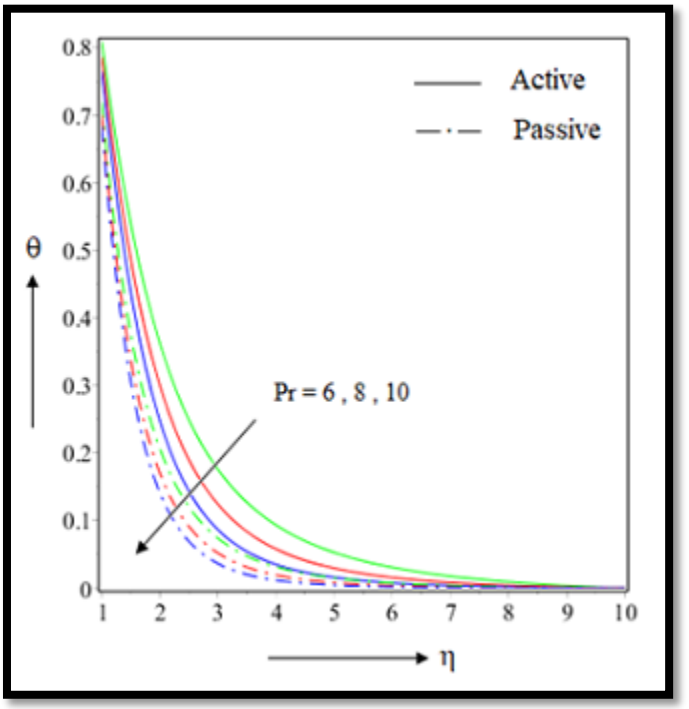

Figure 4.8: Effect of Pr on $\theta(\eta)$.

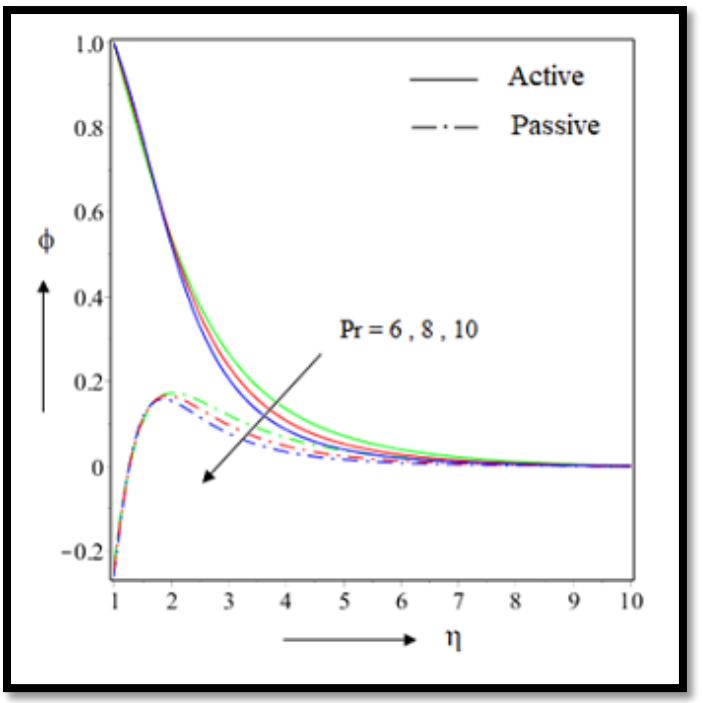

Figure 4.9: Effect of $\Pr$ on $\phi(\eta)$.

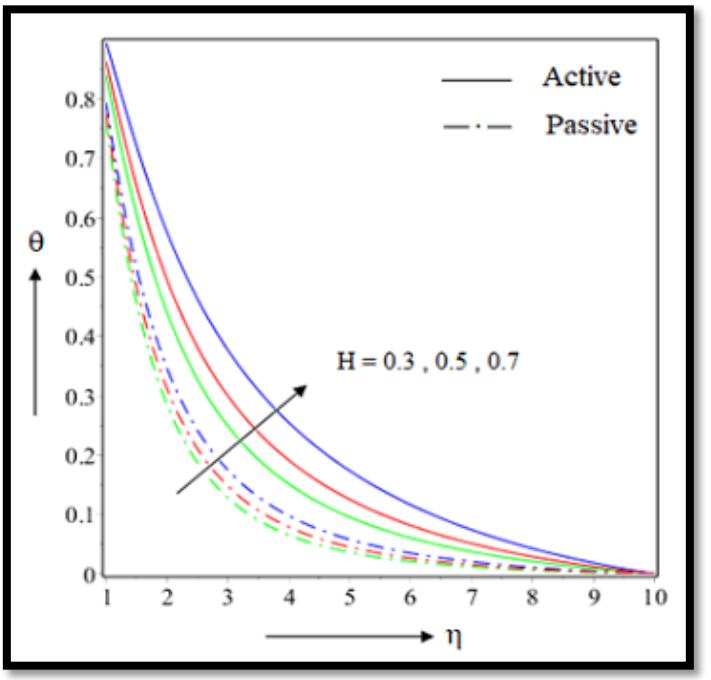

Figure 4.10: Effect of H on $\theta(\eta)$.

4.4.5. Influence of Brownian motion parameter Nb

Brownian motion parameter's effect over temperature θ and concentration ϕ is discussed here. Graphical representation of these things with respect to similarity variable are given in Figures 4.11 and 4.12. From Figure 4.11 we can see that for both active control and passive control temperature profile increases. Different nano particles have various values of Brownian motion parameter which leads to the enhancement of the heat transfer rate. In the graph prominent outcome is observed in the interval $0 \leq \eta \leq 6$ (not accurately determined) after that the graph converges asymptotically. From Table 4.4 we can see that for active control heat transfer quantity is decreased by 9.44% whereas for passive control it is decreased by only 2.33%.

It is clear from Figure 4.12 that due to Brownian motion parameter concentration profile decreases for both active control and passive control. For passive control Sherwood number increases by 1.92% (from Table 4.5).

4.4.6. Influence of Thermophoresis parameter Nt

The effect of thermophoresis parameter Nt over the profiles temperature θ and concentration ϕ on nanofluid particles discussed in this portion. Figures 4.13 and 4.14 portrayed the graphical presentation of the above mentioned scheme with respect to similar variable. In Figure 4.13 we observe temperature has been risen when Nt grown for both active control and passive control. For greater Nt value we get higher thermal diffusivities and for smaller Nt value we get lower thermal diffusivities. It happens because an increment in Nt heeds a powerful thermophoretic force that allows huge migration of the particles in the nanofluid, that is far off from surface and forms a larger temperature and increase the thickness of the thermal layer. Also, temperature profile is greater in active control compared to passive control. Clearly observed in the interval $2 \leq \eta \leq 4$ (not accurately determined). In Table 4.4 we see that the reduced Nusselt number is decreased by 11.54% in active control and 6.12% in passive control.

In Figure 4.14 we observe that an exceptional increase is found in concentration ϕ when the value of Nt mounts in active control and also in passive control. The clear observation is in the range $1 \leq \eta \leq 5$ (not accurately determined). In active control Sherwood number decreased by 8.57% and 4.21 % in passive control from Table 4.5.

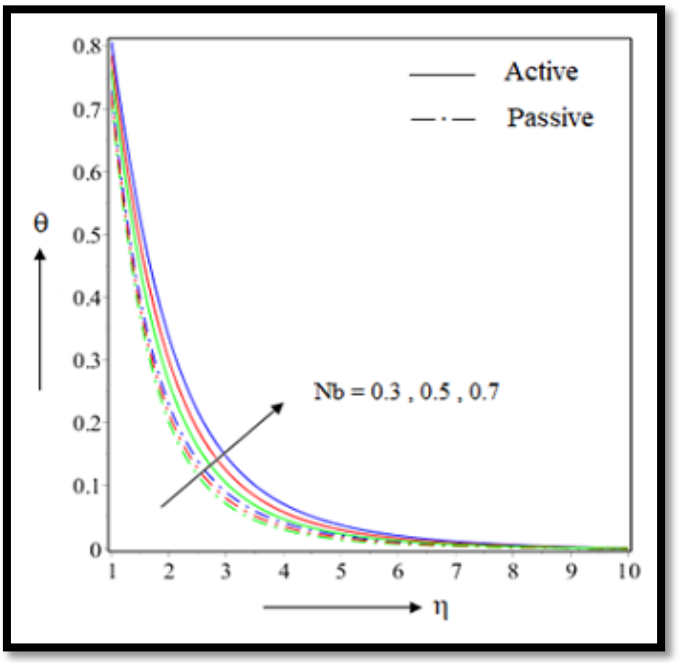

Figure 4.11: Effect of Nb on $\theta(\eta)$.

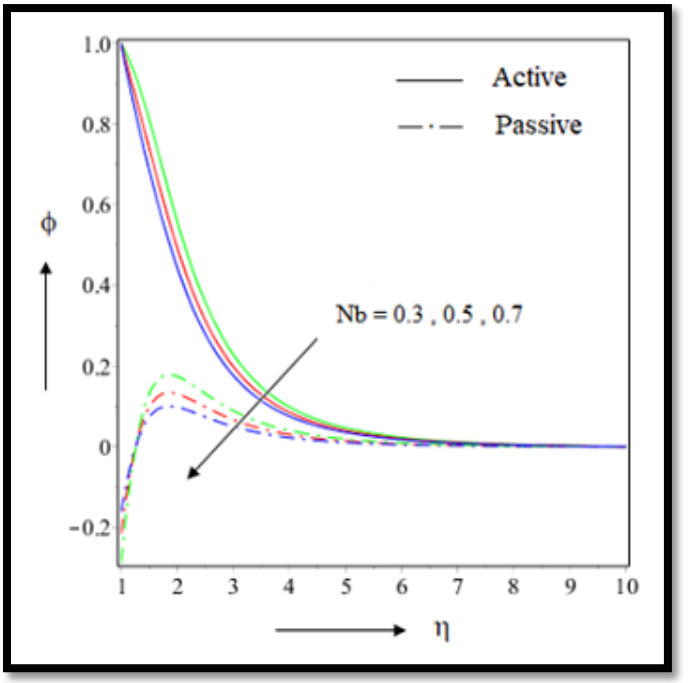

Figure 4.12: Effect of Nb on $\phi(\eta)$.

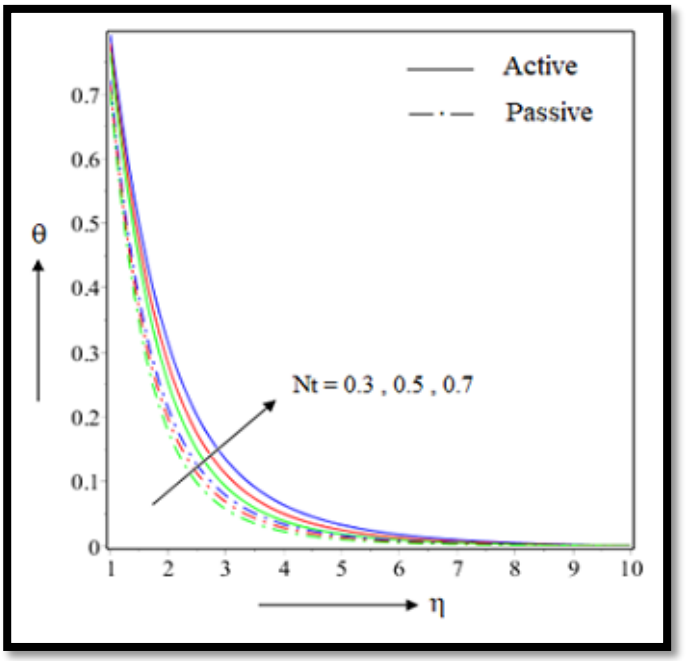

Figure 4.13: Effect of Nt on $\theta(\eta)$.

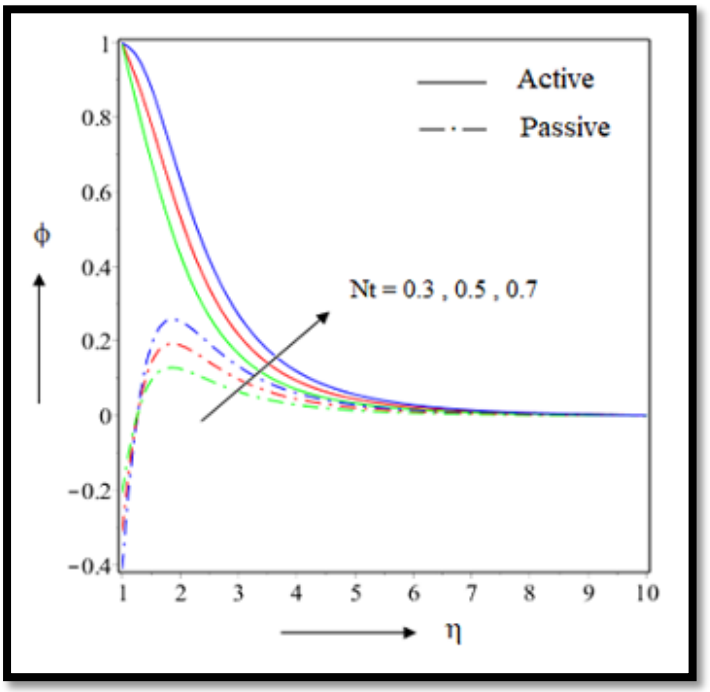

Figure 4.14: Effect of Nt on $\phi(\eta)$.

4.4.7. Influence of Schmidt number Sc

Here we discuss about the effect of Schmidt number Sc over concentration profile of nanofluid. Graphical representation of this with respect to similarity variable is given in Figure 4.15. From Figure 4.15 it is evident that the concentration decreases when Sc increases for both active and passive control. It happens as an increment in Sc corresponds to a weaker solute diffusivity which allows a shallower penetration of solutal effect. Thus, the solute boundary layer is w for smaller values of Schmidt number and vice versa. Noticeable outcome is observed in the interval $1 \leq \eta \leq 7$ for active control and in $2 \leq \eta \leq 6$ for passive control (not accurately determined). After that the graph converges asymptotically. From Table 5 we can see that Sherwood number is increased by 11.36% in case of active control whereas for passive control it is increased by only 8.21 %.

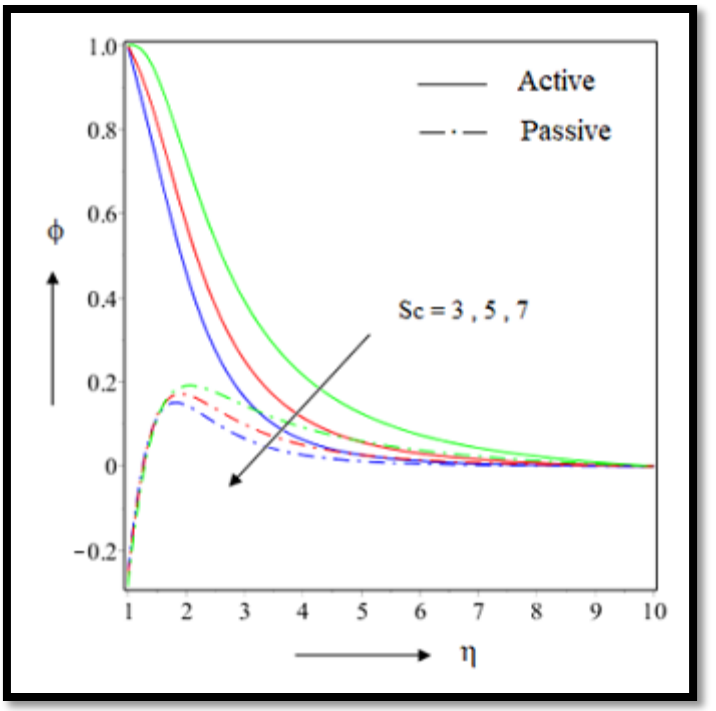

Figure 4.15: Effect of Sc on $\phi(\eta)$.

4.4.8. Influence of Temperature slip parameter *Lst*

The influence of temperature slip parameter *Lst* over the profiles temperature and concentration on Nano fluid particles discussed in this part. Figure 4.16 and 4.17 portrayed the graphical representation of the above mentioned scheme with respect to similar variable. In Figure 4.16 we observe temperature has been curtailed when *Lst* grown for both the active control and passive control cases. The larger temperature slip parameter implies lower thermal diffusivities and the smaller *Lst* implies maximum thermal diffusivities. Also, temperature profile is greater in active control compared to passive control. Clearly observed in the interval $1 \leq \eta \leq 5$ (not accurately determined). In Table 4.4 we observe that the reduce Nusselt number decreased by 23.75% in active control and 17.24% in passive control. In Figure 4.17 we see the concentration diminish when *Lst* getting higher in active control and also in Passive control. The clear observation is in the range $1 \leq \eta \leq 5$ (not accurately determined). In active control Sherwood number is increased by 48.23% and decreased by 6.32% in passive control from Table 4.5.

4.4.9. Influence of Velocity slip parameter *Lsv*

How velocity slip parameter *Lsv* effects the velocity is discussed here. The impact of *Lsv* on velocity with respect to similarity variable is portrayed in the Figure 4.18. From the graph we observe that as value of *Lsv* increases the velocity profile decreases. As velocity slip increases, velocity of fluid decreases because of the fact that pulling of stretching cylinder can transmit the fluid. It is clearly observed in the interval $1 \leq \eta \leq 7$ (not accurately determined). After tis interval the graph converges asymptotically.

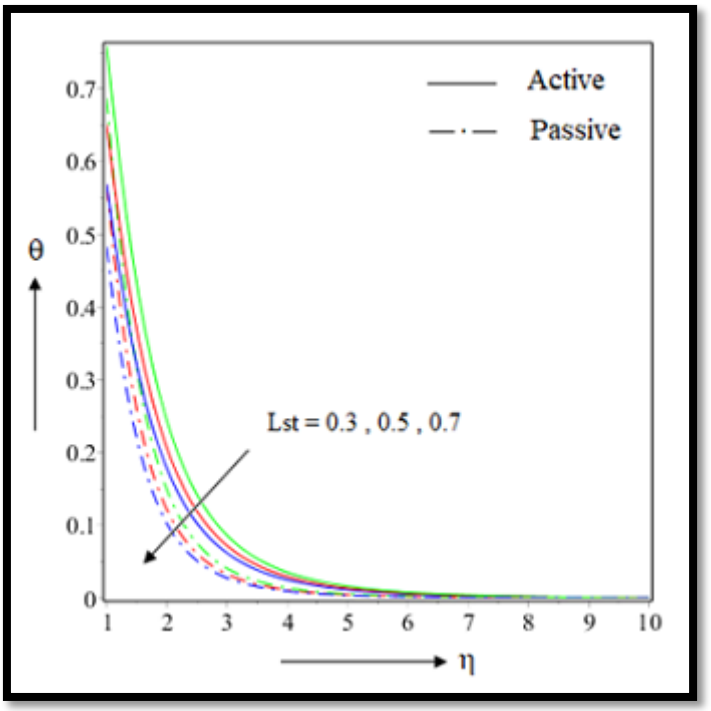

Figure 4.16: Effect of Lst on $\theta(\eta)$.

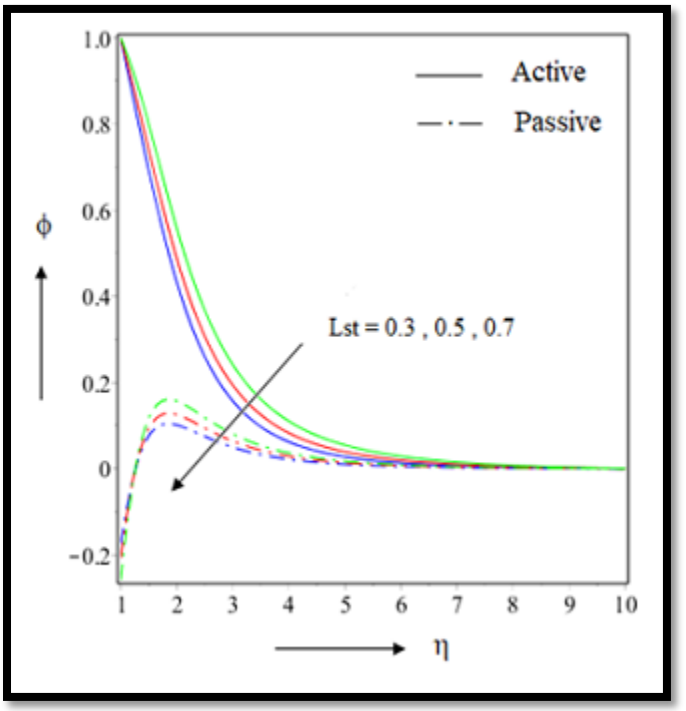

Figure 4.17: Effect of Lst on $\phi(\eta)$.

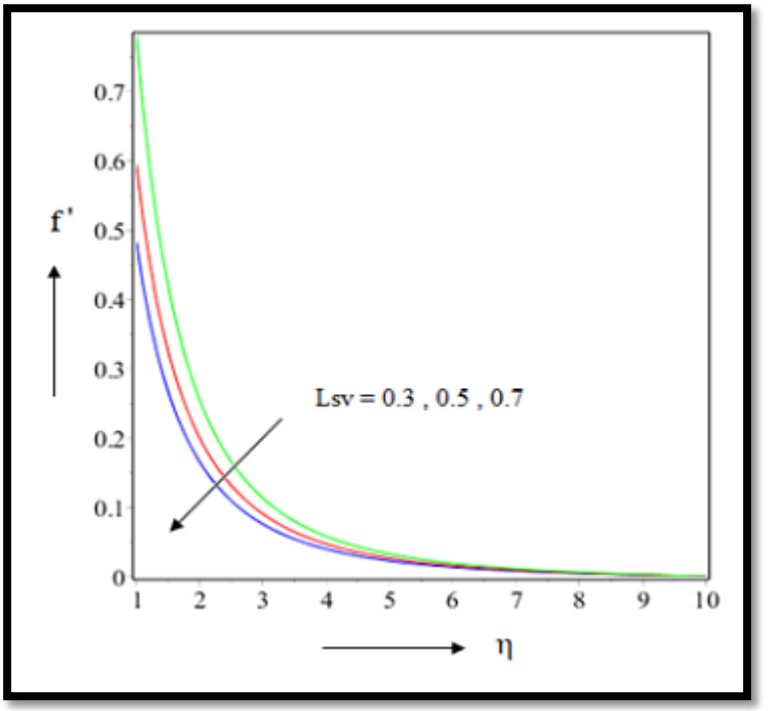

Figure 4.18: Effect of Lsv on $f'(\eta)$.

4.5. Conclusions

We have inspected actively and passively controlled nanoparticle flow over a stretching cylinder. External heat originator, realistic velocity slip and temperature jump also considered. We have seen that passively controlled nanofluid flow is more realistic in nature than actively controlled nanofluid flow. So in application of heat exchanger, nuclear reactor, cooling machine passively controlled nanofluid flow is more useful. Highly nonlinear leading equations are transfigured into ODEs by suitable similarity transmutation and then resolved by RK-4 method. The whole simulation process is done by MAPLE 2019 software. Velocity lines heat lines and concentration lines are compared under active and passive control of nanoparticles. Prominent results are manifested by appropriate graphs and tables. Most important outcomes found in our research is as follows.

- Magnetic influence reduce the velocity profile but increase the heat transfer by 4.15% for passive control. Concentration lines also uplifted for higher value of magnetic parameter.

- Reynolds number diminished velocity temperature and also concentration profile. For slip effect velocity curtails approximately 16%. Active control gives higher magnitude of temperature than passive control of nanoparticles.
- Temperature and concentration both decreased for higher value of Prandtl number and in both cases active control gives higher magnitude. Sherwood number decreased by 25.01% for active control of nanoparticles.
- External heat source increase the temperature and for active control it is higher in magnitude. Temperature jump decrease both heat and concentration lines.
- Brownian migration parameter increase the heat line but diminished the mass transfer. Heat transfer quantity changed by 9.44% for active and 2.33% for passive control of nanoparticles. Thermophoresis parameter increase both mass and heat transfer in case of active and passive control.

More geometrical structure like sphere, cone can be taken under several conditions like radiation joule heating to inspect the comparison between active and passive control of nanoparticles. Proper boundary provisions can be introduced for further investigations.

Table 4.3: Effect of suitable parameters on skin friction

M	Re	Cf_r			
		$Lsv = 0.5$	CPU time (Second)	$Lsv = 0.0$	CPU time (Second)
0.5	2	-0.841057	2.22	-1.215436	2.24
1.0		-0.988014	2.21	-1.439564	2.21
1.5		-1.137548	2.25	-1.814779	2.26
1.0	1	-0.832548	2.26	-1.110059	2.24
	2	-0.910254	2.24	-1.212463	2.23
	3	-0.970014	2.21	-1.311982	2.22

Table 4.4: Effect of suitable parameters on heat transfer

M	Re	H	Nb	Nt	Lst	Pr	Nu_r			
							Active control	CPU time (Second)	Passive control	CPU time (Second)
0.5	2	0.5	0.5	0.5	0.5	8	0.714816	2.26	0.973266	2.26
1.0							0.68244	2.24	0.917587	2.21
1.5							0.659337	2.21	0.876004	2.28
1.0	1						0.622508	2.22	0.777319	2.23
	2						0.714816	2.21	0.937831	2.28
	3						0.859479	2.24	1.096526	2.24
	2	0.3					0.727352	2.28	0.942890	2.25
		0.5					0.793847	2.23	1.005210	2.29
		0.7					0.849121	2.25	1.061472	2.22
		0.5	0.3				0.789369	2.24	0.945087	2.25
			0.5				0.714816	2.29	0.9230567	2.24
			0.7				0.642738	2.28	0.900230	2.29
			0.5	0.3			0.782261	2.28	0.984659	2.28
				0.5			0.736822	2.24	0.952258	2.23
				0.7			0.691604	2.26	0.925735	2.22
				0.5	0.3		0.802667	2.27	1.041077	2.26
					0.5		0.697413	2.21	0.864381	2.21
					0.7		0.615451	2.23	0.738365	2.24
					0.5	6	0.637607	2.26	0.937831	2.25
						8	0.714816	2.24	1.000141	2.27
						10	0.785999	2.27	1.056224	2.24

Table 4.5: Effect of suitable parameters on mass transfer

M	Re	**Pr**	Nb	Nt	Sc	Lst	Sh_r			
							Active control	CPU time (Second)	Passive control	CPU time (Second)
0.5	2	8	0.5	0.5	5	0.5	0.388913	2.21	4.785262	2.23
1.0							0.294686	2.26	4.968650	2.28
1.5							0.215724	2.28	5.173031	2.27
1.0	1						0.435902	2.32	4.959148	2.31
	2						0.650548	2.23	5.465541	2.24
	3						0.875362	2.30	6.034050	2.80
	2	6					0.536261	2.25	4.546671	2.25
		8					0.467161	2.26	4.643850	2.25
		10					0.409837	2.31	4.752525	2.30
		6	0.3				0.274170	2.27	4.721575	2.29
			0.5				0.528050	2.28	4.812367	2.26
			0.7				0.718095	2.28	4.898542	2.27
			0.3	0.3			0.677038	2.32	4.827306	2.30
				0.5			0.375757	2.21	4.817447	2.21
				0.7			0.090062	2.23	4.807670	2.25
				0.5	3		0.022835	2.29	4.383091	2.27
					5		0.282378	2.28	4.725585	2.25
					7		0.550679	2.22	4.909164	2.24
					5	0.3	0.335678	2.31	4.820354	2.29
						0.5	0.508142	2.32	4.807613	2.30
						0.7	0.644847	2.24	4.798093	2.25

CHAPTER 5

Differential Transformed Approach of Unsteady Chemically Reactive Nanofluid Flow over a Bi-directional Stretched Surface in Presence of Magnetic Field*

5.1. Introduction

In this paper differential transformation method (DTM) is used to solve the governing equations of the flow system. This method is the outcome of the Taylor series. In this process the given differential equations are converted into a recursive relation to obtain the Taylor series coefficients. In Taylor series process we have to calculate successive order differentiation which is very laborious and more computational. However, in DTM we do not have to calculate the derivatives instead of that it leads to an easy calculation process. The convergence rate is also faster so we get the result after a few steps. In homotopy analysis method (HAM),homotopy perturbation method (HPM) we have to use perturbation, linearization or discretization methods. However, in DTM these are not required. Consequently linear and non linear both type ODEs can be solved by using DTM.

In this paper, we have considered the nanofluid flow over bidirectional stretching sheet. Brownian motion, thermophoresis and chemical reaction are the main point of interest. The comparison between steady and unsteady flow is also discussed. The governing equations are solved by DTM and also by RK-4 process with shooting mechanism. We get excellent outcomes which are exhibited by the figures and tables.

***This chapter is based on the paper published in: Heat Transfer, 49(6) (2020), 3917-3942, (ESCI).**

5.2. Mathematical formulation

5.2.1. Governing equations

An unsteady viscous laminar three dimensional incompressible nanofluid flow has been taken over a bidirectional stretching sheet. The surface of the sheet has been assumed to be stretched along x *and* y directions with the velocities $u_w(x,t)=\frac{ax}{1-\lambda t}$ and $v_w(x,t)=\frac{by}{1-\lambda t}$ respectively, where a *and* b are non-negative constants and where $1-\lambda t>0$ and λ is of dimension Sec^{-1}. The Cartesian frame (x,y,z) is considered with the extensible sheet placed at $z=0$ and the nanocomposite stream occupies the regime $z>0$ as depicted in Figure 5.1. The velocities along x, y *and* z axis are taken as $u(x,y,z), v(x,y,z)$ and $w(x,y,z)$. We have assumed that the temperature on the sheet is T_w and temperature at far distance from the sheet is T_∞. The magnetic field having the mathematical form $B=\frac{B_0}{\sqrt{1-\lambda t}}$ is included along perpendicular direction with respect to the sheet, where B_0 designates the initial intensity of magnetic field. The magnetic Reynolds's number is considered to be small enough so as to neglect the induction effect. The Brownian motion, thermophoresis have been assumed to be present in the flow and we have also taken chemical reaction within this flow analysis. The concentration of the nanofluid is taken as C_w on the sheet and the same is taken as C_∞ far away from it. Velocity or thermal slip, joule heating and viscous dissipation have been waived in this investigation. Under the above stated circumstances the requisite equations following [123-126] are as follows:

$$\frac{\partial u}{\partial x}+\frac{\partial v}{\partial y}+\frac{\partial w}{\partial z}=0 \tag{5.1}$$

$$\frac{\partial u}{\partial t}+u\frac{\partial u}{\partial x}+v\frac{\partial u}{\partial y}+w\frac{\partial u}{\partial z}=\nu_f\frac{\partial^2 u}{\partial z^2}-\frac{\sigma_f B^2}{\rho_f}u \tag{5.2}$$

$$\frac{\partial v}{\partial t}+u\frac{\partial v}{\partial x}+v\frac{\partial v}{\partial y}+w\frac{\partial v}{\partial z}=\nu_f\frac{\partial^2 v}{\partial z^2}-\frac{\sigma_f B^2}{\rho_f}v \tag{5.3}$$

$$\frac{\partial T}{\partial t}+u\frac{\partial T}{\partial x}+v\frac{\partial T}{\partial y}+w\frac{\partial T}{\partial z}=\alpha_f\frac{\partial^2 T}{\partial z^2}+\tau\left[D_B\frac{\partial C}{\partial z}\frac{\partial T}{\partial z}+\frac{D_T}{T_\infty}\left(\frac{\partial T}{\partial z}\right)^2\right] \tag{5.4}$$

$$\frac{\partial C}{\partial t}+u\frac{\partial C}{\partial x}+v\frac{\partial C}{\partial y}+w\frac{\partial C}{\partial z}=D_B\frac{\partial^2 C}{\partial z^2}+\frac{D_T}{T_\infty}\frac{\partial^2 T}{\partial z^2}-K_r\left(C-C_\infty\right) \tag{5.5}$$

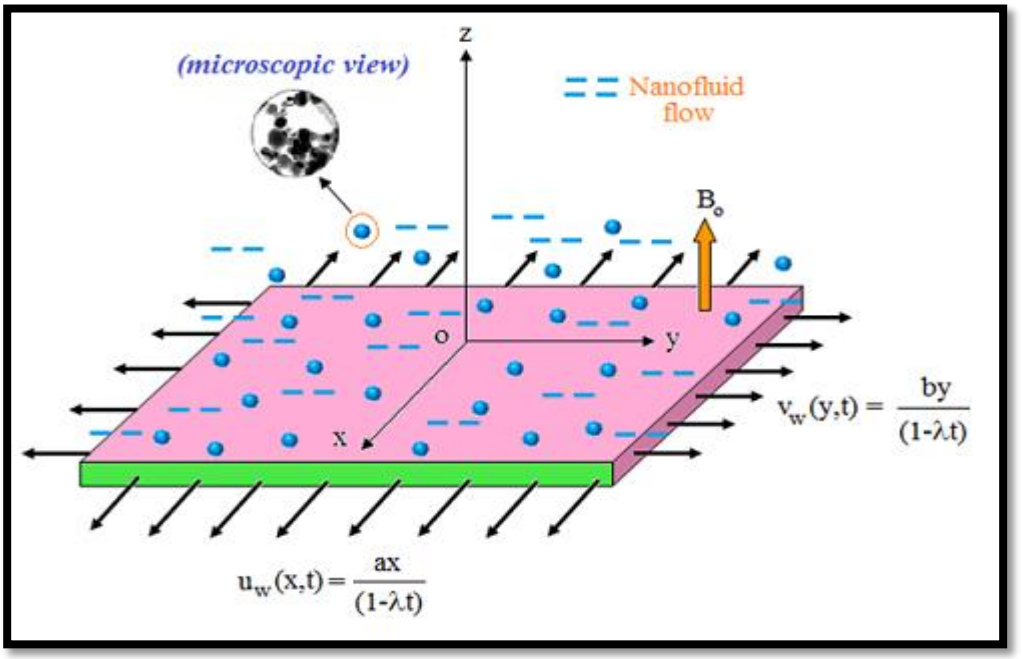

Figure 5.1: Physical geometry of the flow

Where, $\tau=\frac{\left(\rho C_p\right)_s}{\left(\rho C_p\right)_f}$ illustrates the ratio of specific heat of nanoparticles to base fluid. Furthermore, μ_f, ρ_f and ν_f denotes the dynamic viscosity, density and kinematic viscosity involved with the base fluid. Again, $\alpha_f=\frac{k_f}{(\rho C_p)_f}$ where k_f refers to conductivity related to thermal characteristics of the fluid. D_B, D_T *and* σ_f are referred to Brownian diffusion coefficient, thermophoresis coefficient and electrical conductivity of the liquid, K_r denotes the chemical reaction associated within the ingredients. Lastly, C and T assures the concentration and temperature profile of the liquid.

5.2.2. Boundary conditions

The boundary conditions for the above model are given by the following equations:

$$u = u_w(x,t) = \frac{ax}{1-\lambda t},\ v = v_w(y,t) = \frac{by}{1-\lambda t},\ w = 0,\ T = T_w,\ C = C_w \ at\ z = 0 \tag{5.6}$$

$$u \to 0,\ v \to 0,\ T \to T_\infty,\ C \to C_\infty \ \ at\ \ z \to \infty \tag{5.7}$$

5.2.3. Similarity transformations

We convert the foremost flow equations (5.1-5.5) into system of ODEs by the following similarity variables as in [123-126]:

$$\left.\begin{aligned} u = \frac{ax}{1-\lambda t} f'(\eta),\ v = \frac{ay}{1-\lambda t} g'(\eta),\ w = -\sqrt{\frac{a\nu_f}{1-\lambda t}}\left(f(\eta)+g(\eta)\right) \\ \theta(\eta) = \frac{T-T_\infty}{T_w-T_\infty},\ \phi(\eta) = \frac{C-C_\infty}{C_w-C_\infty},\ \eta = \sqrt{\frac{a}{\nu_f(1-\lambda t)}}z \end{aligned}\right\} \tag{5.8}$$

After the needed modernization, the converted ODEs are given by as follows:

$$f''' - \frac{\eta}{2}Sf'' - Sf' - f'^2 + (f+g)f'' - Mf' = 0 \tag{5.9}$$

$$g''' - \frac{\eta}{2}Sg'' - Sg' - g'^2 + (f+g)g'' - Mg' = 0 \tag{5.10}$$

$$\frac{1}{\Pr}\theta'' - \frac{\eta}{2}S\theta' + (f+g)\theta' + Nb\theta'\phi' + Nt\theta'^2 = 0 \tag{5.11}$$

$$\frac{1}{Le}\phi'' - \frac{\eta}{2}S\phi' + (f+g)\phi' + \frac{Nt}{Nb.Le}\theta'' - Kr\phi = 0 \tag{5.12}$$

Where, f and g denote the dimensionless velocities, θ and ϕ stand for dimensionless temperature, concentration respectively. $S = \frac{\lambda}{a}$ Symbolizes the unsteady parameter, $M = \frac{\sigma_f B_0^{\ 2}}{a\rho_f}$ designates the magnetic field parameter, $Nb = \frac{\tau D_B(C_w - C_\infty)}{\nu_f}$ signifies the Brownian motion

parameter, $Nt = \frac{\tau D_T (T_w - T_\infty)}{T_\infty \nu_f}$ indicates the thermophoresis parameter, $Le = \frac{\nu_f}{D_B}$ represents the Lewis number, $\Pr = \frac{\nu_f}{\alpha_f}$ implies the Prandtl number and $Kr = \frac{K_r}{a}$ means Chemical reaction parameter.

Similarly the boundary conditions are also converted to:

$$\left.\begin{array}{c} f'(0)=1,\ g'(0)=\alpha,\ f(0)=0,\ g(0)=0,\ \theta(0)=1,\ \phi(0)=1 \\ f'(\infty)=0,\ g'(\infty)=0,\ \theta(\infty)=0,\ \phi(\infty)=0 \end{array}\right\} \tag{5.13}$$

Where, $\alpha = \frac{b}{a}$ signifies the stretching parameter. We are concentrating to choose the range $0<\alpha<1$ because for $\alpha>1$ the axes $x \text{ and } y$ are interchanged and for $\alpha=1$ the stretching rate becomes alike in both directions, thus the flow profile turns out to be axisymmetric. Also, considering the limiting situation $\alpha \to 0$, the flow becomes unidirectional. Wang [126] reported that without any loss of generality, the condition $f(0)+g(0)=0$ can be restored by $f(0)=0$ and $g(0)=0$.

5.2.4. Physical quantities

The needful physical quantities which are very important with respect to the engineering application at nanolevel are given by the following expressions:

$$C_{fx} = \frac{\tau_{zx}}{\frac{1}{2}\rho_f u_w^2},\quad C_{fy} = \frac{\tau_{zy}}{\frac{1}{2}\rho_f v_w^2} \tag{5.14}$$

Where,
$$\tau_{zx} = \mu_f \left(\frac{\partial u}{\partial z}\right)_{z=0},\quad \tau_{zy} = \mu_f \left(\frac{\partial v}{\partial z}\right)_{z=0} \tag{5.15}$$

$$Nu_x = \frac{x q_w}{k_f (T_w - T_\infty)} \text{ Where, } q_w = -k_f \left(\frac{\partial T}{\partial z}\right)_{z=0} \tag{5.16}$$

$$Sh_x = \frac{xq_m}{D_B\left(C_w - C_\infty\right)} \text{ Where, } q_m = -D_B\left(\frac{\partial C}{\partial z}\right)_{z=0} \tag{5.17}$$

In the aforesaid equations C_{fx} and C_{fy} designate the skin friction along x axis and y axis. Nu_r and Sh_r denote local Nusselt number and local Sherwood number respectively.

Applying the similarity renovation, we obtain the reduced skin friction along both axes and thus reduced Nusselt number and reduced Sherwood number are as:

$$C_{fxr} = \sqrt{\mathrm{Re}_x}C_{fx} = 2f''(0) \text{ Where, } \mathrm{Re}_x = \frac{u_w x}{\nu_f} \tag{5.18}$$

$$C_{fyr} = \sqrt{\mathrm{Re}_y}C_{fy} = 2g''(0) \text{ Where, } \mathrm{Re}_y = \alpha^3 \frac{\nu_w y}{\nu_f} \tag{5.19}$$

$$Nu_r = \left(\mathrm{Re}_x\right)^{-\frac{1}{2}} Nu_x = -\theta'(0) \tag{5.20}$$

$$Sh_r = \left(\mathrm{Re}_x\right)^{-\frac{1}{2}} Sh_x = -\phi'(0) \tag{5.21}$$

5.3. Numerical procedure

5.3.1. Differential Transformation method

A function $f(x)$ is transformed by differential transformation method as [127-130]

$$F(k) = \frac{1}{k!}\left(\frac{d^k f(x)}{dx^k}\right)_{x=x_0} \tag{5.22}$$

Whereas, the inverse differential transformation of $F(k)$ is defined by [127-130]

$$f(x) = \sum_{k=0}^{\infty} F(k)(x - x_0)^k \tag{5.23}$$

Now compiling the above two equations we get

$$f(x)=\sum_{k=0}^{\infty}\frac{1}{k!}\left(\frac{d^k f(x)}{dx^k}\right)_{x=x_0}(x-x_0)^k \tag{5.24}$$

In the next portion, we have used some basics of DTM conversion to solve the obtained ordinary differential equation. The formulas are written below.

Table 5.1: Differential transformed form of some functions [127-130]

Function	**Differential transformed form**
$f(x)=g(x)\pm h(x)$	$F(k)=G(k)\pm H(k)$
$f(x)=cg(x)$	$F(k)=cG(k)$
$f(x)=\frac{d^m g(x)}{dx^m}$	$F(k)=\frac{(k+m)!}{k!}G(k+m)$
$f(x)=g(x)h(x)$	$F(k)=\sum_{r=0}^{k}G(r)H(k-r)$
$f(x)=x^n$	$F(k)=\delta(k-n)$ where $\delta(k-n)=\begin{cases}1,k=n\\0,k\neq n\end{cases}$
$f(x)=h_1(x)h_2(x)\cdots h_n(x)$	$F(k)=\sum_{r_{n-1}=0}^{k}\sum_{r_{n-2}=0}^{r_{n-1}}\sum_{r_{n-3}=0}^{r_{n-2}}\cdots\sum_{r_1=0}^{r_2}H_1(r_1)H_2(r_2-r_1)\cdots H_n(k-r_{n-1})$

5.3.2. DTM solution

Applying this transformation, we obtain the following equations:

$$\left.\begin{aligned}&(k+1)(k+2)(k+3)F(k+3)-(M^2+S)(k+1)F(k+1)-\frac{S}{2}\sum_{r=0}^{k}\delta(r-1)(k-r+1)(k-r+2)F(k-r+2)\\&-\sum_{r=0}^{k}(r-1)(k-r+1)F(k+1)F(k-r+1)+\sum_{r=0}^{k}(k-r+1)(k-r+2)F(r)F(k-r+2)\\&+\sum_{r=0}^{k}(k-r+1)(k-r+2)G(r)F(k-r+2)=0\end{aligned}\right\} \tag{5.25}$$

Where, the boundary conditions are: $F(0)=0, F(1)=1, F(2)=A$ (5.26)

$$\left.\begin{aligned}&(k+1)(k+2)(k+3)G(k+3)-(M^2+S)(k+1)G(k+1)-\frac{S}{2}\sum_{r=0}^{k}\delta(r-1)(k-r+1)(k-r+2)G(k-r+2)\\&-\sum_{r=0}^{k}(r-1)(k-r+1)G(k+1)G(k-r+1)+\sum_{r=0}^{k}(k-r+1)(k-r+2)F(r)G(k-r+2)\\&+\sum_{r=0}^{k}(k-r+1)(k-r+2)G(r)G(k-r+2)=0\end{aligned}\right\}$$

(5.27)

Here, the boundary conditions are transformed as: $G(0)=0, G(1)=\alpha, G(2)=B$ (5.28)

$$\left.\begin{aligned}&\frac{1}{\Pr}(k+1)(k+2)\Theta(k+2)+Nb\sum_{r=0}^{k}(r+1)(k-r+1)\Theta(k+1)\Phi(k-r+1)\\&+Nt\sum_{r=0}^{k}(r+1)(k-r+1)\Theta(k+1)\Theta(k-r+1)-\frac{S}{2}\sum_{r=0}^{k}\delta(r-1)(k-r+1)\Theta(k-r+1)\\&+\sum_{r=0}^{k}(k-r+1)F(r)\Theta(k-r+1)+\sum_{r=0}^{k}(k-r+1)G(r)\Theta(k-r+1)=0\end{aligned}\right\} \quad (5.29)$$

Available boundary provisions are as follows: $\Theta(0)=1, \Theta(1)=C$ (5.30)

$$\left.\begin{aligned}&\frac{1}{Le}(k+1)(k+2)\Phi(k+2)+\frac{Nt}{NbLe}(k+1)(k+2)\Theta(k+2)-Kr\Phi(k)\\&-\frac{S}{2}\sum_{r=0}^{k}\delta(r-1)(k-r+1)\Phi(k-r+1)+\sum_{r=0}^{k}(k-r+1)F(r)\Phi(k-r+1)\\&+\sum_{r=0}^{k}(k-r+1)G(r)\Phi(k-r+1)=0\end{aligned}\right\} \quad (5.31)$$

Requisite boundary provisions are: $\Phi(0)=1, \Phi(1)=D$ (5.32)

Where, $F(k), G(k), \Theta(k), \Phi(k)$ are the transformed form of $f(\eta), g(\eta), \theta(\eta), \phi(\eta)$. The assumed constants A, B, C, D can be found by applying the boundary conditions. The iteration schemes are calculated as follows:

$$\left.\begin{aligned}&F(0)=0,\ F(1)=1,\ F(2)=A,\\&F(3)=\left(\frac{M^2+S+1}{6}\right),\ F(4)=\left(\frac{2M^2A+3SA+2A^2-2\alpha A}{24}\right)\end{aligned}\right\} \quad (5.33)$$

$$\left.\begin{gathered} G(0)=0,\ G(1)=\alpha,\ G(2)=B, \\ G(3)=\left(\frac{\left(M^2+S\right)\alpha+1}{6}\right),\ G(4)=\left(\frac{2M^2B+3SB+2A^2-2A-2B-2\alpha B}{24}\right) \end{gathered}\right\} \quad (5.34)$$

$$\left.\Theta(0)=1,\ \Theta(1)=C,\ \Theta(2)=\left(\frac{-NbCD-NtC^2}{2}\right)\Pr\right\} \quad (5.35)$$

$$\left.\Phi(0)=1,\ \Phi(1)=D,\ \Phi(2)=\left(\frac{Kr+\frac{Nt}{NbLe}\left(NbCD+NtC^2\right)\Pr}{2}\right)Le\right\} \quad (5.36)$$

Putting the above values in the main equations comprising DTM we get the following equations

$$f(\eta)=\eta+A\eta^2+\left(\frac{M^2+S+1}{6}\right)\eta^3+\left(\frac{2M^2A+3SA+2A^2-2\alpha A}{24}\right)\eta^4+\cdots\cdots \quad (5.37)$$

$$g(\eta)=\alpha\eta+B\eta^2+\left(\frac{\left(M^2+S\right)\alpha+1}{6}\right)\eta^3+\left(\frac{2M^2B+3SB+2A^2-2A-2B-2\alpha B}{24}\right)\eta^4+\cdots\cdots$$

(5.38)

$$\theta(\eta)=1+C\eta+\left(\frac{-NbCD-NtC^2}{2}\right)\Pr\eta^2+\cdots\cdots \quad (5.39)$$

$$\phi(\eta)=1+D\eta+\left(\frac{Kr+\frac{Nt}{NbLe}\left(NbCD+NtC^2\right)\Pr}{2}\right)Le\eta^2+\cdots\cdots \quad (5.40)$$

Where, the values of A, B, C, D are respectively -1.179164, 1.468784, -0.858621, 1.100582

5.3.3. RK-4 based shooting scheme

The system of ordinary differential equations is solved by RK-4 based shooting method. We rearrange the ODEs 5.9-5.12 into first order ODEs and change them into an initial value problem. The variables are changed in the following way

$$\begin{pmatrix} f \\ f' \\ f'' \\ g \\ g' \\ g'' \\ \theta \\ \theta' \\ \phi \\ \phi' \end{pmatrix} = \begin{pmatrix} z_1 \\ z_1' = z_2 \\ z_2' = z_3 \\ z_4 \\ z_4' = z_5 \\ z_5' = z_6 \\ z_7 \\ z_7' = z_8 \\ z_9 \\ z_9' = z_{10} \end{pmatrix} \tag{5.41}$$

As per our problem we get the following systems:

$$\begin{pmatrix} z_1' \\ z_2' \\ z_3' \\ z_4' \\ z_5' \\ z_6' \\ z_7' \\ z_8' \\ z_9' \\ z_{10}' \end{pmatrix} = \begin{pmatrix} z_2 \\ z_3 \\ \frac{\eta}{2} S z_3 + S z_2 + z_2^2 - (z_1 + z_4) z_3 + M^2 z_2 \\ z_5 \\ z_6 \\ \frac{\eta}{2} S z_6 + S z_5 + z_5^2 - (z_1 + z_4) z_6 + M^2 z_5 \\ z_8 \\ \Pr\left\{ \frac{\eta}{2} S z_8 - (z_1 + z_4) z_8 - N b z_8 z_{10} - N t z_8^2 \right\} \\ z_{10} \\ Le\left\{ \frac{\eta}{2} S z_{10} - (z_1 + z_4) z_{10} - \frac{Nt}{NbLe} z_8' + K r z_9 \right\} \end{pmatrix} \tag{5.42}$$

$$\begin{pmatrix} z_1(0) \\ z_2(0) \\ z_3(0) \\ z_4(0) \\ z_5(0) \\ z_6(0) \\ z_7(0) \\ z_8(0) \\ z_9(0) \\ z_{10}(0) \end{pmatrix} = \begin{pmatrix} 0 \\ 1 \\ \beta_1 \\ 0 \\ \alpha \\ \beta_2 \\ 1 \\ \beta_3 \\ 1 \\ \beta_4 \end{pmatrix} \tag{5.43}$$

The unknowns $\beta_1, \beta_2, \beta_3$ *and* β_4 are guessed and we have used MAPLE-2017 software to solve the system nonlinear ODEs until $f'(\infty)=0,\ g'(\infty)=0,\ \theta(\infty)=0,\ \phi(\infty)=0$ is reached. The numerical result is calculated up to 10^{-6} degree of exactness.

5.3.4. Code verification

To access the validity of the present problem, we have compared our numeric outcomes with previous literature as reflected in Table 5.2 for incompressible viscous flow and it explores good agreement. Again, the values of $f'(1), g'(1), \theta(1)$ and $\phi(1)$ are compared with the result obtained in DTM method for different values of S. which are given in Table 5.3. The accuracy of the data is found to be excellent during the comparison. Also, in Figure 5.2 graphically we simulate the velocity variations for magnetic parameter and we did this for both DTM and RK-4 based shooting scheme. It uplifts the nice accuracy of the employed DTM scheme as compared to RK-4 scheme.

Table 5.2: Comparison of numerical outcomes with previous studies

$\alpha = 0.0$	$f''(0)$	$g''(0)$	$f(\infty)$	$g(\infty)$
Wang [126]	-1.0	0.0	1.0	0.0
Liu [131]	-1.0	0.0	1.0	0.0
Present study	-1.0	0.0	1.0	0.0
$\alpha = 0.25$	$f''(0)$	$g''(0)$	$f(\infty)$	$g(\infty)$
Wang [126]	-1.048813	-0.194564	0.907075	0.257986
Liu [131]	-1.048813	-0.194565	0.907067	0.257966
Present study	-1.048813	-0.194565	0.907067	0.257966
$\alpha = 0.50$	$f''(0)$	$g''(0)$	$f(\infty)$	$g(\infty)$
Wang [126]	-1.093097	-0.465205	0.842360	0.451671
Liu [131]	-1.093096	-0.465206	0.842360	0.451663
Present study	-1.093096	-0.465206	0.842361	0.451663
$\alpha = 0.75$	$f''(0)$	$g''(0)$	$f(\infty)$	$g(\infty)$
Wang [126]	-1.134485	-0.794622	0.792308	0.612049
Liu [131]	-1.134486	-0.794619	0.792293	0.612128
Present study	-1.134486	-0.794619	0.792293	0.612128
$\alpha = 1.0$	$f''(0)$	$g''(0)$	$f(\infty)$	$g(\infty)$
Wang [126]	-1.173720	-1.173720	0.751527	0.751527
Liu [131]	-1.173721	-1.173721	0.751494	0.751494
Present study	-1.173721	-1.173721	0.751494	0.751494

Table 5.3: Comparison of numerical values by both RK-4 method and DTM

S	$f'(1)$ **(RK-4)**	$f'(1)$ **(DTM)**	$g'(1)$ **(RK-4)**	$g'(1)$ **(DTM)**	$\theta(1)$ **(RK-4)**	$\theta(1)$ **(DTM)**	$\phi(1)$ **(RK-4)**	$\phi(1)$ **(DTM)**
0.0	0.214608	0.214610	0.114042	0.114040	0.193490	0.193487	0.066023	0.066024
0.1	0.212951	0.212954	0.113052	0.113049	0.216729	0.216728	0.072597	0.072599
0.2	0.211235	0.211236	0.112033	0.112032	0.243436	0.243432	0.080014	0.080016
0.3	0.209469	0.209472	0.110989	0.110985	0.274623	0.274619	0.088450	0.088451
0.4	0.207662	0.207664	0.109924	0.109923	0.312252	0.312250	0.098087	0.098090
0.5	0.205822	0.205826	0.108845	0.108843	0.361203	0.361201	0.107320	0.107322

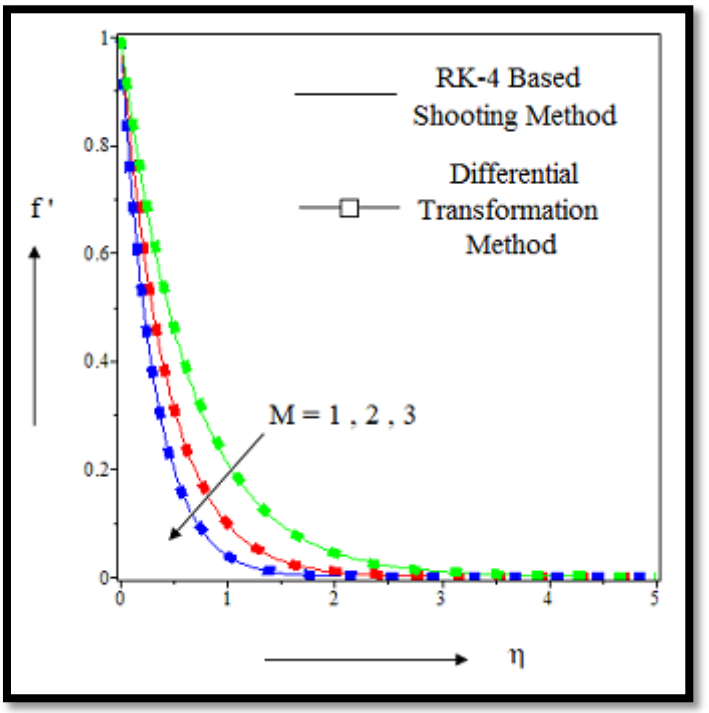

Figure 5.2: Comparison of DTM and RK-4 based shooting method

5.4. Results and discussion

The results obtained in this work are explained in this section. Various range of values for different parameters are used and they are shown through graphs and tables. The effects of magnetic parameter, stretching parameter, Brownian motion, thermophoresis and chemical reaction parameters are discussed in the following section. We have assigned the values as $\Pr = 6.2, M = 2.0, Nb = 0.4, Nt = 0.4, Kr = 0.4, Le = 5.0, \alpha = 0.4$ and in case of unsteady and steady flow we choose $S = 0.5, S = 0.0$ respectively. We have also taken various values of the fixed parameters to simulate the process. Our core intention is to reveal the hydrothermal variations of both unsteady and steady flow.

5.4.1. Effect of magnetic parameter M

The velocities are decreased as we increase the magnetic parameter. As the Lorentz force originated due to magnetic field possesses retardation effect, hence velocities in both directions are reduced. The consequences are exhibited through Figure 5.3 and 5.4. We can notice that the reduction of velocities is much lesser in case of unsteady flow than that of steady flow. Clear pictorial view is seen inside $0.0 \le \eta \le 3.0$. Skin friction in Table 5.4 seems to decline in both directions, but for unsteady flow rate of reduction is lower. As a result frictional force gets increased. More heat is generated for this reason; hence increment in magnetic parameter increases the temperature in Figure 5.5. The concentration profile in Figure 5.6 is also increased as we increase the magnetic parameter. In Figure 5 and 6 for temperature and concentration profile, we noticed that the unsteady flow gives higher temperature as well as concentration profile than that of steady flow. Initially, the consequences are not so promising, but slight away from it ($\eta > 1.0$) results are promising. Table 5.5 and 5.6 enlighten that heat plus mass transport drop off for magnetic intensity, but steady flow provides maximum reduction.

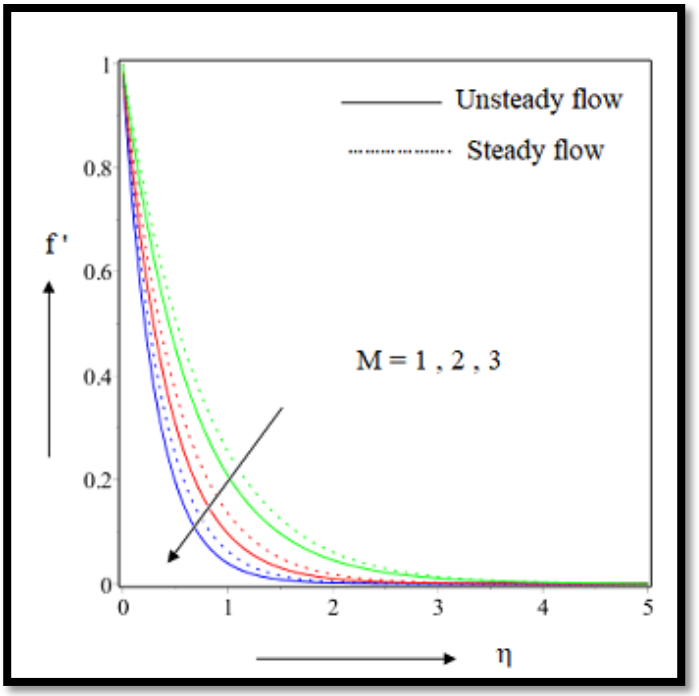

Figure 5.3: Effect of M on $f'(\eta)$

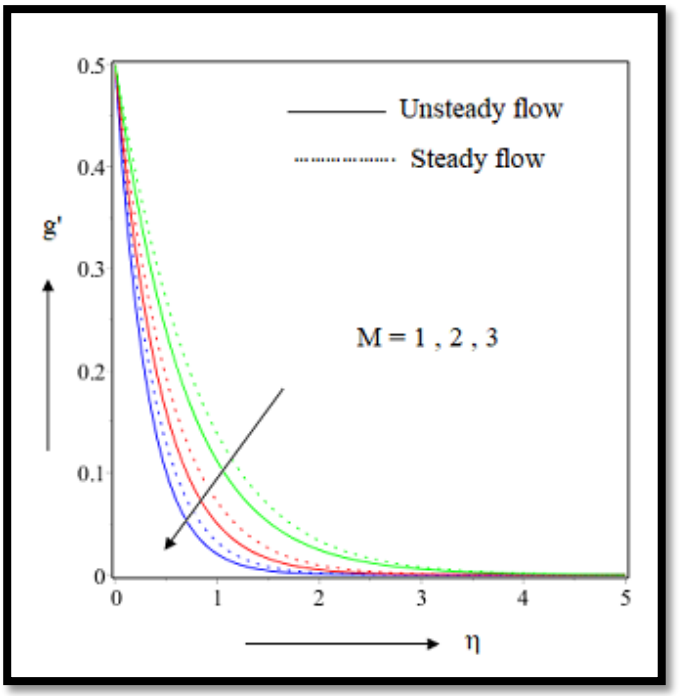

Figure 5.4: Effect of M on $g'(\eta)$

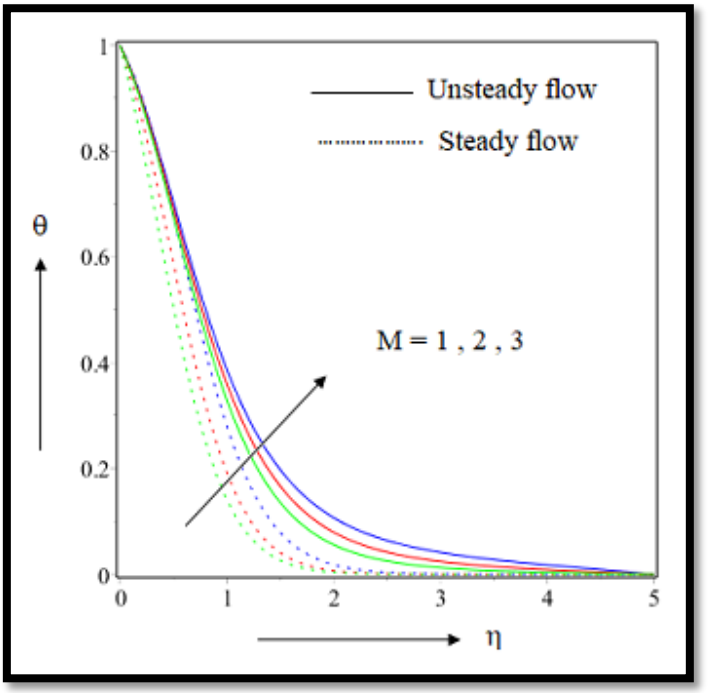

Figure 5.5: Effect of M on $\theta(\eta)$

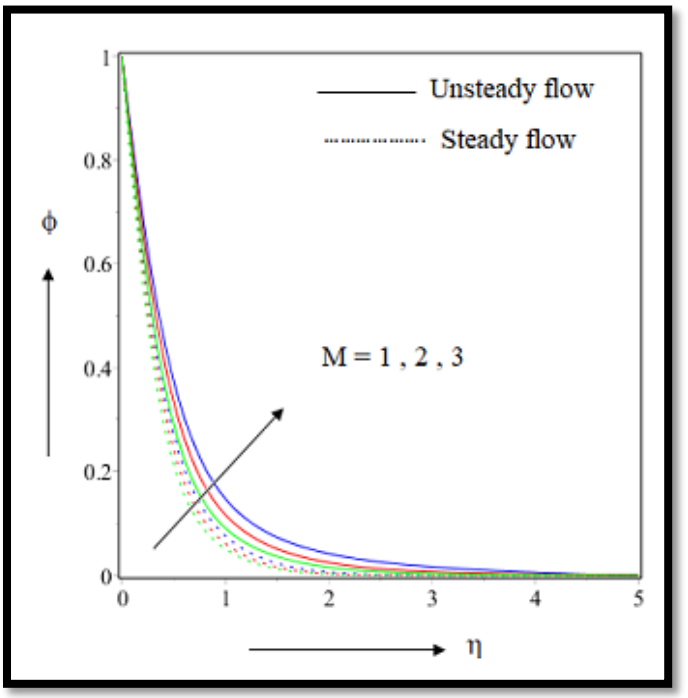

Figure 5.6: Effect of M on $\phi(\eta)$

5.4.2. Effect of stretching parameter α

The stretching parameter $\alpha = \frac{b}{a}$ has a straight effect on both velocities. Increment of stretching parameter declines the value a which is directly related to f'. As a result, the velocity f' in Figure 5.7 is decreased. For unsteady flow, we get lower velocity profile than steady flow of f' *and* g'. Higher stretching parameter implies higher value of b which is straightly related to g'. Consequently, the value of g' gets increased in Figure 5.8 as we increase the value of α. Prominent view is observed within the interval $0.0 \le \eta \le 3.0$ (not precisely determined). Frictional effect has been noted to decrease in Table 5.4. Higher increment is confirmed for steady motion. Temperature and concentration both are declined as we increase α. Maximum thermal and concentration effect are assured for unsteady flow. The effect can be observed in Figure 5.9 and Figure 5.10. Heat and mass transfer are calculated and illustrated in Table 5.5 and 5.6. Heat and mass transport are found to intensify. For heat transport, 17.58% enhancement is noticed for unsteady flow, where as it is 10.40% for steady flow. Again for mass transfer, unsteady motion contributes 10.29% increment and 6.82% for steady flow.

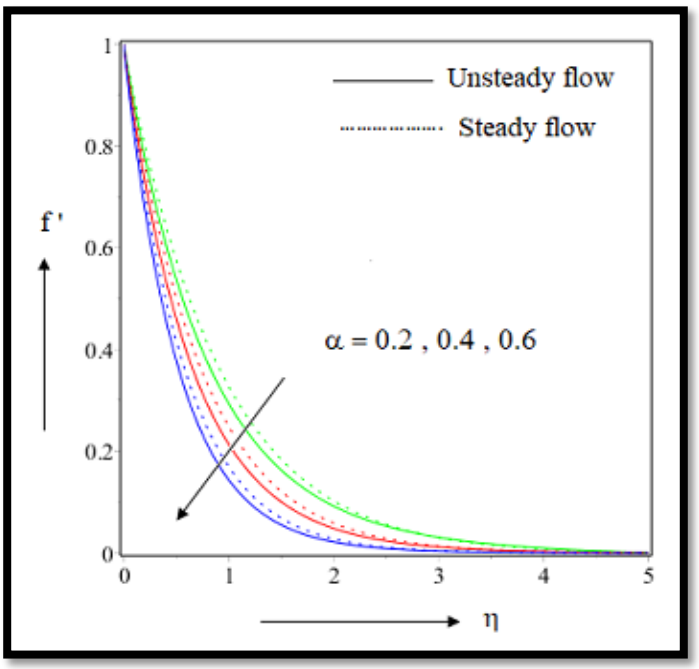

Figure 5.7: Effect of α on $f'(\eta)$

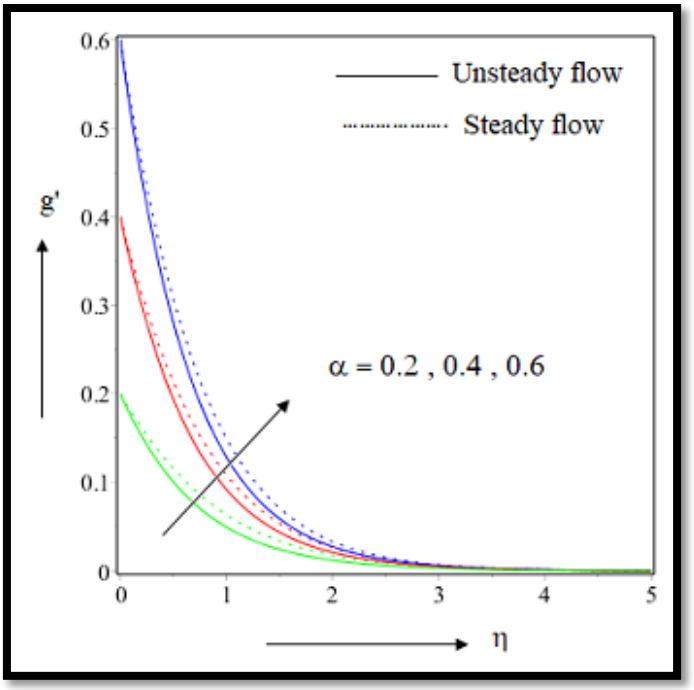

Figure 5.8: Effect of α on $g'(\eta)$

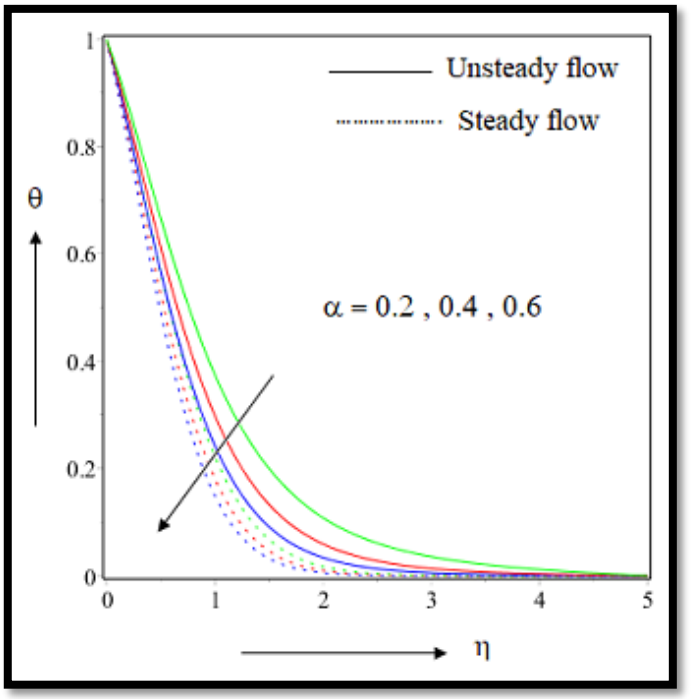

Figure 5.9: Effect of α on $\theta(\eta)$

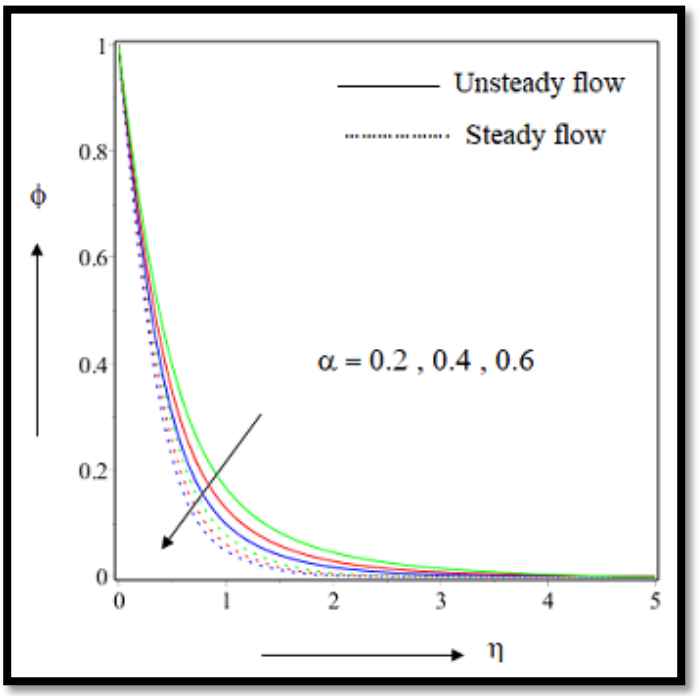

Figure 5.10: Effect of α on $\phi(\eta)$

5.4.3. Effect of Brownian motion parameter Nb

Brownian motion plays an important role for the temperature and concentration prolife. Brownian motion for the nanoparticles frames the temperature profile as well as the concentration. If we increase Nb, the movement of tiny ingredients gets increased and consequently more frequent collision results more heat. The effect is seen in Figure 5.11. The prominent difference lies inside $0.0 \le \eta \le 4.0$. The steady flow gives lower temperature effect than that of unsteady motion. Table 5.5 exhibits reduced heat transport scenario. Elevated Brownian motion parameter decreases the concentration profile gradually. As frequent particles are displaced from one place to other, thus quantity of nanoparticles in per unit volume of nanofluid goes down. Thus concentration drops off in Figure 5.12. Effect is not so convincing except $0.5 \le \eta \le 2.0$. Mass transfer is also decreased in Table 5.6 for both steady and unsteady flow. Unsteady flow in this case creates high concentration than that of steady flow.

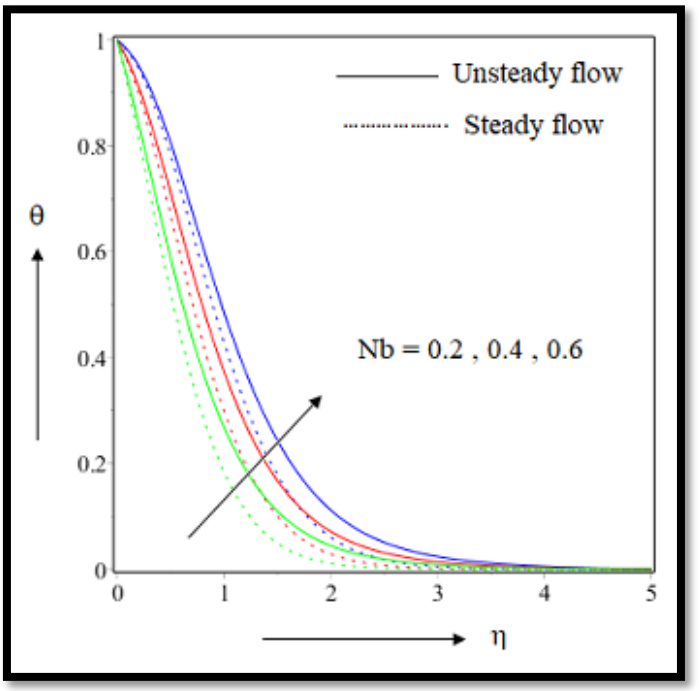

Figure 5.11: Effect of Nb on $\theta(\eta)$

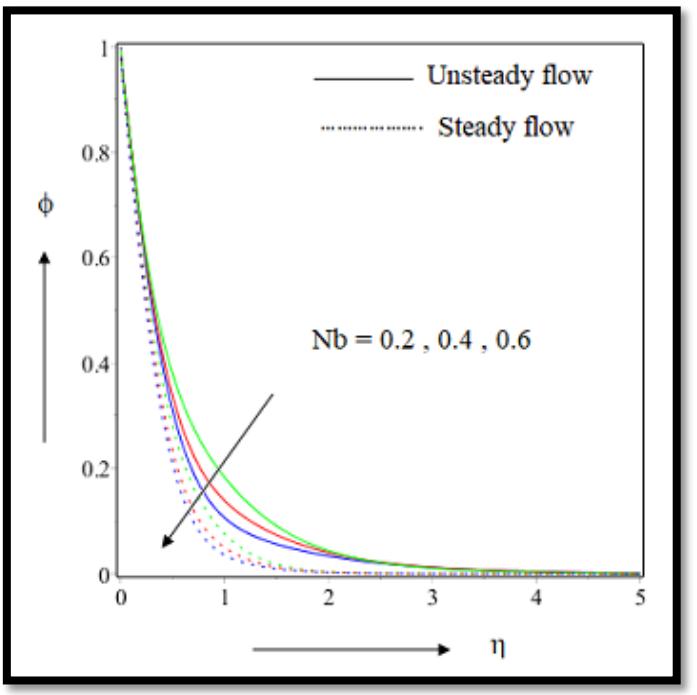

Figure 5.12: Effect of Nb on $\phi(\eta)$

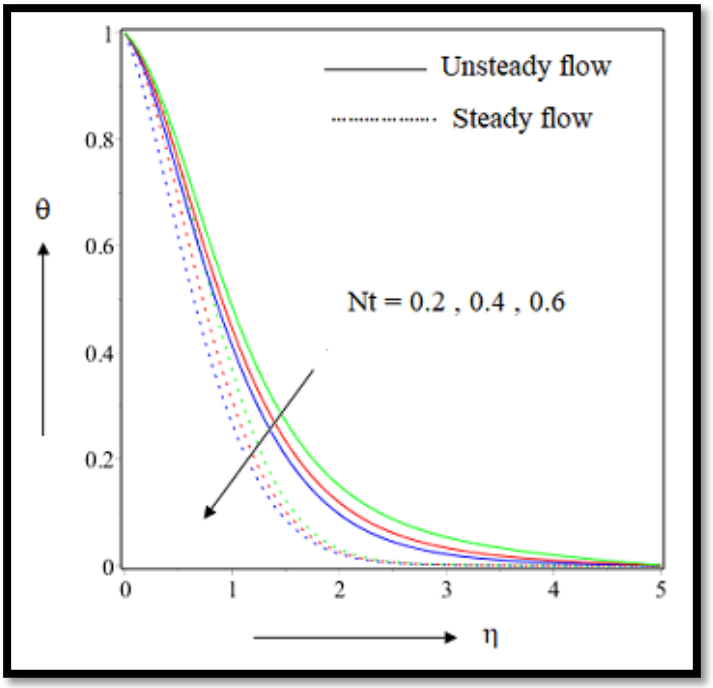

Figure 5.13: Effect of Nt on $\theta(\eta)$

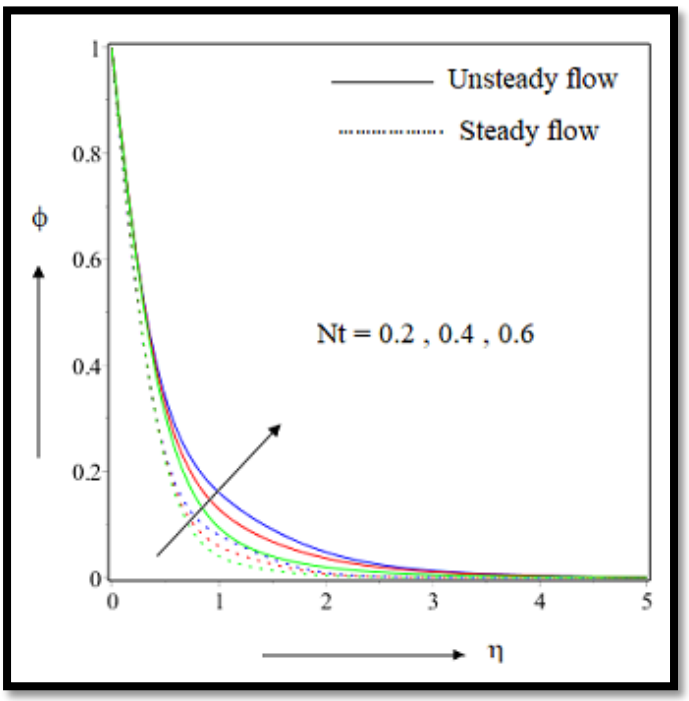

Figure 5.14: Effect of Nt on $\phi(\eta)$

5.4.4. Effect of Thermophoresis parameter Nt

Thermophoresis parameter literally defines the relocation of nanoparticles due to temperature gradient. Higher thermophoretic parameter tries to make thermal equilibrium inside the system. The higher temperature gradient will be balanced through migration of particles. Evidently, the temperature lines will go down in Figure 5.13. Unsteady flow gives higher temperature effect than that of steady flow. Here such difference is quite higher as compared to other parametric consequences. Migration of nanoparticles also affects the concentration account. High thermophoresis parameter increases the concentration profile as explored in Figure 5.14. Near the proximity of the stretched surface, outcomes are not so apparent. Unsteady motion leads to acquire maximum concentration as compared to steady flow. High relocation of particles increases the mass diffusion plus cooling procedure within the system and numerically it has been validated through Table 5.5 and 5.6.

5.4.5. Effect of Chemical reaction parameter Kr

Chemical reaction parameter has great impact on the temperature and concentration because both concentration and temperature equation are coupled with each other as reflected from equations 5.11 and 5.12. So, as we boost up the value of Kr , the temperature gets reduced. Thus, in Figure 5.15 high chemical reaction cuts the thermal effect. However, unsteady flow portrays higher result in heat generation than steady flow. From Table 5.5 we observe that for unsteady flow the heat transport reduction rate is 2.51% whereas for steady flow it is only 1.78%. Thus, effective cooling procedure can be gained for steady flow. The impact of Kr on concentration is also distinctly visible. As we elevate Kr , the concentration falls down slowly in Figure 5.16. Negative sign is correlated with concentration function and Kr in equation 5.12. Thus, lower concentration syndrome is quite predictable. Here also, the unsteady motion gives higher concentration than that of steady drift. Mass diffusion swells for Kr . Table 6 explores 10.09% increment for steady flow, but such data jumps to 17.4% for unsteady controlled flow.

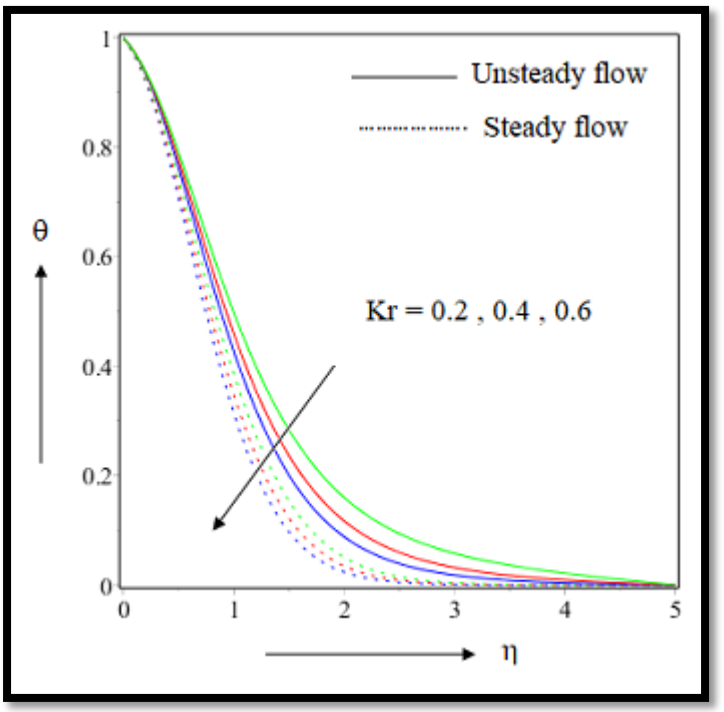

Figure 5.15: Effect of Kr on $\theta(\eta)$

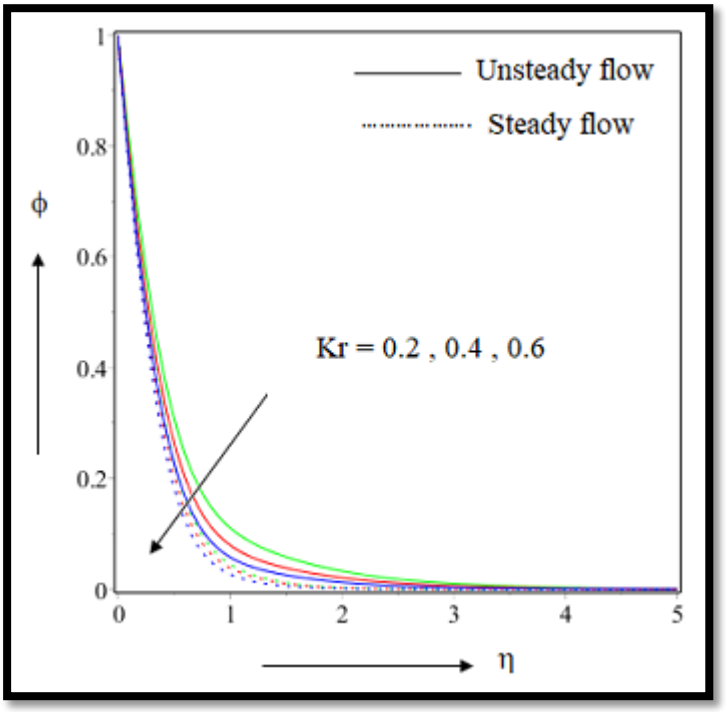

Figure 5.16: Effect of Kr on $\phi(\eta)$

5.5. Conclusions

Chemically reactive unsteady nanoliquid flow over a bidirectional stretched surface is investigated numerically. Brownian and thermophoretic migration have been considered to reveal the hydrothermal outcomes. Resulting equations are solved by differential transformation scheme. Graphs and tables are exhibited to explore the outcomes. Based on the investigation, following interpretations are drawn:

- Increase in magnetic field decreases the velocities in both axes but temperature and concentration profile are increased. In case of stretching parameter, the temperature, concentration profile get decreased when we increase the value of parameter. Velocity in x-direction is reduced and enhanced in y-direction. In every case, we observe that unsteady motion provides low velocity profile as compared to steady flow.
- Brownian motion plus thermophoresis parameter play an important role here. Concentration profile is dropped as we upshot the value of the Brownian parameter and thermophoresis makes it high. When it comes to temperature profile Brownian motion, thermophoresis parameters give different result. Brownian motion increases the temperature and thermophoresis drops it down.
- Chemical reaction declines both temperature and concentration. Unsteady flow always depicts high thermal and concentration profile as compared to steady flow.
- Skin friction reduces for both magnetic and stretching parameter. Steady flow ensures maximum rate of increment in comparison with unsteady motion.
- Heat transport is decreased for magnetic parameter, Brownian motion and chemical reaction but reverse is assured for rest of the parameters. Highest increment in heat transport is observed for unsteady flow. Comparatively, unsteady nanoliquid flow renders effective cooling and mass transport.
- Mass transfer is enhanced for stretching factor, thermophoresis and chemical reaction parameter whereas same is reduced for others. Mass transfer is also escalated for unsteady flow.

Table 5.4: Effect of pertinent parameters on skin friction

M	α	Cf_{xr}		Cf_{yr}	
		unsteady flow	*steady flow*	*unsteady flow*	*steady flow*
1.0	0.4	-2.095431	-1.435580	-1.159551	-1.589173
2.0		-3.644717	-2.249332	-1.844336	-2.865016
3.0		-4.447492	-3.194968	-2.662193	-3.448130
0.5	0.2	-1.371193	-0.529839	-0.406868	-1.212159
	0.4	-1.515682	-1.119694	-0.943046	-1.348704
	0.6	-1.738168	-1.764744	-1.515478	-1.558377

Table 5.5: Effect of pertinent parameters on heat transfer

M	α	Nb	Nt	Kr	Nu_r	
					unsteady flow	*steady flow*
1.0	0.4	0.4	0.4	0.4	0.435656	0.770299
2.0					0.419322	0.530107
3.0					0.406756	0.354151
0.5	0.2				0.538078	0.700737
	0.4				0.632696	0.773650
	0.6				0.713821	0.839864
	0.4	0.2			0.674604	0.782482
		0.4			0.313012	0.351479
		0.6			0.147069	0.160706
		0.4	0.2		0.196304	0.173737
			0.4		0.221304	0.273728
			0.6		0.250134	0.446912
				0.2	0.216744	0.253055
				0.4	0.211298	0.248538
				0.6	0.209673	0.247308

Table 5.6: Effect of pertinent parameters on mass transfer

M	α	Nb	Nt	Kr	Sh_r	
					unsteady flow	*steady flow*
1.0	0.4	0.4	0.4	0.4	2.068919	2.524747
2.0					1.823329	2.285398
3.0					1.656287	2.109559
0.5	0.2				1.643434	1.990934
	0.4				1.812310	2.126823
	0.6				1.966749	2.251340
	0.4	0.2			1.927459	2.099924
		0.4			1.846695	2.183010
		0.6			1.769808	2.296028
		0.4	0.2		1.922105	2.189473
			0.4		1.929478	2.219793
			0.6		1.955416	2.268139
				0.2	1.943810	2.187496
				0.4	2.204178	2.408866
				0.6	2.449095	2.597765

CHAPTER 6

Framing the Hydrothermal Features of Magnetized TiO_2-$CoFe_2O_4$ Water Based Steady Hybrid Nanofluid Flow over a Radiative Revolving Disk*

6.1. Introduction

The hybrid nanosolution containing both titanium oxide (TiO_2) and ferrous ($CoFe_2O_4$) nanoparticles is considered in this chapter. Titanium oxide have good photo catalytic characteristics and thus it has been successfully employed in antibacterial or antiseptic compositions. Titanium oxide nanoparticles are often used in solar cells and in light emitting diodes. Owing to its potential ability to restore energy, semi-conductive characteristics, electronic features, TiO_2 is mostly used in technological and industrial sectors. Magnetic nanoparticles have received significant attention for its biomedical functions. Among them iron-oxide nanoingredients become mostly acceptable due to their elemental compositions that make them degradable and biocompatible. Among different members of spinel ferrites, cobalt ferrite ($CoFe_2O_4$) nanoparticles are proved to be the most explored magnetic nanoingredients. Therefore, the objective of this investigation is to reveal a comprehensive hydrothermal analysis of $TiO_2 - CoFe_2O_4$ water based hybrid nanofluid. To the author's knowledge, no research on the effects of magnetized nanofluid flow over a radiative spinning disk with hybrid nanoparticles has been reported till now. The partial differential equations (PDEs) of the system are transferred to ordinary differential equations (ODEs) by suitable similarity transformations. Rosseland approximation is used to simplify the heat flux radiation. The ODEs are solved by Runge-Kutta-Fehlberg (RK-4) method with the help of MAPLE-17 software. The heat lines are observed and compared for unitary nanoparticle and hybrid nanoparticles. In spite of that, the results are also analyzed for linear and nonlinear radiation.

***This Chapter is based on the published in: Multidiscipline Modeling in Materials and Structures, 16(4) (2019), 765-790, (SCIE).**

6.2. Mathematical formulation

6.2.1. Problem statement

Let us presume a steady laminar incompressible viscous flow with electrically conducted hybrid nanofluid over a rotating disc which rotates with angular velocity Ω. The revolving disk is placed at $z=0$. The fluid is spread over $z \geq 0$. The components u, v, w are the flow velocities in the direction r, ϕ, z respectively. The disk surface has uniform temperature T_w while T_∞ is the same at free stream as depicted in Figure 1. The pressure of free stream is P_∞. A uniform magnetic strength B_0 is applied parallel to $z-axis$. We have employed a novel type of nanosuspension i.e. "*Hybrid nanofluid*" that basically assembles two different tiny ingredients into the host liquid. We chose here *Titanium* (TiO_2) *and Ferrous* $(CoFe_2O_4)$ nanoparticles with water as liquid medium. We continued our searching with few primary considerations that liquid is free from chemically reactive components, thermal or velocity slips are absent, joule heating is overlooked. With this assumption following [132,133] the equations which governed the system are:

$$\frac{\partial u}{\partial r}+\frac{u}{r}+\frac{\partial w}{\partial z}=0 \tag{6.1}$$

$$\rho_{hnf}\left(u\frac{\partial u}{\partial r}-\frac{v^2}{r}+w\frac{\partial u}{\partial z}\right)+\frac{\partial p}{\partial r}=\mu_{hnf}\left(\frac{\partial^2 u}{\partial r^2}+\frac{1}{r}\frac{\partial u}{\partial r}-\frac{u}{r^2}+\frac{\partial^2 u}{\partial z^2}\right)-\sigma_{hnf}B_0{}^2u \tag{6.2}$$

$$\rho_{hnf}\left(u\frac{\partial v}{\partial r}+\frac{uv}{r}+w\frac{\partial v}{\partial z}\right)=\mu_{hnf}\left(\frac{\partial^2 v}{\partial r^2}+\frac{1}{r}\frac{\partial v}{\partial r}-\frac{v}{r^2}+\frac{\partial^2 v}{\partial z^2}\right)-\sigma_{hnf}B_0{}^2v \tag{6.3}$$

$$\rho_{hnf}\left(u\frac{\partial w}{\partial r}+w\frac{\partial w}{\partial z}\right)+\frac{\partial p}{\partial z}=\mu_{hnf}\left(\frac{\partial^2 w}{\partial r^2}+\frac{1}{r}\frac{\partial w}{\partial r}+\frac{\partial^2 w}{\partial z^2}\right) \tag{6.4}$$

$$\left(\rho C_p\right)_{hnf}\left(u\frac{\partial T}{\partial r}+w\frac{\partial T}{\partial z}\right)=k_{hnf}\left(\frac{\partial^2 T}{\partial r^2}+\frac{1}{r}\frac{\partial T}{\partial r}+\frac{\partial^2 T}{\partial z^2}\right)-\frac{\partial q_r}{\partial z} \tag{6.5}$$

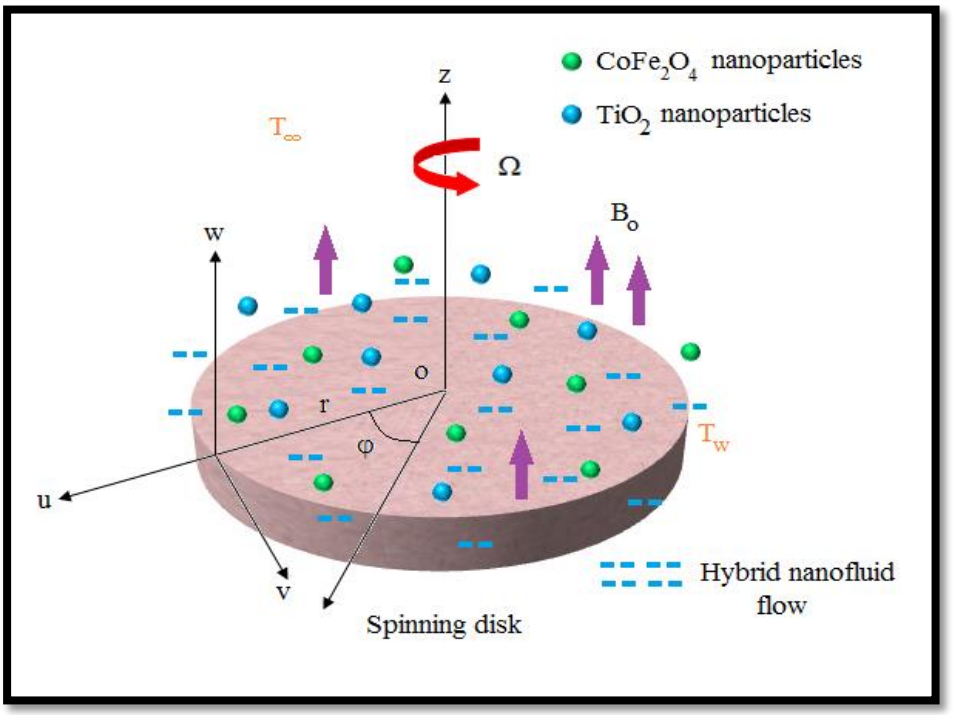

Figure 6.1: Picture of the model

Here the radiated heat flux for radiation is simplified by employing the Rosseland approximation:

$$q_r = -\frac{4\sigma^*}{3\kappa^*}\frac{\partial T^4}{\partial y} = -\frac{16\sigma^*}{3\kappa^*}T^3\frac{\partial T}{\partial y} \qquad (6.6)$$

Now if we apply the non-dimensional expression of T as $\theta(\eta) = \frac{T - T_\infty}{T_w - T_\infty}$ as in equation (6.8), we will have $T = T_\infty\left\{1 + (\theta_w - 1)\theta\right\}$ where, $\theta_w = \frac{T_w}{T_\infty}$.

Table 6.1: Thermophysical models of usual nanofluid and hybrid nanofluid [134-137]

Properties	**Nanofluid(** $TiO_2 / water$ **)**
Density	$\rho_{nf} = (1-\phi)\rho_f + \phi\rho_s$
Heat capacity	$(\rho C_p)_{nf} = (1-\phi)(\rho C_p)_f + \phi(\rho C_p)_s$
Viscosity	$\mu_{nf} = \dfrac{\mu_f}{(1-\phi)^{2.5}}$
Thermal conductivity	$\dfrac{k_{nf}}{k_f} = \dfrac{k_s + (n-1)k_f - (n-1)\phi(k_f - k_s)}{k_s + (n-1)k_f + \phi(k_f - k_s)}$
Electrical conductivity	$\dfrac{\sigma_{nf}}{\sigma_f} = 1 + \dfrac{3(\sigma-1)\phi}{(\sigma+2) - (\sigma-1)\phi}, where\ \sigma = \dfrac{\sigma_s}{\sigma_f}$
Properties	**Hybrid nanofluid (** $CoFe_2O_4 – TiO_2 / water$ **)**
Density	$\rho_{hnf} = (1-\phi_1-\phi_2)\rho_f + \phi_1\rho_1 + \phi_2\rho_2$
Heat capacity	$(\rho C_p)_{hnf} = (1-\phi_1-\phi_2)(\rho C_p)_f + \phi_1(\rho C_p)_1 + \phi_2(\rho C_p)_2$
Viscosity	$\mu_{hnf} = \dfrac{\mu_f}{(1-\phi_1-\phi_2)^{2.5}}$
Thermal conductivity	$\dfrac{\kappa_{hnf}}{\kappa_f} = \left\{\dfrac{\kappa_1\phi_1 + \kappa_2\phi_2}{\phi_1+\phi_2} + 2\kappa_f + 2(\kappa_1\phi_1 + \kappa_2\phi_2) - 2(\phi_1+\phi_2)\kappa_f\right\} \times \left\{\dfrac{\kappa_1\phi_1 + \kappa_2\phi_2}{\phi_1+\phi_2} + 2\kappa_f - 2(\kappa_1\phi_1 + \kappa_2\phi_2) + (\phi_1+\phi_2)\kappa_f\right\}^{-1}$
Electrical conductivity	$\dfrac{\sigma_{hnf}}{\sigma_f} = 1 + \dfrac{3\left(\dfrac{\phi_1\sigma_1 + \phi_2\sigma_2}{\sigma_f}\right) - 3(\phi_1+\phi_2)}{2 + \left\{\dfrac{\phi_1\sigma_1 + \phi_2\sigma_2}{(\phi_1+\phi_2)\sigma_f}\right\} - \left\{\dfrac{\phi_1\sigma_1 + \phi_2\sigma_2}{\sigma_f} - (\phi_1+\phi_2)\right\}}$

6.2.2. Thermophysical properties

In this discussion we will study the effect of nanofluid and hybrid nanofluid under linear and nonlinear radiation. We take TiO_2 and $CoFe_2O_4$ for hybrid nanofluid and only TiO_2 for nanofluid. For model construction we have utilized Takabi and Salehi [134] and Chamkha et al. [135] for hybrid nanoliquids and Oztop and Abu-Nada [136], Maxwell [137] for usual nanolioquids. We also elaborately describe the effect of nanofluid i.e. when $\phi_2 = 0.0$. The model formulation of these nanofluid and hybrid nanofluids are given in Table 6.1 and the thermophysical data of spherically shaped 38 nm nanoparticles are given in Table 6.2.

Table 6.2: Thermophysical properties of base fluid and nanoparticles

Physical properties	Water	TiO_2	$CoFe_2O_4$
C_p	4180	686.2	700
ρ	997	4250	4907
κ	0.6071	8.9538	3.7
σ	5.5×10^{-6}	2.38×10^{6}	5.51×10^{9}

6.2.3. Boundary conditions

The essential boundary conditions are given by

$$\left.\begin{array}{c} u=0, v=\Omega r, w=w_0, T=T_w \quad at\ z=0 \\ and \\ u\to 0, v\to 0, T=T_\infty, P=P_\infty \quad at\ z\to\infty \end{array}\right\} \tag{6.7}$$

6.2.4. Similarity transformation

Here we perform similarity transformation to convert the partial differential equation in the governing equation to ordinary Differential Equation the needful modernizations are as follows:

$$\left.\begin{aligned} u = r\Omega f',\ v = r\Omega g,\ w = -\sqrt{2\Omega\nu_f}\, f,\ \theta(\eta) = \frac{T - T_\infty}{T_w - T_\infty}, \\ P = P_\infty + 2\Omega\mu_f P(\eta),\ \eta = \sqrt{\frac{2\Omega}{\nu_f}}z \end{aligned}\right\} \tag{6.8}$$

Using the above set of similarity transformations as in equation (6.8) we get

$$2f''' + \frac{A_1}{A_4}\left(2ff'' - f'^2 + g^2\right) - \frac{A_5}{A_4}Mf' = 0 \tag{6.9}$$

$$2g'' + \frac{A_1}{A_4}\left(2fg' - 2f'g\right) - \frac{A_5}{A_4}Mg = 0 \tag{6.10}$$

$$\frac{1}{\Pr}\left(\theta'' + \frac{4N}{3A_3}\frac{d}{d\eta}\left\{\left(1 + \theta(\eta)(\theta_w - 1)\right)^3 \frac{d\theta(\eta)}{d\eta}\right\}\right) + \frac{A_2}{A_3} f\theta' = 0 \tag{6.11}$$

$$\text{Where, } A_1 = \frac{\rho_{hnf}}{\rho_f}, A_2 = \frac{(\rho C_p)_{hnf}}{(\rho C_p)_f}, A_3 = \frac{k_{hnf}}{k_f}, A_4 = \frac{\mu_{hnf}}{\mu_f}, A_5 = \frac{\sigma_{hnf}}{\sigma_f}$$

Correspondingly, boundary clauses are changed as:

$$\left.\begin{aligned} f = -f_w,\ f' = 0,\ g = 1,\ \theta = 1\ at\ \eta = 0, \\ f' \to 0,\ g \to 0,\ \theta \to 0\ as\ \eta \to \infty. \end{aligned}\right\} \tag{6.12}$$

Here $f_w > 0.0$ represents suction and $f_w < 0.0$ for injection. It is vital to mark that for $\theta_w = 1.0$ we converge to the simple radiative case, whereas, for $\theta_w > 1.0$ we have the nonlinear radiative aspects

6.2.5. Physical quantities

Significant physical quantities in this context are skin friction, Nusselt number. This is remarkable for engineering impetus of equipment design at nanolevel. It is mathematically composed as:

$$C_f = \frac{2\mu_{hnf}\left(\frac{\partial u}{\partial z}\right)_{z=0}}{\rho_{hnf}\left(r\Omega\right)^2},\ C_g = \frac{2\mu_{hnf}\left(\frac{\partial v}{\partial z}\right)_{z=0}}{\rho_{hnf}\left(r\Omega\right)^2}, Nu = \frac{r}{\kappa_f\left(T_w - T_\infty\right)}\left(q_r - \kappa_{hnf}\frac{\partial T}{\partial z}\right)_{z=0} \tag{6.13}$$

Using similarity renovation in equation (6.8) we get reduced form as

$$C_{fr} = \sqrt{\mathrm{Re}_z}\ .\ C_f = \left(\frac{\left(1-\phi_1-\phi_2\right)^{-2.5}}{\left(1-\phi_1-\phi_2\right)+\phi_1\left(\frac{\rho_1}{\rho_f}\right)+\phi_2\left(\frac{\rho_2}{\rho_f}\right)} \right) f''(0) \tag{6.14}$$

$$C_{gr} = \sqrt{\mathrm{Re}_z}\ .\ C_g = \left(\frac{\left(1-\phi_1-\phi_2\right)^{-2.5}}{\left(1-\phi_1-\phi_2\right)+\phi_1\left(\frac{\rho_1}{\rho_f}\right)+\phi_2\left(\frac{\rho_2}{\rho_f}\right)} \right) g'(0) \tag{6.15}$$

$$Nu_r = \frac{Nu}{\sqrt{\mathrm{Re}_z}} = -\frac{k_{hnf}}{k_f}\left(1+\frac{4N}{3A_3}\left\{1+(\theta_w-1)\theta(0)\right\}^3\right)\theta'(0) \tag{6.16}$$

6.3. Numerical procedure

6.3.1. Solution technique

Analytical method of solution is difficult to apply in the obtained group of differential equations with its boundary condition; therefore this system is solved numerically. Shooting method in constitution of RK-4 method is pre-owned to procure the required solution. To achieve this we first reconstruct the nonlinear ODEs (6.9-6.11) into first order ODEs and subsequently restore them into an initial value problem. We relabeled the variables as:

$$\left(f,\ f',\ f'',\ g,\ g',\ \theta,\ \theta'\right)^T = \left(z_1,\ z_1' = z_2,\ z_2' = z_3,\ z_4, z_4' = z_5,\ z_6,\ z_6' = z_7\right)^T \tag{6.17}$$

As per our preferred numerical process we achieve the subsequent systems:

$$\begin{pmatrix} z_1' \\ z_2' \\ z_3' \\ z_4' \\ z_5' \\ z_6' \\ z_7' \end{pmatrix} = \begin{pmatrix} z_2 \\ z_3 \\ \frac{1}{2}\left\{\frac{A_5}{A_4}Mz_2 - \frac{A_1}{A_4}\left(2z_1z_3 - z_2^2 + z_4^2\right)\right\} \\ z_5 \\ \frac{1}{2}\left\{\frac{A_5}{A_4}Mz_4 - \frac{A_1}{A_4}\left(2z_1z_5 - 2z_2z_4\right)\right\} \\ z_7 \\ -\frac{A_2}{A_3}\Pr z_1z_7 - \frac{4N}{3A_3}\left(\left\{1+z_5\left(\theta_w-1\right)\right\}^3 z_7\right)' \end{pmatrix} \tag{6.18}$$

$$\begin{pmatrix} z_1(0) \\ z_2(0) \\ z_3(0) \\ z_4(0) \\ z_5(0) \\ z_6(0) \\ z_7(0) \end{pmatrix} = \begin{pmatrix} -f_w \\ 0 \\ \beta_1 \\ 1 \\ \beta_2 \\ 1 \\ \beta_3 \end{pmatrix} \tag{6.19}$$

Unknown inputs of β_1, β_2 *and* β_3 are guessed and calculations are implemented via MAPLE-17 software in anticipation of the required conditions $f' \to 0,\ g \to 0,\ \theta \to 0$ *as* $\eta \to \infty$ are fulfilled. The internal iterative procedure continues until we acquired the preferred degree of accuracy say 10^{-7}.

6.3.2. Establishment of code

We compared the values of Cf_r *and* Nu_r for $TiO_2 - Water$ nanofluid for various values of nanoparticle concentration (ϕ_1) and suction/injection parameter (f_w) in Table 6.3-6.4. In this process we restore the magnetic parameter, radiation parameter, and θ_w as zero. The obtained outcome is better enough compared to that of previously obtained data as in Bachok et al. [138].

Table 6.3: Comparison of values of Cf_r

ϕ	f_w	Cf_r for $TiO_2 - Water$ nanofluid	
		Bachok et al. [138]	Present
0.00	1	0.3896	0.389642
	-1	0.4895	0.489511
	2	0.2424	0.242421
	0	0.5102	0.510205
	-2	0.3989	0.398936
	1	0.3896	0.389618
	0	0.5101	0.510141
	-1	0.4889	0.488931
0.1	1	0.6031	0.603121
	0	0.5502	0.550277
	-1	0.5167	0.516733

Table 6.4: Comparison of values of Nu_r

ϕ	Pr	f_w	Nu_r for $TiO_2 - Water$ nanofluid	
			Bachok et al.[138]	Present
0.00	0.64	1	0.7202	0.720242
		-1	0.0906	0.090675
	0.71	2	1.4378	1.437812
		0	0.3259	0.325969
		-2	0.0114	0.011404
	6.2	1	6.2722	6.272213
		0	0.9337	0.933725
		-1	0.0002	0.000211
0.1	6.2	1	4.6574	4.657438
		0	0.8215	0.821517
		-1	0.0016	0.001638

6.4. Result and analysis

This section frames the parametric influence on the flow. Here, we elaborately reconnoiter the traits of velocities and temperatures. The effects are revealed with the help of diagrams and tables. We assign the values of $\Pr = 6.2$, $M = 0.5$, $\phi_1 = 0.09$, $\phi_2 = 0.09$, $N = 0.5$, $f_w = 0.2$ and in case of linear and nonlinear radiation $\theta_w = 1.0$, $\theta_w = 1.3$ respectively if anything is not mentioned. Irrespective of that we take a variety range of values of parameters to simulate the process.

6.4.1. Effect of magnetic parameter M

The upshot of magnetic force is very much interesting over velocity profile which is shown in Figure 6.2. It shows high velocity when magnetic field gets zero. As per we increase the value of magnetic field the speed f' is decreased effectively. The magnetic field together with the electrical force creates Lorentz force which is the key factor of retardation in the fluid. Clear pictorial view of velocity drop is seen in $1.0 \le \eta \le 5.0$ (not quite exactly determined), outside this

interval we can observe the asymptotic convergence of the curve. For both hybrid nanofluid and nanofluid the velocity drop takes place as the value of M is enhanced. Hybrid nanofluid takes higher magnitude in velocity than velocity of usual nanosuspension. Radial drag friction is decreased for both hybrid nanosuspension and ordinary nanocomposite, but decreasing rate is lower for the hybrid nanofluid. From Table 6.5 it is obtained that Cf_r diminishing rate for usual nanosolution is 16.28% whereas for hybrid nanosuspension it is 14.77% only. Cross radial velocity also exhibits the decreasing nature as we increase the value of magnetic field. It shows understandable contrast in vicinity of surface and converges asymptotically far away from it. In the region $1.0 \le \eta \le 5.0$ (not quite exactly determined) the difference is very clear. Here also the Lorentz force creates the retardation force and so the consequences are visible in the Figure 6.3. Higher magnitude in cross radial velocity is observed in case of hybrid nanofluid related to that of nanofluid. Cg_r is also decreased in this occasion. Table 6.6 clarifies the rate of decreasing which is higher for hybrid nanocomposite as 52.19% than the usual one measured as 44.85%

Consequences of magnetic parameter are shown in image Figure 6.4 and 6.5. At first we observe the effect of magnetic parameter for nanofluid and hybrid nanofluid under nonlinear radiation. It is clear that as the values of M increases the temperature gets decrease and the clear pictorial view is found inside $0 \le \eta \le 6$ (not quite exactly determined). A Lorentz Force is created due to electrically conducted suspension flow. It helps to reduce friction force and then the heat generation is reduced but comparatively hybrid nanofluid gets more magnitude of $\theta(\eta)$ than that of ordinary nanofluid due to its existence of double particles in the suspension which consumes some extra heat. From Table 6.7 it is clear that higher increment in magnetic parameter gives higher heat transport rate. For nanofluid, it is changed as 42.71% whereas hybrid nanofluid gives the same at 52.97% which is significant. Next, we consider the effect of magnetic field on hybrid nanofluid under linear and nonlinear radiation. Here also the heat generation cuts down for increasing magnetic field for linear and nonlinear radiation both. But compared to linear, we get higher magnitude of $\theta(\eta)$ in case of nonlinear radiation which is clearly viewed in the region $0 \le \eta \le 6$. From Table 6.8 it is clear that here also rate of heat transport amplifies as the magnetic field is enriched. Linear radiation gives 39.79% heat transport rate while nonlinear radiation gives the same as 36.58%. Lower heat transport rate is observed for nonlinear radiation. But elevated

heat transport magnitude is assured for nonlinear radiation. Also, hybrid nanocomposite sustains maximum heat transfer as compared to unitary nanosolution.

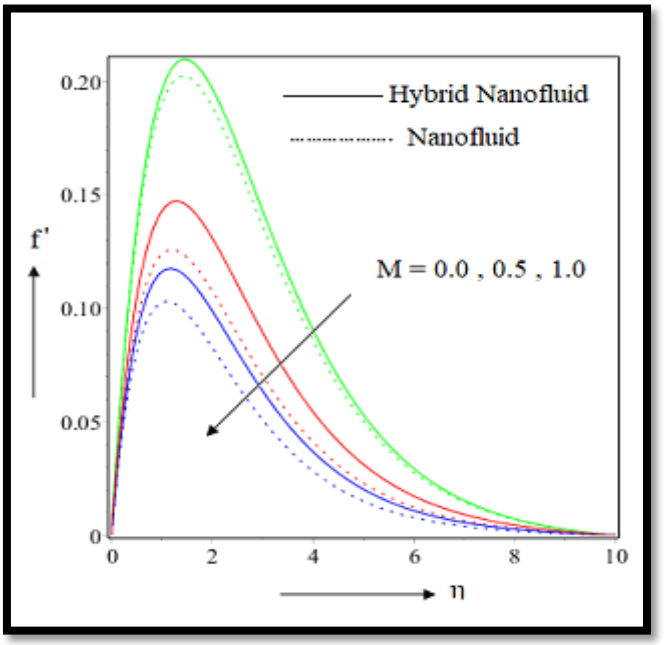

Figure 6.2: Magnetic parameter effect on radial velocity.

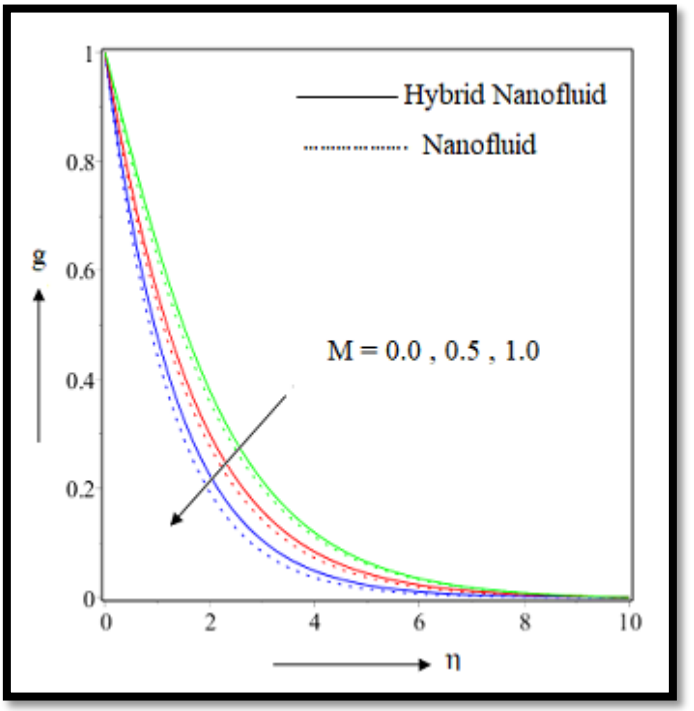

Figure 6.3: Magnetic parameter effect on cross-radial velocity.

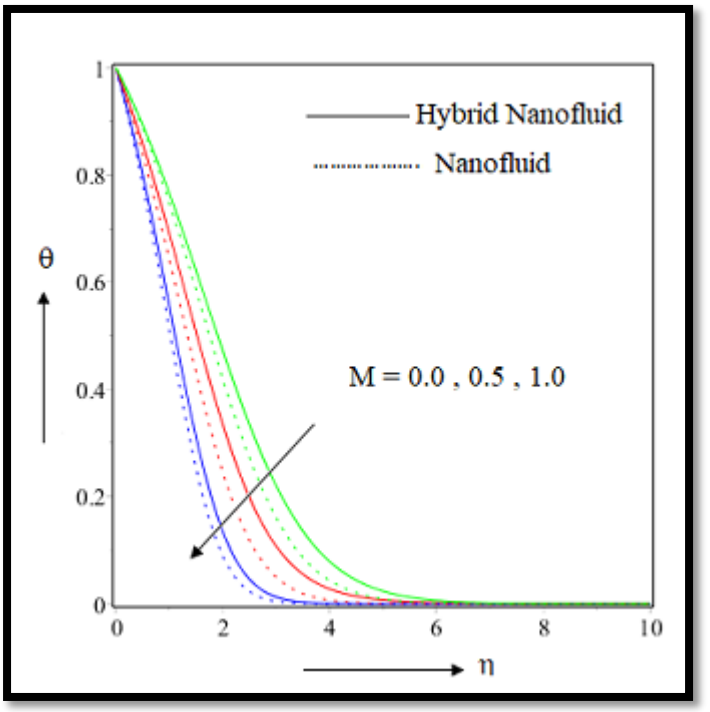

Figure 6.4: Magnetic parameter effect on temperature of hybrid vs. usual nanofluid

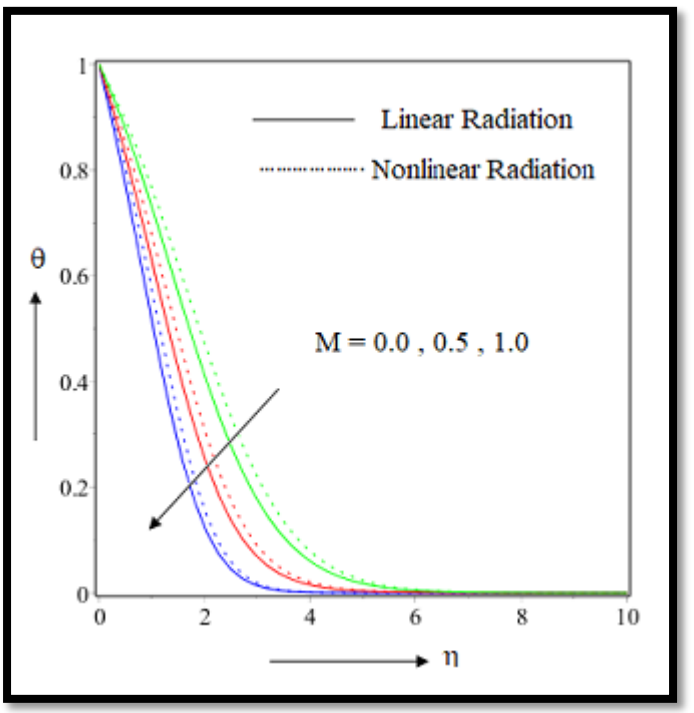

Figure 6.5: Magnetic parameter effect on temperature of linear vs. nonlinear radiation.

6.4.2. Effect of radiation parameter N

In this section, we will discuss the obtained result for variation of radiation parameter. As the rate of radiation gets increased the magnitude of heat i.e. $\theta(\eta)$. So under nonlinear radiation, thermal magnitude of the hybrid nanofluid is getting more increment than that of usual nanofluid in Figure 6.6. Clear view is shown inside $0.0 \le \eta \le 5.0$ (not accurately determined). Physically, intensified radiation connotes faster Brownian movement and thus random migrating tendency results more molecular collision. Thus arousing frictional symptom augments the thermal effect. Nanofluid loses more heat than hybrid nanofluid which is reflected on the graph. From the table of Nusselt number i.e. Table 6.7; it is evident that the accretion in radiation parameter gives higher heat transfer rate which is almost double. Here hybrid nanofluid gives higher heat transmission rate than that of nanofluid. We get an interesting result when the comparison is done over linear and nonlinear radiation in Figure 6.7. The hybrid nanosuspension is taken into account and the value of radiation parameter is varied diversely. Observation is found that temperature is improved for improvement of radiation but nonlinear radiation comparatively gives higher magnitude of $\theta(\eta)$ than that of linear radiation. Increment in radiation parameter provides higher heat transport rate which is confirmed by Table 6.8. Linear radiation gives it at the rate of 64.47% but nonlinear radiation surprisingly increases it almost 2.5 times i.e. the rate goes beyond the expectation.

6.4.3. Effect of Prandtl number Pr

Fascinating result comes during the study of Prandtl number effect over the hybrid nanofluid. The velocity equations are free from $\Pr$, but temperature profile depends upon Prandtl number. The dimensionless temperature is varying inversely in Figure 6.8. Clear field of vision is within $1.0 \le \eta \le 6.0$ (approximately determined). Heat transport amplifies in both cases as in Table 6.7. But hybrid nanofluid temperature decreasing rate is higher than that of nanofluid. In case of comparison between linear and nonlinear radiation the results remain unaltered for both the nanofluid and hybrid nanofluid, i.e. temperature reduces as Prandtl number decreases in Figure 6.9. Here nonlinear radiation gives elevated magnitude of temperature than linear radiation. Transparent view is seen in $2.0 \le \eta \le 6.0$ (not precisely determined). Table 6.8 exhibits reduction in heat transmission.

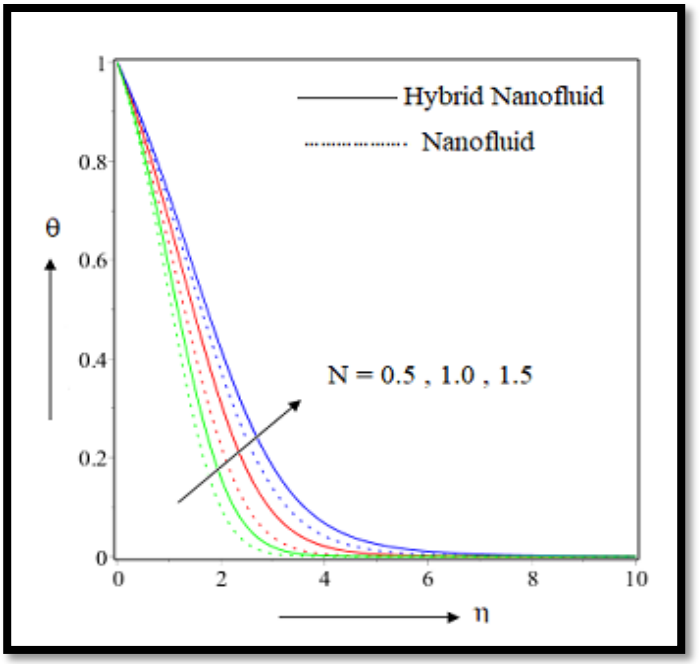

Figure 6.6: Radiation parameter effect on temperature of hybrid vs. usual nanofluid.

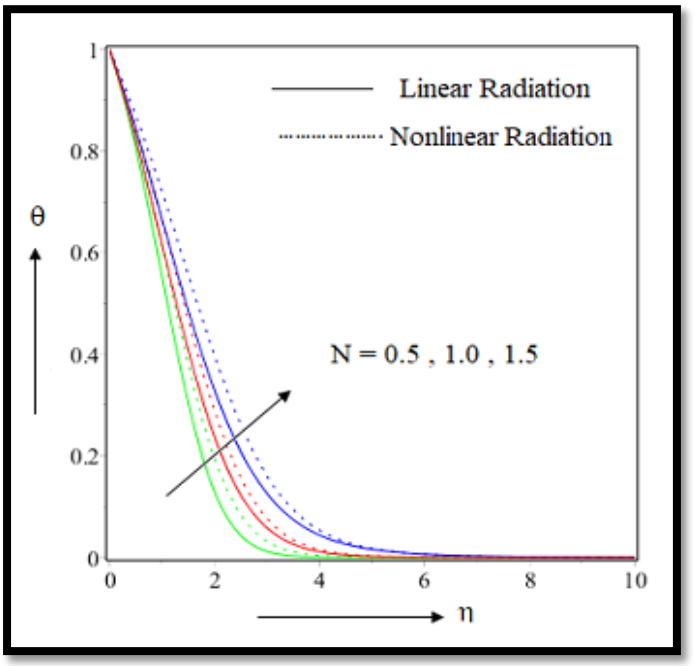

Figure 6.7: Radiation parameter effect on temperature of linear vs. nonlinear radiation.

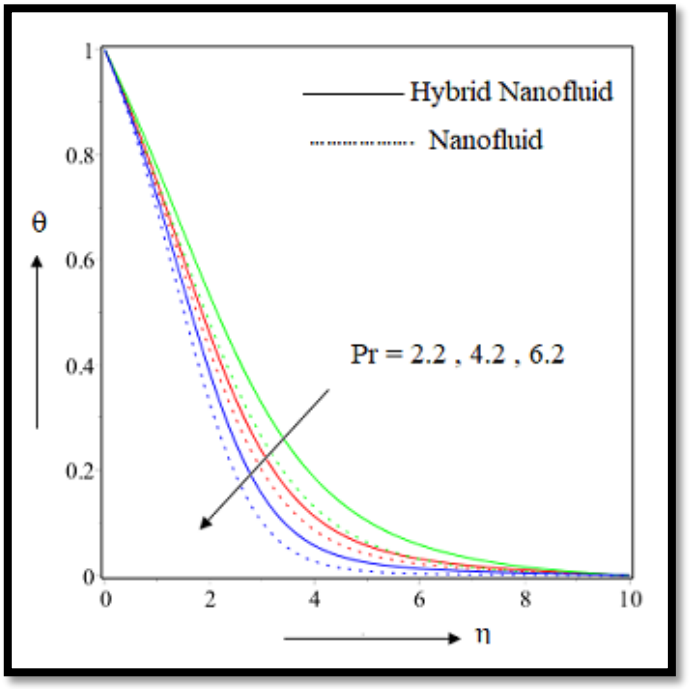

Figure 6.8: Prandtl number effect on temperature of hybrid vs. usual nanofluid.

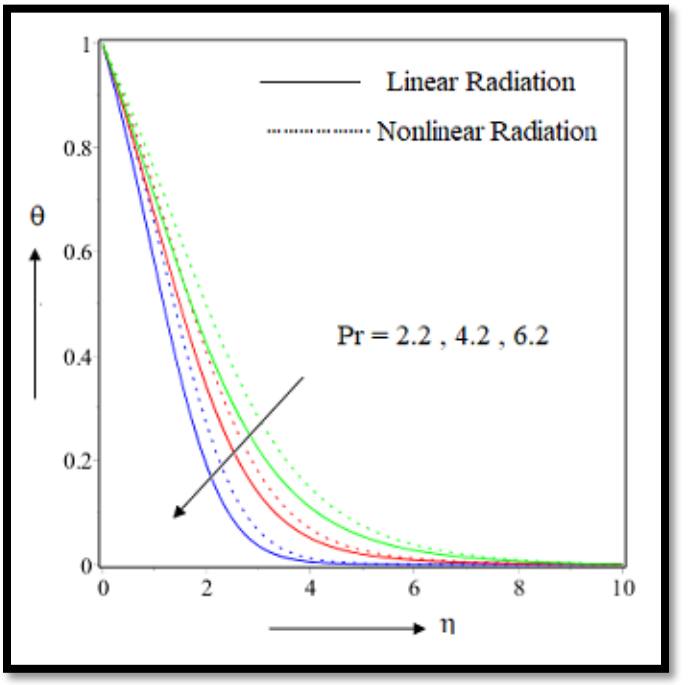

Figure 6.9: Prandtl number effect on temperature of linear vs. nonlinear radiation.

6.4.4. Effect of suction and injection parameter f_w

Consequences of suction and injection specification on velocity outline are shown in Figure 6.10. High amplification in suction parameter has the property to send the liquid into unoccupied or vacant space which cause the enhancement in velocity for both nanofluid i.e. TiO_2 water and hybrid nanofluid i.e. TiO_2 and $CoFe_2O_4$ water. Precise outcome has been perceived in $0.5 \le \eta \le 5.0$ (not quite exactly determined). Interesting fact is that the hybrid nanofluid displays higher magnitude in radial velocity than velocity of nanofluid. For injection we perceive reverse outcome. Skin friction for radial velocity increases as we increase the value of f_w. The rate of increment of Cf_r is quite higher for the usual nanosuspension. The calculation from the data in Table 6.5 gives us the rate for hybrid nanofluid is 8.97% compared to that of nanofluid is 15.06%. Cross radial velocity shows the same nature like radial velocity with equivalent reason. In this instance we observe the hike is comparatively lower than radial velocity. Prominent observation is found a little away from the surface. Hybrid nanosuspension has higher magnitude in velocity g than that of nanosuspension. Both the curves converge asymptotically far away from the surface. The details analysis graphically displayed in Figure 6.11. Skin friction for cross radial velocity is elevated as we inflated the value of f_w. Rate of elevation of ordinary nanofluid is lower 14.05% than hybrid nanofluid 15.16%. Table 6.6 establishes the truth.

We get an outstanding result when diversity of suction injection parameter came into account. In case of negative values of f_w as we increase the modulus the temperature profile decreases in Figure 6.12. It helps to lower the temperature magnitude but in case of hybrid nanofluid the magnitude is little higher than that of nanofluid. The observation stands highly in $0.0 \le \eta \le 3.0$. As the rate is increased i.e. from 0.0 to -0.2 and onwards the rate of transport of heat increased. Nanofluid covers it at the rate 49.72% while the hybrid nanofluid cover is with only 47.16%. The lower heat transport rate is significant in this segment which is confirmed in Table 6.7. When the comparison is done in between linear and nonlinear radiation we get same results that are higher magnitude of f_w gives lower temperature in Figure 6.13. Nonlinear radiation gives higher magnitude than that of linear radiation. Now it highly stands on the same interval $0.0 \le \eta \le 3.0$. From Table 6.8 we get a concept on linear and nonlinear radiation effect. The heat delivering rate

here also increased. Linear radiation delivers it at 56.97% whereas nonlinear radiation delivers it at the rate of 47.16%. Lower the heat deliver rate observed in case of nonlinear radiation.

Positive values of f_w gives opposite result in Figure 6.14. Increment in magnitude of f_w also increase the temperature. Perception becomes acceptable in $0.0 \le \eta \le 4.0$. Hybrid nanofluid is higher in magnitude than that of nanofluid. From Table 6.7 it is apparent that heat shifting rate decrease for both nanofluid and hybrid nanofluid with higher rate of suction. Nanofluid shifted heat at the rate of 37.38% but hybrid nanofluid shift the heat comparatively slow rate i.e. 35.49% only. When the comparison is done between linear and nonlinear radiation we observe the same result, i.e. the higher magnitude of f_w gives higher magnitude of temperature. Temperature magnitude is higher for nonlinear radiation than that of linear radiation in Figure 6.15. It can be lucidly perceive. Table 6.8 confirms that in case of linear and nonlinear radiation also rate of heat transport is lower as we increase the rate of suction. Interestingly here also nonlinear radiation gives lower heat transport rate. As per data the rate for nonlinear radiation it is 44.71% while for linear radiation it is 38.48%.

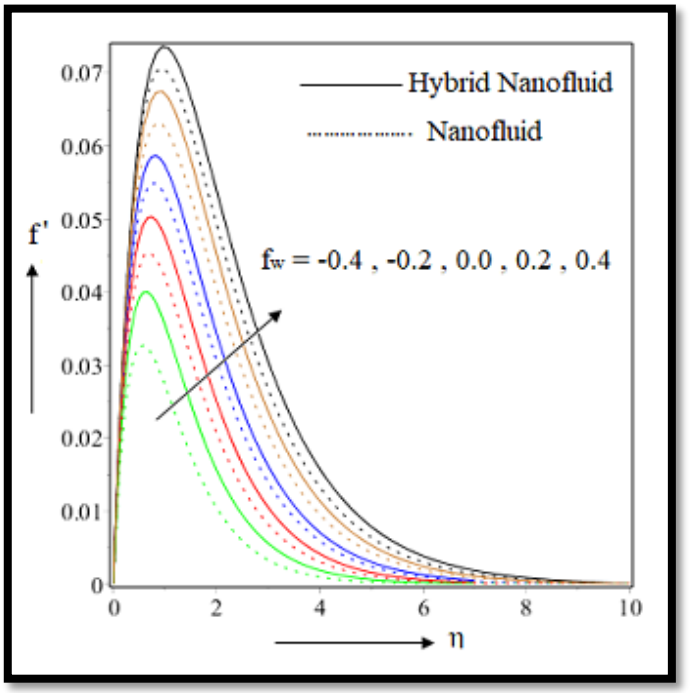

Figure 6.10: Suction/Injection parameter effect on radial velocity.

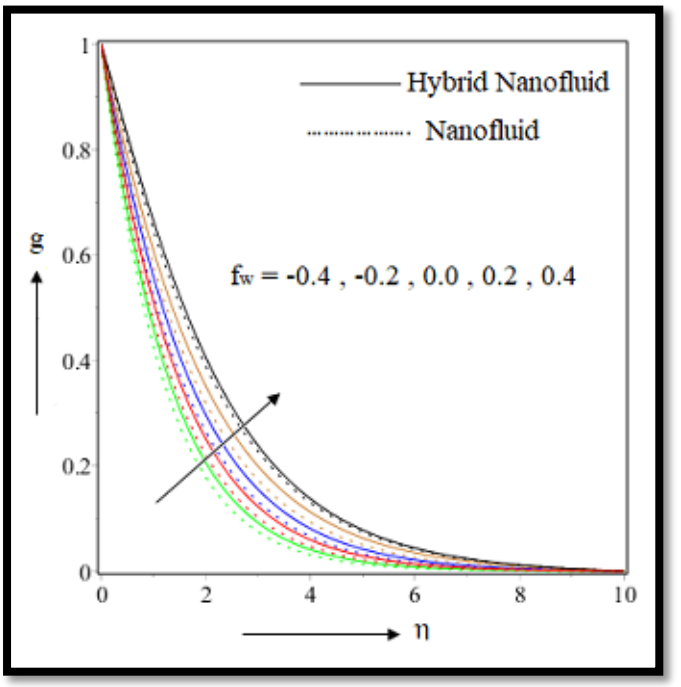

Figure 6.11: Suction/Injection parameter effect on cross-radial velocity

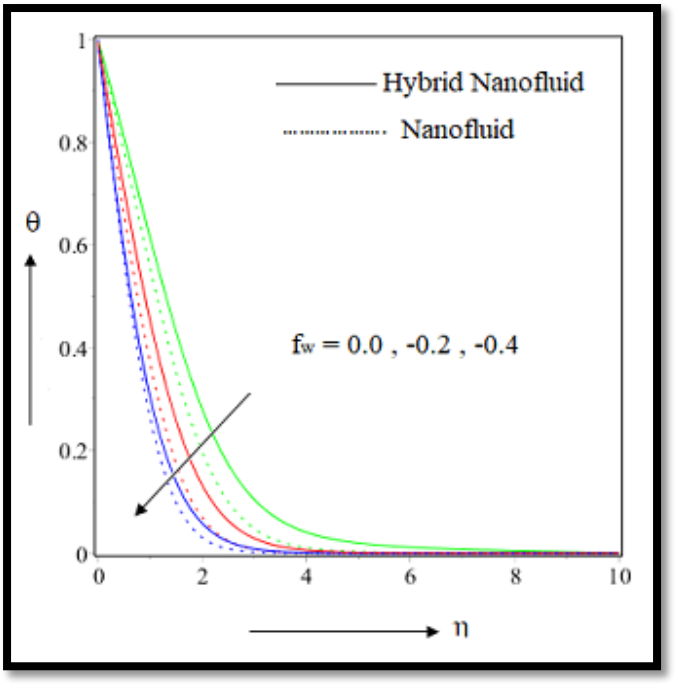

Figure 6.12: Injection parameter effect on temperature of hybrid vs. usual nanofluid.

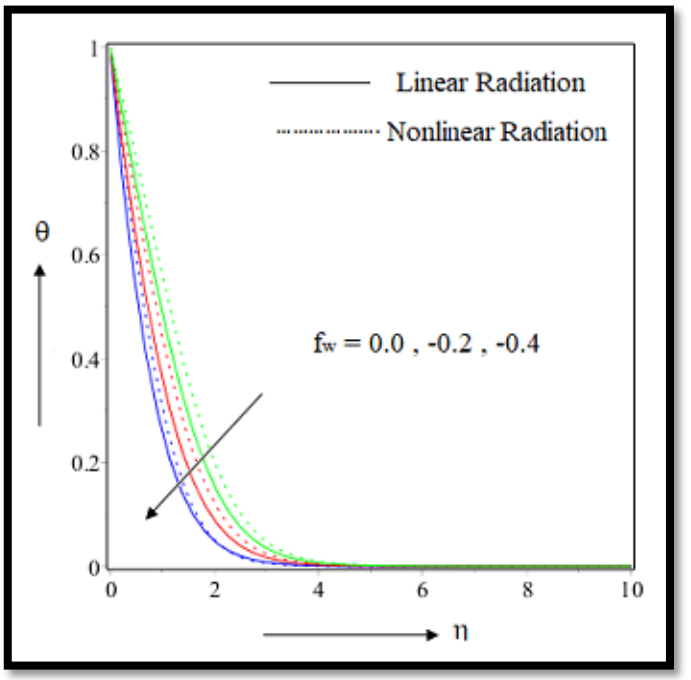

Figure 6.13: Injection parameter effect on temperature of linear vs. nonlinear radiation.

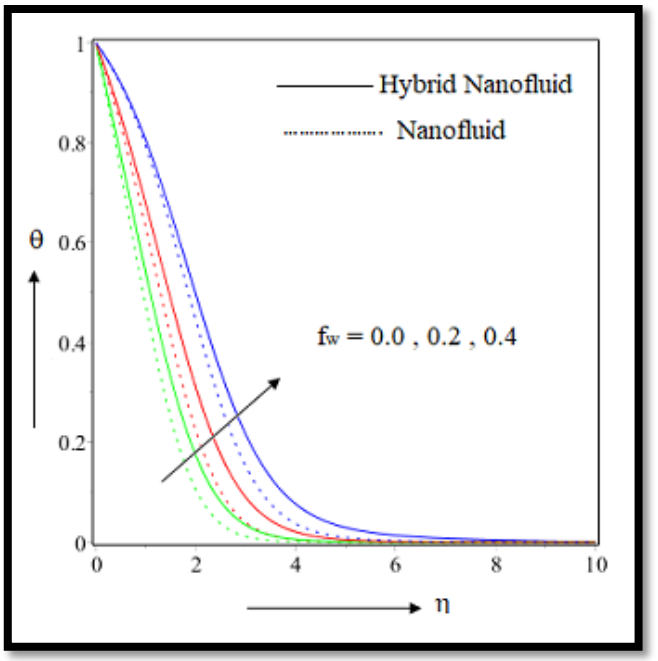

Figure 6.14: Suction parameter effect on temperature of hybrid vs. usual nanofluid.

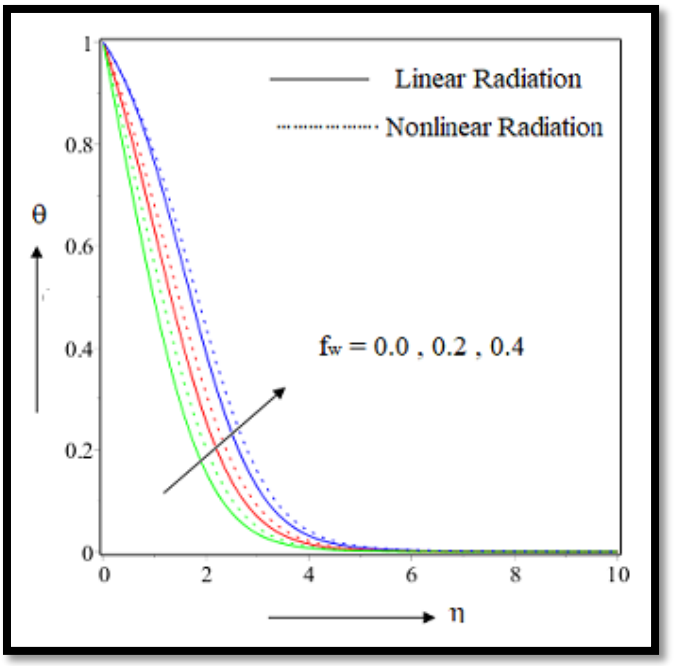

Figure 6.15: Suction parameter effect on temperature of linear vs. nonlinear radiation.

6.4.5. Effect of volume fraction ϕ_1

The concentration profile of the suspension gives different result for velocity f'. The hike in concentration of fluid results the hike in speed of the fluid which is shown in Figure 6.16. Both nanosuspension and hybrid nanosuspension give same result but the magnitude of dimensionless velocity of composite nanofluid is higher than that of nanofluid. Clear view is observed near the surface beyond that we see asymptotic convergence. An important result is that the velocity increases very high near to the surface and away from surface the curve became very steep. The radial skin friction goes higher as we increase the concentration profile of the suspension. The hybrid nanoliquid is also get increased as nanoliquid but rate of increment is too slower than nanocomposite. From Table 6.5 we get 16.28% is the rate foe nanosuspension whereas only 2.83% for hybrid nanosuspension. Nature of cross radial velocity due to change in concentration profile is viewed in Figure 6.17. The cross radial velocity is hiked as we increase the concentration of the suspension. Precise difference is observed in $1 \le \eta \le 4$ (not quite exactly determined). Asymptotical convergence also occurs far away from the surface. Magnitude of velocity g is

comparatively higher for the hybrid nanosuspension. Cg_r Value for this purpose also hiked as per hike in concentration. Cross radial drag friction's hiking rate is slower for hybrid nanoliquid (14.61%) than that of nanoliquid (18.82%). Table 6.6 confirms the result stated above.

Volume fraction plays an important role for temperature factor. It is clearly seen that higher rate of ϕ_1 gives higher temperature in Figure 6.18. The More we concentrate the suspension more particle come into action and their friction generate temperature. A clear and transparent graphical view is shown within $1.0 \le \eta \le 4.0$ (not quite exactly determined). The hybrid suspension gives more magnitude than usual nanosuspension as the number of particles present in hybrid suspension is greater than that of nanosuspension. Hence, frictional force is provoked and which is reflected in the temperature. Higher concentration within the fluid gives higher heat transport rate. This is clear from the data in Table 6.7 that hybrid nanofluid gives increment in heat transport rate. Mono nanofluid changes it at 3.40% whereas hybrid nanofluid changes it at 3.79%.

Relevance between linear and nonlinear radiation is also done with attention. Here also higher concentration gives higher temperature profile in Figure 6.19. The reason is same as in the above case but here we observe that nonlinear radiation gives higher magnitude in temperature than linear radiation. Clear illustration is shown inside $1.0 \le \eta \le 3.5$. In case of linear and nonlinear radiation, we get different result that is clearly detectable through Table 6.8. Higher concentration of immersed nanoparticles gives lower heat transport rate. For nonlinear radiation transport rate is 7.73% that appears to be little higher than that of linear radiation rate i.e. 7.61%.

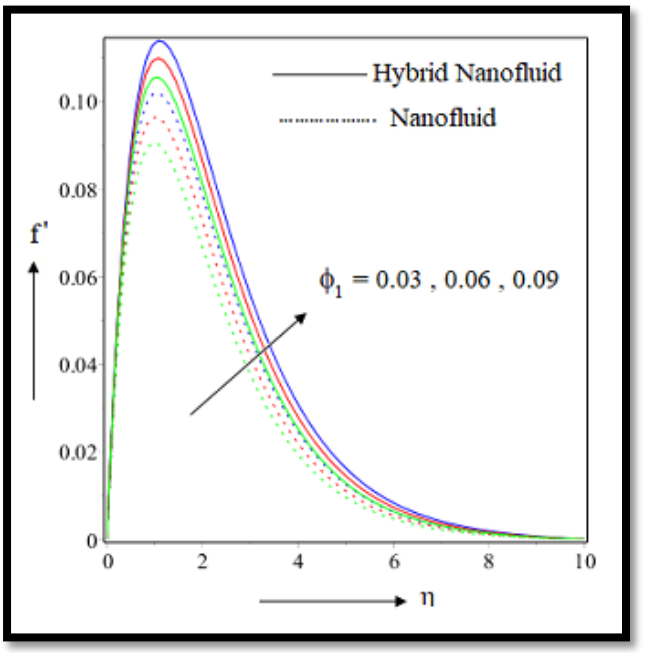

Figure 6.16: Effect of volume fraction on radial velocity.

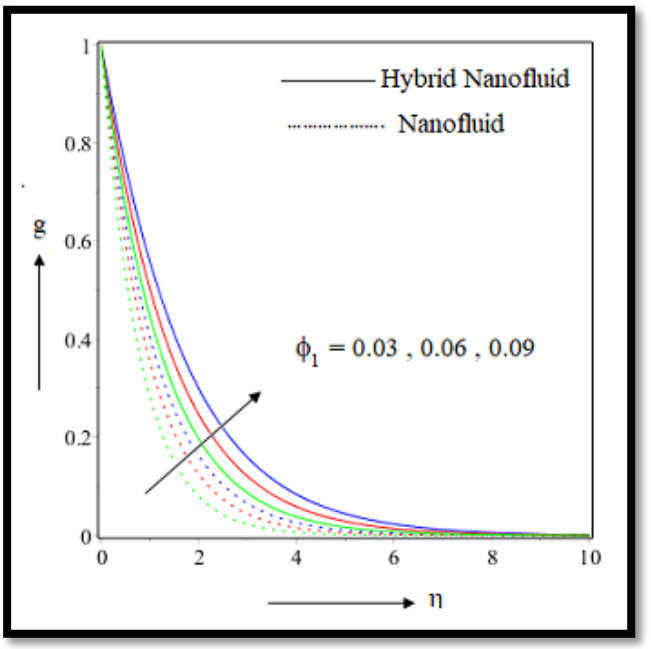

Figure 6.17: Effect of volume fraction on cross-radial velocity.

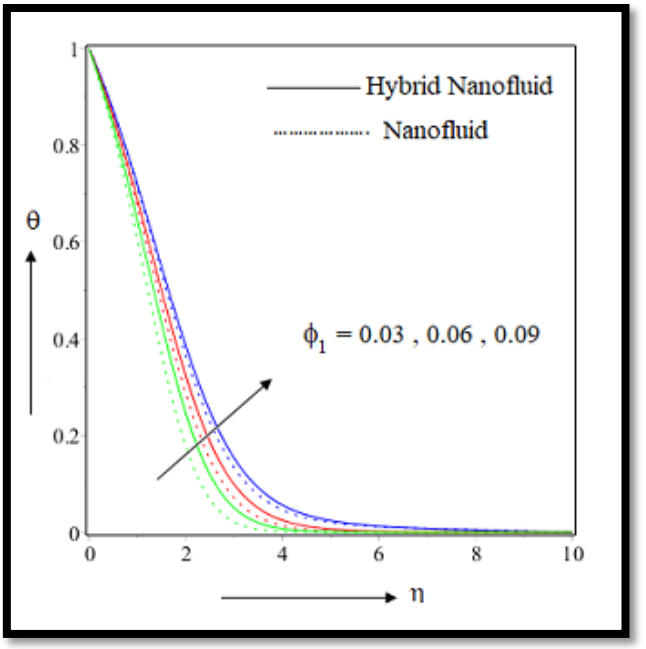

Figure 6.18: Volume fraction on thermal features of hybrid vs. usual nanofluid.

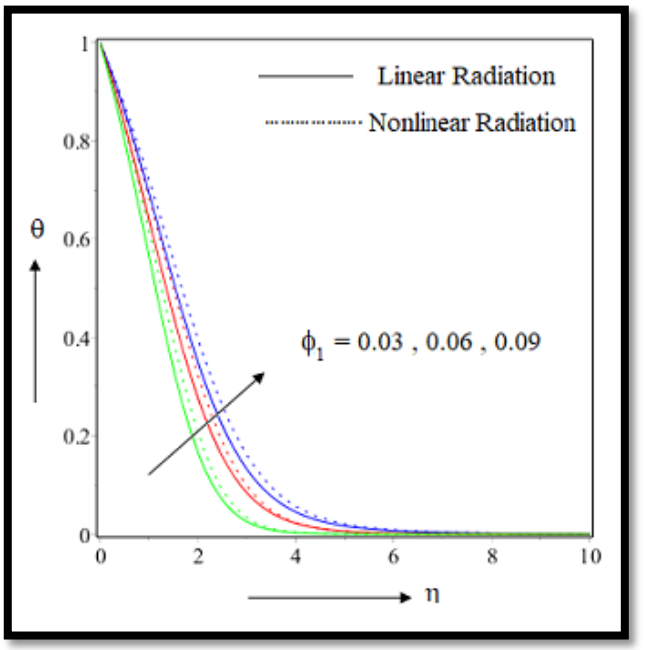

Figure 6.19: Volume fraction on temperature of linear vs. nonlinear radiation.

6.5. Conclusion

In this study, we have given attention to visualize the hydrothermal profile of a hybrid nanofluid over a radiative spinning disk. Both linear and nonlinear radiation is taken to collate the results. The regulating equations are transfigured by similarity transformations and then solved numerically by RK-4 mechanism. We observed that the effect of linear and nonlinear radiation is quite different for the system, and gives diverse temperature magnitude. Furthermore, the comparison between hybrid nanosuspension and unitary nanosuspension is also done. There is also disparate effect for various specific parameters. They accord discrete results on temperature outline. Assorted parameters like magnetic, radiation, concentration, Prandtl number, suction and injection are casted off to study the effects diversely. The results are established by graphs and tabulated format to accord a clear observation on the results. The whole study is dedicatedly framed over temperature portrait for various parameters in a hybrid nanocomposite configuration. In our whole research we shot out the following consequences.

- For Magnetic parameter M we get lower velocity profiles for radial and cross radial directions.
- The upshot of concentration parameter ϕ_1 and suction parameter $f_w > 0.0$ exhibit increasing property for both radial and cross radial velocity outline, whereas injection $f_w < 0.0$ discloses reverse traits.
- For M, N, Pr, $f_w < 0.0$ we get higher transport rate in heat whereas for $f_w > 0.0$ and ϕ_1 we get lower heat transport rate. This holds accurate for both nanoliquids.
- The same is observed for linear and nonlinear radiation only the parameter Pr gives reverse result.
- Double particle suspension amplifies the thermal efficiency than that of single particle.
- Magnetic parameter increases the heat transport at 36.58% and 42.71% for nonlinear radiation and hybrid nanosuspension respectively.
- Nonlinear radiation gives higher heat transport rate and for parameter N it is almost double. This result is very significant for comparison between linear and nonlinear radiation.

Table 6.5: Effect of pertinent parameters on radial skin friction

M	ϕ_1	f_w	Cf_r *nonlinear radiation*	
			hybrid nanofluid	*nanofluid*
0.0	0.09	0.2	0.426719	0.401246
0.5			0.345287	0.312468
1.0			0.294568	0.261298
0.5	0.03		0.352394	0.314562
	0.06		0.365612	0.326587
	0.09		0.372651	0.332197
	0.09	-0.4	0.245546	0.174432
		-0.2	0.253359	0.200125
		0.0	0.267745	0.216658
		0.2	0.272566	0.224788
		0.4	0.279544	0.231534

Table 6.6: Effect of pertinent parameters on cross radial skin friction

M	ϕ_1	f_w	Cg_r *nonlinear radiation*	
			hybrid nanofluid	*nanofluid*
0.00	0.09	0.2	-0.625532	-0.675548
0.5			-0.845687	-0.877956
1.0			-1.177895	-1.216647
0.5	0.03		-1.166444	-1.855521
	0.06		-1.001178	-1.600214
	0.09		-0.899547	-1.344178
	0.09	-0.4	-1.277214	-1.266458
		-0.2	-1.008774	-1.000473
		0.0	-0.882619	-0.960025
		0.2	-0.721655	-0.814459
		0.4	-0.611472	-0.722154

Table 6.7: Effects of pertinent parameters on heat transport hybrid vs. usual nanofluid

M	N	f_w	ϕ_1	Pr	Nu_r *nonlinear radiation*	
					hybrid nanofluid	*nanofluid*
0.0	0.5	0.2	0.09	6.2	0.778451	0.642354
0.5					1.011457	1.001124
1.0					1.418528	1.201007
0.5	0.5				0.600784	0.588724
	1.0				1.322156	1.114727
	1.5				1.868454	1.485584
	0.5	-0.4			2.966246	2.988451
		-0.2			2.277851	2.214478
		0.0			1.701123	1.549985
		0.2			1.002243	1.011471
		0.4			0.704108	0.599675
		0.2	0.03		0.994712	0.911452
			0.06		0.944578	0.899747
			0.09		0.912201	0.841213
			0.09	2.2	0.8142251	0.745991
				4.2	0.912265	0.894782
				6.2	1.122635	1.007451

Table 6.8: Effects of pertinent parameters on heat transport nonlinear vs. linear radiation

M	N	f_w	ϕ_1	Pr	Nu_r *hybrid nanofluid*	
					nonlinear radiation	*linear radiation*
0.0	0.5	0.2	0.09	6.2	0.599214	0.426445
0.5					0.833216	0.625879
1.0					1.145215	0.841213
0.5	0.5				0.311456	0.388745
	1.0				0.899457	0.688121
	1.5				1.194977	0.877582
	0.5	-0.4			2.584964	2.578891
		-0.2			2.097771	1.994561
		0.0			1.385214	1.216698
		0.2			0.788946	0.623541
		0.4			0.411236	0.296654
		0.2	0.03		0.874632	0.622456
			0.06		0.794451	0.544632
			0.09		0.697124	0.400156
			0.09	2.2	0.645512	0.554129
				4.2	0.201464	0.198663
				6.2	0.100964	0.115627

CHAPTER 7

Influence of second order slip and multiple convective conditions on magnetized nanofluid flow over a permeable stretching cylinder*

7.1. Introduction

In this research investigation is done for second order slip effect with multiple convective conditions over a permeable stretching cylinder. Radiation and suction/injection effect are also taken into account. We have taken magnetic field, Brownian notion and thermophoresis in our model. Leading equations are transformed into non linear ODEs by suitable similarity transformation and simulated by MAPLE-2019 software to obtain proper graphs and tables related to various parameters. Convective condition over nanofluid plays an important role. Slip condition also have diverse effect on heat and mass transfer. We believe that our novel and unique attempt will serve the field of science and technology. The core research topics that we are looking for to the entire investigation are prescribed below:

- The changes of velocity profile when the related flow parameters are varied and also the effect of suction and injection phenomena on the flow lines.
- The changes of thermal profile when the related flow parameters are varied and also the effect of suction and injection profile on the flow lines.
- The changes of concentration profile when the related flow parameters are varied and also the effect of suction injection parameter on the concentration lines.

***This chapter is based on the paper published in: International Journal of Modern Physics B, 37(30) (2023), 2350270, (SCIE).**

7.2. Mathematical formulation

7.2.1. Governing equations

Let us consider a steady incompressible laminar flow of nanofluid over a stretching cylinder. Where velocity u along r axis which is measured along radial direction and w along z axis which is along axial direction. Radius of the cylinder taken as b. In Fig (1) the physical geometry of the system is described. A magnetic influence $B = B_0$ is admitted in the radial direction. Velocity slip of second order is considered in the system. Thermal radiation effect is taken into account but we have assumed that there is no chemical reaction between nanoparticles and base fluid. Brownian migration and thermophoresis effect are also incorporated in the flow. Magnetic Reynolds number admitted in this study is so small that influence of induced magnetic field become negligible. Hall effects Ohmic heating and viscous dissipation is omitted in this inspection. Under these assumptions, the governing equations [139-144] are

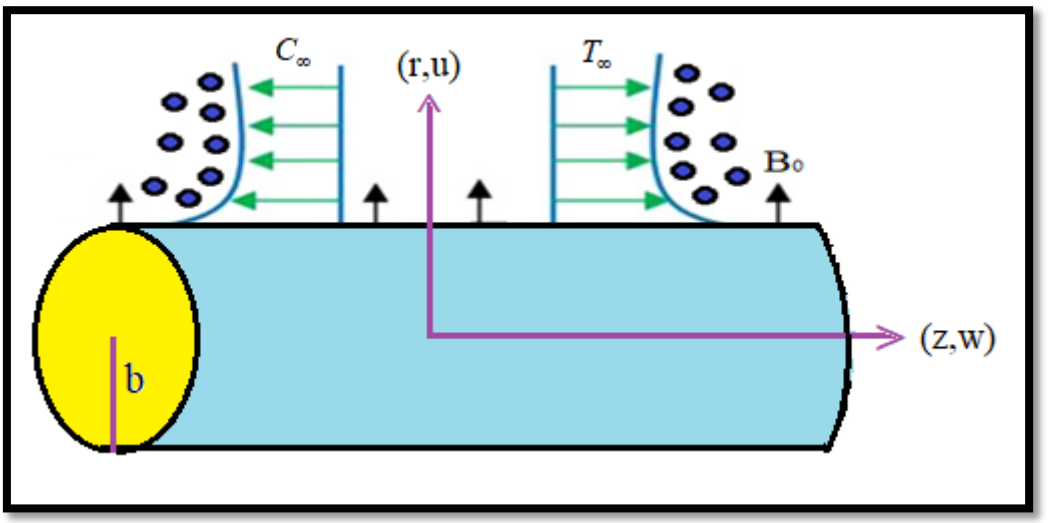

Figure 7.1: Physical geometry of the flow.

$$\frac{\partial}{\partial z}(rw)+\frac{\partial}{\partial r}(ru)=0 \tag{7.1}$$

$$\rho_f\left(w\frac{\partial w}{\partial z}+u\frac{\partial w}{\partial r}\right)=\mu_f\left(\frac{\partial^2 w}{\partial z^2}+\frac{1}{r}\frac{\partial w}{\partial r}\right)-\sigma_f B_0^2 w \tag{7.2}$$

$$\rho_f\left(w\frac{\partial u}{\partial z}+u\frac{\partial u}{\partial r}\right)=-\frac{\partial p}{\partial r}+\mu_f\left(\frac{\partial^2 u}{\partial r^2}+\frac{1}{r}\frac{\partial u}{\partial r}-\frac{u}{r^2}\right) \tag{7.3}$$

$$\left(\rho C_p\right)_f\left(w\frac{\partial T}{\partial z}+u\frac{\partial T}{\partial r}\right)=\kappa_f\left(\frac{\partial^2 T}{\partial r^2}+\frac{1}{r}\frac{\partial T}{\partial r}\right)-\frac{\partial q}{\partial r}+\tau\left[D_B\frac{\partial C}{\partial r}\frac{\partial T}{\partial r}+\frac{D_T}{T_\infty}\left(\frac{\partial T}{\partial r}\right)^2\right] \tag{7.4}$$

$$\left(w\frac{\partial C}{\partial z}+u\frac{\partial C}{\partial r}\right)=D_B\left(\frac{1}{r}\frac{\partial}{\partial r}\left(r\frac{\partial C}{\partial r}\right)\right)+\frac{D_T}{T_\infty}\left(\frac{1}{r}\frac{\partial}{\partial r}\left(r\frac{\partial T}{\partial r}\right)\right) \tag{7.5}$$

Radiative heat flux is simplified by Rosseland approximation and the reduced expression is given below. $\frac{\partial q}{\partial r}=-\frac{4\sigma^*}{3\kappa^*}\frac{\partial T^4}{\partial r}=-\frac{16\sigma^*}{3\kappa^*}T^3\frac{\partial T}{\partial r}$ Where the term T^4 is linearized by Taylor series about T_∞ by $T^4\cong 4T_\infty^3T-3T_\infty^4$.

7.2.2. Boundary conditions

The boundary provisions [139-144] for the above introduced model are given by the following equations:

$$u=u_w, w=w_w+w_{slip}, -\kappa_f\frac{\partial T}{\partial r}=h_f\left(T_f-T_\infty\right), -D_m\frac{\partial C}{\partial r}=h_m\left(C_f-C_\infty\right) \text{ at } r=b \tag{7.6}$$

$$w\to 0, T\to T_\infty, C\to C_\infty \text{ at } r\to\infty \tag{7.7}$$

Where u and w are the velocity components along the r and z axes respectively. Velocity slip is reported by Nandeppanavar [235] given by

$$w_{slip}=\frac{2}{3}\left(\frac{3-\alpha l^2}{\alpha}-\frac{3}{2}\frac{1-l^2}{K_n}\right)\beta\frac{\partial w}{\partial r}-\frac{1}{4}\left(l^4+\frac{2}{K_n^2}\left(1-l^2\right)\right)\beta^2\frac{\partial^2 w}{\partial r^2}=A^*\frac{\partial w}{\partial r}+B^*\frac{\partial^2 w}{\partial r^2} \tag{7.8}$$

Where $l=Min\left(\frac{1}{K_n},1\right)$, α stands for momentum accommodation coefficient with its property $0\le\alpha\le 1$. Free molecular path is denoted by β. Kundsen number K_n signified by $K_n=\frac{\beta}{L}$ where $0\le L<1$. Here $A^*>0$ and $B^*<0$ are constants. $u_{slip_{wall}}=g\frac{2-\alpha_1}{\alpha_1}\lambda\left.\frac{\partial u}{\partial y}\right|_{y=wall}$ is the expression of 1st order slip approximation. g is a constant. Higher order terms are rejected for 1st order slip calculations. When local Kundsen number tends towards unity the second order

slip term cannot be ignored. Amplification of the velocity slip effect is the main outcome. [145,146] u_w represents the suction/injection parameter. $w_w = 2az$ where a is a positive constant. We presumed the bottom section temperature of the fluid is T_f. Heat transmission coefficient and Thermal conductivity is denoted as h_f and k_f. h_m and D_m stand for wall mass transfer coefficient and thermal diffusivity.

7.2.3. Similarity transformations

We convert the foremost flow equations (7.1-7.5) into system of ODEs by the following similarity variables as in [147]

$$u = -\frac{abf(\eta)}{\sqrt{\eta}}\ ,\ w = 2azf'(\eta)\ ,\ \theta(\eta) = \frac{T - T_\infty}{T_f - T_\infty}\ ,\ \phi(\eta) = \frac{C - C_\infty}{C_f - C_\infty}$$
$$\eta = \left(\frac{r}{b}\right)^2 \qquad (7.9)$$

After needed modernization equation (7.1) satisfies automatically. After dropping pressure Equation (7.2) and (7.5) changed as follows.

$$\eta f''' + f'' + \mathrm{Re}\left(ff'' - f'^2\right) - Mf' = 0 \qquad (7.10)$$

$$(1 + \frac{4}{3}Rd)\left(\eta\theta'' + \theta'\right) + \mathrm{Re}\,\mathrm{Pr}\ f\theta' + \eta\left(Nb\theta'\phi' + Nt\theta'^2\right) = 0 \qquad (7.11)$$

$$\eta\phi'' + \left(\frac{1}{2} + \mathrm{Re}\,Scf\right)\phi' + \frac{Nt}{Nb}\left(\frac{1}{2}\theta' + \eta\theta''\right) = 0 \qquad (7.12)$$

Corresponding boundary equations are also changed as follows.

$$f(1) = S,\ f'(1) = 1 + \delta f''(1) + \gamma f'''(1), \theta'(1) = -Bi_t\left(1 - \theta(1)\right), \phi'(1) = -Bi_m\left(1 - \phi(1)\right) \quad \text{at } r = b$$

(7.13)

$$f'(\infty) = 0, \theta(\infty) = 0, \phi(\infty) = 0 \text{ at } r = \infty \qquad (7.14)$$

Suction and injection features are represented by $S > 0$ and $S < 0$

7.2.4. Physical quantities

We also calculate the physical quantities which is noteworthy for engineering applications.

$$\left.\begin{aligned} C_f &= \frac{2\tau_w}{\rho w_w^2} \text{ where } \tau_w = \mu_f \left(\frac{\partial w}{\partial r}\right)_{r=b} \\ Nu &= \frac{aq_w}{\kappa_f \left(T_f - T_\infty\right)} \text{ where } q_w = \kappa_f \left(\left(1+\frac{16\sigma^* T_\infty^3}{3\kappa^* \kappa_f}\right)\frac{\partial T}{\partial r}\right)_{r=b} \\ Sh &= \frac{aq_m}{D_B \left(C_f - C_\infty\right)} \text{ where } q_m = -D_B \left(\frac{\partial C}{\partial r}\right)_{r=b} \end{aligned}\right\} \quad (7.15)$$

τ_{rs}, q_w, j_w Designates surface shear stress, heat flux and mass flux respectively.

Registering similarity variables on the above equations, we came into the reduced parameters as

$$\left.C_{f_r} = f''(1), Nu_r = -\left(1+\frac{4}{3}Rd\right)\theta'(1), Sh_r = -\phi'(1)\right\} \quad (7.16)$$

7.3. Numerical procedure

7.3.1. Solution technique

The leading equations and corresponding boundary conditions are transformed by similarity transformation. We came to a set of highly non linear ODEs which is very difficult to solve analytically. In this situation numerical framework is used to solve the system. We have employed RK-4 method accompanied by shooting technique to solve the system. MAPLE-2019 software is used to solve the whole simulation. Important outcomes are framed by graphs and tables in proper section. We have taken the exactness of numerical outcome up to 10^{-6}. In our study we found the parameters like $M, S, \mathrm{Re}, Rd, Bi_t, Bi_m, \delta, \gamma, Nb, Nt, \mathrm{Pr}, Sc$ signified as Magnetic parameter, Suction/injection parameter, Reynolds number, Radiation parameter, Thermal and mass Biot number, 1st and 2nd order slip parameter, Brownian migration and thermophoresis parameter, Prandtl number and Schmidt number respectively. There are several researches on Brownian migration, thermophoresis, Prandtl number and Schmidt number so we overlooked the

graphs of this parameter and mainly focus on the remaining parameters. Comparison of the outcomes are done under suction and injection effect.

7.3.2. Code verification

To validate our code we have compared our outcomes with similar type of previous results reported by Wang [121]. We have adjusted the values of $M = 0, Rd = 0, Bi_t = 0, Bi_m = 0$ and neglected the slip effect to compare the results with the preceding consequences. Brownian motion and thermophoresis also derelict in the comparability process. The values of $f''(1)$ is analogized in the Table (7.1) for different values of Reynolds number and found to be matched almost correctly. Table (7.2) designates the comparison of $\theta'(1)$ for separate values of Prandtl number fixing the value of Reynonds number unity.

Table 7.1: Comparison of numerical outcomes of $f''(1)$ with previous studies

Re	**Wang [121]**	**Present Results**
	$f''(1)$	$f''(1)$
0.1	-0.48181	-0.48182
1	-1.17776	-1.17775
2	-1.59390	-1.59391
5	-2.41745	-2.41745
10	-3.34445	-3.34447

Table 7.2: Comparison of numerical outcomes of $\theta'(1)$ with previous studies

Pr	**Wang [121]**	**Present Results**
	$\theta'(1)$	$\theta'(1)$
0.2	-0.2572	-0.25721
0.7	-0.5880	-0.58802
2	-1.0650	-1.06502
7	-2.0590	-2.05901
20	-3.5210	-3.52100

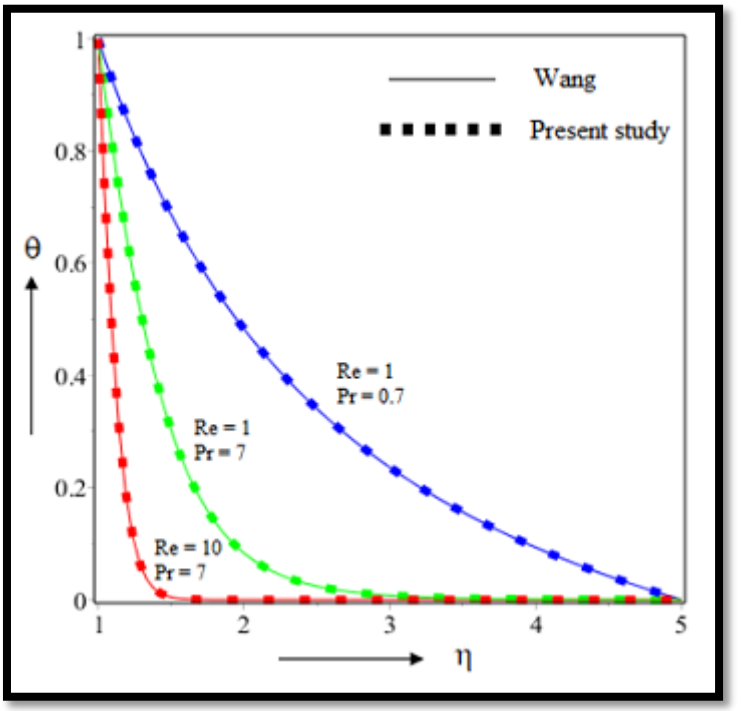

Figure 7.2: Comparison of temperature profile for different value of Reynolds number and Prandtl number.

7.4. Results and discussions

In the subsequent section we have describe the results and findings found in this investigation. The basic values of parameter are taken as $M = 1.5, \mathrm{Re} = 2.0, Rd = 1.0, Bi_t = 0.5, Bi_m = 0.5, \delta = 2.0, \gamma = 1.0, \mathrm{Pr} = 8, Nb = 0.5, Nt = 0.5, Sc = 5$ throughout our study where it is not specified. Upshots of various parameters on velocity lines heat lines and mass lines are described. Our main focus is to compare the upshots under suction and injection effect. Corresponding table of engineering interest is also reported.

7.4.1 Influence of several parameters on velocity

Magnetic parameter influence the velocity profile and it is found from Figure 7.3 that for higher value of magnetic profile velocity goes down. High value of magnetic force create a Lorentz force which executed as obstruction force. Prominent offshoot found in $1 \le \eta \le 6$ after that velocity lines converges asymptotically. From Table 7.3 we get 3.2% demotion in case of suction effect. For injection situation we also get the similar upshots but the magnitude is higher. Reduced skin friction coefficient goes down by 3.86% in this case. Mishra and Kumar [148] also got similar result in their study of MHD nanofluid flow.

Surprisingly Reynolds number gives us different effect for suction and injection. Suction effect reduce the velocity framework but injection effect increase the same. Notable difference is observed for $1 \le \eta \le 4$ beyond this we get asymptotically converged lines in Figure 7.4. For suction effect we get more turbulent flow for higher Reynolds number which is the main reason behind the increment in velocity. Reduced skin friction diminished by 2.52% for under suction effect and increased by 2.68% for injection effect.

Velocity slip parameter of 1st order lessen the velocity profile for both suction and injection effect. 2nd order velocity slip effect does not make any significant effect for higher value but it make difference for suction and injection which is observed in Figure 7.6. Figure 7.5 gives us significant output where we observe the difference in $1 \le \eta \le 5$ beyond that velocity lines converges. Reduced skin friction increased by 5.40% (from Table 7.3) for injection situation than suction effect in presence of second order slip parameter.

We further inspect the effect of suction/injection parameter over velocity lines. As we increase the values of S we get reduced velocity lines. Shifting of parameter value from injection to suction skin friction coefficient also get increased by almost 5% from Table 7.6. Magnification in the parameter value also thinner the boundary layer. Notable difference is observed in $1 \le \eta \le 6$ (not accurately determined) which is found in Figure 7.7.

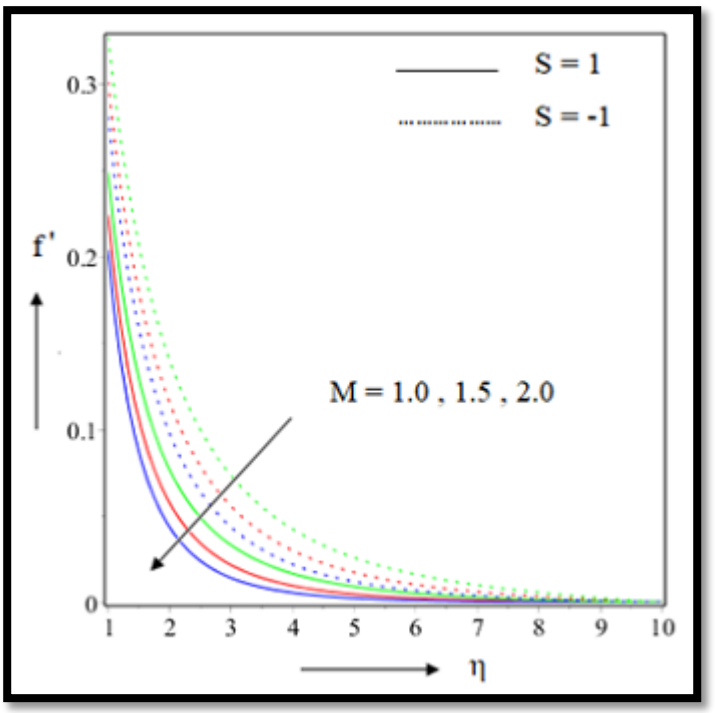

Figure 7.3: Effect of M on $f'(\eta)$.

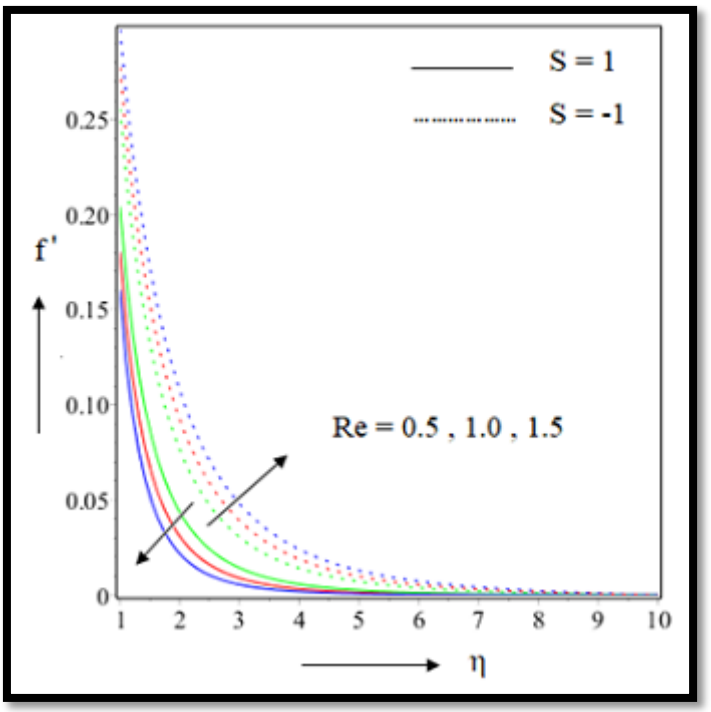

Figure 7.4: Effect of Re on $f'(\eta)$.

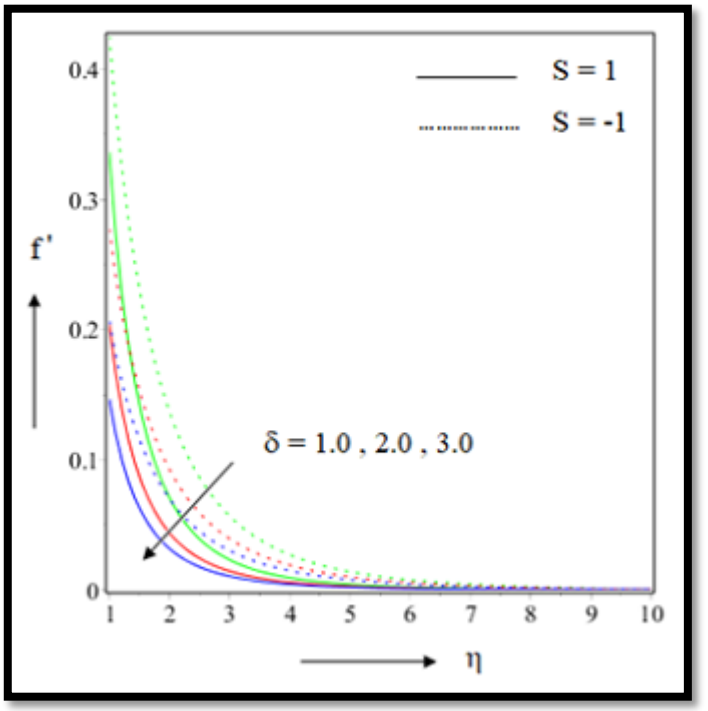

Figure 7.5: Effect of δ on $f'(\eta)$.

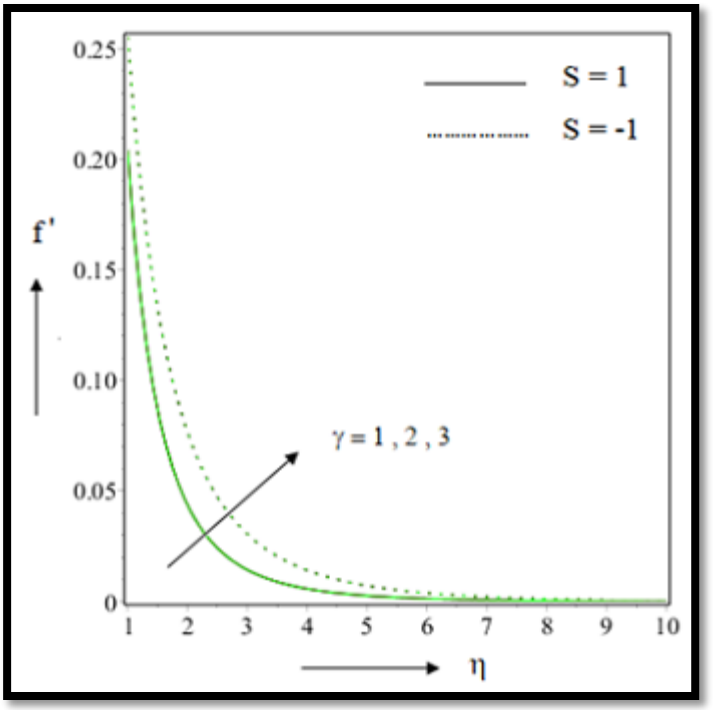

Figure 7.6: Effect of γ on $f'(\eta)$.

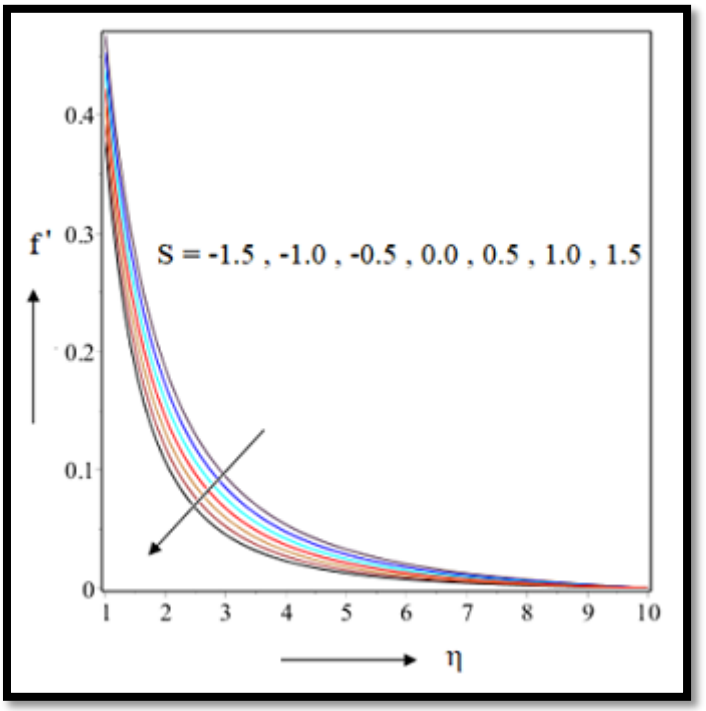

Figure 7.7: Effect of S on $f'(\eta)$.

7.4.2 Influence of several parameters on temperature

In case velocity profile we observed a drag force reduce the velocity lines which also creates friction effect. This friction increase the temperature of the system. For injection of nanofluid we get higher magnitude in heat transfer but for both suction and injection amplified magnetic parameter magnify temperature profile (Figure 7.8 referred). It is reported from Table 7.4 reduced nusselt number diminished by 1.92% for fluid suction but fluid injection diminished it by 9.31%. Reynolds number also curtail temperature profile for both suction and injection effect. From Figure 7.9 we found heat lines shows prominent difference in $1 \le \eta \le 4$ for fluid suction and in$1 \le \eta \le 7$ for fluid injection.

We found ascending property of heat lines for thermal radiation parameter. Higher radiation parameter leads us to curtailment in Rosseland radiation. Diminished absorption coefficient increase the radiative heat flux. As a result inflated temperature profile is observed. Same upshots are found for both fluid suction and injection situation but high magnitude is found in case of injection. Nusselt number magnified by 8.51% for suction and 11.21% for injection found form Table 7.4. Figure 7.10 shows that proper contrast is observed for the value of similarity variable in $1 \le \eta \le 4$ for suction and in $1 \le \eta \le 7$ for injection after that it converge asymptotically.

First order slip parameter increase the heat lines for suction and injection of fluid found in Figure 7.11. Velocity profile reduced due to first order slip parameter which creates a frictional force. Frictional force generates more heat in the system. Higher magnitude of heat lines originate in case of injection of nanofluid. From Table 7.4 we found 2.03% curtail down in reduced nusselt number for suction effect whereas it is reduced by 5.26% for injection effect. Figure 7.12explore the effect of Thermal Biot number which escalates heat transfer for higher value of $Bi_t = \frac{h_f}{k_f}\sqrt{\frac{\nu_f}{a}}$ parameter. Increment in thermal Biot number refers to magnified ν_f which generates some frictional force. Higher magnitude in heat transfer is found for injection of nanofluid. Distinguished outcomes noted form Figure 7.12 in the interval $1 \le \eta \le 4$ for nanofluid suction and in $1 \le \eta \le 5$ for nanofluid injection. Beyond that heat lines converge asymptotically.

From Figure 7.13 we inspect that for switching the parameter value from injection to suction heat lines is descending in nature. Prominent difference observed in $1 \le \eta \le 7$ and for

higher value similarity variable heat lines tends to zero. From Table 7.6 we found that Nusselt number increased by 17.52%.

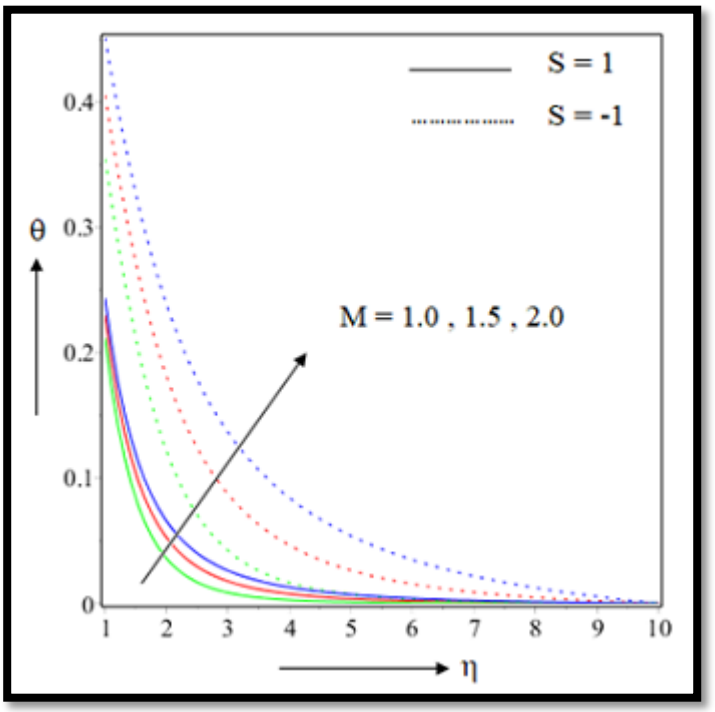

Figure 7.8: Effect of M on $\theta(\eta)$

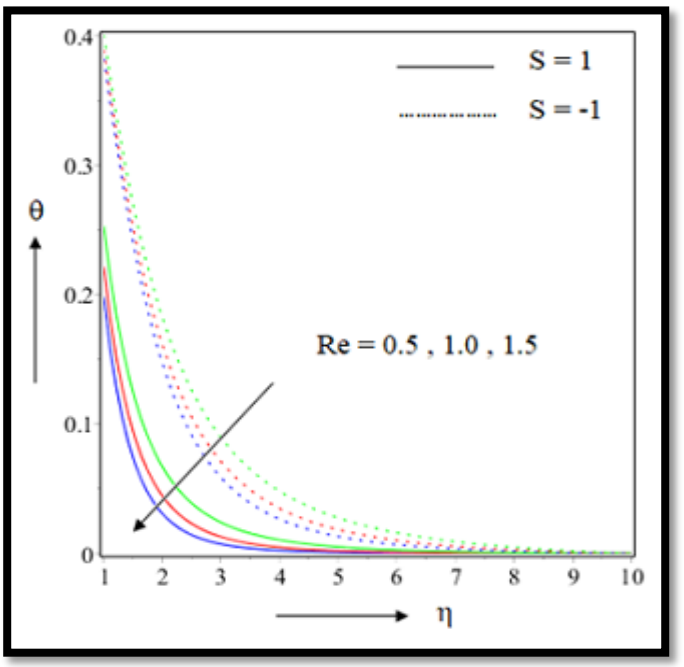

Figure 7.9: Effect of Re on $\theta(\eta)$.

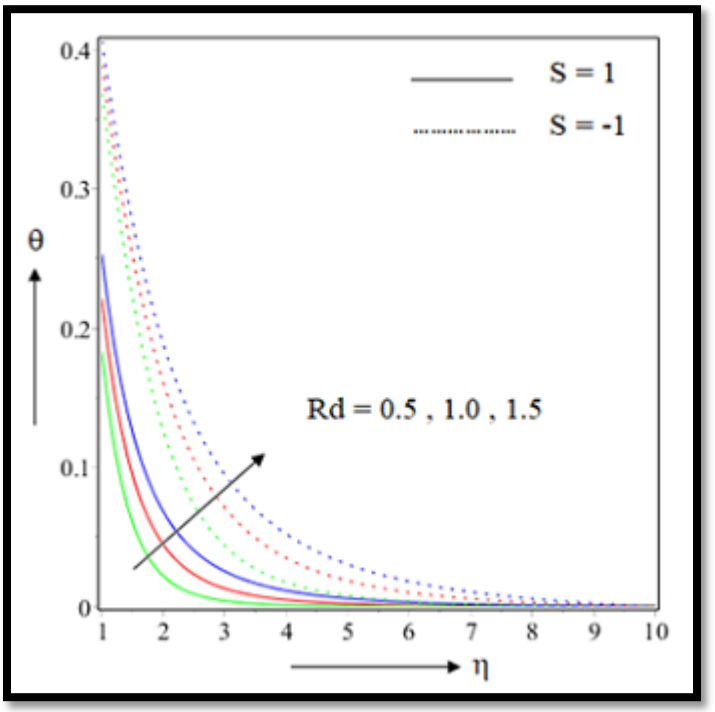

Figure 7.10: Effect of Rd on $\theta(\eta)$.

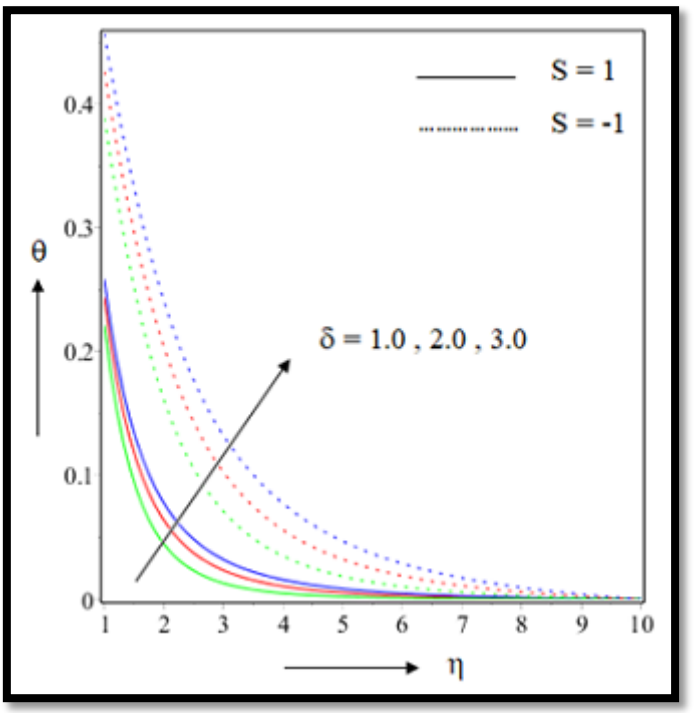

Figure 7.11: Effect of δ on $\theta(\eta)$.

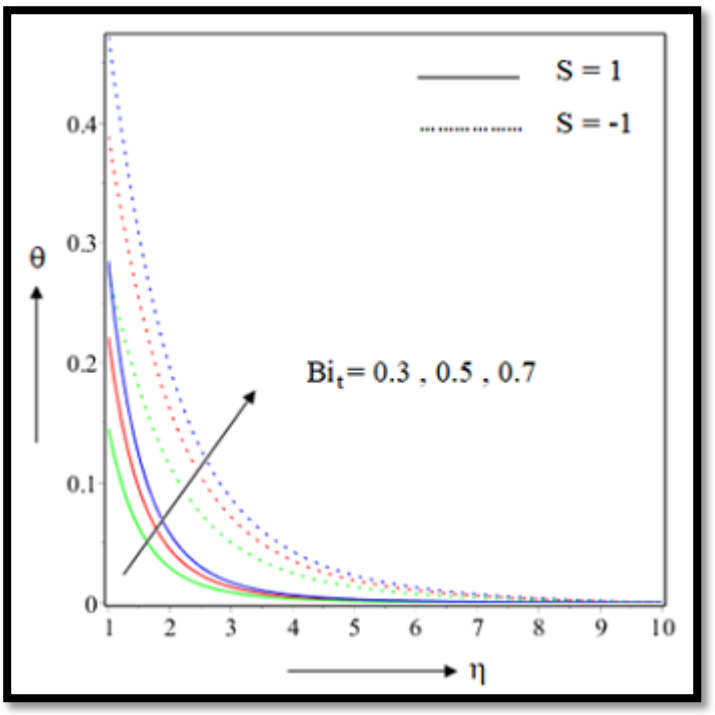

Figure 7.12: Effect of Bi_t on $\theta(\eta)$.

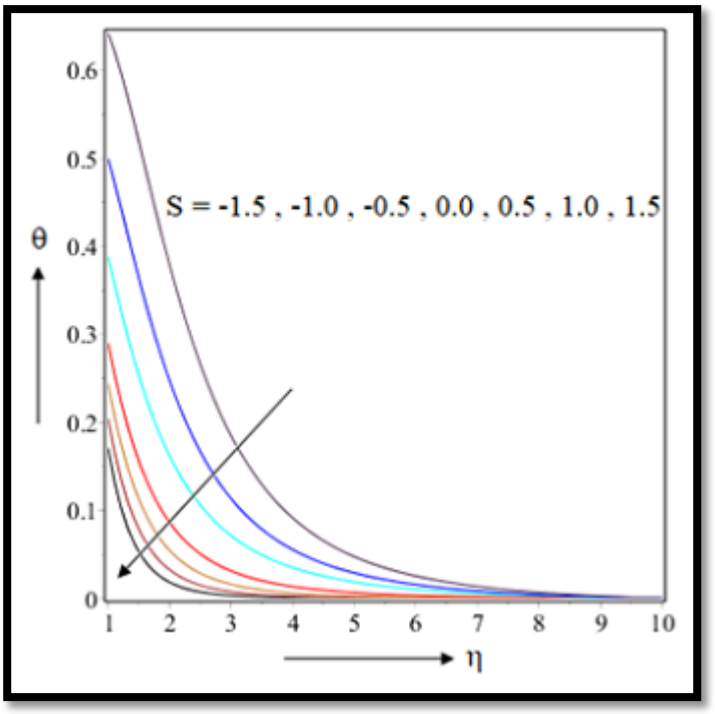

Figure 7.13: Effect of S on $\theta(\eta)$.

7.4.3 Influence of several parameters on concentration

Upshots on concentration lines for different parameter is discussed in this section. From Figure 7.14 we detect that for higher value of magnetic parameter concentration profile increase for suction and injection effect. Value of Sherwood number is most important for engineering interest and it is found to be 2.94% curtailed in case of nanofluid suction whereas 4.34% curtailment observed for injection of nanofluid. Figure 7.15 shows that high Reynolds number is responsible for descending function of concentration profile. We also found from Table 7.5 6.61% change in local Sherwood number for nanofluid suction. Radiation parameter also grip on concentration profile. Here we observe a switch over near $\eta = 2$ before that a descending nature of concentration is found but after that it switch to ascending nature. Suction and injection of nanofluid shows same nature but magnitude is higher for injection of nanofluid (Figure 7.16 referred). Effect of velocity slip parameters are shown on Figure 7.17 and 7.18. It is noteworthy that the concentration profile goes upward for higher value of slip parameter but for second order slip parameter the change is negligible.

When we compare the results under suction and injection condition higher magnitude in concentration is given by injection condition. Second order slip parameter also gives higher concentration for injection of nanofluid than that of suction condition. Dimensionless Sherwood number changed by 5.88% for suction condition but it is changed by 12.11 % for injection of nanofluid into the system.

Convective condition is also taken in our system to make it more practical hence we also find the outcomes of concentration profile for thermal and mass Biot number (Figure 7.19 and 7.20). Interestingly both parameters give similar results. For higher value of thermal and mass Biot number we observe rising profile in concentration and for injection of nanofluid its magnitude up scaled. Table 7.5 reported that Sherwood number is changed by 5.54% for suction of nanofluid and 8.04% for injection of nanofluid in case of thermal Biot number. Lastly in Figure 7.21 we found that for several values of suction/injection parameter it concentration profile also changed. When nanofluid injected into the system concentration increases but for suction it decreases. Dimensionless Sherwood number increased by 9.52%. Prominent difference is observed in $1 \le \eta \le 6$ after it converges asymptotically.

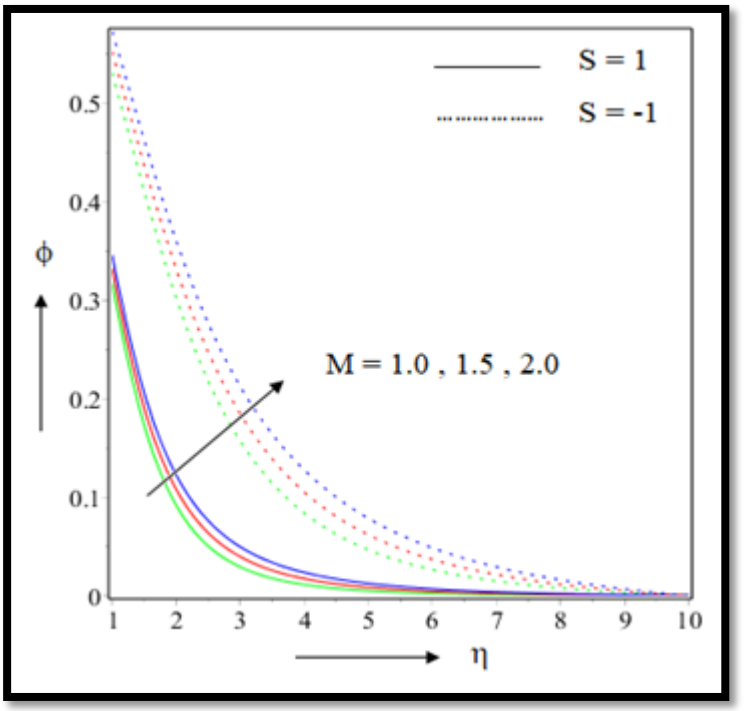

Figure 7.14: Effect of M on $\phi(\eta)$

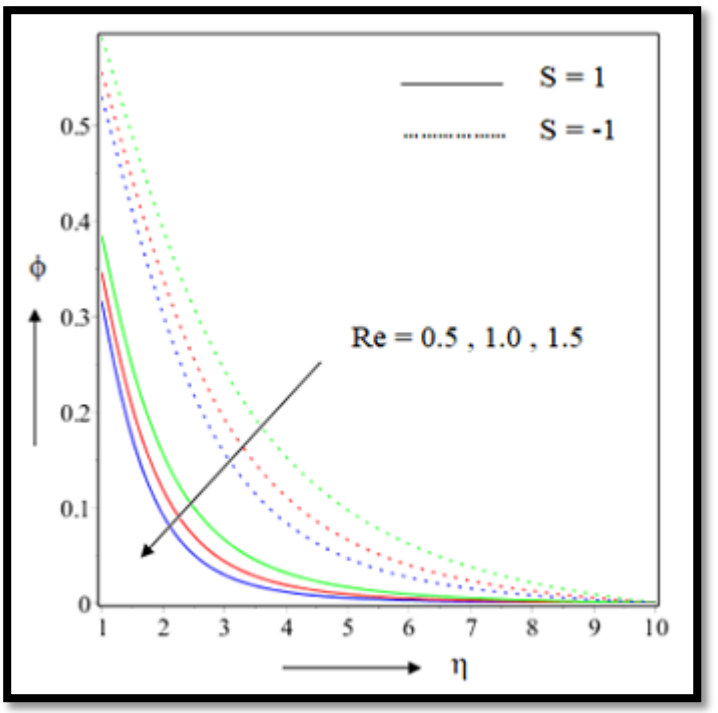

Figure 7.15: Effect of Re on $\phi(\eta)$.

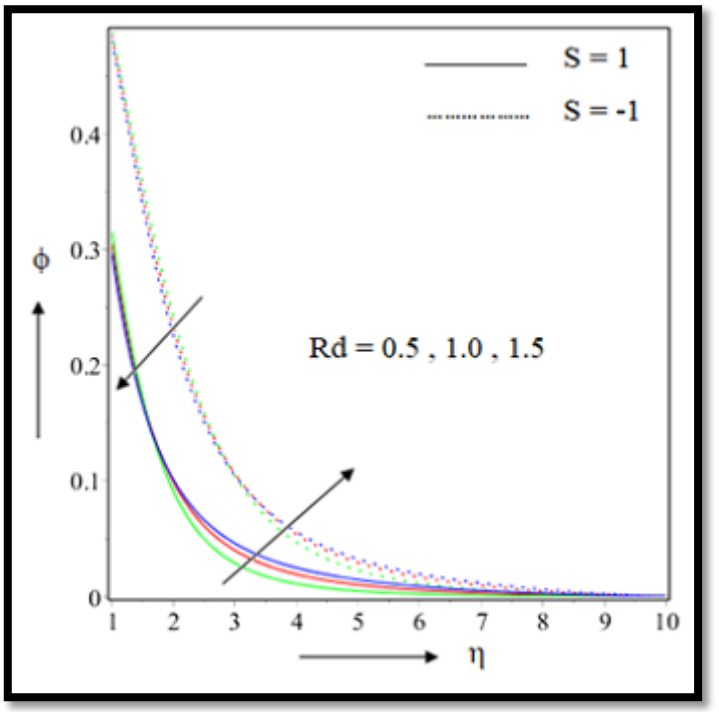

Figure 7.16: Effect of Rd on $\phi(\eta)$.

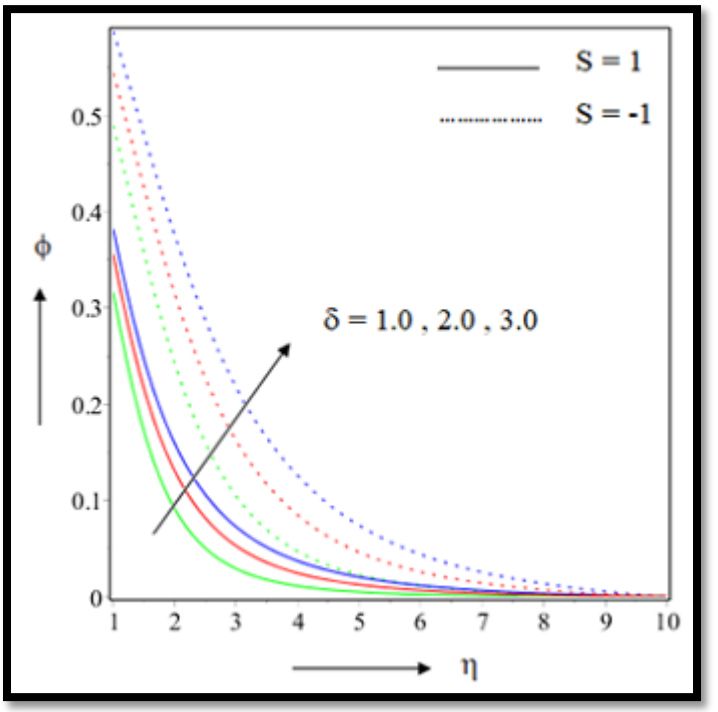

Figure 7.17: Effect of δ on $\phi(\eta)$.

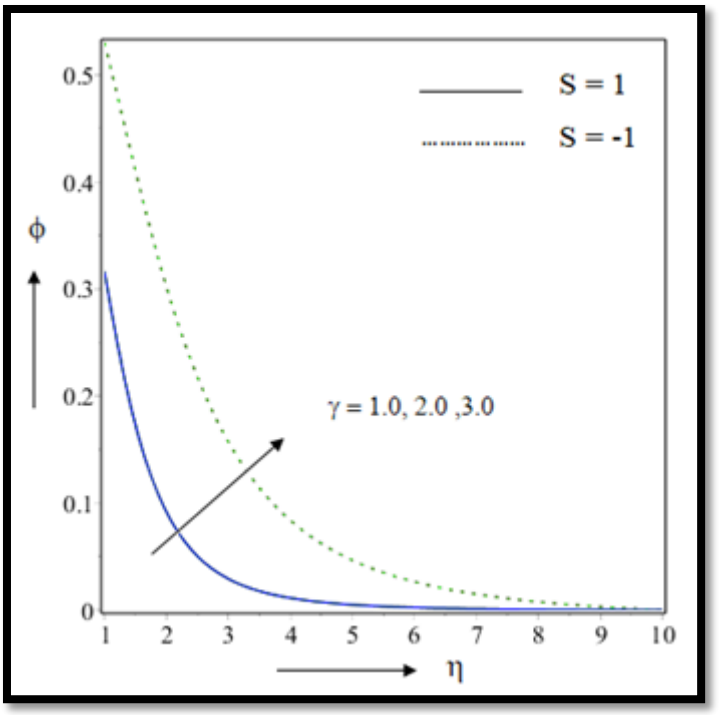

Figure 7.18: Effect of γ on $\phi(\eta)$.

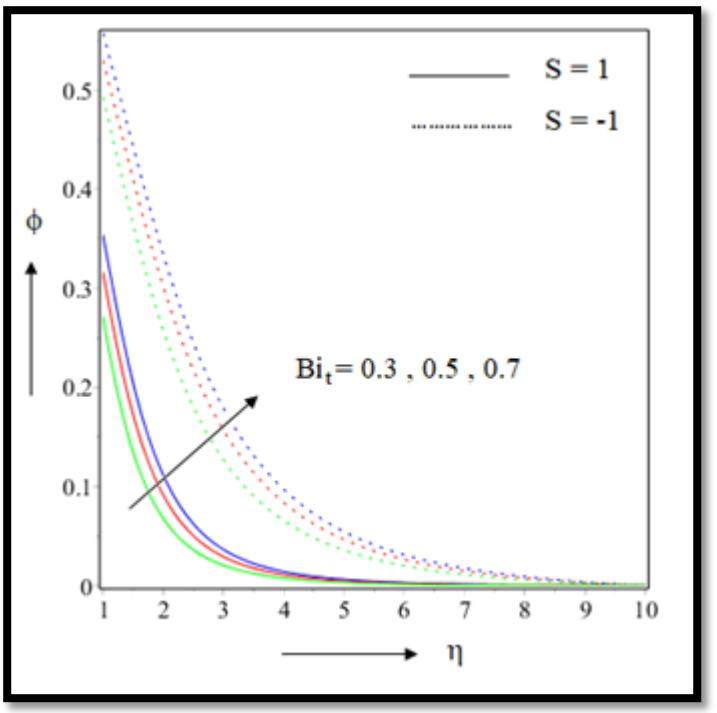

Figure 7.19: Effect of Bi_t on $\phi(\eta)$.

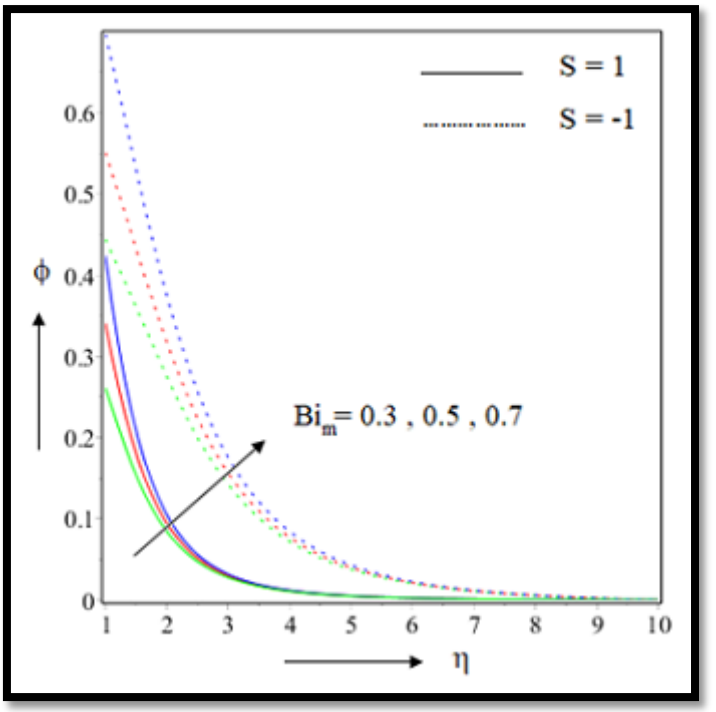

Figure 7.20: Effect of Bi_m on $\phi(\eta)$.

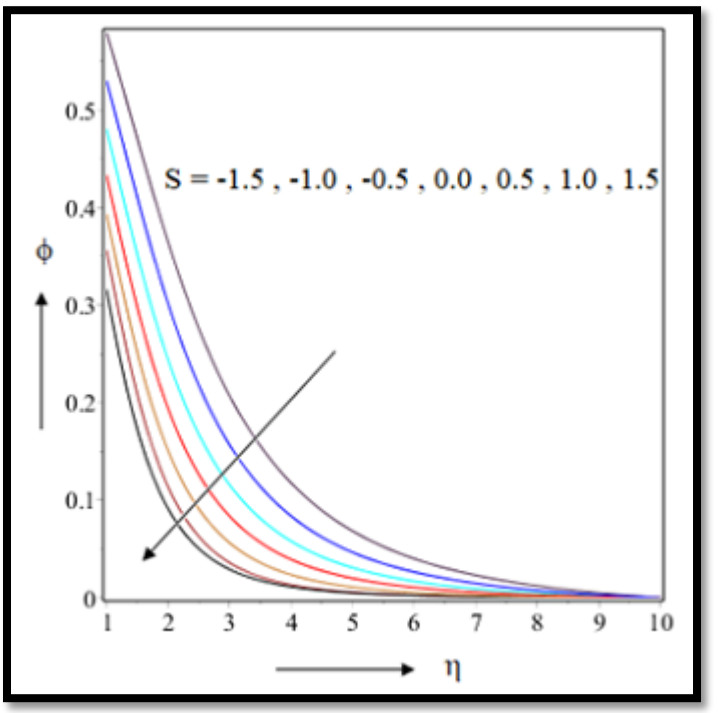

Figure 7.21: Effect of S on $\phi(\eta)$.

7.5. Conclusions

In this investigation we have inspected nanofluid flow over a stretching cylinder under mixed convective condition. Second order slip also incorporated together with suction injection condition. We have transfigured our leading equations with suitable similarity renovation into non linear ODEs. The system is solved by RK-4 shooting technique and simulated by MAPLE-2019 software. Velocity lines heat lines and concentration lines are compared for Suction and injection of nanofluid. Several graphs and tables are used to justify our findings. Most important findings are stated below.

- Magnetic influence reduce the velocity profile but increase temperature and concentration both. Sherwood number curtailed down by 2.94% in case of nanofluid suction whereas 4.34% curtailment observed for injection of nanofluid.
- Higher value of velocity slip parameter decrease the velocity lines but it escalates heat lines and concentration lines. Reduced skin friction increased by 5.40% for injection situation than suction effect in presence of second order slip parameter.
- Thermal Biot number improve the temperature and concentration profile for both suction and injection conditions. Reduced Sherwood number is changed by 5.54% for suction of nanofluid and 8.04% for injection of nanofluid.
- Interestingly Reynolds number parameter increase velocity profile for injection of nanofluid but it decrease velocity lines for suction of nanofluid.
- When we changed the value of parameter S from injection to suction we observe that velocity temperature and concentration are diminished. Change in dimensionless Nusselt number is found to be 17.52%.

Extension of research can be done by taking other geometrical structures like sphere, wedge, and cone with different suitable conditions like Joule heating active and passive control of nanofluid. Moreover several nanofluid and hybrid nanofluid can also be taken to extend the investigation.

Table 7.3: Effect of suitable parameters on skin friction

M	Re	δ	γ	Cf_r	
				$S=1$	$S=-1$
1.0	2.0	2.0	1.0	-0.375466	-0.336336
1.5				-0.387724	-0.349322
2.0				-0.397868	-0.359425
1.5	1.0			-0.397868	-0.372246
	2.0			-0.409778	-0.361386
	3.0			-0.419786	-0.351340
	2.0	1.0		-0.663212	-0.574360
		2.0		-0.397868	-0.361386
		3.0		-0.284423	-0.264515
		2.0	1.0	-0.397868	-0.372246

Table 7.4: Effect of suitable parameters on heat transfer

M	Re	Rd	Bi_t	δ	γ	Nu_r	
						$S=1$	$S=-1$
1.0	2.0	1.0	0.5	2.0	1.0	0.525663	0.430370
1.5						0.513321	0.396478
2.0						0.504185	0.365823
1.5	1.0					0.497991	0.399591
	2.0					0.518973	0.407513
	3.0					0.534318	0.411767
	2.0	0.5				0.476514	0.368467
		1.0				0.518973	0.408014
		1.5				0.560136	0.445403
		1.0	0.3			0.341803	0.289821
			0.5			0.518973	0.407513
			0.7			0.666964	0.493121
			0.5	1.0		0.518973	0.407854
				2.0		0.503862	0.382438
				3.0		0.494013	0.361968
				2.0	1.0	0.517969	0.408016

Table 7.5: Effect of suitable parameters on mass transfer

M	Re	Rd	Bi_t	Bi_m	δ	γ	Sh_r	
							$S=1$	$S=-1$
1.0	2.0	1.0	0.5	0.5	2.0	1.0	0.341739	0.234838
1.5							0.333956	0.224225
2.0							0.327155	0.213968
1.5	1.0						0.307379	0.203452
	2.0						0.326587	0.221682
	3.0						0.341739	0.234838
	2	0.5					0.341739	0.255180
		1.0					0.347015	0.256832
		1.5					0.351048	0.259081
		1.0	0.3				0.364073	0.253407
			0.5				0.341739	0.234838
			0.7				0.322908	0.221203
			0.5	0.3			0.221590	0.166704
				0.5			0.395326	0.224499
				0.7			0.575957	0.303384
				0.5	1.0		0.341739	0.255180
					2.0		0.322020	0.228025
					3.0		0.308781	0.206149
					2.0	1.0	0.3417392	0.234838

Table 6: Effect of Suction/Injection parameters on skin friction, heat transfer and mass transfer

S	Cf_r	Nu_r	Sh_r
-1.5	-0.378333	0.238369	0.210102
-1.0	-0.394046	0.333539	0.234838
-0.5	-0.407517	0.407513	0.259584
0.0	-0.360528	0.473289	0.283197
0.5	-0.341069	0.503847	0.303193
1.0	-0.320636	0.537201	0.321536
1.5	-0.300008	0.552501	0.341739

CHAPTER 8

Magnetically driven chemically reactive Casson nanofluid flow over curved surface with thermal radiation*

8.1 Introduction

Problems innvolving non-Newtonian fluid flow has attracted the attention of many researchers sice long back due to its various applications. Casson nanofluid is one type of non – Newtonian fluid. Prolems involving Casson nanofluid has some applications in different fields e.g. producing pharmaceutical products, china clay, paints, synthetic lubricants, and biological liquids like synovial fluids, jelly, sewage sludge, tomato sauce. Acharya et al. [149] illustrated the effects of chemically reacted Williamson nanofluid flow in permeable medium. Thermophoresis, Multiple slips and Brownian motion were considered in [149]. They found that mass transfer rate gets enhanced for high rate of chemical reaction.

In this research we have considered Casson nanofluid flow over a curved stretching surface under slip effect, radiation, higher order chemical reaction and multiple convection. The governing equations are transferred to ODEs by proper similarity transformation. The ODEs thus obtained are solved numerically by RK-4 method with the help of MAPLE-2019 software. The simulation process is observed under various parameters. Velocity profile is compared both in presence and in asence of slip effect. The concentration and thermal profiles are compared in existence of chemical reaction and radiation respectively. All outcomes are designed graphically. The co-efficient of skin friction and Nusselt number are presented in the form of tables for different parameters.

***This chapter is based on the paper published in: Heat Transfer, 51(6) (2022), 4882-4905, (ESCI).**

8.2. Mathematical formulation

8.2.1. Governing equations

Let us consider a steady, incompressible 2-D, MHD drift of Casson nanoliquid. The flow is over a stretching sheet curved in nature which is being stretched through a semicircle of radius R. Curved surface is supposed to be flat for larger value of radius R. Chemical reaction of higher order is considered. Thermal radiation together with velocity slip effect is also put in. Termal slip and concentration slips are overlooked. We have also employed Brownian migration and thermophoresis effect. Viscous dissipation together with joule heating profile is avoided. We have assumed magnetic Reynolds number to be insignificant in order to avoid the induced effect compared to applied superficial magnetic field. The arrangement system (r, s) is grasped as manifest in the Figure 1. Where direction of flow clutched along s and r axis is orthogonal to it. Stretching velocity of the sheet is taken as $u_w = as$ where a is stretching constant. The magnetic field of strength $B = B_0$ is applied along r direction. The magnetic Reynolds number is treated sufficiently small to overlook the induced impact. Temperature and concentration of liquid at the sheet are T_f and C_f respectively while ambient fluid warmth and concentration are T_∞ and C_∞. The upshot of thermal radiation, slip of velocity and higher order chemical reaction are considered in this flow model. Under this assumption the equations of the flow [150-152] are as follows.

$$\nabla \cdot V = 0 \tag{8.1}$$

$$(V \cdot \nabla)V - \Omega^* \times V = \frac{1}{\rho_f}\left[\nabla(\mu \cdot \nabla V) + J \times B\right] \tag{8.2}$$

$$(V \cdot \nabla)T = \frac{1}{\left(\rho C_p\right)_f}\left[\begin{array}{l}\nabla\left(k_f \cdot \nabla T\right) + \dfrac{J \cdot J}{\sigma_f} + \dfrac{D_m k_T \rho_f}{C_s}\nabla \cdot \left(\nabla C\right)\rho_s C_{p_s}\left(D_B\left(\nabla T \cdot \nabla C\right) + \dfrac{D_T}{T_\infty}\left(\nabla T \cdot \nabla T\right)\right) \\ +Q_0\left(T - T_\infty\right) + \phi - \nabla \cdot q_r\end{array}\right] \tag{8.3}$$

$$V \cdot \left(\nabla C\right) = \nabla \cdot \left[D\nabla C + \frac{D_T}{T_\infty}\nabla T\right] + K_r\left(C - C_\infty\right)^n \tag{8.4}$$

After converting the above equations in (r,s) form under suitable circumstances we get the following equations.

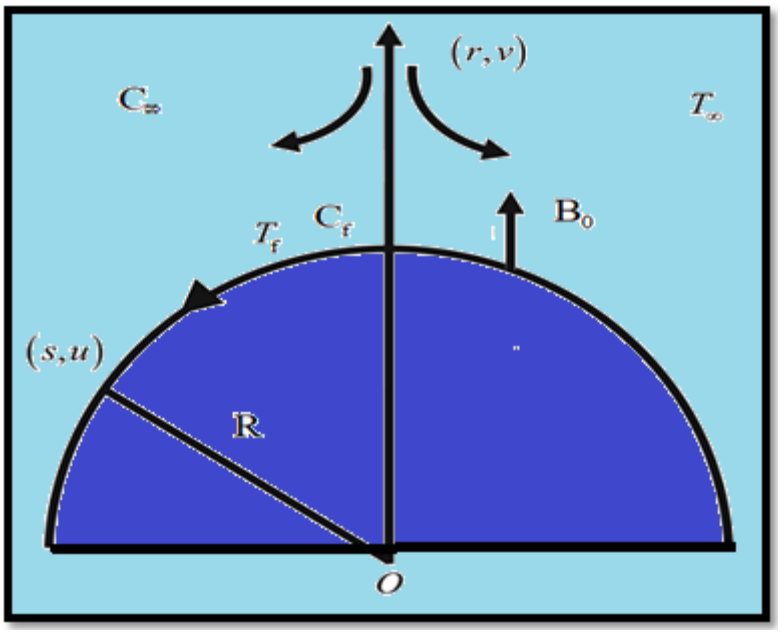

Figure 8.1: Physical geometry of the flow.

$$\frac{\partial}{\partial r}\{(r+R)v\}+R\frac{\partial u}{\partial s}=0 \tag{8.5}$$

$$\frac{u^2}{r+R}=\frac{1}{\rho_f}\frac{\partial p}{\partial r} \tag{8.6}$$

$$v\frac{\partial u}{\partial r}+\frac{Ru}{r+R}\frac{\partial u}{\partial s}+\frac{uv}{r+R}=-\frac{R}{\rho_f(r+R)}\frac{\partial p}{\partial s}+\nu_f\left(1+\frac{1}{\beta}\right)\left[\frac{\partial^2 u}{\partial r^2}+\frac{1}{r+R}\frac{\partial u}{\partial r}-\frac{u}{(r+R)^2}\right]-\frac{\sigma_f B_0^2 u}{\rho_f} \tag{8.7}$$

$$v\frac{\partial T}{\partial r}+\frac{Ru}{r+R}\frac{\partial T}{\partial s}=\frac{\kappa_f}{(\rho C_p)_f}\left(\frac{\partial^2 T}{\partial r^2}+\frac{1}{r+R}\frac{\partial T}{\partial r}\right)+\tau\left[D_B\frac{\partial C}{\partial r}\frac{\partial T}{\partial r}+\frac{D_T}{T_\infty}\frac{\partial T}{\partial r}\right]-\frac{1}{(\rho C_p)_f(r+R)}\frac{\partial}{\partial r}[(r+R)q_r] \tag{8.8}$$

$$v\frac{\partial C}{\partial r}+\frac{Ru}{r+R}\frac{\partial C}{\partial s}=D_B\left(\frac{\partial C^2}{\partial r^2}+\frac{1}{r+R}\frac{\partial C}{\partial r}\right)+\frac{D_T}{T_\infty}\left(\frac{\partial^2 T}{\partial r^2}+\frac{1}{r+R}\frac{\partial T}{\partial r}\right)-K_r(C-C_\infty)^n \tag{8.9}$$

C and T assures the concentration and temperature profile of the working liquid. Simplification of radiative heat flux can be calculated by Rosseland approximation $q_r = -\frac{4\sigma^*}{3\kappa^*}.\frac{\partial T^4}{\partial r}$ where σ^* acts for Stefan boltzmann constant and κ^* speaks for mean absorption coefficient. We get $T^4 \approx 4T.T_\infty^3 - 3T_\infty^3$ from Taylor series expansion of T^4 about T_∞ neglecting the higher order expressions.

8.2.2. Boundary conditions

The boundary provisions for the above introduced model are given by the following equations:

$$u = u_w + L\left(\frac{\partial u}{\partial r} - \frac{u}{r+R}\right),\ v = v_w,\ -\kappa_f \frac{\partial T}{\partial r} = h_f\left(T_f - T_\infty\right),\ -D_m \frac{\partial C}{\partial r} = h_m\left(C_f - C_\infty\right) \text{ at } r = 0 \quad (8.10)$$

$$u \to 0,\ \frac{\partial u}{\partial r} \to 0,\ T \to T_\infty,\ C \to C_\infty \text{ as } r \to \infty \quad (8.11)$$

v_w Designates suction injection velocity where positive value of v_w represents injection i.e. insertion of fluid in the system and negative value of v_w represents suction i.e. extraction of fluid from the system.

8.2.3. Similarity transformations

We convert the foremost flow equations (8.5-8.9) into system of ODEs by the following similarity variables as in [150-152]:

$$\left.\begin{aligned} &\eta = \sqrt{\frac{a}{\nu_f}}r, u = asf'(\eta), v = -\frac{R}{r+R}\sqrt{a\nu_f}\, f(\eta), \\ &p = \rho_f (as)^2\, p(\eta), \theta(\eta) = \frac{T - T_\infty}{T_f - T_\infty}, \phi(\eta) = \frac{C - C_\infty}{C_f - C_\infty} \end{aligned}\right\} \quad (8.12)$$

After needed modernization equation (8.5) satisfies automatically. Equation (8.6) and (8.7) changed as follows.

$$p' = \frac{f'^2}{\eta + k} \tag{8.13}$$

$$\frac{2k}{\eta + k} p = \left(1 + \frac{1}{\beta}\right)\left[f''' + \frac{f''}{\eta + k} - \frac{f'}{(\eta + k)^2} \right] - \frac{k}{\eta + k} f'^2 + \frac{k}{\eta + k} ff'' + \frac{k}{(\eta + k)^2} ff' - M^2 f' \tag{8.14}$$

Eliminating pressure p from equation (8.13) and (8.14) we get

$$f^{iv} + \frac{2f'''}{\eta + k} - \frac{f''}{(\eta + k)^2} + \frac{f'}{(\eta + k)^3} - \frac{1}{\left(1 + \frac{1}{\beta}\right)}\left[\frac{k}{\eta + k}(f' - ff''') + \frac{k}{(\eta + k)^2}(f'^2 - ff'') + \frac{k}{(\eta + k)^3} ff' + M^2\left(f'' + \frac{f'}{\eta + k} \right) \right] = 0 \tag{8.15}$$

Equation (8.8) and (8.9) changed as follows

$$\left(\theta'' + \frac{\theta'}{\eta + k}\right)\left(1 + \frac{4}{3} Rd\right) + \Pr\left(\frac{k}{\eta + k} \theta' f + Nb\theta'\phi' + Nt\theta'^2 \right) = 0 \tag{8.16}$$

$$\phi'' + \left(\frac{k}{\eta + k} Scf + \frac{1}{\eta + k} \right)\phi' + \frac{Nt}{Nb}\left(\theta'' + \frac{1}{\eta + k}\theta' \right) - KrSc\phi^n = 0 \tag{8.17}$$

Similarly the boundary provisions are also converted to:

$$\left.\begin{array}{l} f'(0) = 1 + Ls\left(f''(0) - \dfrac{f'(0)}{k} \right),\ f(0) = S, \theta'(0) = -Bi_t\left(1 - \theta(0)\right), \phi'(0) = -Bi_m\left(1 - \phi(0)\right) \\ f'(\infty) = 0,\ f''(\infty) = 0, \theta(\infty) = 0, \phi(\infty) = 0 \end{array}\right\} \tag{8.18}$$

Where $S \succ 0$ indicates injection and $S \prec 0$ indicates suction.

8.2.4. Physical quantities

The needful physical quantities which are very important for engineering application are

$$C_f = \frac{\tau_{rs}}{\rho_f u_w^2} \quad \text{Where} \quad \tau_{rs} = \mu_f \left(1+\frac{1}{\beta}\right)\left(\frac{\partial u}{\partial r} - \frac{u}{r+R}\right)_{r=0}$$

$$Nu = \frac{sq_w}{\kappa_f \left(T_f - T_\infty\right)} \quad \text{Where} \quad q_w = -\kappa_f \left(\frac{\partial T}{\partial r}\right)_{r=0} + \left(q_r\right)_{r=0}$$

$$Sh = \frac{sj_w}{D_B \left(C_f - C_\infty\right)} \quad \text{Where} \quad j_w = -D_B \left(\frac{\partial C}{\partial r}\right)_{r=0}$$

Here C_f denotes local skin friction Nu stands for local Nusselt number and Sh represents local Sherwood number respectively. τ_{rs}, q_w, j_w Designates surface shear stress, heat flux and mass flux respectively.

Applying similarity renovation, we procure the reduced skin friction as

$$C_{fr} = \sqrt{\mathrm{Re}_s} C_f = \left(1+\frac{1}{\beta}\right)\left(f''(0) - \frac{f'(0)}{k}\right)$$

Analogously reduced Nusselt number as

$$Nu_r = \left(\mathrm{Re}_s\right)^{-\frac{1}{2}} Nu = -\left(1+\frac{4}{3}Rd\right)\theta'(0)$$

and also reduced Sherwood number as

$$Sh_r = \left(\mathrm{Re}_s\right)^{-\frac{1}{2}} Sh = -\phi'(0)$$

Where $\mathrm{Re}_s = \frac{as^2}{\nu_f}$ represents local Reynolds number.

8.3. Numerical procedure

8.3.1. Solution technique

Analytical method of solution is difficult to apply in the obtained group of equations with its boundary condition. To overcome this difficulty we use numerical structures to solve our framework. Shooting method in constitution of RK-4 method is pre-owned to procure the required

solution. The whole process is programmed by MAPLE-2019 software and the outcomes are discussed in the consequent sections with the help of graphs and charts.

8.3.2. Code verification

To access the validity of the present problem, we have compared our numeric outcomes with previous literature where an incompressible viscous fluid is considered. The comparison is reflected in Table 8.1.We remove the slip effect and chemical reaction effect by taking $Ls = 0$ and $Kr = 0$. To make our model similar to Abbas et al. [153] radiation parameter also taken as zero. For the various values of dimensionless curvature parameter skin friction co-efficient has been compared.

Table 1: Comparison of numerical outcomes with previous studies

k	**Abbas et al. [153]**	**Present Results**
	Cf_r	Cf_r
5	-1.15763	-1.15764
10	-1.07349	-1.07348
20	-1.03561	-1.03561
30	-1.02353	-1.02354
40	-1.01759	-1.01759
50	-1.01405	-1.01405
100	-1.00704	-1.00703
200	-1.00356	-1.00356
1000	-1.00079	-1.00079

8.4. Result and discussion

The results obtained in this work are explained in this section. The effects of magnetic parameter, curvature parameter, suction injection parameter , Casson parameter, Brownian motion, thermophoresis radiation, Biot number for temperature and mass both, Schmidt number , chemical reaction parameters ,slip parameter , higher order chemical reaction parameter are discussed in the following section. We have assigned the values as $\Pr = 6.2, M = 2.0, k = 5, S = 0.4, \beta = 0.4, Nb = 0.4, Nt = 0.4, Sc = 5, Bi_t = 0.3, Bi_m = 0.3$ by default. We have also taken various values of the fixed parameters to simulate the process. Our core intention is to reveal the variation of velocity profile temperature profile and concentration profile under presence and absence of slip parameter, radiation parameter and chemical reaction parameter respectively.

8.4.1. Influence of Slip parameter *Ls*

In our study we have taken two different conditions presence of slip effect and absence of slip effect. The velocity profile is compared for this two cases and results for different parameters are shown graphically.

We have seen that the fluid velocity goes down as we increase the magnetic parameter. Lorentz force is produced when extra magnetic field is applied in the system. This force is the reason behind slow down process of the velocity. Skin friction coefficient has reduced by 3.94%. It is also noticed that the magnitude of the velocity is greater in case of without slip condition than that of under slip effect. Clear effect is seen in the interval $0.0 \le \eta \le 3.0$. Which can be observed in Figure 8.2. Similar result has been observed by Oyelakin et al. [154]

The curvature parameter shows different result. As we increase the curvature parameter the stretching sheet became more flat. The liquid can passed with more speed in the flatter surface. Consequently velocity profile up rise due to higher curvature parameter. Again here also higher magnitude of velocity profile is observed in case of without slip condition. Skin friction co efficient increased 8.34% in case slip effect whereas 10.05% in case of without slip condition. Similar outcome observed by Hayat et al. [155]. Precise pictorial view is seen in the interval $0.0 \le \eta \le 3.0$. Figure 8.3 shows the clear comparison and profile character.

For change in Casson parameter of the fluid an interesting outcome is observed in Figure 8.4. Under no slip condition when Casson parameter get increased, it also increases the shear thickness of liquid and hence suppressing of the fluid flow occurred. But when we consider the slip effects different phenomenon has been observed. In the interval $0.0 \le \eta \le 3.0$ the clear pictorial view is observed. Skin friction is increased by 12.9% and here also higher magnitude velocity is observed for no slip condition.

Suction injection parameter also effect the velocity differently under different condition. As we increase the suction injection parameter the sheet allows more fluid in the system and as a result the velocity get increased. 35.32% increment in skin friction c efficient make sense of the above outcome. Figure 8.5 should be observed for particular results. Higher magnitude in velocity profile is seen in case of no slip condition. The observation is quite distinct in the interval $0.0 \le \eta \le 3.0$ .When we observe the fluid flow under slip effect an interesting result arises. We observe that fluid flow become slower under higher slip value (Figure 8.6 referred). As the slip resists the fluid flow as a result the velocity reduced. 35.62% change in skin friction shows the importance of this parameter in the velocity profile of Casson flow.

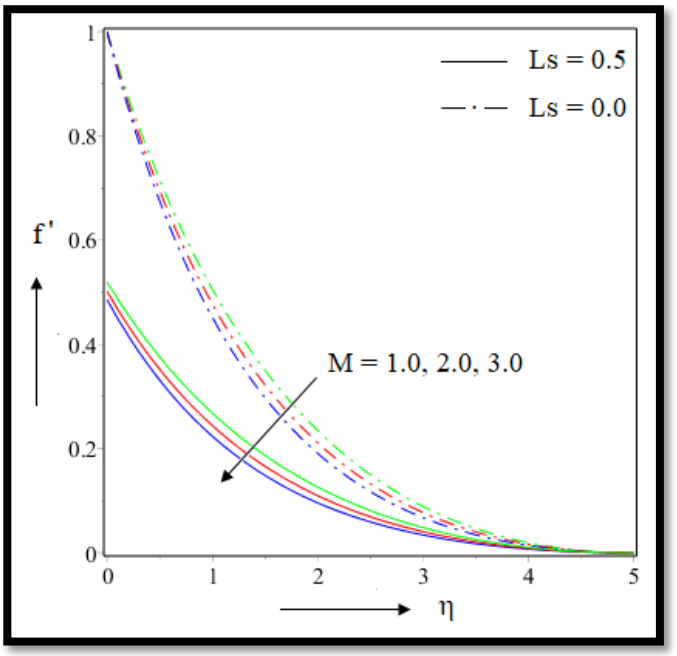

Figure 8.2: Effect of M on $f'(\eta)$.

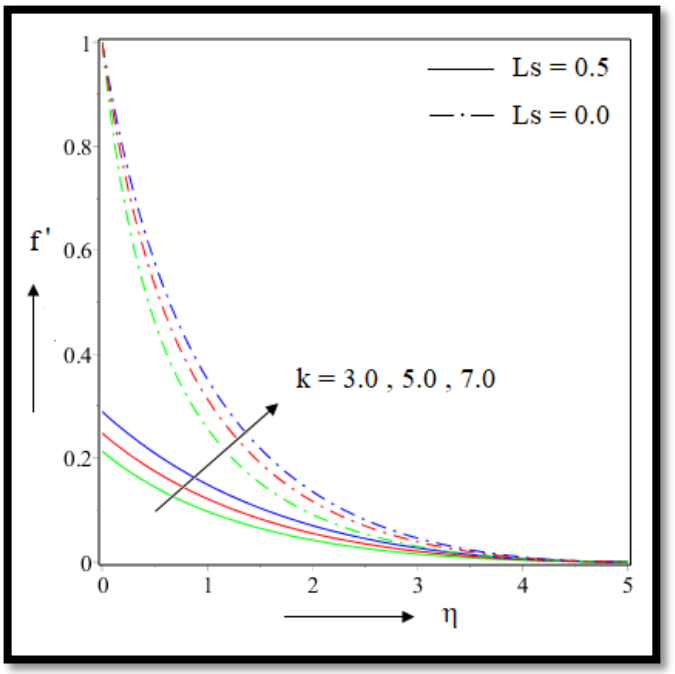

Figure 8.3: Effect of k on $f'(\eta)$.

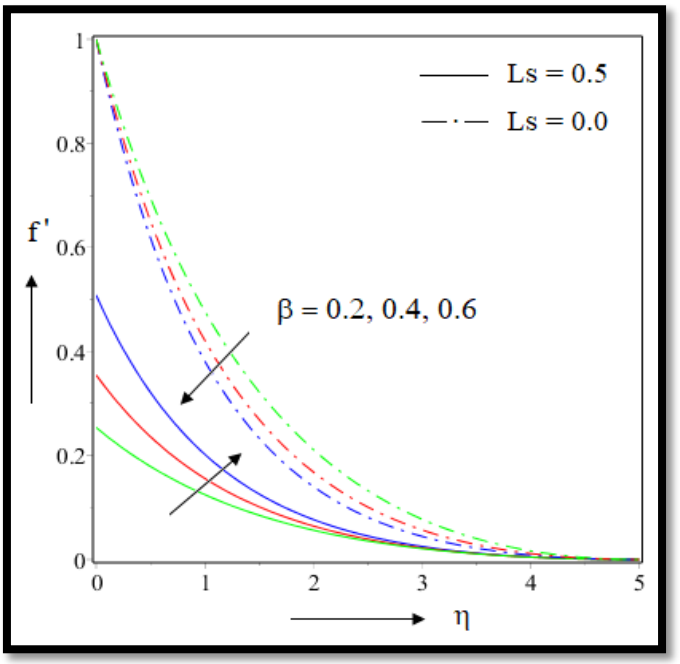

Figure 8.4: Effect of β on $f'(\eta)$.

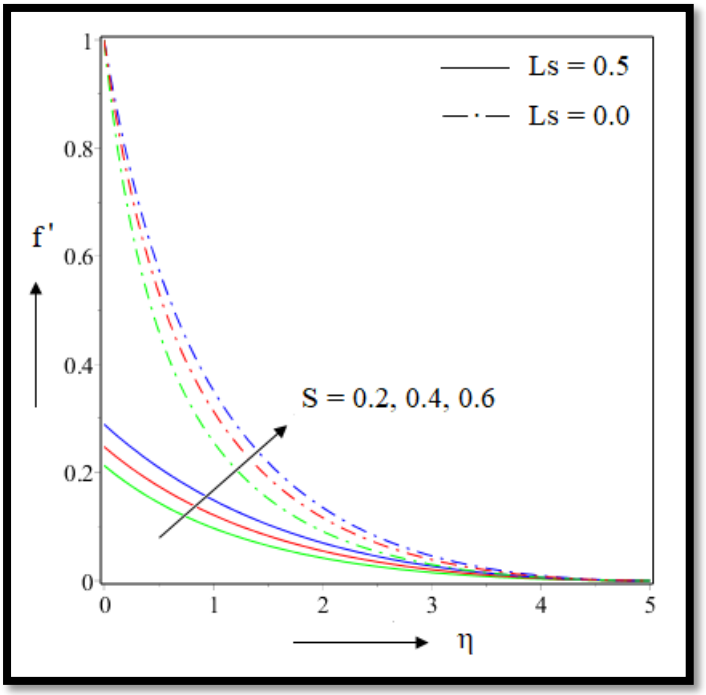

Figure 8.5: Effect of S on $f'(\eta)$.

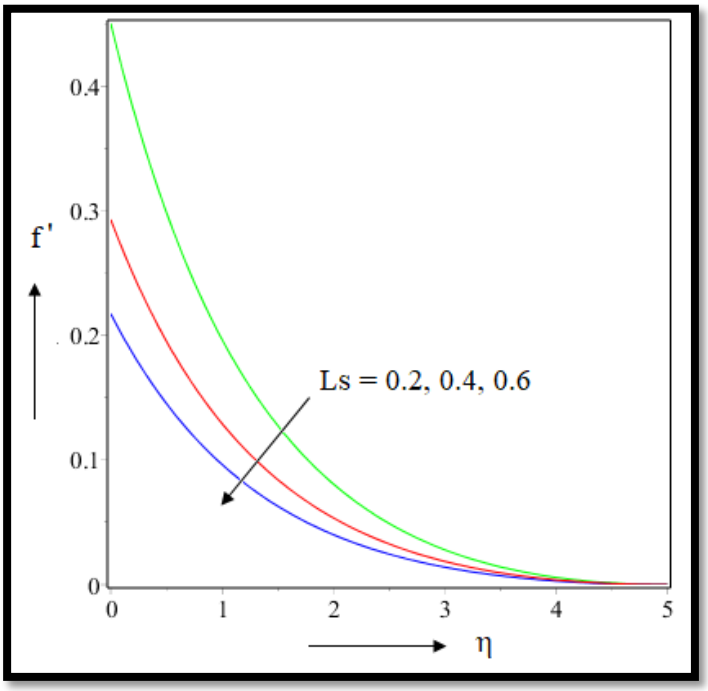

Figure 8.6: Effect of Ls on $f'(\eta)$

8.4.2. Effect of Radiation parameter Rd

The effect of radiation parameter is crucial over temperature profile. Here also we compared the temperature profile under the presence and absence of radiation parameter. The effect is radiation is directly related to the heat generation of the system. Enhancement in magnetic parameter results slowdown in velocity and this increase the frictional force of the system. This force creates more heat in the system and thus the temperature profile get increased. Reduced Nusselt number is decreased by 2.56% in this case. We observed higher magnitude in case of flow with radiation. Figure 8.7 shows the effect clearly. Finest observation is depicted in the interval $0.0 \le \eta \le 3.0$. Oyelakin et al. [154] observed the similar result when they take Casson flow over stretching sheet. Curvature parameter reduce the temperature profile. Increment in curvature parameter makes the surface more flat and the heat can be radiated more highly. As a result the temperature get reduced. Clear observation is shown in the interval $0.0 \le \eta \le 2.0$. Figure 8.8 refers to the above result. 2.57% reduction in reduced nusselt number prove the fact. In case of zero radiation it reduced under 1%. Effect of Casson parameter under radiation and without radiation is observed in Figure 8.9. As the velocity get increased due to increment in Casson parameter under the slip effect so the temperature get reduced due to the same condition. Radiation keeps the heat lines above the lines without radiation. The effect is precisely shown in the interval $0.0 \le \eta \le 2.0$. 2.63% increment in reduced Nusselt number is found in the Table 8.3. Oyelakin [154] also found similar analysis in their study where they have taken a stretching sheet. When we compare the suction effect under presence and nonappearance of radiation parameter we realized that temperature get reduced due higher suction value. The velocity was increased for higher suction value and hence friction force get increased. Elevated temperature is an outcome of high friction value. 21.21% increment is seen in reduced Nusselt number which is the supporting fact of our graphical observation.

The graph in Figure 8.10 shows higher magnitude of temperature profile in case of radiative flow. Figure 8.11 establish that temperature is increased due higher value of slip parameter. In appearence of radiation magnitude heat transport is greater than that of under zero radiation. $0.0 \le \eta \le 3.0$ Interval precisely shows the repercussion of slip parameter. 2.03% increment in Nusselt number is spotted in Table 8.3. Brownian motion parameter increase the heat transport rate in the system. The movement of small ingredients gets increased and consequently more

frequent collision results more heat. The accuracy of the transportation rate observed in the interval $0.0 \le \eta \le 3.0$. A small change in Nusselt is seen which is less that 1%. Figure 8.12 exhibits the effect graphically. Thermophoresis parameter literally defines the relocation of nanoparticles due to temperature gradient. Higher thermophoretic parameter tries to make thermal equilibrium inside the system. Figure 8.13 shows the effect graphically. As thermal biot number increases, transfer of heat through convection takes place largely. Hence, up rise in temperature field can be seen. 26.5% change in Nusselt number depict the fact shown in Figure 8.14. Radiation developed the higher magnitude of temperature profile compared to the zero radiation flow. The higher temperature gradient will be balanced through migration of particles. Evidently, the temperature lines will go down in Figure 8.15 Enhancement of radiation effect manifest higher heat transport rate.

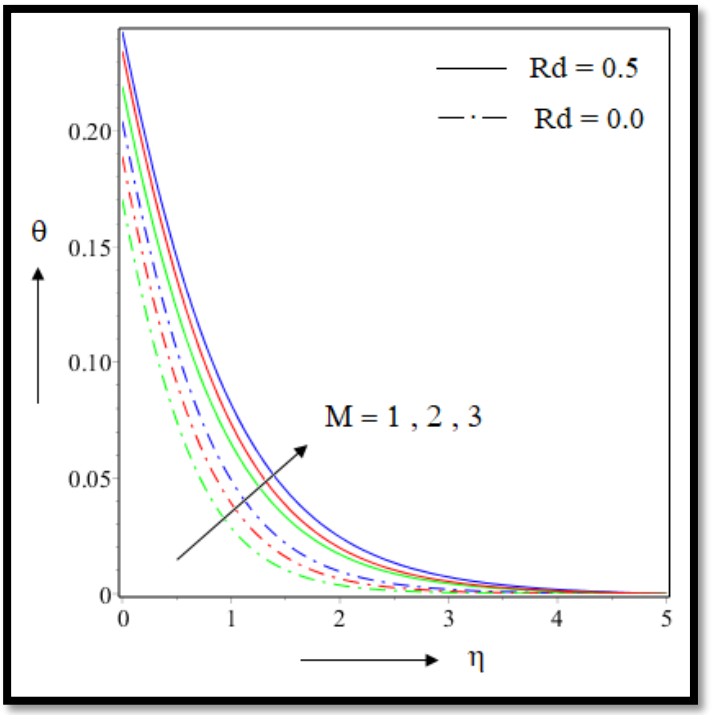

Figure 8.7: Effect of M on $\theta(\eta)$.

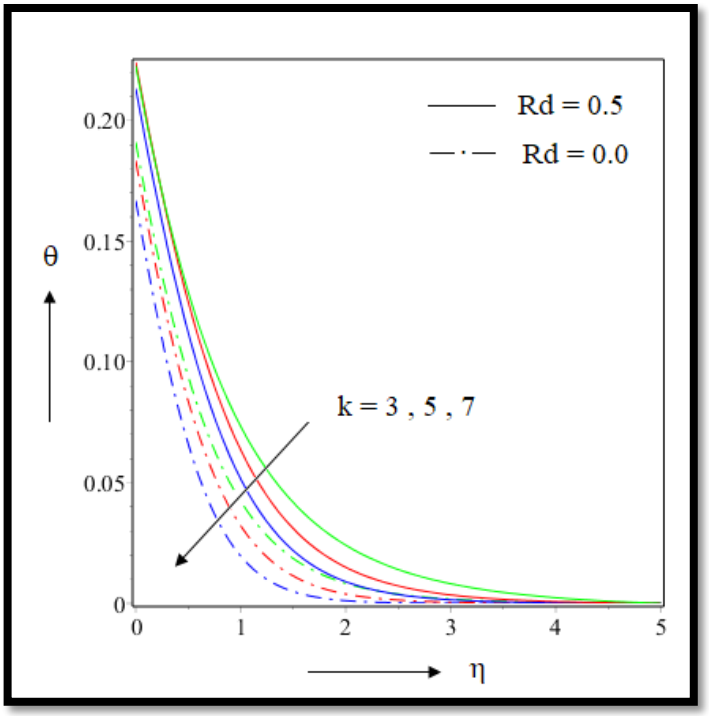

Figure 8.8: Effect of k on $\theta(\eta)$.

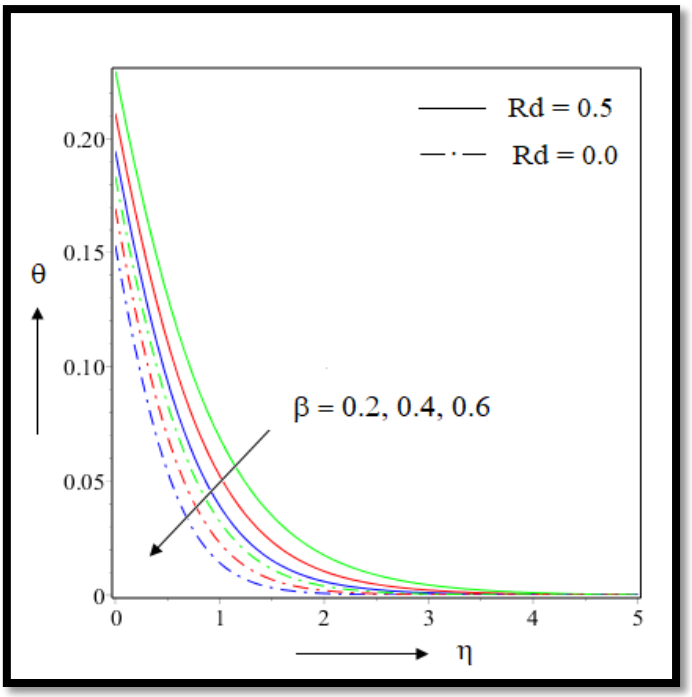

Figure 8.9: Effect of β on $\theta(\eta)$.

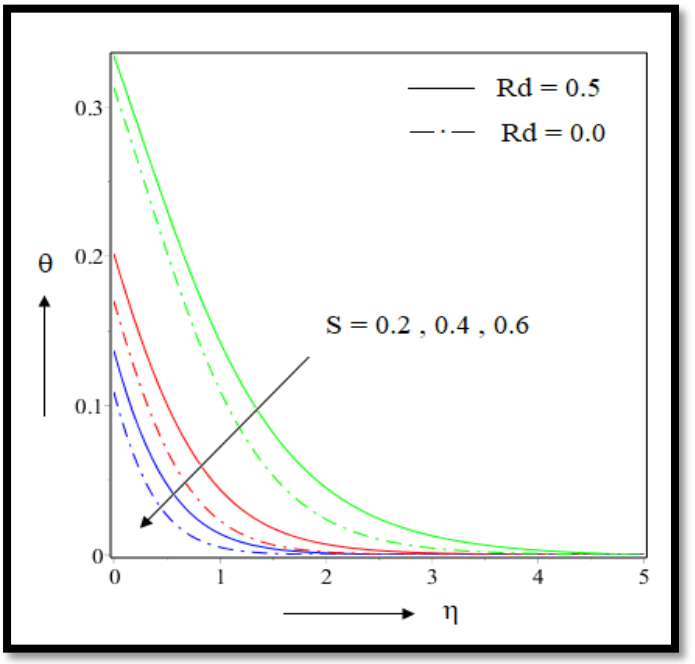

Figure 8.10: Effect of S on $\theta(\eta)$.

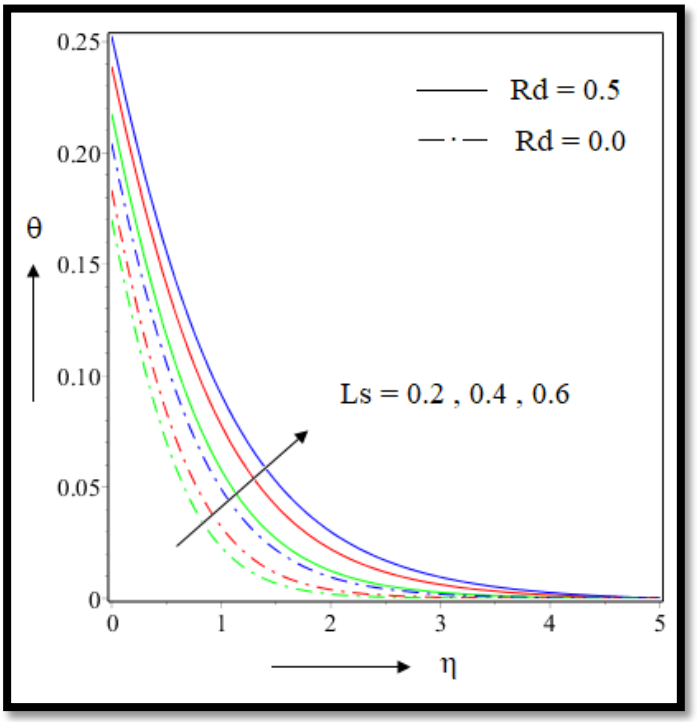

Figure 8.11: Effect of Ls on $\theta(\eta)$.

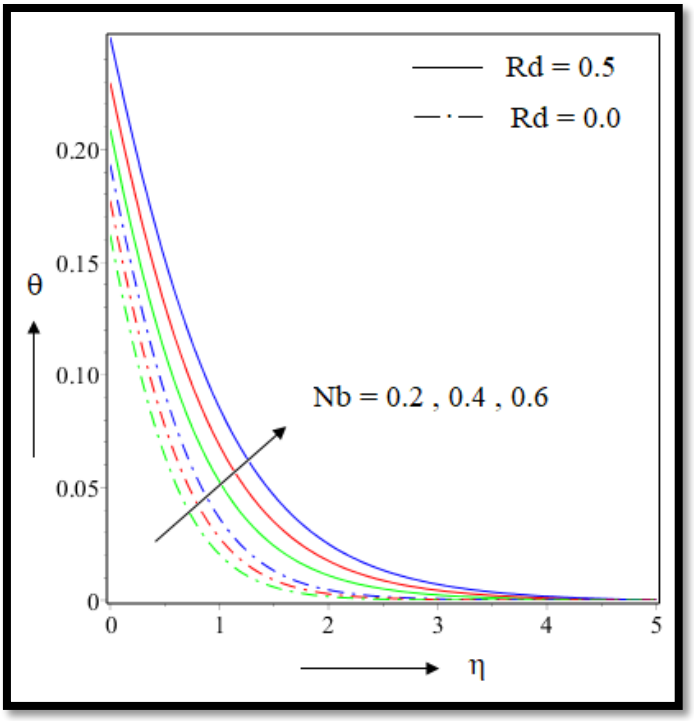

Figure 8.12: Effect of Nb on $\theta(\eta)$.

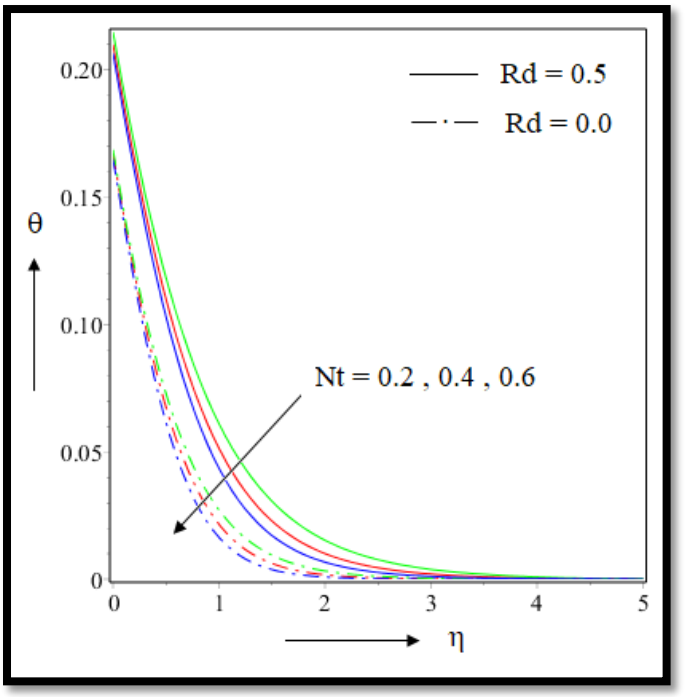

Figure 8.13: Effect of Nt on $\theta(\eta)$.

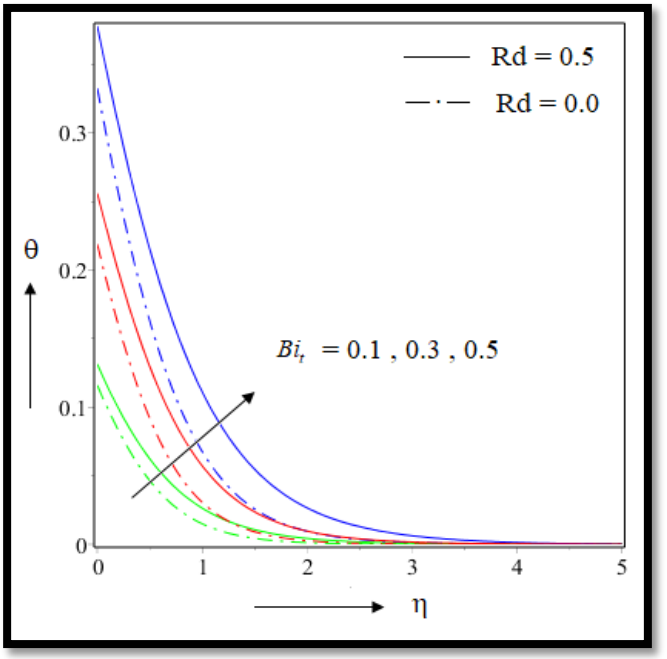

Figure 8.14: Effect of Bi_t on $\theta(\eta)$.

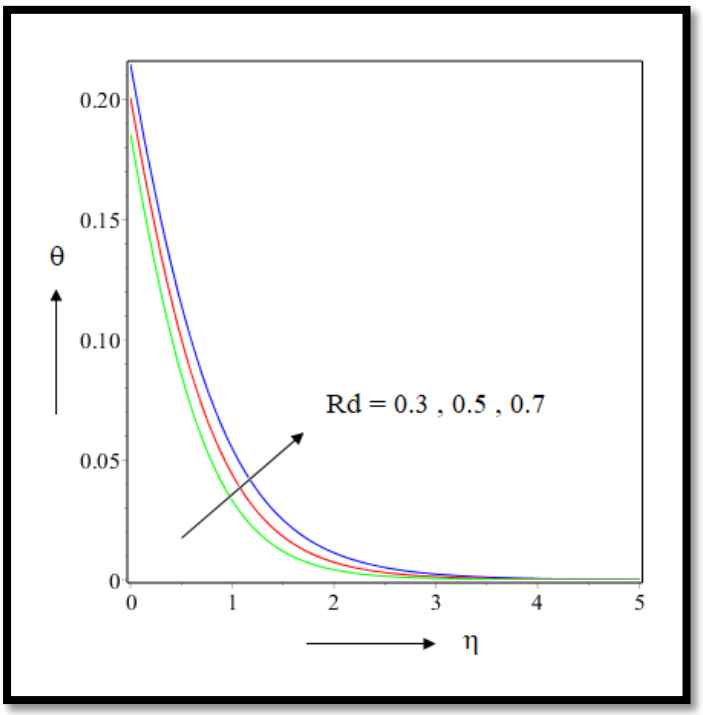

Figure 8.15: Effect of Rd on $\theta(\eta)$.

8.4.3. Effect of Chemical reaction parameter Kr

The concentration lines in Figure 8.16 is also increased as we increase magnetic parameter. We noticed that the chemical reaction free flow gives higher concentration profile. Consequences are promising in the interval $0.0 \le \eta \le 3.0$. 6.94% deflection of Sherwood number focused the obtained result. In Table 8.4 we can observe the deflection of Sherwood number for various parameter. As we increased the curvature parameter value the system get more flat. The flat surface get more space to flow the fluid. The fluid concentration get reduced and the flow identified to be smoother. The Sherwood number changed less than 1% for flow with chemical reaction but without chemical reaction it jumps to greater than 1%. Figure 8.17 displays the effect graphically. The negative sign in front of chemical reaction parameter in the system equation is the reason behind this. The sequel of Casson parameter over concentration profile is also similar like curvature parameter which can be seen in Figure 8.18. A decay in concentration is found for higher value of Casson parameter. Chemical reaction swallow the fluid chemicals owing to this we notice turn down in concentration. Sherwood number increased by 2.1% in case of flow with chemical reaction whereas it increased 3.03% for flow without chemical reaction. As we increase the suction injection parameter more fluid is injected into the system and as a sequel the velocity get increased. Figure 8.19 confirms that the concentration profile is decreased due to higher value of this parameter. The reduced governing equation bears a negative sign in the co efficient of chemical reaction variable and thus the concentration profile reduced. For flow with chemical reaction 7.94% increment in Sherwood number is found in Table 8.4 but for chemical reaction free flow it is reduced to 6.31% only. It is seen from Figure 8.20 that the concentration of liquid in boundary layer increases with an augmentation in the concentration Biot number.

Surprisingly the Sherwood number deflected by 54.32% for higher value of Biot number. The dominance is confirmed in the interval $0.0 \le \eta \le 2.0$. Slip parameter also behave analogous to the Biot number. The higher magnitude is observed for chemical reaction free flow. The upshot is more prominent in the interval $0.0 \le \eta \le 3.0$. Sherwood number is declined by 2.89% for Casson flow with chemical reaction. When we remove the chemical reaction from the system the deflection in Sherwood number is changed to 3.29%. Figure 8.21 confirms that concentration profile is increased due to higher value of slip parameter. We can observe that as Sc increases, concentration profile diminishes. Reason behind this is inversely proportionate of Sc to mass

diffusivity. Therefore, an enhancement in values of Sc brings down mass diffusion and in turn reduces concentration Profile. From Figure 8.22 it is easily observed that chemical reaction free flow gives higher magnitude of concentration profile. 8.52% change in Sherwood number is seen in Table 8.4. The accurate observation can be detected in the interval $0.0 \le \eta \le 3.0$. Higher order chemical reaction increase the concentration of boundary layer which is depicted by Figure 8.23. When we take the quadratic order chemical reaction the concentration increased suddenly very high. Change in Sherwood number by 6.48% is seen in Table 8.4. Cubic order chemical; reaction also increase the concentration profile but with low rate. 1.63% deflection in Sherwood number confirms the fact. Higher value of chemical reaction parameter reduce the concentration profile. In the reduced governing equation 8.13 we observe that co efficient of chemical reaction parameter is equipped with a negative sign. So as we increase the chemical reaction parameter the concentration reduced. The graph in Figure 8.24 shows more accurate observation in the interval $0.0 \le \eta \le 3.0$ .In Table 8.5 we can see 2.51% deflection of Sherwood number.

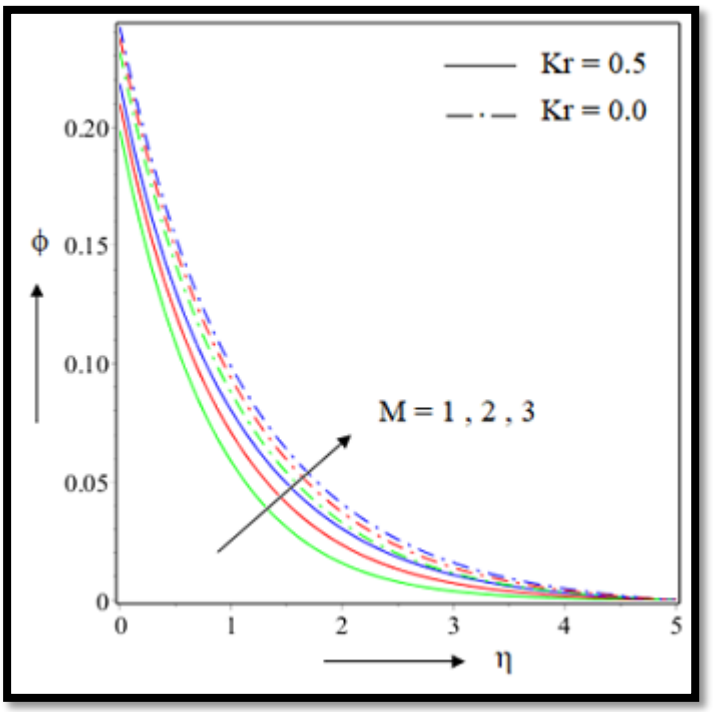

Figure 8.16: Effect of M on $\phi(\eta)$.

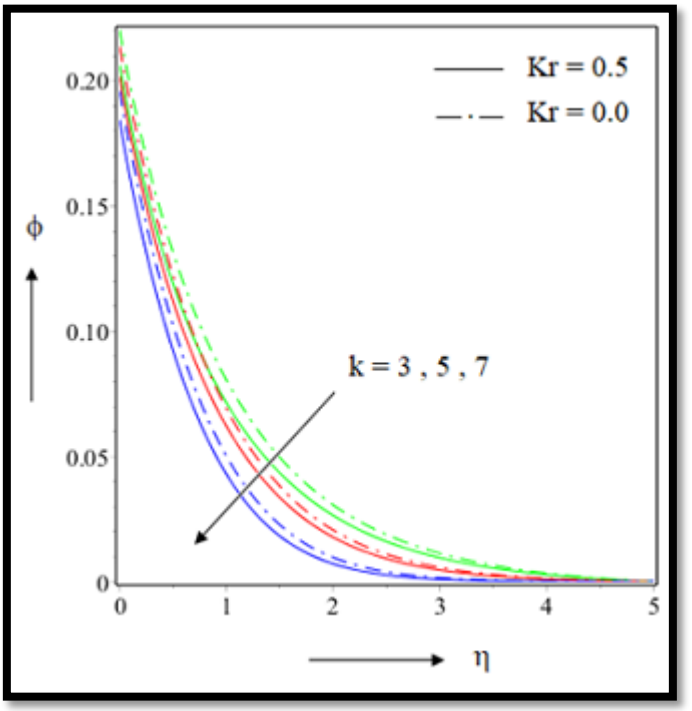

Figure 8.17: Effect of k on $\phi(\eta)$.

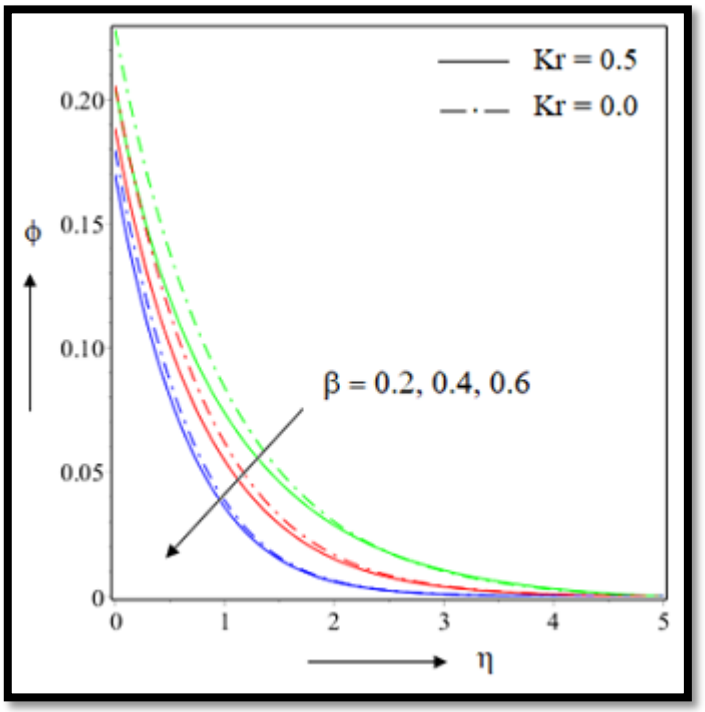

Figure 8.18: Effect of β on $\phi(\eta)$.

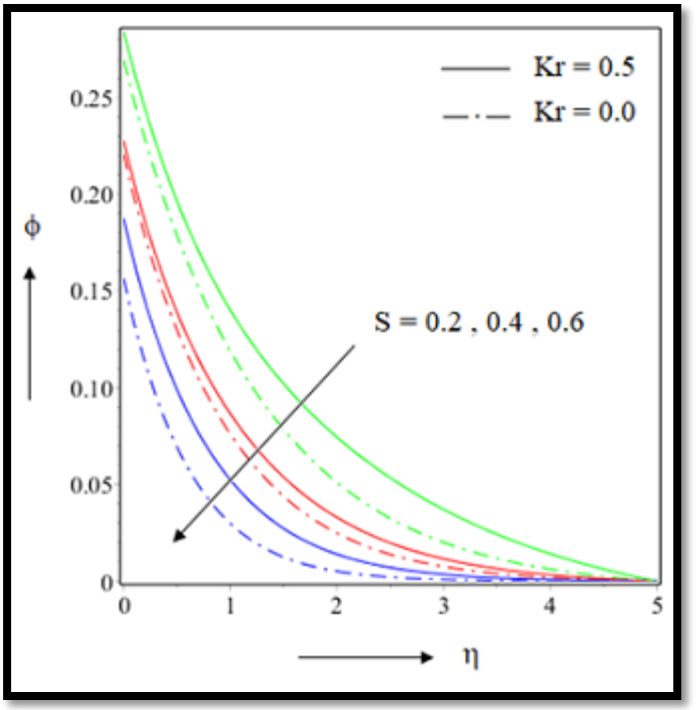

Figure 8.19: Effect of S on $\phi(\eta)$.

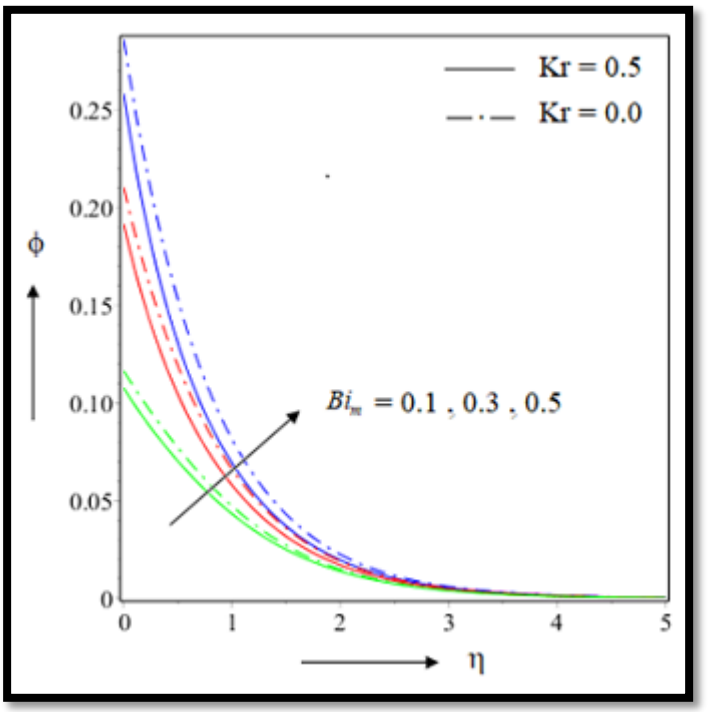

Figure 8.20: Effect of Bi_m on $\phi(\eta)$.

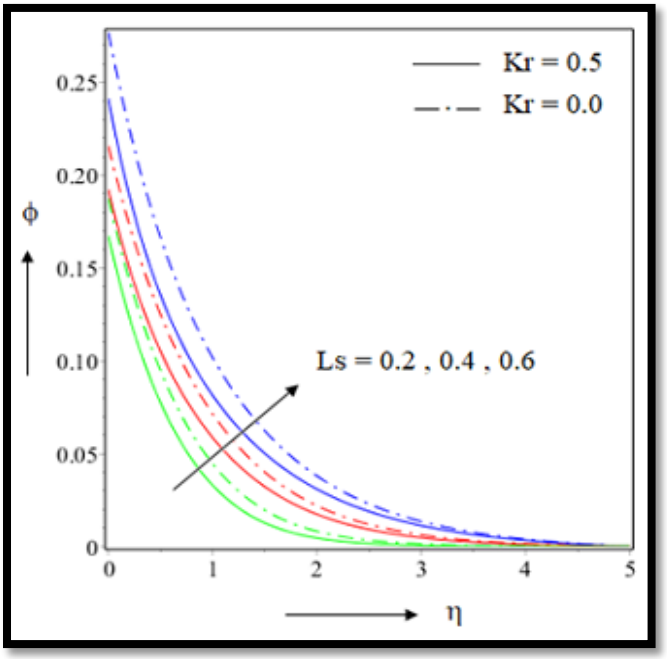

Figure 8.21: Effect of Ls on $\phi(\eta)$.

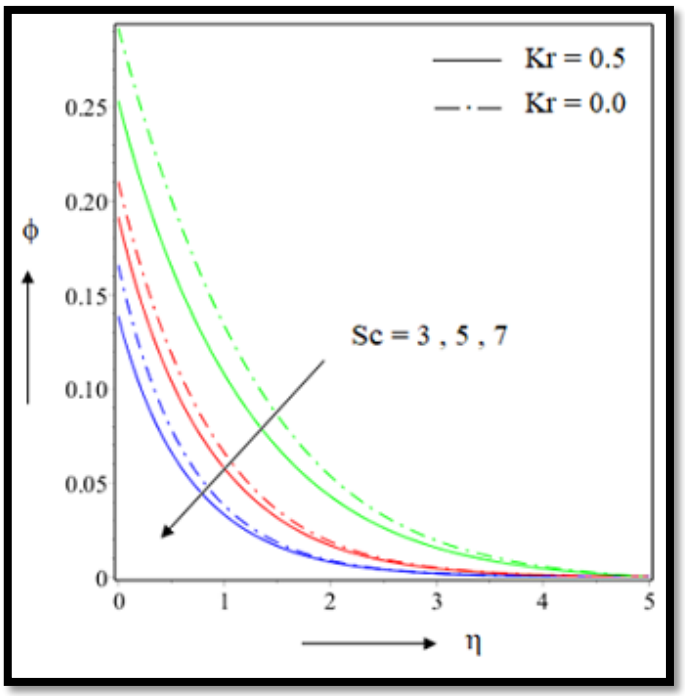

Figure 8.22: Effect of Sc on $\phi(\eta)$.

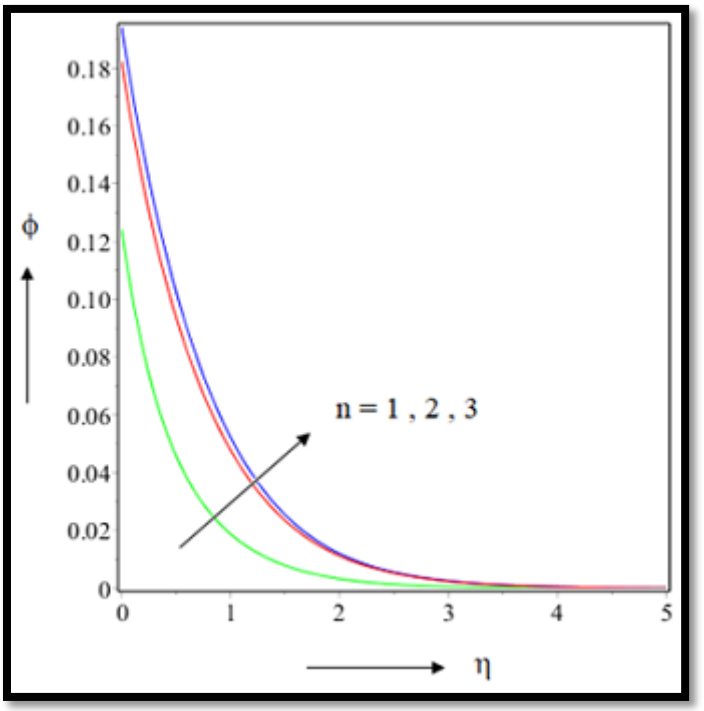

Figure 8.23: Effect of n on $\phi(\eta)$.

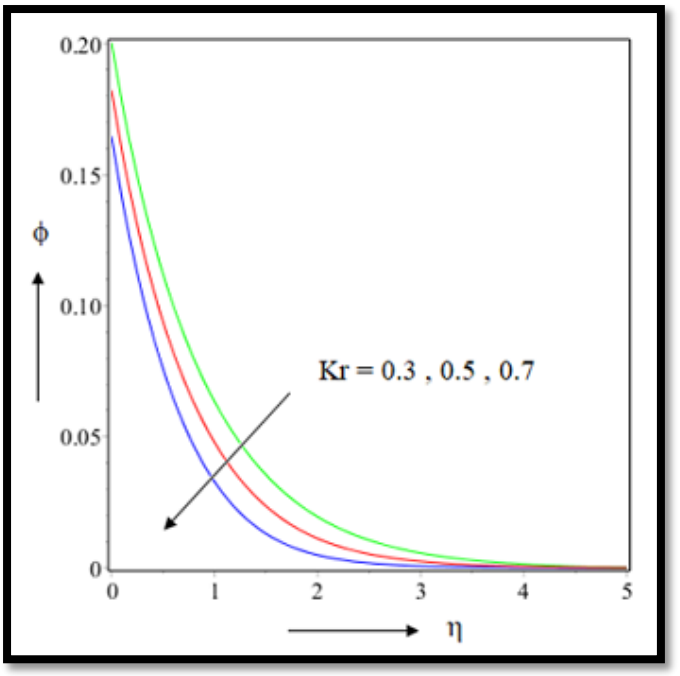

Figure 8.24: Effect of Kr on $\phi(\eta)$.

8.5. Conclusion

Chemically reactive Casson nanofluid flow over a curved stretching sheet is investigated numerically. Comparison is done over slip and no slip condition, radiative and non radiative condition and chemically reactive and chemically non-reactive condition. Brownian and thermophoretic migration have been considered to reveal the hydrothermal outcomes. Graphs and tables are exhibited to explore the outcomes. Based on the investigation, following interpretations are drawn:

- Increase in magnetic field decreases the velocities but temperature and concentration profile are increased. In case of Casson parameter, the temperature, concentration profile get decreased when we increase the value of parameter. But velocity in slip condition is increased and in no slip condition it is reduced.
- For curvature parameter as we increase the value the stretching sheet became more flat and the velocity enhanced but temperature and concentration is decayed.
- Velocity profile is also similarly increased for higher value suction parameter but temperature and concentration reduced. No slip condition and chemically non-reactive condition give higher magnitude of velocity and temperature but in non radiative condition we get lower magnitude of temperature profile.
- Brownian motion parameter increase the temperature profile but thermophoresis parameter reduce it but in both case we get lower magnitude for non radiative flow.
- Mass Biot number and temperature Biot number both increase the concentration of boundary layer and temperature of the system.
- Schmidt number and chemical reaction parameter decrease the concentration profile but when we increase the order of chemical reaction it makes the concentration value higher.

Table 8.2: Effect of suitable parameters on skin friction

M	k	β	S	Cf_r	
				$Ls = 0.5$	$Ls = 0.0$
1.0	5	0.4	0.4	-1.526717	-3.008002
2.0				-1.580573	-3.227564
3.0				-1.634578	-3.434991
2.0	3			-0.834533	-1.760820
	5			-0.772102	-1.583935
	7			-0.758156	-1.495653
	3	0.2		-1.559704	-4.332966
		0.4		-1.254667	-3.702597
		0.6		-1.055894	-2.852080
		0.4	0.2	-1.814009	-3.040878
			0.4	-1.171977	-2.360969
			0.6	-0.742106	-1.868016

Table 8.3: Effect of suitable parameters on heat transfer

M	k	Nb	Nt	Ls	β	S	Bi_t	Nu_r	
								$Rd=0.5$	$Rd=0.0$
1.0	5	0.4	0.4	0.4	0.4	0.4	0.3	0.390353	0.248883
2.0								0.382697	0.243331
3.0								0.378515	0.238744
2.0	3							0.388684	0.246693
	5							0.387944	0.245995
	7							0.386864	0.244949
	5	0.2						0.392529	0.249404
		0.4						0.394958	0.249836
		0.6						0.396723	0.250482
		0.4	0.2					0.395545	0.251391
			0.4					0.385158	0.246821
			0.6					0.375055	0.242022
			0.4	0.2				0.391129	0.248961
				0.4				0.380503	0.244995
				0.6				0.373707	0.238710
				0.4	0.2			0.385158	0.244995
					0.4			0.394450	0.249216
					0.6			0.402733	0.254042
					0.4	0.2		0.332810	0.206201
						0.4		0.399115	0.248961
						0.6		0.431536	0.267301
						0.4	0.1	0.289501	0.176798
							0.3	0.495998	0.312430
							0.5	0.621936	0.400404

Table 8.4: Effect of suitable parameters on mass transfer

M	k	β	Ls	Sc	η	Bi_m	S	Sh_r	
								$Kr = 0.5$	$Kr = 0.0$
1.0	5	0.4	0.4	5	2	0.3	0.4	0.240399	0.230425
2.0								0.236991	0.228637
3.0								0.234445	0.227209
0.5	3							0.238084	0.233869
	5							0.239426	0.235842
	7							0.244606	0.241148
	5	0.2						0.238390	0.231457
		0.4						0.243370	0.238207
		0.6						0.248961	0.246045
		0.4	0.2					0.249738	0.243725
			0.4					0.242272	0.235215
			0.6					0.303402	0.289126
			0.4	3				0.223927	0.212296
				5				0.242489	0.236853
				7				0.215254	0.250139
				5	1			0.262736	_
					2			0.245303	_
					3			0.241737	_
					2	0.1		0.089234	0.088360
						0.3		0.242489	0.236853
						0.5		0.370743	0.356818
						0.3	0.2	0.214758	0.219207
							0.4	0.231672	0.233794
							0.6	0.243714	0.253001

Table 8.5: Effect of suitable parameters on skin friction, heat transfer and mass transfer

Ls	Kr	Rd	Cf_r	Nu_r	Sh_r
0.2	0.5	0.5	1.603502	_	_
0.4			1.031205	_	_
0.6			0.760928	_	_
0.4	0.3		_	_	0.239836
	0.5		_	_	0.245303
	0.7		_	_	0.250573
	0.5	0.3	_	0.406999	_
		0.5	_	0.399428	_
		0.7	_	0.392480	_

CHAPTER 9

Active and passive control of nanoparticles under the influence of magnetized nanofluid flow over a convectively heated slippery wedge*

9.1. Introduction

Laminar flow through a surface is an important problem in fluid dynamics. Among them in Blasius problem fluid velocity is likely to be constant. Here free stream flows parallel to the surface. Sometimes surface makes an angle with free stream, which is termed as Wedge flow problem. Falkner and Skan [156] first investigated the wedge problem assuming two dimensional viscous compressible fluid flow. In general the wedge angle is taken as $\beta\pi$. When $\beta = 0$, the flow corresponds to a flat plate, which reduces the well known Blasius problem. However, for $\beta > 0$ and $\beta < 0$ the flow goes towards the wedge and opposite to it respectively. Unique solution of Falkner equation is achieved by Stewartson [157] and Hastings [158].

To the author's knowledge, any investigation for wedge flow of nanofluid with active and passive controlled nanoparticle volume fraction has not been reported in the literature. Velocity slip and convective condition are included to get more realistic structure. Moreover, we have taken an external heat source and magnetic field over the system. Leading equations of the system are converted to ODEs with the help of suitable similarity transformation. MAPLE-2019 software is used to solve the system numerically by RK-4 shooting technique. The results thus obtained have beenverified with the previous results [159]. Several graphs and tables are included, which gives a prominent knowledge about the characteristics of the nanofluid flow. We mainly focus on the following points.

- The effect of several parameters over velocity profile and related skin friction coefficients.
- The effect of several parameters over temperature profile and related Nusselt numbers.

***This chapter is based on the paper published in: Journal of Nanofluids, 12(8) (2023), 2273-2284, (ESCI).**

- The effect of several parameters over concentration profile and related Sherwood numbers.

9.2. Mathematical formulation

9.2.1. Governing equations

Let us assume

- A steady laminar nanofluid flow over a permeable stretching wedge.
- The angle of wedge is given by $\Omega = \beta\pi$ and $\beta = \frac{2m}{m+1}$ is known as wedge angle parameter.
- The flow is along the x axis which is taken along the direction of the wedge and y axis is taken perpendicular to it.
- Fluid suction and injection is also incorporated on the wedge surface.
- T_f and C_w is respectively wedge surface temperature and concentration. Ambient temperature and concentration are taken as T_∞ and C_∞.
- We have taken fluid velocity as $U(x) = ax^m$.
- We have neglected the body forces and also we have assumed that there is no chemical reaction and radiative heat transmission between fluid and nanoparticles.

Under this assumption the governing equation [159,160] of system is as follows.

$$\frac{\partial u}{\partial x} + \frac{\partial v}{\partial y} = 0 \tag{9.1}$$

$$u\frac{\partial u}{\partial x} + v\frac{\partial v}{\partial y} = -\frac{1}{\rho_f}\frac{\partial p}{\partial x} + \nu\frac{\partial^2 u}{\partial y^2} - \frac{\sigma_f}{\rho_f}B_0^2\left(u - U(x)\right) \tag{9.2}$$

$$u\frac{\partial T}{\partial x} + v\frac{\partial T}{\partial y} = \frac{\kappa_f}{\left(\rho C_p\right)_f}\frac{\partial^2 T}{\partial y^2} + \frac{Q}{\left(\rho C_p\right)_f}\left(T - T_\infty\right) + \tau\left[D_B\frac{\partial C}{\partial y}\frac{\partial T}{\partial y} + \frac{D_T}{T_\infty}\left(\frac{\partial T}{\partial y}\right)^2\right] \tag{9.3}$$

$$u\frac{\partial C}{\partial x}+v\frac{\partial C}{\partial y}=D_B\frac{\partial^2 C}{\partial y^2}+\frac{D_T}{T_\infty}\frac{\partial^2 T}{\partial y^2} \tag{9.4}$$

Here u and v are the velocity components along x and y axis respectively.

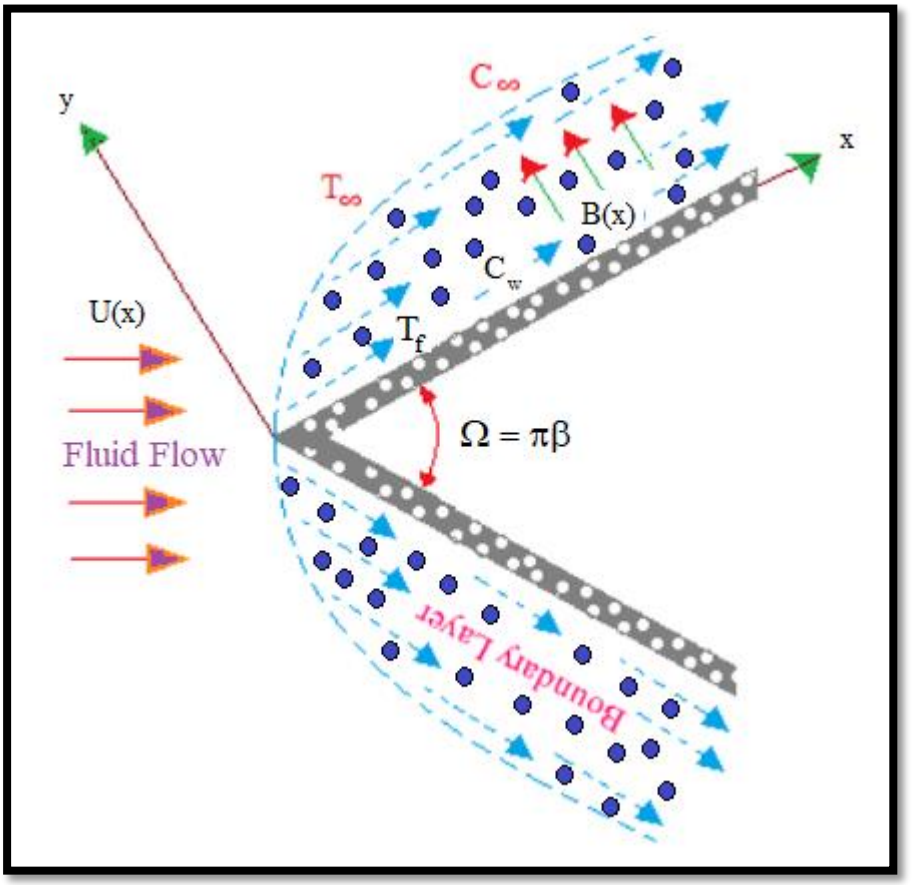

Figure 9.1: Physical geometry of the flow

9.2.2. Boundary conditions

The boundary provisions [159,160] for the above introduced model are given by the following equations:

$$u=u_{slip}=\lambda_0\left(\frac{2-\sigma_M}{\sigma_M}\right)\left.\frac{\partial u}{\partial n}\right|_{wall}+\frac{3v}{4T_g}\left.\frac{\partial T}{\partial s}\right|_{wall},\ v=v_w\ ,\ k\frac{\partial T}{\partial y}=h_f\left(T_f-T\right) \tag{9.5}$$

$$\begin{cases} D_B \dfrac{\partial C}{\partial y} + \dfrac{D_T}{T_\infty}\dfrac{\partial T}{\partial y} = 0, & \text{for passive control of } \phi \\ C = C_w\,, & \text{for active control of } \phi \end{cases} \text{, at } y = 0 \qquad (9.6)$$

$$u = U(x)\,,\ T \to T_\infty\,,\ C \to C_\infty \quad \text{at} \quad y \to \infty \qquad (9.7)$$

Here u_{slip} is wall slip velocity, λ_0 is the free molecular mean path. σ_M is tangential momentum accommodation coefficient. $\dfrac{\partial u}{\partial n}$ and $\dfrac{\partial T}{\partial s}$ are velocity gradient along normal to the wall and temperature gradient along the wall. $U(x)$ is the free stream velocity.

9.2.3. Similarity transformations

We convert the foremost flow equations (9.1-9.4) into system of ODEs by the following similarity variables [159,160] as in

$$\eta = y\sqrt{\frac{m+1}{2}\frac{a}{\upsilon_\infty}}x^{\frac{m-1}{2}} \qquad \psi = \sqrt{\frac{2a\upsilon_\infty}{m+1}}x^{\frac{m+1}{2}} f(\eta) \qquad \theta(\eta) = \frac{T - T_\infty}{T_w - T_\infty}$$

$$\begin{cases} \phi(\eta) = \dfrac{C}{C_\infty} - 1\,, & \text{for passive control of } \phi \\ \phi(\eta) = \dfrac{C - C_\infty}{C_w - C_\infty}\,, & \text{for active control of } \phi \end{cases} \qquad (9.8)$$

$\upsilon_\infty = \dfrac{\mu_\infty}{\rho}$ is the ambient kinematic viscosity of the fluid. ψ Stands for stream function.

Free stream function $\psi(x, y)$ can be defined as $u = \dfrac{\partial \psi}{\partial y}$ and $v = -\dfrac{\partial \psi}{\partial x}$

The velocity components along the axes are given by as follows.

$$u = U(x) f'(\eta)$$

$$v=-\sqrt{\frac{m+1}{2}\upsilon_\infty a x^{m-1}}\left[f(\eta)+\frac{m-1}{m+1}\eta f'(\eta)\right]$$

Applying non dimensional structure we found equation (9.1) satisfies automatically. After dropping pressure term equations (9.2-9.4) are transfigured as follows.

$$f'''+ff''+\beta\left(1-f'^2\right)+M\left(\frac{2}{m+1}\right)(1-f')=0 \tag{9.9}$$

$$\theta''+\Pr\, f\theta'+\Pr\, Nb\theta'\phi'+\Pr\, Nt\theta'^2+\frac{2}{m+1}\delta\theta=0 \tag{9.10}$$

$$\phi''+Lef\,\phi'+\frac{Nt}{Nb}\theta''=0 \tag{9.11}$$

Corresponding boundary equations are also changed as follows.

$$\begin{cases} f(0)=S,\ f'(0)=Lsf''(0),\theta'(0)=Bi_t\sqrt{2-\beta}\left(\theta(0)-1\right) \\ \begin{cases} Nb\phi'(0)+Nt\theta'(0)=0\,, & \text{for passive control of } \phi \\ \phi(0)=1\,, & \text{for active control of } \phi \end{cases} \end{cases} \tag{9.12}$$

$$f'(\infty)=1,\theta(\infty)=0,\phi(\infty)=0 \tag{9.13}$$

$S=\dfrac{v_w\sqrt{1-\beta}}{\upsilon x^{\frac{m-1}{2}}}$ Represents wall mass transfer co efficient which is positive for suction and negative for injection. Here we have v_w proportional to $x^{\frac{m-1}{2}}$ so we get constant value of parameter S.

Here $Ls=\sqrt{\dfrac{m+1}{2}}\left(\dfrac{2-\sigma_M}{\sigma_M}\right)Kn_x\,\mathrm{Re}_x^{1/2}$ denoted as slip parameter where $Kn_x=\dfrac{\lambda}{x}$ is the local Kundsen number. In the above expression we observe that Ls, Kn_x, Re_x are function of x. So they are called local parameters and we are going to find local similarity solution. [161-163] Local similarity technique also conserves the mass and momentum equations [164] so the investigation of flow analysis is quite noteworthy. Hence the equations (9.9-9.11) are locally similar for fixed values of x.

$M = \dfrac{\sigma B_0^2 x}{\rho U(x)}$, $\delta = \dfrac{Qx}{(\rho C_p)_f U(x)}$

$Bi_t = \dfrac{h_f x}{k} \mathrm{Re}_x^{-1/2}$ and $\mathrm{Pr} = \dfrac{\nu_f}{\alpha_f}$ stands for Thermal Biot number and Prandtl number. h_f is the convective heat transfer coefficient. $M = \dfrac{\sigma_f B_0^{\ 2}}{a\rho_f}$ designates Magnetic parameter, δ and Le designates external heat source parameter and Lewis number. $Nt = \dfrac{\tau D_T (T_w - T_\infty)}{T_\infty \nu_f}$ is thermophoresis parameter.

$$\begin{cases} Nb = \dfrac{\tau D_B C_\infty}{\nu_f}, & \text{for passive control of } \phi \\ Nb = \dfrac{\tau D_B (C_w - C_\infty)}{\nu_f}, & \text{for active control of } \phi \end{cases}$$

is denoted as Brownian migration parameter.

9.2.4. Physical quantities

Appropriate physical quantities which are most useful for engineering applications are

$$\left.\begin{aligned} C_f &= \frac{2\mu_f}{\rho_f U^2}\left(\frac{\partial u}{\partial y}\right)_{y=0} \\ Nu &= -\frac{x\kappa}{\kappa_\infty (T_w - T_\infty)}\left(\frac{\partial T}{\partial y}\right)_{y=0} \\ Sh &= -\frac{x}{(C_w - C_\infty)}\left(\frac{\partial C}{\partial y}\right)_{y=0} \end{aligned}\right\} \qquad (9.14)$$

Here C_f denotes local skin friction Nu stands for local Nusselt number and Sh stands for local Sherwood number respectively. Applying similarity variables, we came into the reduced parameters as

$$C_{f_r} = \frac{2}{\sqrt{2-\beta}} f''(0)$$

$$Nu_r = -\frac{1}{\sqrt{2-\beta}} \theta'(0)$$

$$Sh_r = \begin{cases} -\frac{1}{\sqrt{2-\beta}} \frac{\phi'(0)}{\phi(0)}, & \text{for passive control of } \phi \\ -\frac{1}{\sqrt{2-\beta}} \phi'(0), & \text{for active control of } \phi \end{cases} \quad (9.15)$$

9.3. Numerical procedure

9.3.1. Solution technique

The system of equations (9.1-9.4) are highly non linear. So it is very difficult to solve by any analytical method. In this case the framework is solved by numerical structure. Rk-4 method with shooting technique is adopted to solve the required solution. The whole simulation is done by MAPLE – 2019 software. Outcomes of the inspection is described by graphs and tables in subsequent sections. Proper programme of the above problem leads us to a numerical outcomes up to 10^{-6} degree of exactness. The code is also validated by appropriate results.

9.3.2. Code verification:

We validate our results and outcomes by comparing it with similar type of previous results. We have computed the values of $f(\eta)$ and $f'(\eta)$ to check the efficiency of our programme. We have dropped velocity slip parameter and take suitable values of other parameter to covert our system similar with Rahaman and Eltayeb [159]. The values of $f(\eta)$ and $f'(\eta)$ are compared with our present work and it is noted that the values are well justified. Hence our numerical code is properly written.

Table 9.1: Comparison of numerical outcomes of $f(\eta)$ and $f'(\eta)$ with previous studies

η	**Rahaman and Eltayeb [159]**	**Present Results**	**Rahaman and Eltayeb [159]**	**Present Results**
	$f(\eta)$	$f(\eta)$	$f'(\eta)$	$f'(\eta)$
0.0	0.000000	0.00000000	0.000000	0.00000000
0.1	0.002347	0.00234719	0.046959	0.04695971
0.2	0.093910	0.09391084	0.093905	0.09390554
0.3	0.021127	0.02112717	0.140805	0.14080521
0.4	0.037549	0.03754926	0.187605	0.18760568
0.5	0.058642	0.05864277	0.234227	0.23422714

9.4. Result and discussion

In this section we have discussed the results and outcomes found in our study. The upshots of various parameter are compared under active and passive control of nanofluid flow. Velocity lines are compared for suction and injection effect. Heat lines and mass lines are portrayed by appropriate graphs. We mainly emphasize on the comparison of active and passive controlled flow. The base values of several parameters are taken as follow throughout our simulation process.

The following sections contained the results and facts found in this inspection. The effect of various parameters are compared under active and passive control of nanoparticles. Magnetic parameter and Reynolds number are also compared und with slip and no slip conditions. Temperature slip parameter is analogized under active and passive control. Our main focus in this research is to observe the difference between active control and passive control of nanoparticles. The basic value of the parameter throughout the simulation is takes as follows.

$M = 2.0$, $\beta = 0.5$, $\mathrm{Ls} = 0.5, Bi_t = 0.5$, $\delta = 0.5$, $\mathrm{Le} = 1.0, Nb = 0.5$, $\mathrm{Nt} = 0.5$ }

9.4.1. Influence of Suction/Injection on Velocity

In the following section we have discussed the upshots of Magnetic parameter, wedge angle parameter, slip parameter and thermal Biot number on velocity under the influence of suction/injection effect. From Figure 9.2 it is clearly seen that for higher value of magnetic parameter velocity upraised for both suction and injection effect. Magnetic field is appointed in normal direction to the fluid flow. Which evidently help the nanofluid to get higher speed. Higher magnitude is observed for suction effect and skin friction value is increased by 7.31% but for injection situation 9.32% change is depicted from Table 9.2. Velocity lines are quite accurate in for similarity variable $0 \le \eta \le 2$ and converges asymptotically beyond that.

The upshots of wedge angle parameter on velocity profile is portrayed in figure 9.3. Here also the dimensionless velocity profile get increased due to greater wedge angle parameter value. It is clear from our assumption that for $\beta = 0$ we get flat plate and for $\beta = 0.5$ we get a vertical plate. Higher value of wedge angle parameter increase the X component of velocity and hence we observe increasing nature in the velocity lines. Rahaman and Eltayeb [159] also found similar result in their study with variable transport properties. For suction effect we observe higher magnitude than injection effect. Skin friction coefficient is changed by 23.01% suction effect and 37.23% for injection effect (Table 9.2 referred.). Prominent separation is observed for similarity variable lies between $0 \le \eta \le 2$.

Velocity slip parameter depends on velocity gradient along normal to the wall and temperature gradient along the wall. So for higher slip value velocity gradient escalates and as a result velocity lines also increased. Figure 9.4 shows the fact and also we observe prominent separation for similarity variable in $0 \le \eta \le 2$ and then it converges asymptotically. Injection effect i.e. for negative value of suction/injection parameter gives us lower magnitude of velocity.

In figure 9.5 effect of thermal Biot number is shown. Here also we get similar result like slip parameter. Large thermal Biot value produce more surface convection. Hence more heat is supplied to the surface of wedge. So we get a temperature difference between wedge surface and nanofluid which in turns escalates the velocity profile. Injection parameter reduce the magnitude of velocity. From Table 9.2 we get 10.56% increment in skin friction for suction effect and 7.25%

for injection effect. Prominence of velocity lines is observed for $0 \le \eta \le 2$ (not accurately determined) beyond that it converges asymptotically.

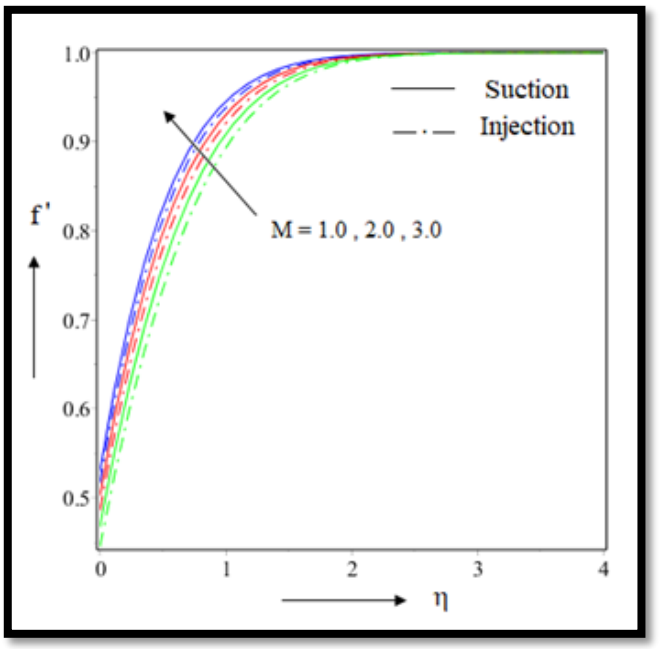

Figure 9.2: Effect of M on $f'(\eta)$.

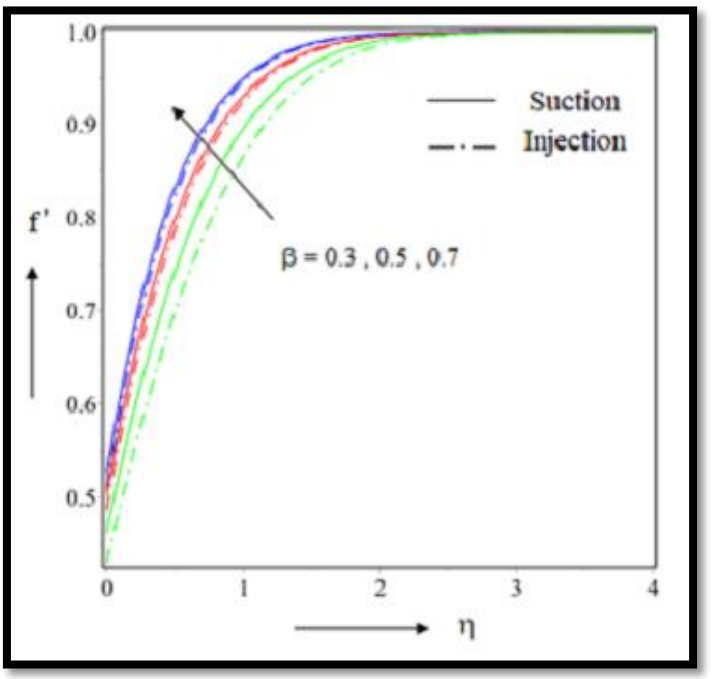

Figure 9.3: Effect of β on $f'(\eta)$.

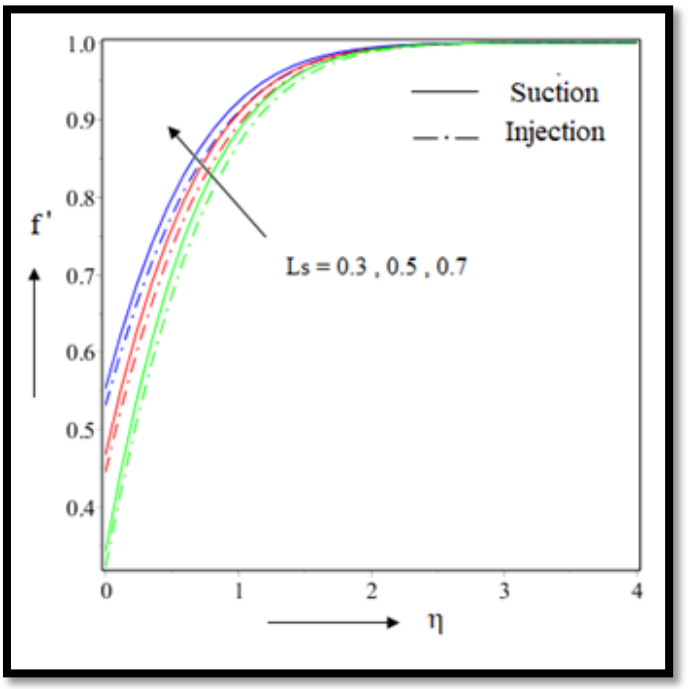

Figure 9.4: Effect of Ls on $f'(\eta)$.

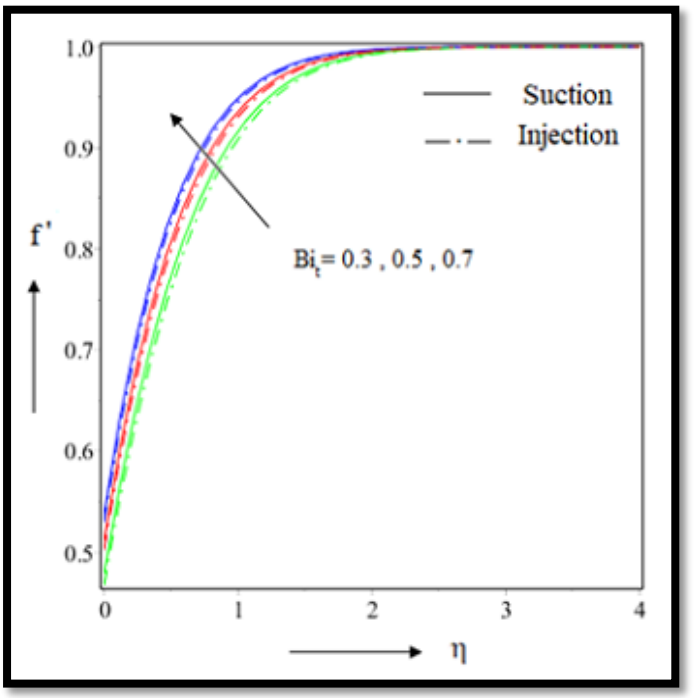

Figure 9.5: Effect of Bi_t on $f'(\eta)$.

9.4.2. Influence of active and passive control on Temperature

In figure 9.6 we observe the upshots of magnetic parameter over temperature. It is clear that foe higher value of magnetic parameter temperature upraised for both active and passive control. In case passively controlled nanofluid we get lower magnitude. Prominence is observed for similarity variable lies $0 \le \eta \le 0.5$ beyond that it converges asymptotically. Velocity profile got increased due to higher value of magnetic profile and hence more drag force is created in the system. This drag force generates more heat and as a result temperature got increased.

Wedge angle parameter also control the heat lines. In figure 9.7 we observe the outcomes of parameter effect. It is clear that temperature curtail down for higher value of wedge angle parameter. We compare it for both actively and passively controlled nanofluid flow and found lower magnitude of heat lines for passively controlled flow. The flow plate getting more flat for less value of wedge angle parameter and for $\beta = 0$ it changes to flat surface. So as this angle increased nanofluid can't run smoothly and more friction is created hence heat lines upraised. When the flow is controlled actively Nusselt number increased by 8.82% for active flow but for passively controlled flow the increment reduced by 8.51% only.

In figure 9.8 we portrayed upshots of velocity slip parameter on heat lines. Velocity slip is mainly the measurement of difference between flow velocity and surface. As the value of slip parameter increased the difference also increased and the flow get smoother hence less drag force created. Heat lines are decreased due to the lower value of drag force. Prominent difference is observed for $0 \le \eta \le 0.5$ and after that it converges asymptotically. For passive controlled flow less temperature value is found.

Heat source parameter and Lewis number increased the temperature profile almost similarly. For both cases passively controlled flow gives lower temperature value. Figure 9.9 and 9.10 shows the upshots of these parameter on heat lines. For both parameter we get less temperature value for passively controlled flow. Heat source parameter generates more heat in the system and that escalates the heat lines. Lewis number is the ratio between thermal diffusivity and mass diffusivity. Increment in Lewis number gives higher thermal diffusivity. High thermal diffusivity literally transfer the heat more rapidly. This is the main reason behind the elevated het lines.

Brownian motion and thermophoresis also gives analogous result on heat transfer profile. Generally we assumed there is no normal flux at surface. Nanoparticle fraction values adjusted this feature accordingly. For constant nanoparticle concentration at surface we take active controlled flow but when a new set of boundary condition is introduced to get more realistic approach of flow it is called passively controlled flow. Here Brownian motion Thermophoresis value is more realistic than actively controlled flow. Heat lines are upraised for higher value of Nb and Nt parameter ehich is shown in figure 9.11 and 9.12 Prominent difference is observed for $0 \le \eta \le 0.5$. Passively controlled flow gives less temperature value than that of actively controlled flow. From Table 9.3 we observe that reduced nusselt number is decreased by 2.63% for passively controlled nanofluid flow.

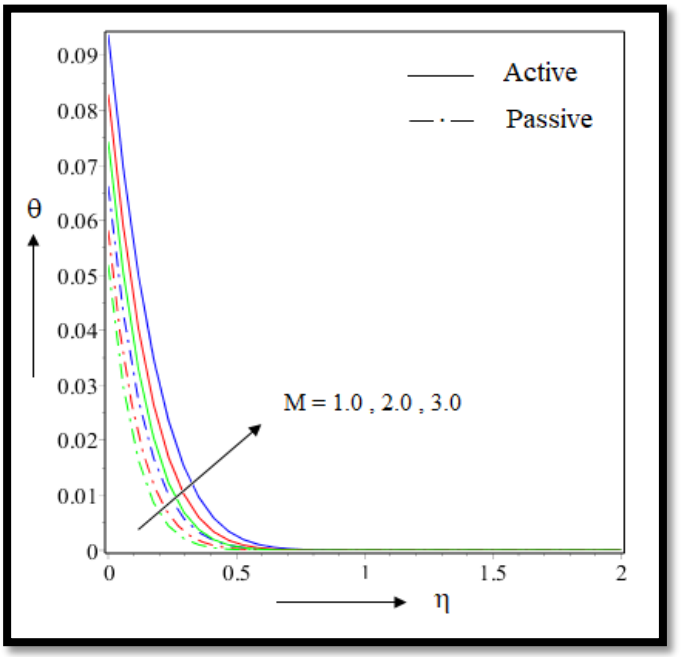

Figure 9.6: Effect of M on $\theta(\eta)$.

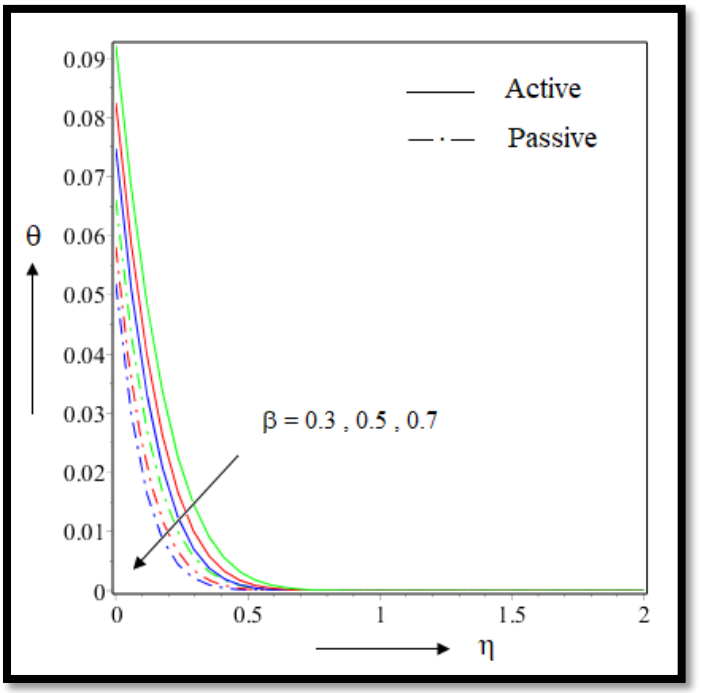

Figure 9.7: Effect of β on $\theta(\eta)$.

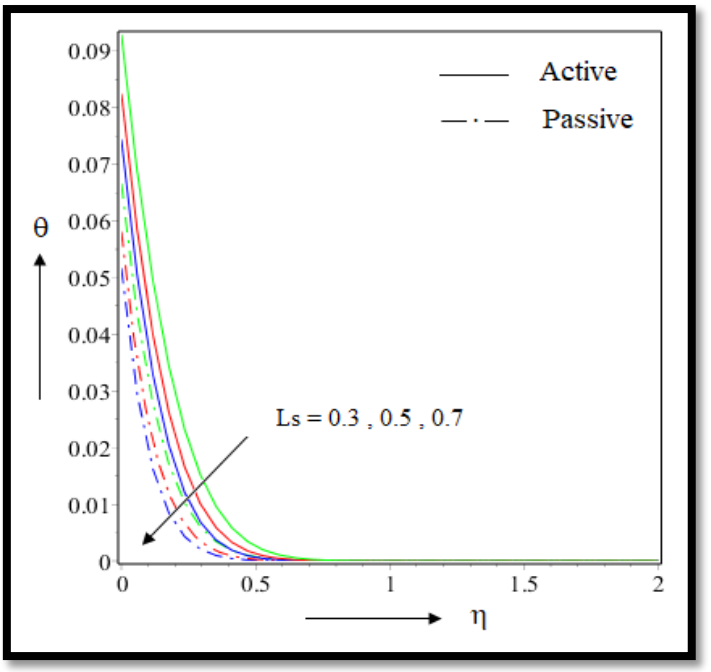

Figure 9.8: Effect of Ls on $\theta(\eta)$.

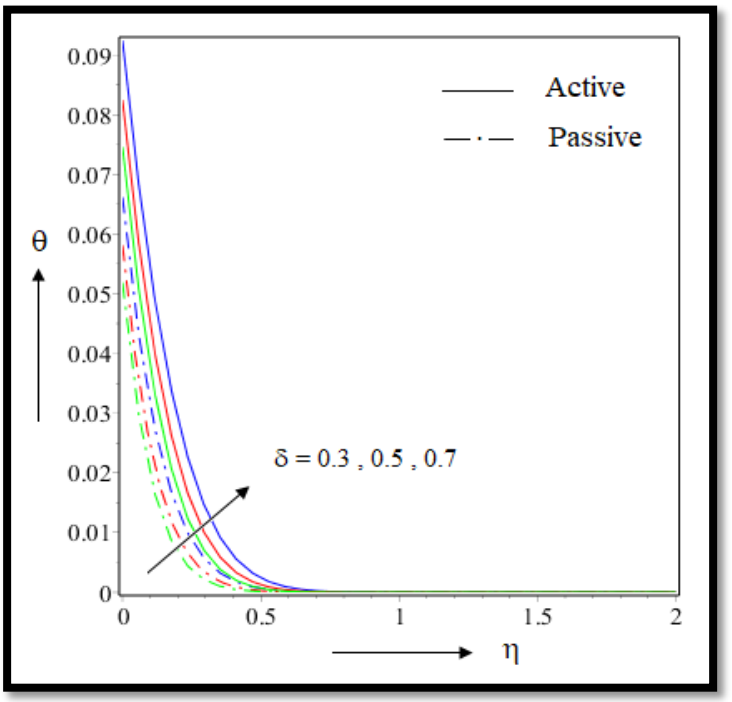

Figure 9.9: Effect of δ on $\theta(\eta)$.

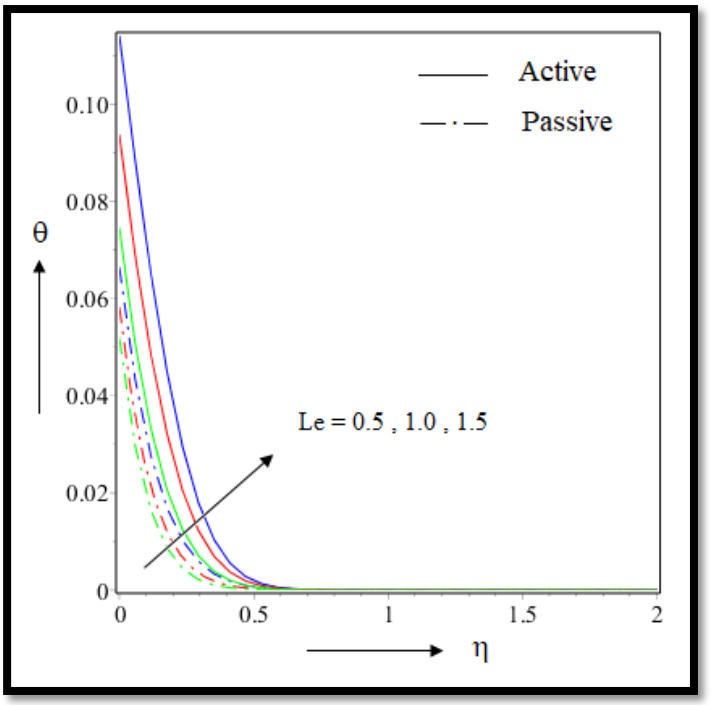

Figure 9.10: Effect of Le on $\theta(\eta)$.

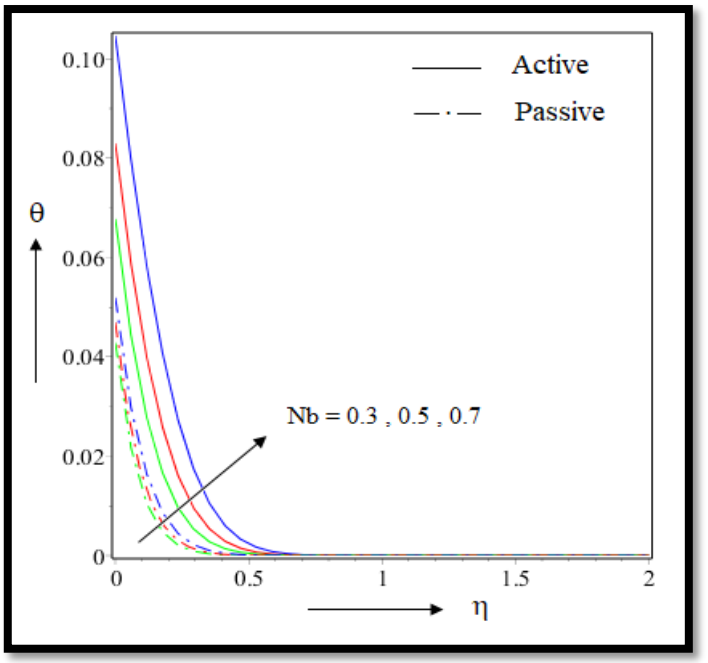

Figure 9.11: Effect of Nb on $\theta(\eta)$.

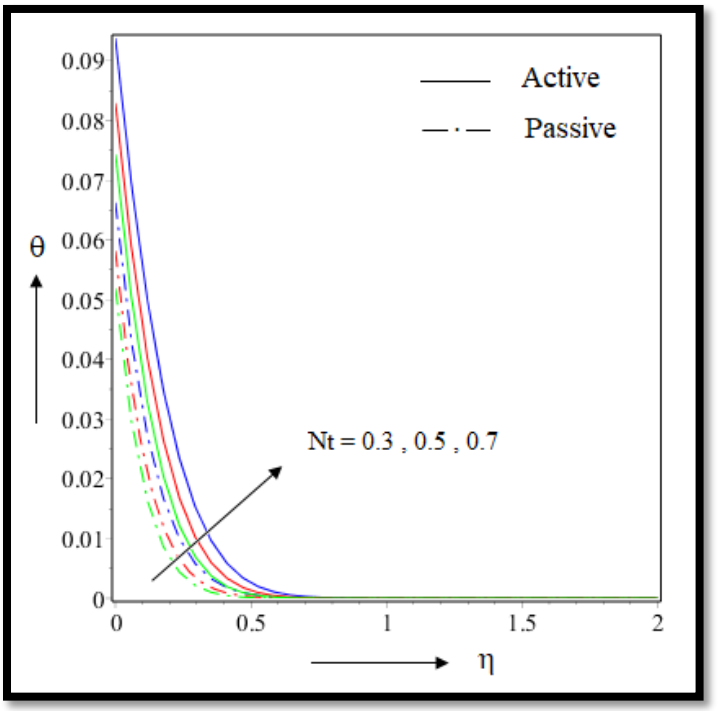

Figure 9.12: Effect of Nt on $\theta(\eta)$.

9.4.3. Influence of active and passive control on Concentration

In this section we discuss the upshots of various parameter on concentration profile. Magnetic parameter escalates the mass transfer for both active and passive control. Dimensionless Sherwood number is reduced by 3.91% for actively controlled flow. Prominent outcome is observed in $0 \le \eta \le 2.5$ beyond that it converges. Figure 9.13 portrayed the fact graphically. In figure 9.14 the upshots of Lewis number is displayed. Mass lines are reduced for higher value of Lewis number. Higher mass diffusivity value is responsible for this upshots. Both actively and passively controlled flow have same nature but Sherwood number is reduced by 22.83% for passively controlled for which is quite lower than actively controlled flow.

Mass transfer is decreased due to higher value Brownian motion parameter. Random movement of particles is known as Brownian motion. As we increase the value of the parameter, randomness also increased. More collisions is observed in the system due to this mass transfer is curtailed down. From figure 9.15 it is clear that for similarity variable between $0 \le \eta \le 2$ the prominent outputs is observed. Passive controlled nanofluid flow reduced the mass line and the magnitude is sufficiently lower than that of actively controlled flow. Thermophoresis parameter shows reverse effect of Brownian motion for mass transfer. Mass lines escalated due to higher values of *Nt* parameter. Already we have observed higher temperature profile for high thermophoresis value. Thus temperature gradient also increased and nanoparticles move to cold region from high energy level region. Concentration profile is upraised due to that reason. Sherwood number which is highly required value for engineering interest is reduced by 15.62%. Figure 9.16 shows all the outcomes graphically and here active and passive controlled framework is clearly observed.

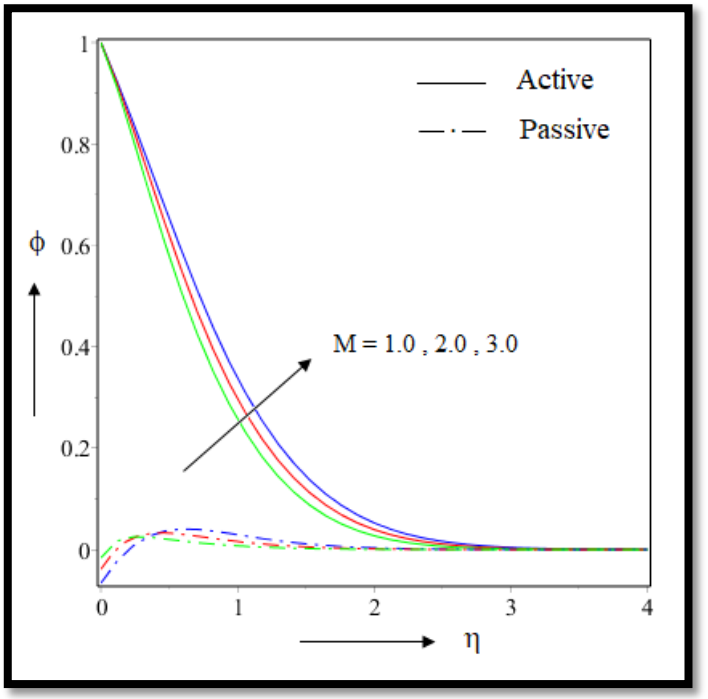

Figure 9.13: Effect of M on $\phi(\eta)$.

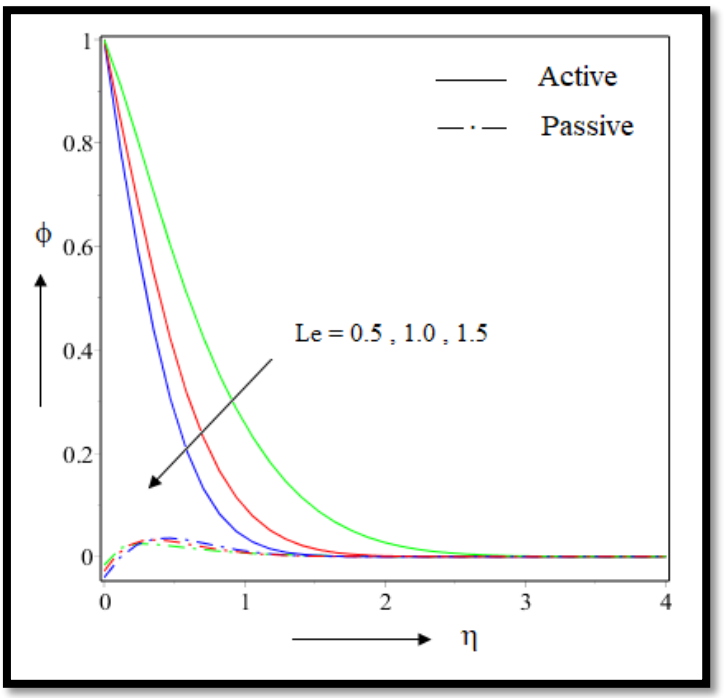

Figure 9.14: Effect of Le on $\phi(\eta)$.

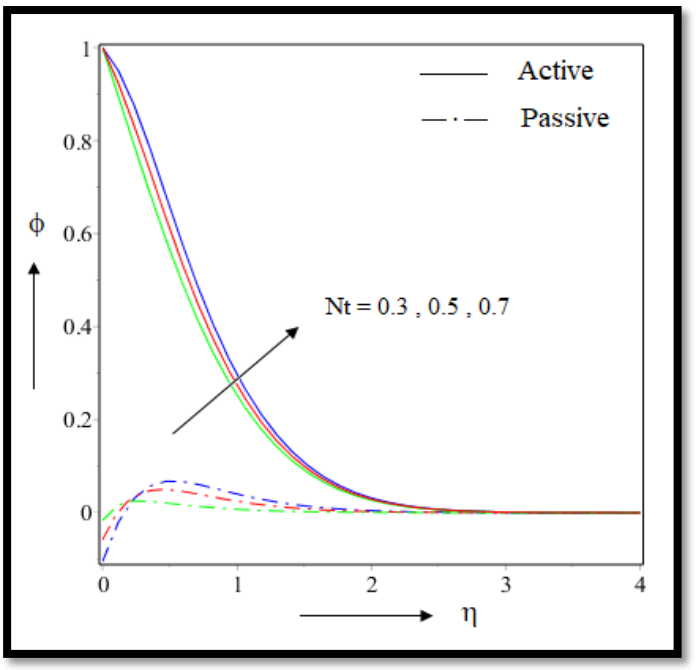

Figure 9.15: Effect of Nb on $\phi(\eta)$.

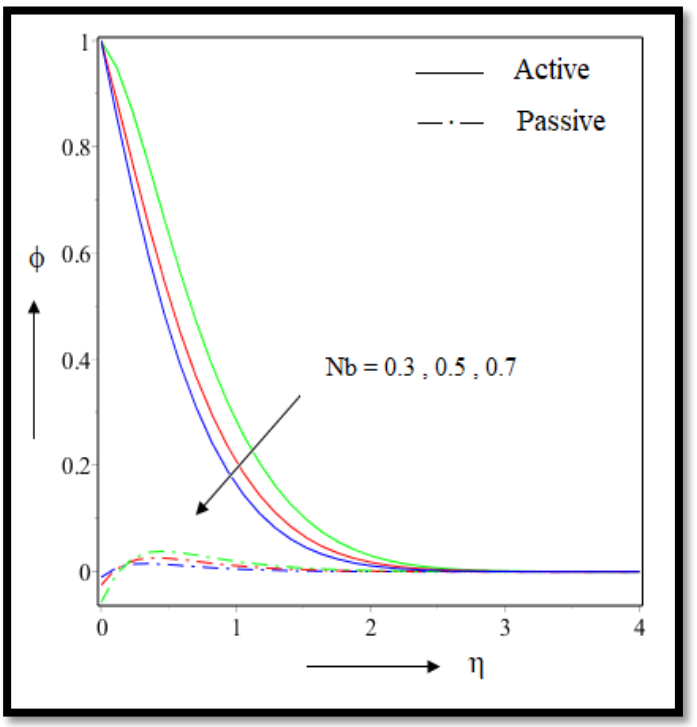

Figure 9.16: Effect of Nt on $\phi(\eta)$

9.5. Conclusion

Nanofluid flow under velocity slip is taken in this research. Active and passive control of nanofluid flow is also taken into account. Some other parameter like external heat source, magnetic parameter are incorporated to make this model more realistic in nature. The leading equations are changed to ODEs by suitable similarity variable. This highly non linear ODEs along with its boundary provisions are solved numerically with help of RK-4 shooting technique. We draw velocity lines with the comparison between slip and no slip condition. Mass lines and heat lines are portrayed under comparison of active and passive control of flow. The simulations is expressed by MAPLE-2019 software. Corresponding values of engineering interest are also tabulated. Most important outcomes which are found in this investigation is given below.

- Magnetic parameter escalate velocity profile. Reduced skin friction coefficient value is increased by 7.31% but for injection situation and 9.32% or suction effect.
- Increment in thermal Biot number gives us elevated velocity profile. We get 10.56% increment in skin friction for suction effect and 7.25% for injection effect.
- Heat lines are diminished for higher value of wedge angle parameter .Nusselt number increased by 8.82% for actively controlled flow but for passively controlled flow the increment reduced by 8.51% only.
- Heat lines are upraised for higher value Brownian motion and Thermophoresis parameter. Lower magnitude of temperature profile is observed for passively controlled flow.
- Mass lines are reduced for higher value of Lewis number. Both actively and passively controlled nanofluid flow have same nature but the magnitude of concentration is lower for passive control of nanofluid flow.
- Concentration profile is upraised for escalated value of thermpophoresis parameter. Sherwood number is reduced by 15.62% for passive control of nanofluid flow.

The application of nanofluid flow over several geometry has a vast application. Heat exchanger, cooling machine, nuclear reactor are some example of its reputed application. Wedge flow also has several applications like gas mixing and blending, compressing air, control of burner and many more. This investigation can be extended by taking other geometry like sphere , cylinder, cone , stretching sheet and also different parameter can be taken like multiple slip, multiple convection etcetera.

Table 9.3: Effect of suitable parameters on skin friction

M	β	Ls	Bi_t	Cf_r	
				$S=1$ Suction	$S=-1$ Injection
1.0	0.5	0.5	0.5	1.245456	1.187126
2.0				1.339109	1.295464
3.0				1.412323	1.377741
2.0	0.3			1.085502	0.978560
	0.5			1.339109	1.339994
	0.7			1.610643	1.625476
	0.5	0.3		1.521700	1.433125
		0.5		1.245456	1.187126
		0.7		1.052545	1.011434
		0.5	0.3	1.237632	1.245456
			0.5	1.362821	1.339606
			0.7	1.431435	1.412323

Table 9.4: Effect of suitable parameters on heat transfer

M	β	Ls	δ	Le	Nb	Nt	Nu_r	
							Active control	Passive control
1.0	0.5	0.5	0.5	1.0	0.5	0.5	0.362352	0.367855
2.0							0.370728	0.377102
3.0							0.380387	0.387150
2.0	0.3						0.348140	0.358141
	0.5						0.374582	0.389546
	0.7						0.405745	0.415768
	0.5	0.3					0.370311	0.381056
		0.5					0.374582	0.384524
		0.7					0.377880	0.387161
		0.5	0.3				0.377802	0.387080
			0.5				0.374582	0.384525
			0.7				0.370511	0.381238
			0.3	0.5			0.377734	0.387053
				1.0			0.369913	0.384437
				1.5			0.361594	0.381087
				1.0	0.3		0.380578	0.390759
					0.5		0.374369	0.389086
					0.7		0.365528	0.387052
					0.5	0.3	0.377898	0.387073
						0.5	0.374389	0.384500
						0.7	0.369949	0.381198

Table 9.5: Effect of suitable parameters on mass transfer

M	Le	Nb	Nt	Sh_r	
				Active control	Passive control
1.0	1.0	0.5	0.5	0.538288	6.481259
2.0				0.514147	5.506396
3.0				0.512569	4.243331
2.0	0.5			0.538288	6.481259
	1.0			1.096331	5.077356
	1.5			1.606720	4.487083
	1.0	0.3		0.215536	4.569677
		0.5		0.761858	5.600017
		0.7		1.023326	6.273870
		0.5	0.3	0.722282	6.481259
			0.5	0.481878	5.488234
			0.7	0.243891	4.882751

CHAPTER 10

Influence of multiple slips on magnetically driven nanofluid flow over externally heated stretching cylinder*

10.1. Introduction

In this chapter we have considered nanofluid flow on a stretching cylinder in appearance of external heat source together with velocity slip and solutal slip effect. Here, the governing equations are transformed to ordinary differential equations with the assistance of proper similarity transformations. MAPLE-2019 software is used to decode the system with RK-4 method. Velocity lines, heat lines and concentration lines are compared in presence and in absence of velocity slip, thermal slip and concentration slip parameters. Effect of other parameters, like Hartmann number, Schmidt number and external heat source parameter are also discussed. Graphical analysis of several other parameters of physical interest are also included in the discussion. The following results are derived from the outcomes of the present investigation:

- The effects of several parameters on velocity profile for both velocity slip and no slip conditions.
- The effects of parameters on frictional drag for velocity slip and no slip conditions.
- The effects of several parameters on temperature profile for both temperature jump and without temperature jump conditions.
- The effects of several parameters on heat transmission for both temperature jump and without temperature jump conditions.
- The effects of several parameters on concentration profile for both concentration slip and without concentration slip conditions.
- The effects of several parameters on mass transmission for both concentration slip and without concentration slip conditions.

***This chapter is based on the paper published in: Heat Transfer, 52(2) (2023), 1395-1412, (ESCI).**

10.2. Mathematical formulation

10.2.1. Governing equations

We have Consider an incompressible, steady, axisymmetric laminar stream of a nanofluid along a stretching cylinder having radius b. Where the z-axis is marked along the axis of tube and r-axis is measured in the radial direction as depicted in Figure 1. The flow is symmetric about $z=0$ plane and axisymmetric to the z axis. Assumed that surface constant temperature is T_w whereas the same concentration is C_w and the ambient concentration C_∞, ambient fluid temperature T_∞. An undeviating magnetic influence B_0 was registered in the radial direction. We have also employed Brownian migration and thermophoresis effect. Here (w,u) are the component of velocity along axes (z,r). The upshot of the induced magnetic influence is negligible, which is valid when the magnetic Reynolds number is small. Viscous dissipation together with Ohmic heating and Hall effects are mistreated. Under these assumptions, the governing equations [165-167] are

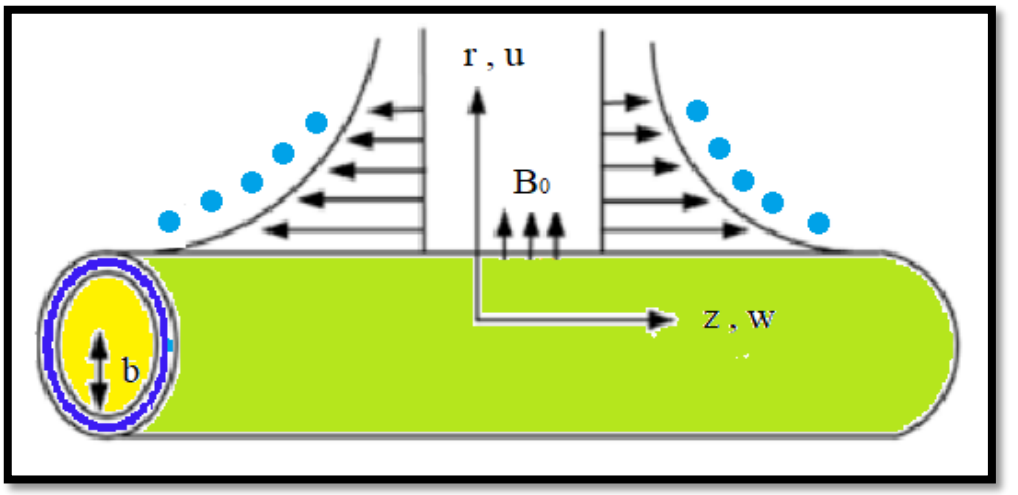

Figure 10.1: Physical geometry of the flow

$$\frac{\partial}{\partial z}(rw)+\frac{\partial}{\partial r}(ru)=0 \tag{10.1}$$

$$\rho_f\left(w\frac{\partial w}{\partial z}+u\frac{\partial w}{\partial r}\right)=\mu_f\left(\frac{\partial^2 w}{\partial z^2}+\frac{1}{r}\frac{\partial w}{\partial r}\right)-\sigma_f B_0^2 w \tag{10.2}$$

$$\rho_f\left(w\frac{\partial u}{\partial z}+u\frac{\partial u}{\partial r}\right)=-\frac{\partial p}{\partial r}+\mu_f\left(\frac{\partial^2 u}{\partial r^2}+\frac{1}{r}\frac{\partial u}{\partial r}-\frac{u}{r^2}\right) \tag{10.3}$$

$$\left(\rho C_p\right)_f\left(w\frac{\partial T}{\partial z}+u\frac{\partial T}{\partial r}\right)=\kappa_f\left(\frac{\partial^2 T}{\partial r^2}+\frac{1}{r}\frac{\partial T}{\partial r}\right)+Q\left(T-T_\infty\right)+\tau\left[D_B\frac{\partial C}{\partial r}\frac{\partial T}{\partial r}+\frac{D_T}{T_\infty}\left(\frac{\partial T}{\partial r}\right)^2\right] \tag{10.4}$$

$$\left(w\frac{\partial C}{\partial z}+u\frac{\partial C}{\partial r}\right)=D_B\left(\frac{1}{r}\frac{\partial}{\partial r}\left(r\frac{\partial C}{\partial r}\right)\right)+\frac{D_T}{T_\infty}\left(\frac{1}{r}\frac{\partial}{\partial r}\left(r\frac{\partial T}{\partial r}\right)\right) \tag{10.5}$$

Here, p is the pressure, ρ_f is fluid density, σ_f is electrical conductivity related to the fluid, T is temperature connected to the liquid, We have assumed that the temperature on the cylinder is T_w and temperature at far span from the sheet is T_∞. D_B, D_T are referred to Brownian diffusion coefficient, thermophoresis coefficient. κ_f refers to conductivity related to thermal attributes of the fluid. $\left(\rho C\right)_f$ is the heat capacitance of fluid, $\tau=\frac{\left(\rho C\right)_p}{\left(\rho C\right)_f}$ illustrates the (Effective heat capacity of the fluid)/(Heat capacity of the fluid). Q is the heat generation/absorption parameter.

10.2.2. Boundary conditions

The boundary provisions [165-167] for the above introduced model are given by the following equations:

$$u=0, w=w_w+L_{vel}\frac{\partial w}{\partial r}, T=T_w+L_{temp}\frac{\partial T}{\partial r}, C=C_w+L_{con}\frac{\partial C}{\partial r} \text{ at } r=b \tag{10.6}$$

$$w\to 0, T\to T_\infty, C\to C_\infty \text{ at } r\to\infty \tag{10.7}$$

where u and w are the velocity components along the r and z axes, respectively, and $w_w = 2az$ where a is a positive constant. L_{vel} , L_{temp} , L_{con} are velocity , thermal and concentration slip factor respectively.

10.2.3. Similarity transformations

We convert the foremost flow equations (10.1-10.5) into system of ODEs by the following similarity variables as in [167]

$$u = -\frac{abf(\eta)}{\sqrt{\eta}} \ , \ w = 2azf'(\eta) \ , \ \theta(\eta) = \frac{T - T_\infty}{T_w - T_\infty} \ , \ \phi(\eta) = \frac{C - C_\infty}{C_w - C_\infty} \ , \ \eta = \left(\frac{r}{b}\right)^2 \tag{10.8}$$

After needed modernization equation (10.1) satisfies automatically. After dropping pressure Equation (10.2) and (10.5) changed as follows.

$$\eta f''' + f'' + \mathrm{Re}\left(ff'' - f'^2\right) - Mf' = 0 \tag{10.9}$$

$$\eta\theta'' + \left(1 + \mathrm{Re}\,\mathrm{Pr}\, f\right)\theta' - H\theta + \eta\left(Nb\theta'\phi' + Nt\theta'^2\right) = 0 \tag{10.10}$$

$$\eta\phi'' + \left(\frac{1}{2} + \mathrm{Re}\, Scf\right)\phi' + \frac{Nt}{Nb}\left(\frac{1}{2}\theta' + \eta\theta''\right) = 0 \tag{10.11}$$

Corresponding boundary equations are also changed as follows.

$$f(1) = 0,\ f'(1) = 1 + Lsvf''(1), \theta(1) = 1 + Lst\theta'(1), \phi(1) = 1 + Lsc\phi'(1) \text{ at } r = b \tag{10.12}$$

$$f'(\infty) = 0, \theta(\infty) = 0, \phi(\infty) = 0 \text{ at } r = \infty \tag{10.13}$$

Where $\mathrm{Pr} = \frac{\nu_f}{\alpha_f}$ stands for Prandtl number , $\mathrm{Re} = \frac{ab^2}{2\nu_f}$, $Sc = \frac{\nu_f}{D_B}$, $H = \frac{Qb^2}{4\alpha_f}$, $M = \frac{\sigma_f B_0{}^2}{a\rho_f}$ designates Reynolds number , Schmidt number , external heat source parameter and magnetic parameter. $Nb = \frac{\tau D_B\left(C_w - C_\infty\right)}{\nu_f}$, $Nt = \frac{\tau D_T\left(T_w - T_\infty\right)}{T_\infty \nu_f}$ are respectively Brownian migration and thermophoresis parameter. Slip parameters for velocity, temperature and concentration denoted by

$$Lsv = \frac{2L_{vel}}{b}, Lst = \frac{2L_{temp}}{b}, Lsc = \frac{2L_{con}}{b}$$

10.2.4. Physical quantities

The needful physical quantities which are very important for engineering applications are

$$\left.\begin{aligned} C_f &= \frac{2\tau_w}{\rho w_w^2} \text{ where } \tau_w = \mu_f \left(\frac{\partial w}{\partial r}\right)_{r=b} \\ Nu &= \frac{aq_w}{\kappa_f \left(T_w - T_\infty\right)} \text{ where } q_w = -\kappa_f \left(\frac{\partial T}{\partial r}\right)_{r=b} \\ Sh &= \frac{aq_m}{D_B \left(C_w - C_\infty\right)} \text{ where } q_m = -D_B \left(\frac{\partial C}{\partial r}\right)_{r=b} \end{aligned}\right\} \quad (10.14)$$

Here C_f denotes local skin friction Nu stands for local Nusselt number and Sh represents local Sherwood number respectively. τ_w, q_w, q_m Designates surface shear stress, heat flux and mass flux respectively. Applying similarity renovation, we procure the reduced skin friction as

$$\left.\begin{aligned} C_{f_r} &= f''(1) \\ Nu_r &= -2\theta'(1) \\ Sh_r &= -\phi'(1) \end{aligned}\right\} \quad (10.15)$$

10.3. Numerical procedure

10.3.1. Solution technique

Analytical method of solution is difficult to apply in the obtained group of equations with its boundary condition. To overcome this difficulty we use numerical structures to solve our framework. Shooting method in constitution of Runge Kutta -4 method is pre-owned to procure the required solution. The whole process is programmed by MAPLE-2019 software and the outcomes are discussed in the consequent sections with the help of graphs and charts. The validation of our simulation also checked by previous results. Suitable programming is done for calculating the numerical outcomes up to 10^{-6} degree of exactness.

10.3.2. Code verification

To validate the results of our research we have compared our outcomes by making our system analogous to the previous results. Wang [121] has taken the viscous fluid through stretching cylinder. The values of various parameters are adjusted as $M = 0, H = 0, Lsv = 0, Lst = 0, Lsc = 0$ to compare the result with previous outcomes. In the following Table 10.1 we have compared the values of $f''(1)$ for different values of Reynolds number parameter and observe that it matched almost correctly. In the other Table 10.2 the values of $\theta'(1)$ is compared for different values of Prandtl number keeping the Reynolds number fixed to its value 1.

Table 10.1: Comparison of numerical outcomes of $f''(1)$ with previous studies

R	Wang [121]	Present Results
	$f''(1)$	$f''(1)$
0.1	-0.48181	-0.48182
1	-1.17776	-1.17775
2	-1.59390	-1.59391
5	-2.41745	-2.41745
10	-3.34445	-3.34447

Table 10.2: Comparison of numerical outcomes of $\theta'(1)$ with previous studies

Pr	Wang [121]	Present Results
	$\theta'(1)$	$\theta'(1)$
0.2	-0.2572	-0.25721
0.7	-0.5880	-0.58802
2	-1.0650	-1.06502
7	-2.0590	-2.05901
20	-3.5210	-3.52100

10.4. Result and discussion

The results obtained in this research is explained in the following section. The effect of various parameters are compared under slip effects. Magnetic parameter and Reynolds number effect is compared under velocity slip presence and absence. Heat transfer profile is investigated under presence and absence of temperature jump for Schmidt number Brownian motion thermophoresis etcetera. Solutal slip also investigated for several parameters like magnetic parameter, Reynolds number and schmidt number. Our main focus is to compare the velocity lines heat lines and concentration lines under corresponding slip framework and no slip framework. We have taken the basic values of various parameters throughout our simulation as follows.

$M = 1.0$, $\mathrm{Re} = 5$, $Sc = 5, Nb = 0.5$, $Nt = 0.5$, $H = 0.5, Lsv = 0.5$, $Lst = 0.5$, $Lsc = 0.5\}$

10.4.1. Influence of velocity slip parameter *Lsv*

In this research we have compared the system for presence and nonappearance of slip parameter. Here we have taken value of slip specification 0.5. Under this situation the output are compared in the same graph to get more comparative view. In Figure 10.2 it is observed that for Reynolds number parameter velocity profile decreased. Increment in Re parameter makes the fluid flow more turbulent hence the velocity get detained. Fluid drift in occupancy of velocity slip gives lower magnitude of velocity contrast to the flow without slip. It is also noticed from Table 10.3 that skin friction coefficient is increased by 13.42%. Clear pictorial view is perceived in the interval $1.0 \le \eta \le 5.0$ and hence the curve asymptotically converge to zero.

The velocity lines manifest that rate of transport is reduced adequately with the growth of M. It clearly designates that the transverse magnetic field opposes the transport framework. This is owing to the variation of M leads to the variation of the Lorentz effort owing to magnetic influence and Lorentz force brings out more resistance to transport framework. The observation is clear in the interval $1.0 \le \eta \le 5.0$ in Figure 10.3. Here also magnitude of velocity without slip provision is larger than velocity with slip parameter. Skin friction coefficient also increased by 16.21% which is noticed in Table 10.3 Higher slip value also effects the transport property. We observe that velocity profile is lesser in magnitude for high value of slip parameter. Figure 10.4 describes the velocity lines which are prominent in the interval $1.0 \le \eta \le 4.0$.

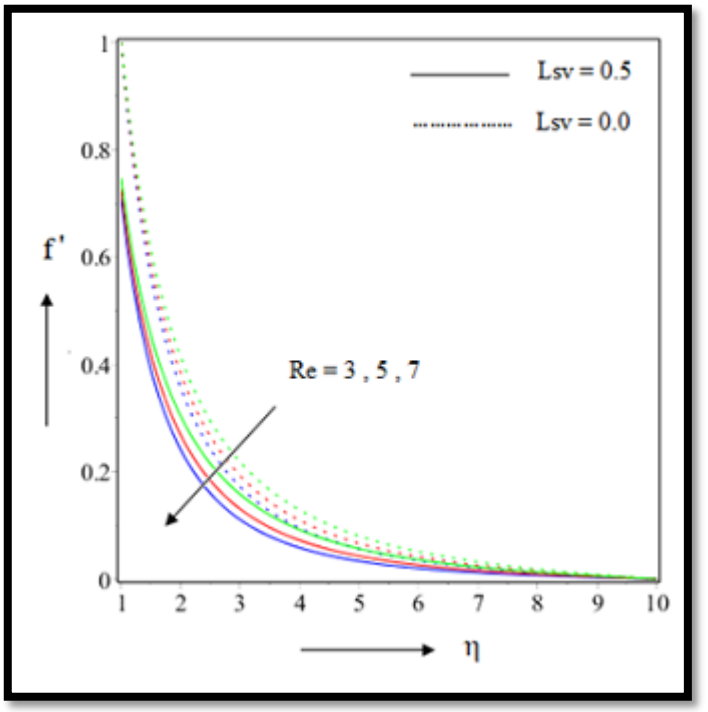

Figure 10.2: Effect of Reynolds number on velocity profile

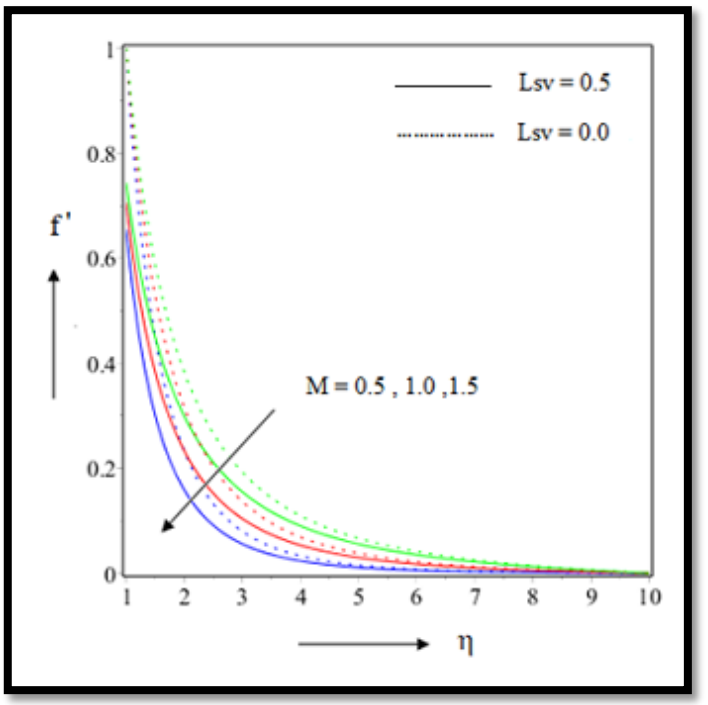

Figure 10.3: Effect of Magnetic parameter on velocity profile

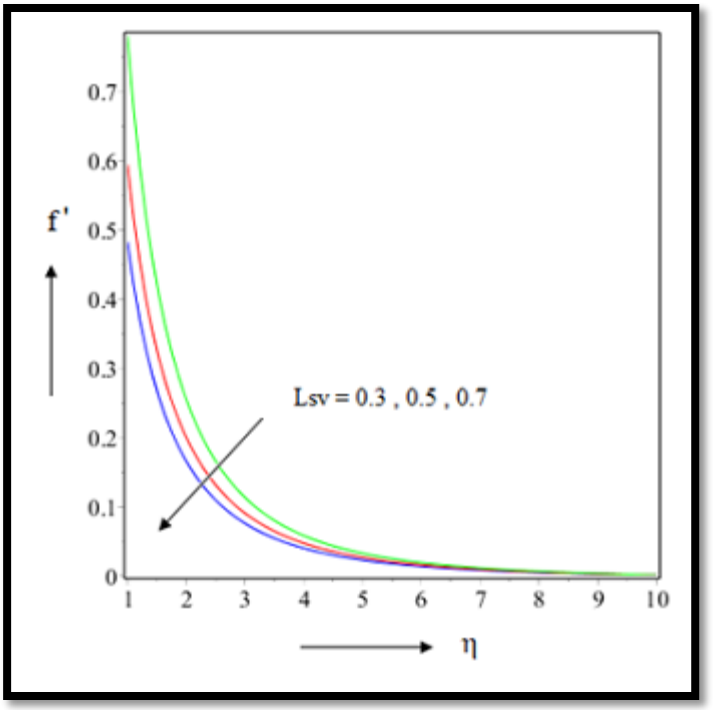

Figure 10.4: Effect of velocity slip parameter on velocity profile

10.4.2. Influence of temperature slip parameter *Lst*

Heat lines are increasing in nature for higher value of magnetic, Brownian motion , thermophoresis parameter and also schmidt number. In all this cases the magnitude of temperature is higher for inflated value of temperature slip parameter. Nusselt number is reduced by 6.69% and 6.79% for Brownian motion and thermophoresis parameter. For this two parameter prominent difference is observed in $1.0 \le \eta \le 7.0$ after that temperature diminish to zero. 4.71% drop is observed in case of Schmidt number parameter but surprisingly this value drop to 13.10% for magnetic parameter. Similar effect of magnetic parameter is observed by Mukhopadhyay [168]. Figure 10.5-10.8 shows clear pictorial effect and Table 10.4 shows the data of Nusselt number. For higher Reynolds number and external heat parameter heat lines show diminishing nature. 14.98% inflation in reduced Nusselt number is observed from the Table 10.4 whereas only 6.96% inflated Nusselt number value is observed for Reynolds number and external heat parameter. The negative sign in front of heat source parameter is the reason behind the diminished heat transfer

rate for external heat source parameter. In both cases higher magnitude of heat is found for without slip condition. In Figure 10.9-10.11 we observe the clear pictorial view.

Temperature slip parameter also diminish the heat lines observed in Figure 10.11. 20.93% drop in reduced Nusselt number noticed from Table 10.4. The temperature profile diminished beyond $\eta = 6$ and going towards zero. Prominent difference is observed in the interval $1.0 \le \eta \le 6.0$.

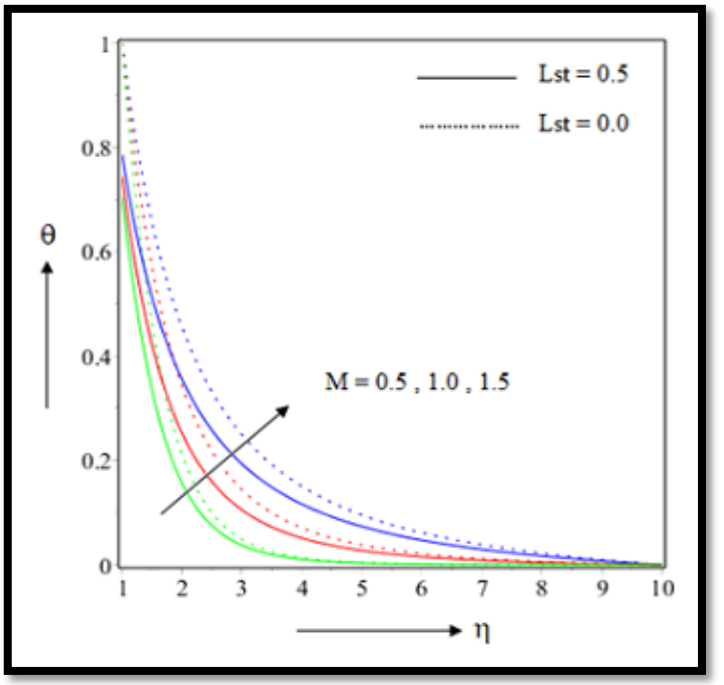

Figure 10.5: Effect of Magnetic parameter on Temperature profile.

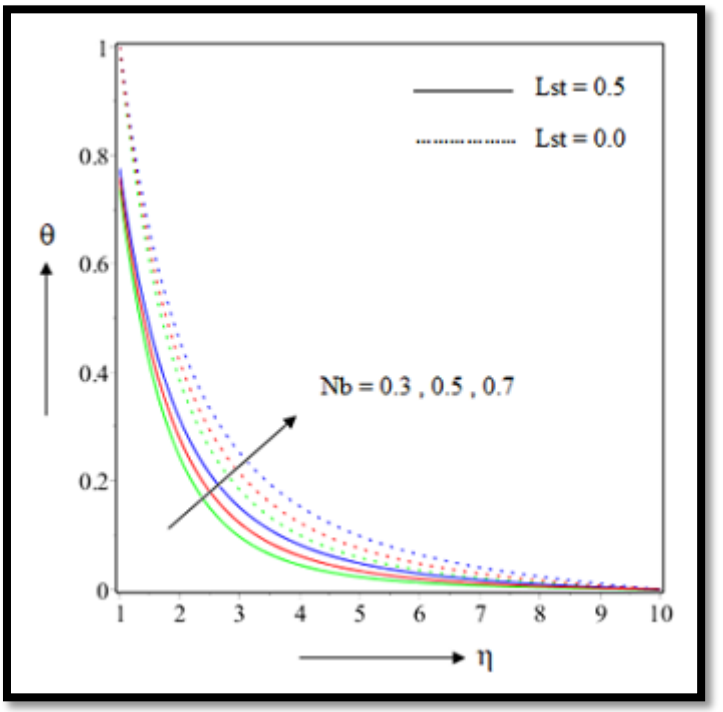

Figure 10.6: Effect of Brownian motion parameter on Temperature profile.

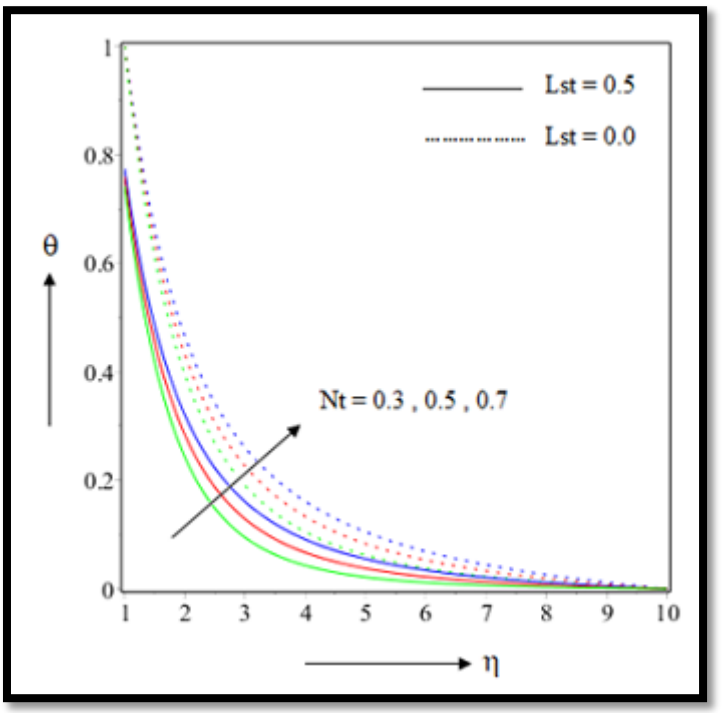

Figure 10.7: Effect of Thermophoresis parameter on Temperature profile.

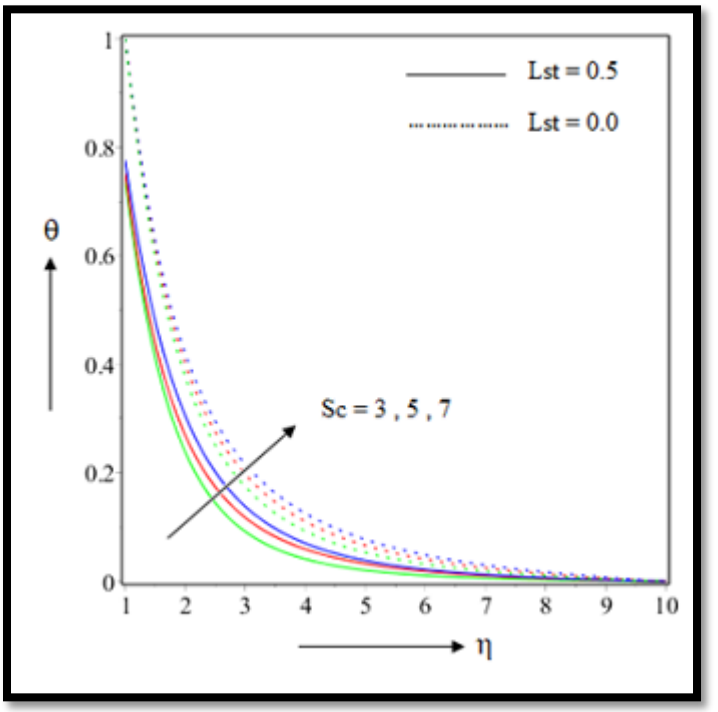

Figure 10.8: Effect of Schmidt number Temperature profile.

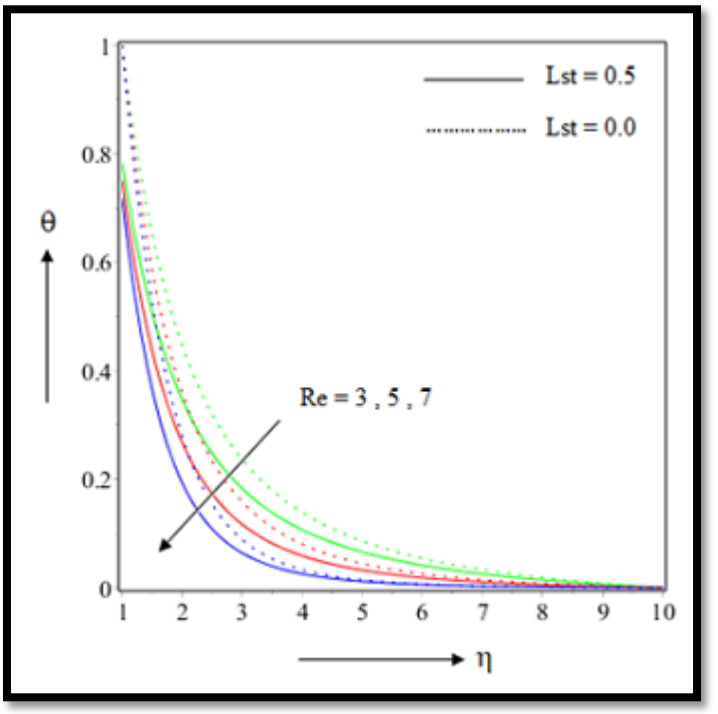

Figure 10.9: Effect of Reynolds number on Temperature profile.

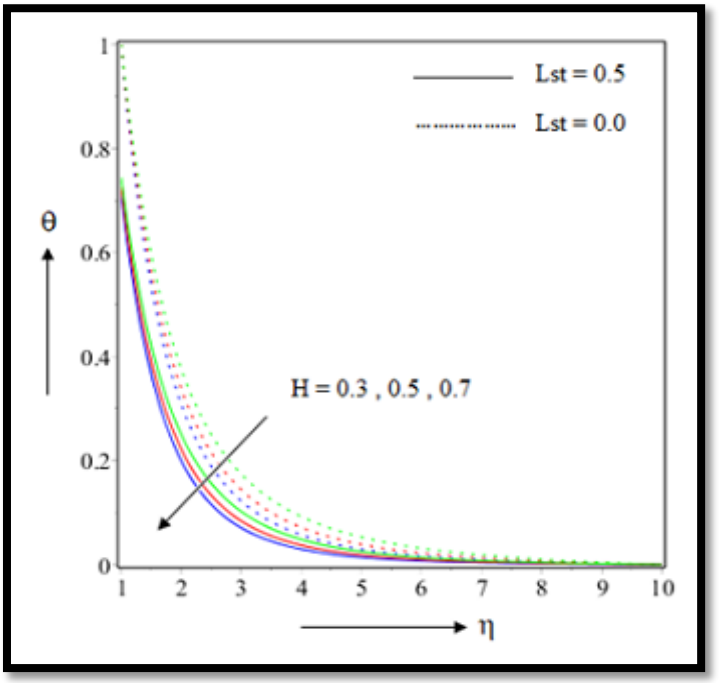

Figure 10.10: Effect of External heat source parameter on Temperature profile.

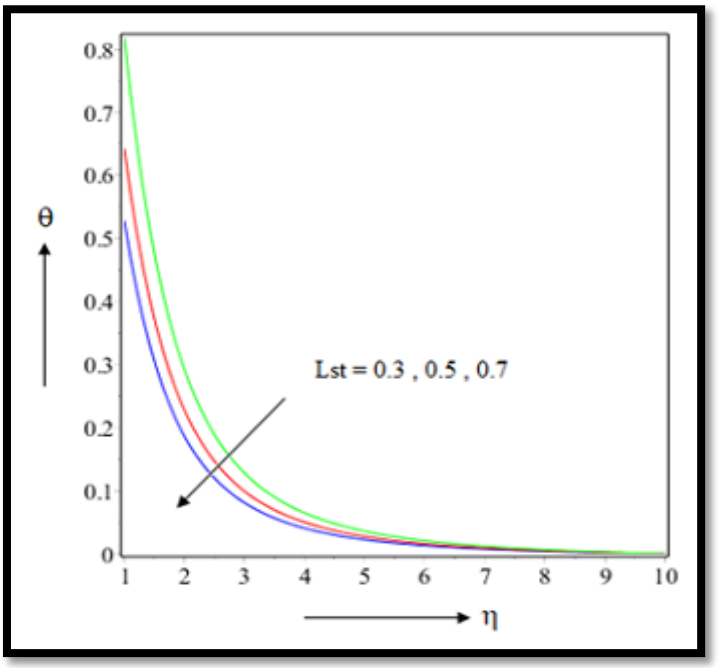

Figure 10.11: Effect of Thermal slip parameter on Temperature profile.

10.4.3. Influence of concentration slip parameter *Lsc*

Concentration profile shows inflated outcomes for higher magnetic Thermophoresis parameter. Nanoparticle migration rate differ for change in thermophoresis parameter. For high value thermophoresis parameter the smaller particles accumulate at heated wall which out turn higher heat transfer rate. But for higher value Schmidt number we observe reverse effect. Heat transfer rate decreased and lower magnitude is returned by flow without temperature jump. In Figure 10.12 the solutal lines shows prominent result in the interval $1.0 \le \eta \le 9.0$ for thermophoresis parameter and in Figure 10.13 the same is observed in the interval $1.0 \le \eta \le 6.0$ for magnetic parameter. In both cases lower magnitude is found for flow with solutal slip.

Magnetic parameter increase the concentration profile of fluid flow as it creates Lorentz force which opposes the fluid flow and more heat is produced due to friction. As a result thermal boundary layer as well as concentration boundary layer get thicken. In our study concentration slip parameter gives lower magnitude of concentration than no solutal slip condition. Figure 10.14 shows the effect of magnetic parameter. On the other hand Reynolds number diminish the concentration profile but here also we observe that for no slip condition lower magnitude of concentration is found. Prominent difference is seen in the interval $1.0 \le \eta \le 6.0$ in Figure 10.15. Sherwood number jumped almost 54.11% in appearance of slip parameter for Reynolds number (Table 10.5 referred). Figure 10.16 and Figure 10.17 upshot of Brownian migration parameter and solutal slip parameter is portrayed. In both cases concentration profile declined. For higher Brownian migration parameter migration of particle get increased which effect the concentration framework. In appearance of slip parameter magnitude of concentration reduced more. Similarly higher slip value also decrease the fluid concentration. Increment in Sherwood number for higher concentration slip value is observed by 1.57% from Table 10.6.

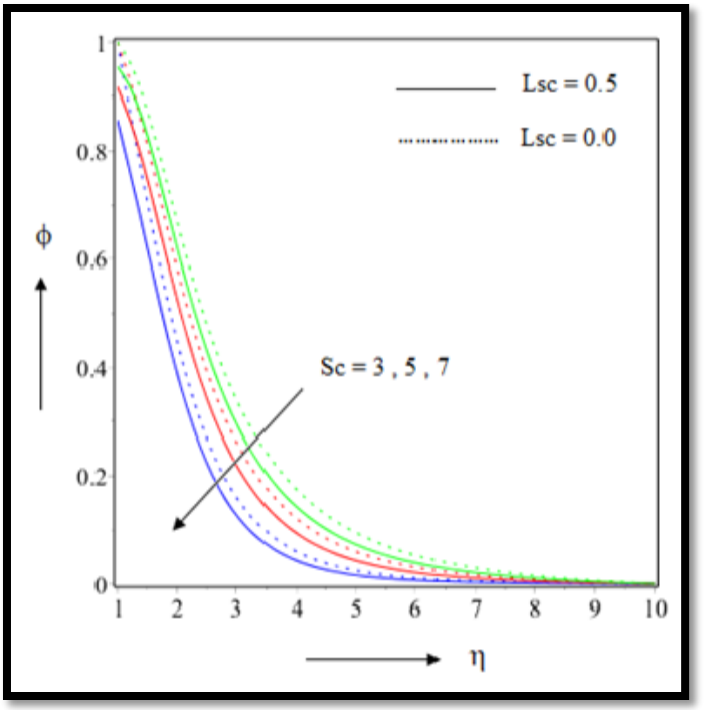

Figure 10.12: Effect of Schmidt number on Concentration profile.

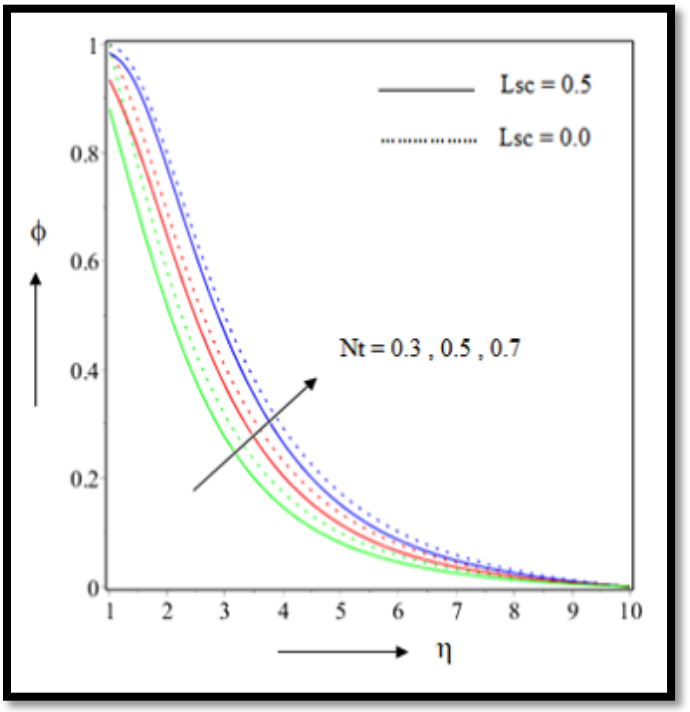

Figure 10.13: Effect of Thermophoresis parameter on Concentration profile.

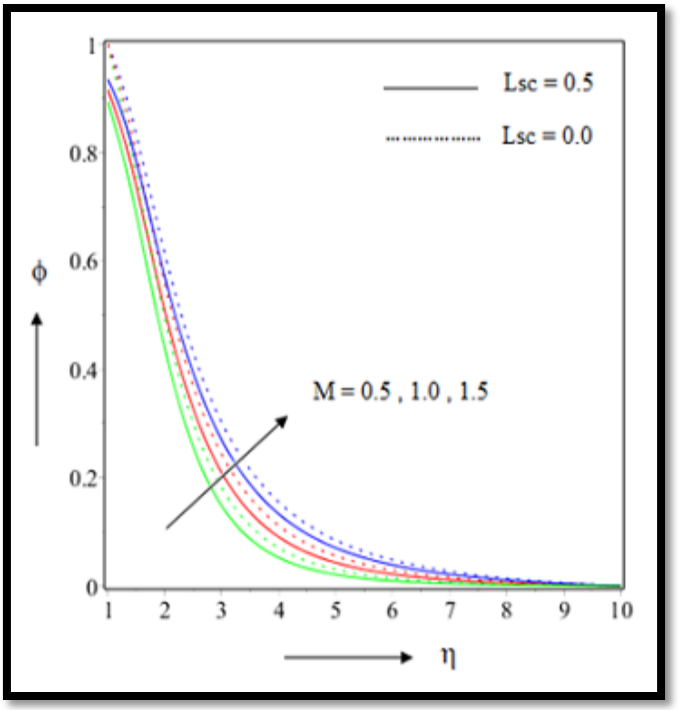

Figure 10.14: Effect of Magnetic parameter on Concentration profile.

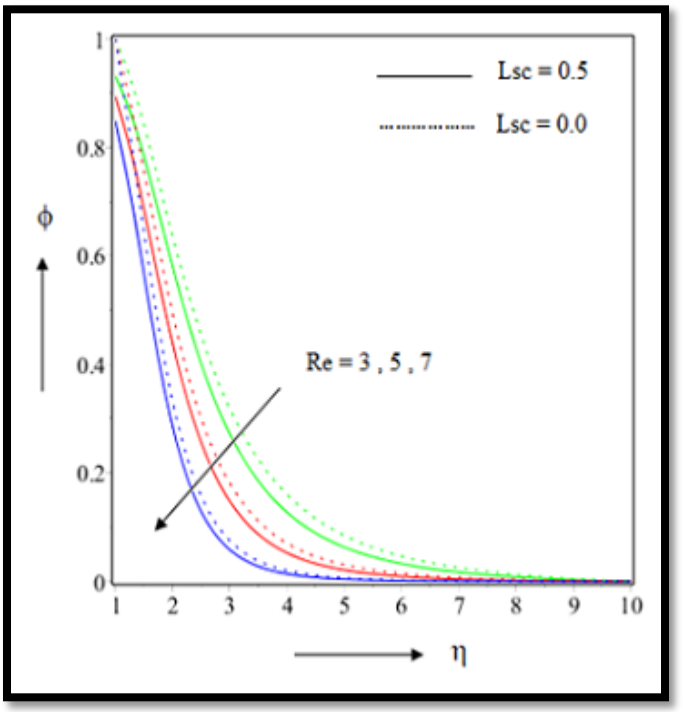

Figure 10.15: Effect of Reynolds number on Concentration profile

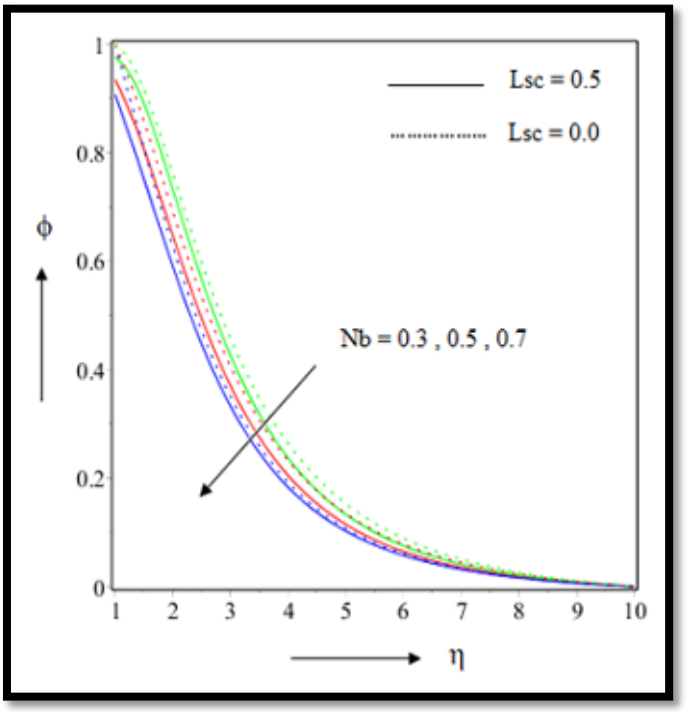

Figure 10.16: Effect of Brownian motion parameter on Concentration profile.

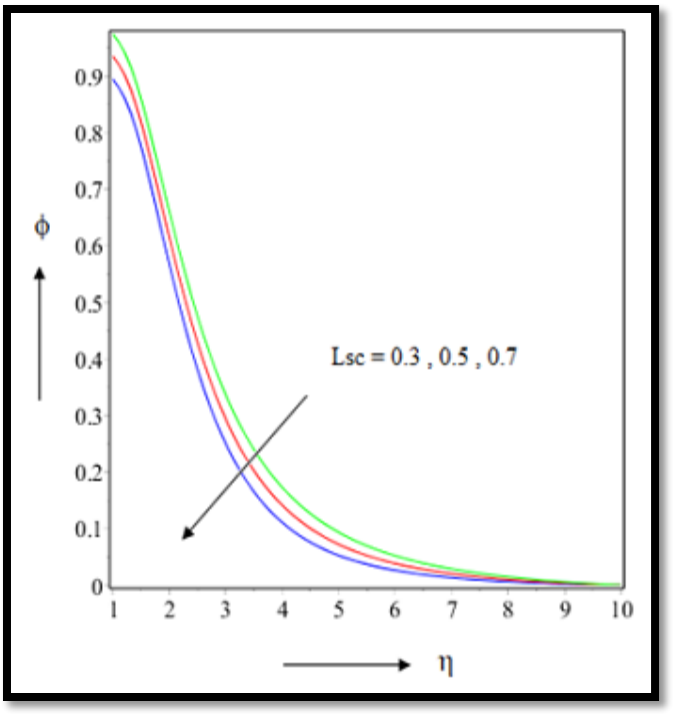

Figure 10.17: Effect of Concentration slip parameter on Concentration profile

10.5. Conclusion

In this inspection nanofluid flow along magnetically driven stretching cylinder is observed under presence of external heat originator parameter and multiple slip effect. Dimensionless leading equations are worked out by RK4 method with help of Maple software. Velocity lines, heat lines and concentration lines are compared for no slip and with slip conditions. Appropriate graphs and tables for prominent view are also produced. The following important outcomes are found in our research.

- Reynolds number and Magnetic influence reduced the velocity profile but presence of slip parameter reduce the magnitude of velocity than no slip condition.
- Schmidt number as well as magnetic influence escalate the heat transport for their inflated values. But dual nature is seen for Reynolds number. Surprisingly all these parameter has lower heat profile for thermal jump parameter.
- Brownian migration and thermophoresis produced inflated heat lines. 6.69% and 6.79% drop in reduced Nusselt number is observed. Here also thermal slip parameter plays the same role by lowering the magnitude of heat lines.
- Concentration profile is inflated due to higher value of magnetic and thermophoresis parameter but Brownian motion reduced the concentration boundary layer. Concentration slip effect drop the value for all three cases.
- Reynolds number and Schmidt number reduce the concentration slip effect. 54.11% jump is seen in Sherwood number for Reynolds number. Concentration slip parameter also reduce the concentration value.

The improved quality of nanofluid is the reason for its vast applicability in food as well as industrial application, biomedicine, sterilization, nuclear reactor, transportation, chemical industry and polymer coating. Multiple slip conditions make the system more realistic which also has vast application in the field of cooling mechanism. Some other geometrical structure with radiation, joule heating effect can be introduced. Reliable geometric conditions and boundary provisions are to be included. Further investigation can be done under above noted circumstances.

Table 10.3: Effect of suitable parameters on skin friction

M	Re	Cf_r	
		$Lsv = 0.5$	$Lsv = 0.0$
0.5	5	-0.852957	-1.209792
1.0		-0.978020	-1.443203
1.5		-1.149455	-1.808004
1.0	3	-0.864112	-1.110256
	5	-0.910458	-1.219945
	7	-0.977450	-1.326485

Table 10.4: Effect of suitable parameters on heat transfer

M	Re	Sc	Nb	Nt	H	Nu_r	
						$Lst = 0.5$	$Lst = 0$
0.5	5	5	0.5	0.5	0.5	0.980132	1.437874
1.0						0.851788	1.132360
1.5						0.712179	0.896626
1.0	3					0.721527	0.911711
	5					0.829701	1.093289
	7					0.941643	1.216194
	5	3				0.868058	1.061331
		5				0.827129	1.014659
		7				0.745479	0.977837
		5	0.3			0.859412	1.042736
			0.5			0.801931	0.954393
			0.7			0.745238	0.863369
			0.3	0.3		0.858578	1.020431
				0.5		0.800216	0.938465
				0.7		0.750171	0.866764
				0.5	0.3	0.851305	1.061331
					0.5	0.910698	1.182253
					0.7	0.961207	1.287235

Table 10.5: Effect of suitable parameters on mass transfer

M	Re	Sc	Nb	Nt	Sh_r	
					$Lsc = 0.5$	$Lsc = 0$
0.5	5	5	0.5	0.5	0.353798	0.454005
1.0					0.280302	0.349222
1.5					0.216331	0.261406
1.0	3				0.229537	0.259325
	5				0.353798	0.454005
	7				0.503199	0.720539
	5	3			0.150849	0.154364
		5			0.274900	0.327506
		7			0.474488	0.633889
		3	0.3		0.079500	0.075028
			0.5		0.215955	0.252453
			0.7		0.306823	0.397533
			0.5	0.3	0.393299	0.478915
				0.5	0.215955	0.252453
				0.7	0.053954	0.040885

Table 10.6: Effects of suitable parameters on skin friction, heat transfer and mass transfer

Lsv	*Lst*	*Lsc*	Cf_r	Nu_r	Sh_r
0.3	0.5	0.5	-1.093412		
0.5			-0.809847		
0.7			-0.646052		
0.5	0.3			0.902666	
	0.5			0.713672	
	0.7			0.589301	
	0.5	0.3			0.127633
		0.5			0.129582
		0.7			0.131787

CHAPTER 11

Magnetically driven nanofluid flow over a slippery bended Surface under thermal radiation and higher order chemical reaction*

11.1. Introduction

Problems involving flow analysis of nanofluid have been considered by several investigators [138, 145, 168] in recent past assuming various geometric models e.g. rotating disk, stretching cylinder, stretching sheet and cone. Manjunatha et al. [72] investigated the flow over a curved stretching sheet. They also included convective condition in their model. Raza et al. [150] investigated the effects of nonlinear radiative flow over a curved stretching surface. They found that thermal properties are improved due to entropy generation. Sevaral investigations are done on curved stretching sheet for different parameters and different boundary conditions.

This leads us to consider nanofluid flow over a curved stretching surface under actively and passively controlled nanoparticles. We have also introduced velocity slip, convective condition and suction injection effect in our model. To make the model more realistic, we again included chemical reaction of higher order and radiation effect into the system. The governing PDEs are transformed to highly nonlinear ODEs with the help of appropriate similarity transformation. The transformed problem is then solved by MAPLE -2021 software and the whole simulation is observed for different parameters. Velocity lines are compared under suction and injection whereas the heat lines and mass lines are compared under active and passive control of nanoparticles. Graphical representations of various parameters are included and the values of physical interest are tabulated. To the author's knowledge, the flow model considered here assuming the above mentioned conditions and parameters, has not been reported in the literature till now.

***This chapter is based on the paper published in: Modern Physics Letters B, 38(18) (2024), 2450131, (SCIE).**

11.2. Mathematical formulation

11.2.1. Governing equations

A steady incompressible magnetohydrodynamic flow is taken through a curved stretching sheet. The surface is bended like a semicircle of radius R. It seems to be more flat for higher value of R. Radiation effect of heat transfer and higher order chemical reaction is included into the system. The surface is porous in nature and hence suction/injection parameter is applied. Velocity slip and convective thermal transmission framework also added to the system. To make the flow analysis more realistic we use active and passive control of nanoparticles. The system is shown by Figure 11.1. Velocity u is taken along s axis and v is along r axis. In r direction we implement a magnetic field B_0. Joule heating is neglected and magnetic Reynolds number is also taken very small to neglect the induced upshots. Stretching velocity $u_w = as$ is considered where a is stretching constant. Under the above assumption the flow equations [150-152,169,170] are taken as follows

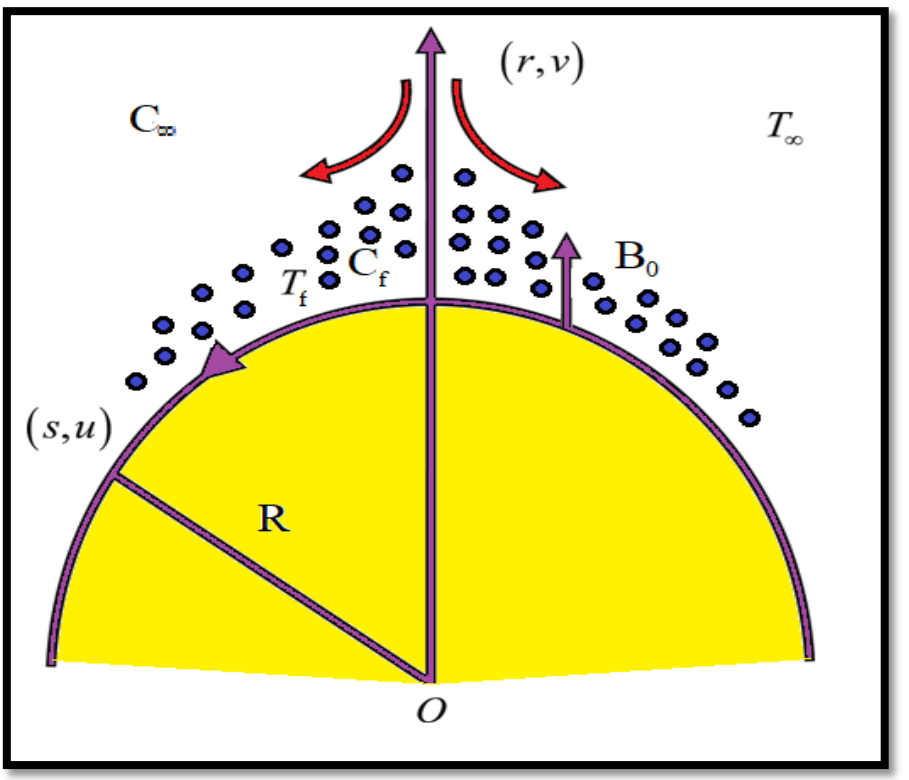

Figure 11.1: Physical geometry of the flow

$$\frac{\partial}{\partial r}\{(r+R)v\}+R\frac{\partial u}{\partial s}=0 \tag{11.1}$$

$$\frac{u^2}{r+R}=\frac{1}{\rho_f}\frac{\partial p}{\partial r} \tag{11.2}$$

$$v\frac{\partial u}{\partial r}+\frac{Ru}{r+R}\frac{\partial u}{\partial s}+\frac{uv}{r+R}=-\frac{R}{\rho_f(r+R)}\frac{\partial p}{\partial s}+\nu_f\left[\frac{\partial^2 u}{\partial r^2}+\frac{1}{r+R}\frac{\partial u}{\partial r}-\frac{u}{(r+R)^2}\right]-\frac{\sigma_f B_0^2 u}{\rho_f} \tag{11.3}$$

$$v\frac{\partial T}{\partial r}+\frac{Ru}{r+R}\frac{\partial T}{\partial s}=\frac{\kappa_f}{(\rho C_p)_f}\left(\frac{\partial^2 T}{\partial r^2}+\frac{1}{r+R}\frac{\partial T}{\partial r}\right)+\tau\left[D_B\frac{\partial C}{\partial r}\frac{\partial T}{\partial r}+\frac{D_T}{T_\infty}\frac{\partial T}{\partial r}\right]-\frac{1}{(\rho C_p)_f(r+R)}\frac{\partial}{\partial r}\left[(r+R)q_r\right] \tag{11.4}$$

$$v\frac{\partial C}{\partial r}+\frac{Ru}{r+R}\frac{\partial C}{\partial s}=D_B\left(\frac{\partial C^2}{\partial r^2}+\frac{1}{r+R}\frac{\partial C}{\partial r}\right)+\frac{D_T}{T_\infty}\left(\frac{\partial^2 T}{\partial r^2}+\frac{1}{r+R}\frac{\partial T}{\partial r}\right)-K_r(C-C_\infty)^n \tag{11.5}$$

Simplification of radiative heat flux can be calculated by Rosseland approximation $q_r=-\frac{4\sigma^*}{3\kappa^*}.\frac{\partial T^4}{\partial r}$ .We get $T^4\approx 4T.T_\infty^3-3T_\infty^3$ from Taylor series expansion of T^4 about T_∞ neglecting the higher order expressions.

11.2.2. Boundary conditions

The boundary provisions for the above introduced model are given by the following equations:

$$u=u_w+L\left(\frac{\partial u}{\partial r}-\frac{u}{r+R}\right)\ ,\quad v=v_w\ ,\quad -\kappa_f\frac{\partial T}{\partial r}=h_f(T_f-T_\infty)\ ,$$

$$\begin{cases} D_B\dfrac{\partial C}{\partial r}+\dfrac{D_T}{T_\infty}\dfrac{\partial T}{\partial r}=0, & \text{for passive control of } \phi \\ C=C_w\ , & \text{for active control of } \phi \end{cases} \quad \text{At } r=0 \tag{11.6}$$

$$u\to 0\ ,\ \frac{\partial u}{\partial r}\to 0\ ,\ T\to T_\infty\ ,\ C\to C_\infty \text{ as } r\to\infty \tag{11.7}$$

Suction injection and velocity slip is introduced in equation (11.6) moreover we have incorporate convective heat transfer in the same equation. Active and passive control of nanoparticles also considered and different equations represent the different scenario. Equation (11.7) represents the value of ambient velocity temperature and concentration.

11.2.3. Similarity transformations

The leading equations (11.1-11.5) and its boundary provisions (11.6, 11.7) can be transformed into nonlinear ODEs by following similarity renovation [150-152,169,170].

$$\left.\begin{aligned} &\eta=\sqrt{\frac{a}{\nu_f}}r, u=asf'(\eta), v=-\frac{R}{r+R}\sqrt{a\nu_f}\,f(\eta),\\ &p=\rho_f(as)^2\,p(\eta), \theta(\eta)=\frac{T-T_\infty}{T_f-T_\infty},\\ &\begin{cases}\phi(\eta)=\dfrac{C}{C_\infty}-1, & \text{for passive control of } \phi\\ \phi(\eta)=\dfrac{C-C_\infty}{C_w-C_\infty}, & \text{for active control of } \phi\end{cases}\end{aligned}\right\} \tag{11.8}$$

After needed modernization equation (11.1) satisfies automatically. Equation (11.2) and (11.3) changed as follows.

Applying the transformation we found equation (11.1) satisfies automatically and equations (11.2, 11.3) changes as follows.

$$p'=\frac{f'^2}{\eta+k} \tag{11.9}$$

$$\frac{2k}{\eta+k}p=\left[f'''+\frac{f''}{\eta+k}-\frac{f'}{(\eta+k)^2}\right]-\frac{k}{\eta+k}f'^2+\frac{k}{\eta+k}ff''+\frac{k}{(\eta+k)^2}ff'-M^2f' \tag{11.10}$$

Eliminating pressure p from equation (11.9) and (11.10) we get

$$f^{iv}+\frac{2f'''}{\eta+k}-\frac{f''}{(\eta+k)^2}+\frac{f'}{(\eta+k)^3}-$$
$$\left[\frac{k}{\eta+k}(f'-ff''')+\frac{k}{(\eta+k)^2}(f'^2-ff'')+\frac{k}{(\eta+k)^3}ff'+M^2\left(f''+\frac{f'}{\eta+k}\right)\right]=0 \quad (11.11)$$

Equation (11.4, 11.5) changed as follows

$$\left(\theta''+\frac{\theta'}{\eta+k}\right)\left(1+\frac{4}{3}Rd\right)+\Pr\left(\frac{k}{\eta+k}\theta' f+Nb\theta'\phi'+Nt\theta'^2\right)=0 \quad (11.12)$$

$$\phi''+\left(\frac{k}{\eta+k}Scf+\frac{1}{\eta+k}\right)\phi'+\frac{Nt}{Nb}\left(\theta''+\frac{1}{\eta+k}\theta'\right)-KrSc\phi^n=0 \quad (11.13)$$

Similarly the boundary provisions are also converted to:

$$\left.\begin{array}{l} f'(0)=1+Ls\left(f''(0)-\dfrac{f'(0)}{k}\right),\ f(0)=S,\theta'(0)=-Bi_t\left(1-\theta(0)\right), \\ \begin{cases} Nb\phi'(0)+Nt\theta'(0)=0, & \text{for passive control of } \phi \\ \phi(0)=1, & \text{for active control of } \phi \end{cases} \\ f'(\infty)=0,\ f''(\infty)=0,\theta(\infty)=0,\phi(\infty)=0 \end{array}\right\} \quad (11.14)$$

S stands for suction injection parameter $S=\frac{v_w}{\sqrt{av_f}}$, where $S\succ 0$ indicates injection and $S\prec 0$ indicates suction.

11.2.4. Physical quantities

The requisite physical quantities which has prime application in engineering are

$$C_f=\frac{\tau_{rs}}{\rho_f u_w^2} \quad \text{Where } \tau_{rs}=\mu_f\left(\frac{\partial u}{\partial r}-\frac{u}{r+R}\right)_{r=0}$$

$$Nu=\frac{sq_w}{\kappa_f\left(T_f-T_\infty\right)} \quad \text{Where} \quad q_w=-\kappa_f\left(\frac{\partial T}{\partial r}\right)_{r=0}+\left(q_r\right)_{r=0}$$

$$Sh = \frac{sj_w}{D_B\left(C_f - C_\infty\right)} \quad \text{Where} \quad j_w = -D_B\left(\frac{\partial C}{\partial r}\right)_{r=0}$$

Here C_f denotes local skin friction Nu stands for local Nusselt number and Sh represents local Sherwood number respectively. τ_{rs}, q_w, j_w Designates surface shear stress, heat flux and mass flux respectively.

Applying similarity renovation, we found the reduced skin friction as

$$C_{fr} = \sqrt{\mathrm{Re}_s} C_f = \left(f''(0) - \frac{f'(0)}{k}\right)$$

Analogously reduced Nusselt number as

$$Nu_r = \left(\mathrm{Re}_s\right)^{-\frac{1}{2}} Nu = -\left(1 + \frac{4}{3}Rd\right)\theta'(0)$$

And also reduced Sherwood number as

$$Sh_r = \begin{cases} -\dfrac{\phi'(0)}{\phi(0)}, & \text{for passive control of } \phi \\ -\phi'(0), & \text{for active control of } \phi \end{cases}$$

Where $\mathrm{Re}_s = \dfrac{as^2}{\nu_f}$ represents local Reynolds number.

11.3. Numerical procedure

11.3.1. Solution technique

The leading equations of the system is a set of partial differential equation. At first this system is transfigured into a set Ordinary differential equations with the help of appropriate similarity transformation. This reduced system is highly nonlinear so it is difficult to solve by any analytical method. We use numerical framework to solve this, RK-4 method with shooting technique is implemented here. The simulation process is done by MAPLE-2021 software. Adequate number of graphs and tables are included to cover the result more appropriately.

11.3.2. Code verification

We validate our problem and coding with previously published result and we found excellent matching. We have compare it with Abbas et al. [153] by removing slip effect and chemical reaction parameter (please see figure 11.2). To make this possible we use $Kr = 0, Ls = 0$ in our problem. Again we also pull out radiation term by making $Rd = 0$. In Table 11.1 we can observe that for different values of curvature parameter reduce skin friction values are almost similar. Hence our code is verified.

Table 11.1: Comparison of numerical outcomes with previous studies

k	**Abbas et al. [153]**	**Present Results**
	Cf_r	Cf_r
5	-1.15763	-1.15764
10	-1.07349	-1.07348
20	-1.03561	-1.03561
30	-1.02353	-1.02354
40	-1.01759	-1.01759
50	-1.01405	-1.01405
100	-1.00704	-1.00703
200	-1.00356	-1.00356
1000	-1.00079	-1.00079

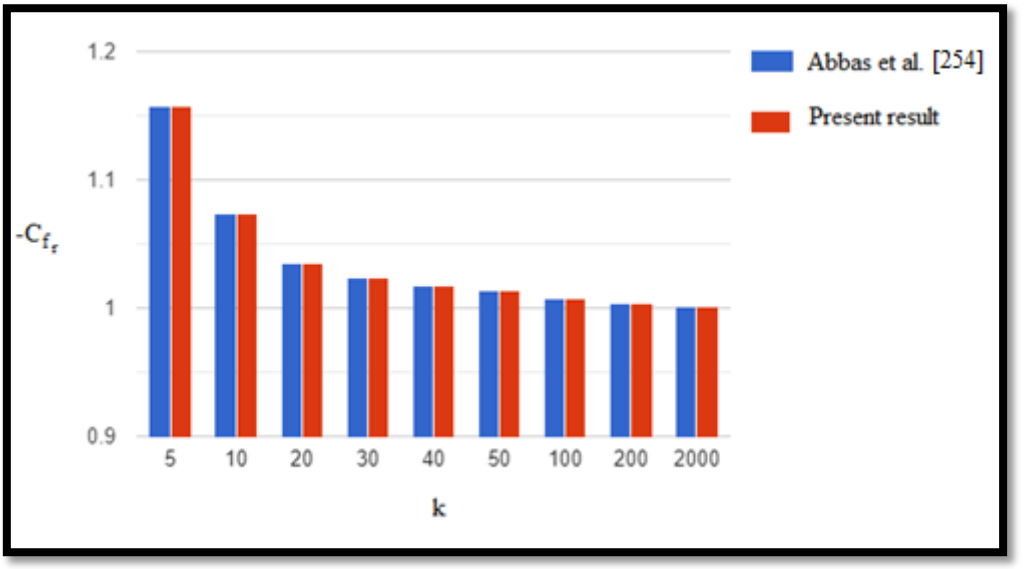

Figure 11.2: Comparison between Abbas et al. and present result

11.4. Results and discussion

In this section we have discussed the outcomes of several parameters on velocity thermal and concentration profile. Range of parameters are varied to extend our results more realistic. Velocity lines are compared under suction and injection effect. Heat lines and mass lines are compared under active and passive control of nanoparticles. In subsection 11.4.1 velocity profile is discussed and the upshots of magnetic parameter, curvature parameter, velocity slip and Schmidt number is shown with graphs. Skin friction values are also given in Table 11.2 for engineering applications.

In subsection 11.4.2 and 11.4.3 thermal profile and concentration profile under magnetic, curvature, chemical reaction parameter, Brownian migration thermophoresis parameter and other parameters is canvassed. Separate tables for Nusselt number and Sherwood number also provided. Throughout the investigation we have assumed the values of several parameter as follow if not mentioned.

$$\mathrm{Pr} = 6.2, M = 2.0, k = 5, S = 0.3, Nb = 0.5, Nt = 0.5, Sc = 5, Bi_t = 0.5, Ls = 0.5, Kr = 0.5, Rd = 0.5$$

11.4.1. Velocity Profile

The upshots of magnetic profile on velocity is shown in Figure 11.3. Magnetic field creates Lorentz force due to electrically conducted nanofluid flow. In this situation a drag force is induced

in the system which reduces velocity. Lower magnitude of velocity is found in case of injection condition. The velocity lines asymptotically converge beyond and prominent outcome found in the interval $0 \le \eta \le 3$. When nanofluid injected in the system we found 16.55% change for higher magnetic profile but in case of suction of nanofluid it changes to 18.04% (Table 11.2 referred.). Similar result has been observed by Oyelakin et al [154]. In Figure 11.4 upshots of curvature parameter is shown. Opposite nature of velocity is found here. As we increase the curvature parameter the surface become more flat. Nanofluid can move faster in a flat surface than a curved surface so velocity get increased. Nanofluid injection in the system curtail down the velocity. Prominent difference is seen in the interval $0 \le \eta \le 2$ and converges asymptotically beyond that. Velocity slip decrease velocity profile for both suction and injection framework. Slip parameter resist the flow of nanofluid. Injection of fluid in the system gives lower magnitude of velocity. From Table 11.2 we found 24.13% increment in reduce skin friction for injection of nanofluid where it is 22.55% for suction of nanofluid. Velocity difference (Figure 11.5) is prominent in $0 \le \eta \le 2$ and goes to zero for the similarity variable value beyond 2. Schmidt number is also an important parameter for velocity framework. Analogous nature like slip parameter is observed here. Figure 11.6 shows the nature prominently. Here also higher velocity magnitude is found for suction of nanofluid from the system. Figure 11.7 shows the influence of suction/injection parameter over velocity. More suction value gives higher magnitude of velocity. Prominent difference is observed in the interval $0 \le \eta \le 3$. Velocity profile tends to zero for higher value of similarity variable.

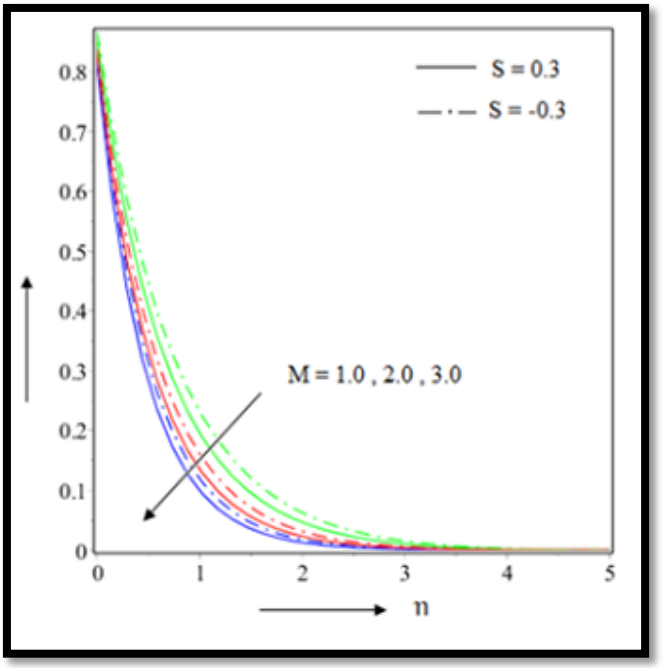

Figure 11.3: Effect of M on $f'(\eta)$.

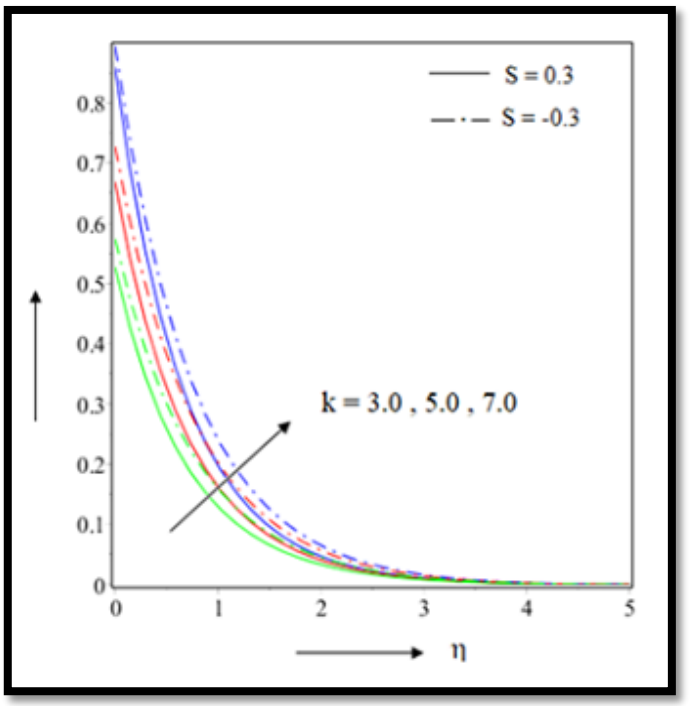

Figure 11.4: Effect of k on $f'(\eta)$.

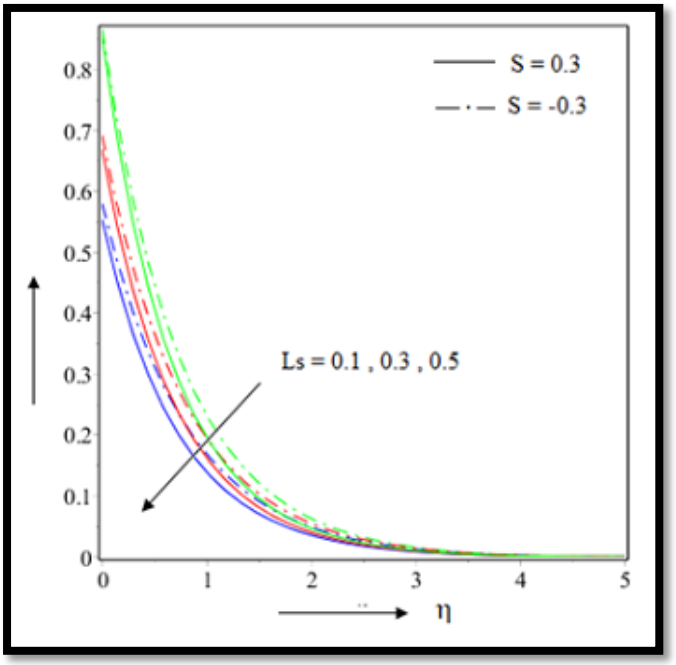

Figure 11.5: Effect of Ls on $f'(\eta)$.

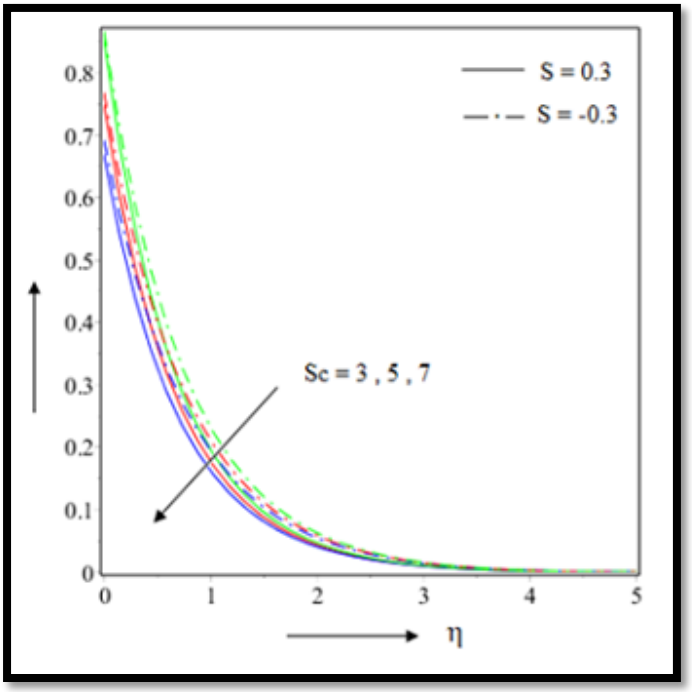

Figure 11.6: Effect of Sc on $f'(\eta)$.

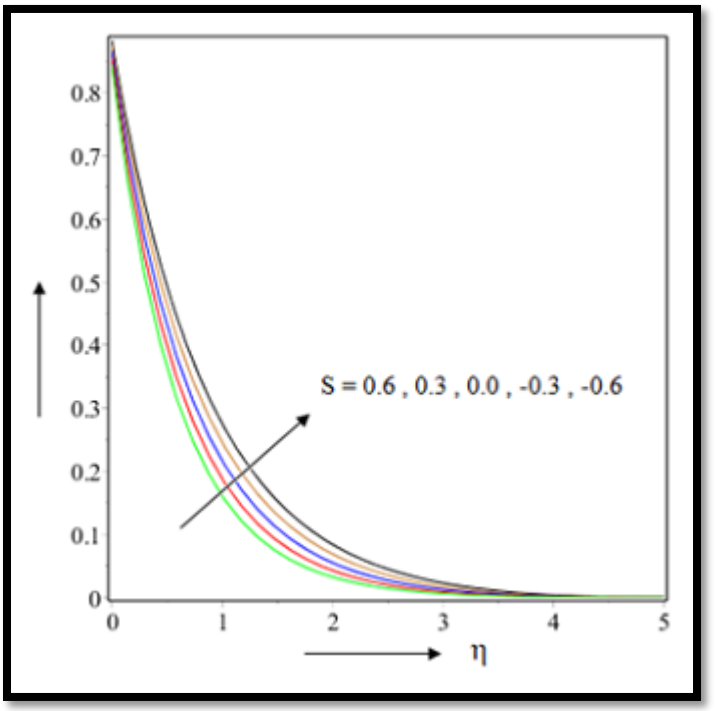

Figure 11.7: Effect of S on $f'(\eta)$

11.4.2. Temperature Profile

In this section upshots on thermal profile due to several parameter is discussed. Magnetic parameter increase the temperature of the system. We have already observed that due to drag force velocity is decreased but this drag force creates friction in the system which increase the thermal profile. Prominent outcome found in $0 \le \eta \le 2$ in Figure 11.8 and beyond that it converges asymptotically. Active control of nanoparticles gives higher temperature value than passive control of nanoparticles. From Table 11.3 we found 7.01% reduction in reduced Nusselt number for actively controlled flow but it is only 1.62% passively controlled flow. Upshots of curvature parameter is shown in Figure 11.9. Temperature value diminished for higher value of curvature parameter. For higher curvature parameter the surface become more flat. Nanofluid open surface area increased and more heat can be radiate from the system. Due to this system temperature get reduced and lower magnitude of thermal profile is found in case of passively controlled flow. Figure 11.10 depict the influence of suction/injection parameter on temperature profile. More we inject fluid in the system velocity get decreased. Passively controlled nanoparticles give lower magnitude of velocity. Influence of Brownian migration and thermophosis is depicted in Figure

11.11 and 11.12. In both cases we found similar result of uplifted temperature. Passively controlled flow gives low thermal profile than actively controlled flow. Reduced Nusselt number detained by 16.06% (Table 11.3 referred) for actively controlled Brownian motion but for actively controlled thermophoresis parameter it is only 3.93%.(Table 11.3 referred) Passively controlled Brownian motion parameter reduce the same by only 2.73% . Actually higher Brownian motion parameter indicates higher number collision between the nanoparticles which generates more frictional force and that results into higher thermal output. Velocity slip parameter also relate to the thermal profile. We have already seen in the previous section that velocity get declined by higher slip value as it resist the flow. This resistance generate more heat into the system. In Figure 11.13 it is clear that thermal profile escalated due to inflated slip parameter. We introduce thermal radiation and convective condition into our model. Both parameter give inflated thermal profile. For both cases passively controlled nanofluid flow gives lower thermal profile. Afify [171] consider non Newtonian fluid on stretching surface and found similar result. Increment in Nusselt number is observed 11.04% for actively controlled flow whereas for passively controlled flow it is 27.50% for thermal Biot number parameter (Table 11.3 referred). In Figure 11.14 and 11.15 influence of radiation and thermal Biot number is described graphically.

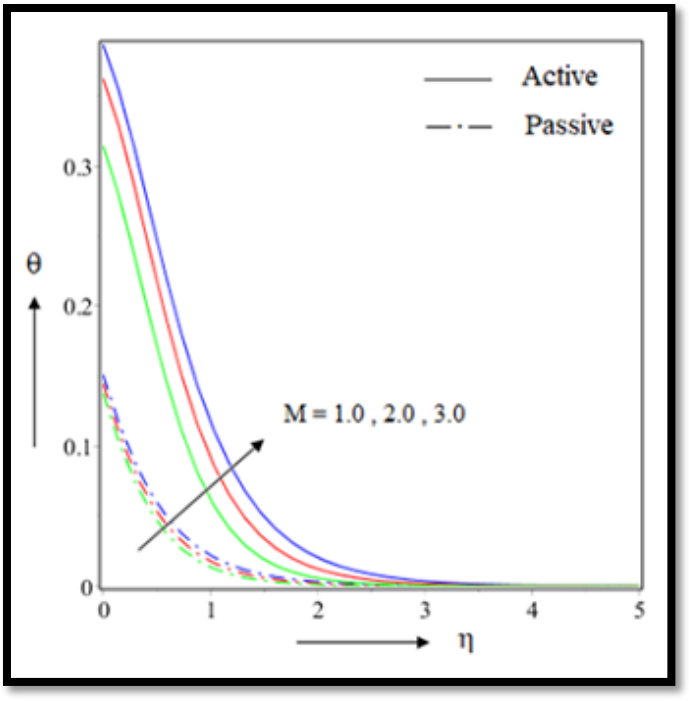

Figure 11.8: Effect of M on $\theta(\eta)$.

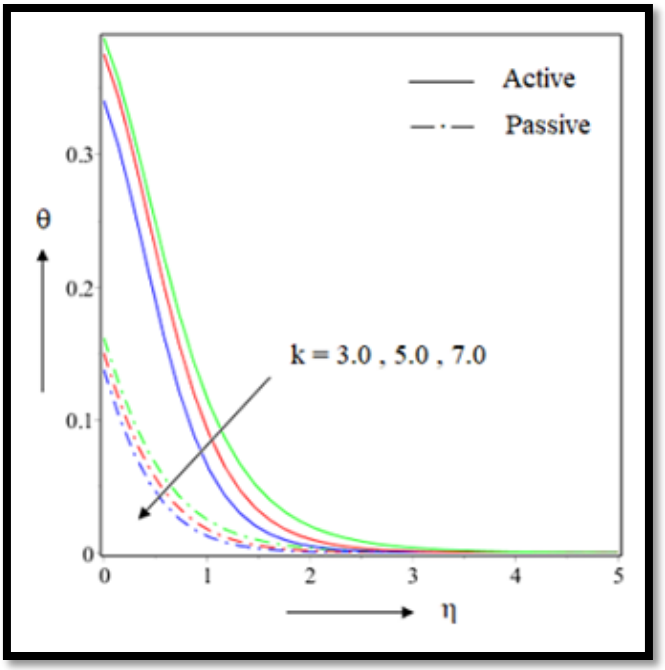

Figure 11.9: Effect of k on $\theta(\eta)$.

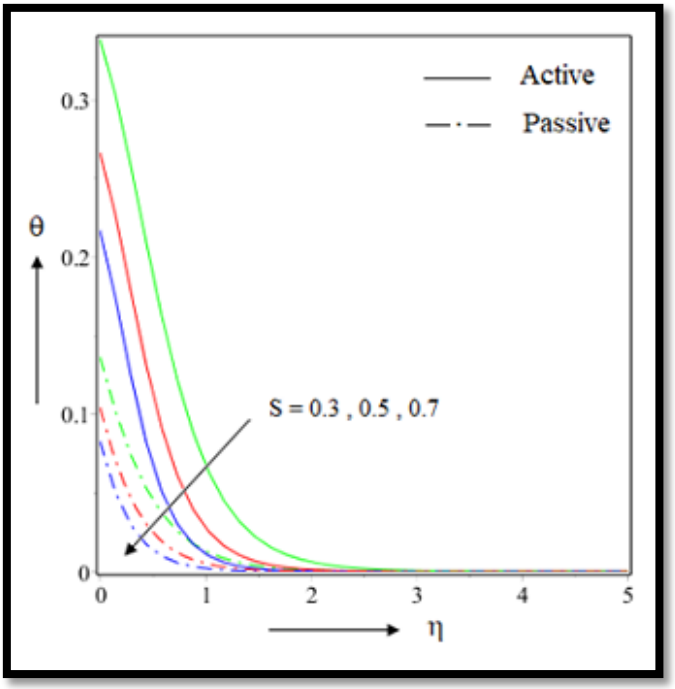

Figure 11.10: Effect of S on $\theta(\eta)$

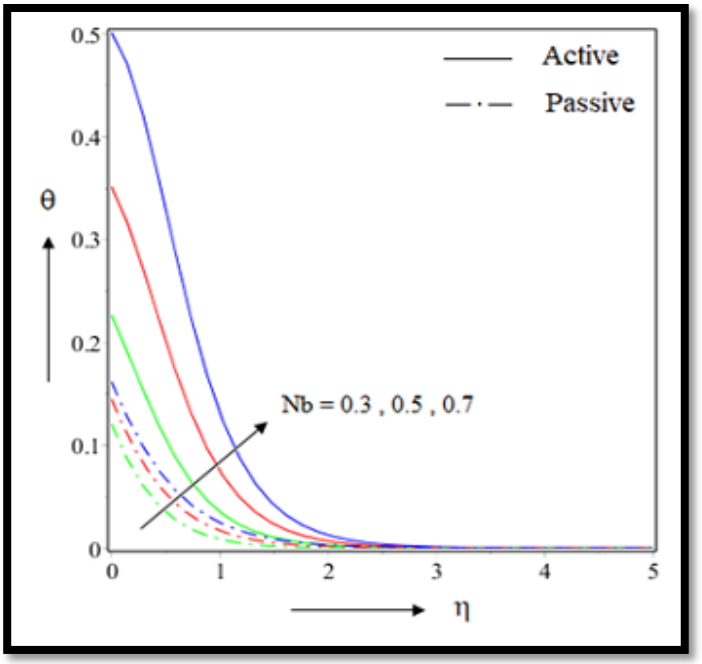

Figure 11.11: Effect of Nb on $\theta(\eta)$.

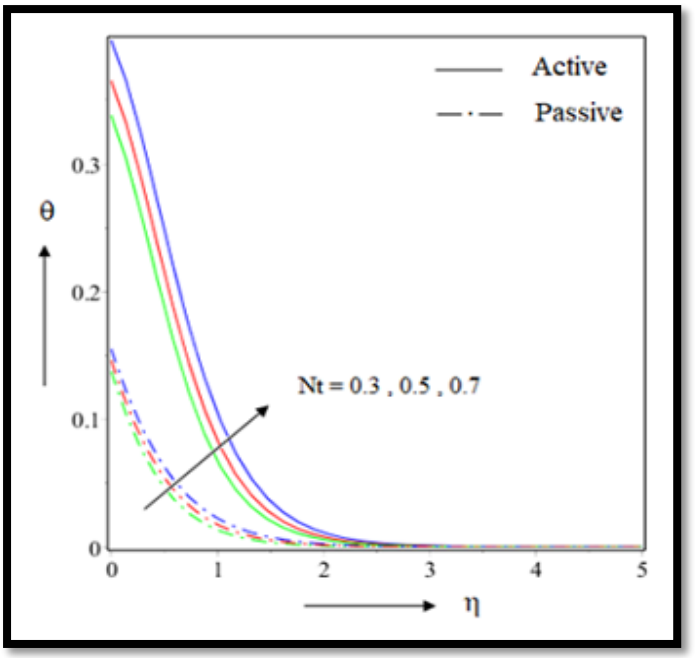

Figure 11.12: Effect of Nt on $\theta(\eta)$.

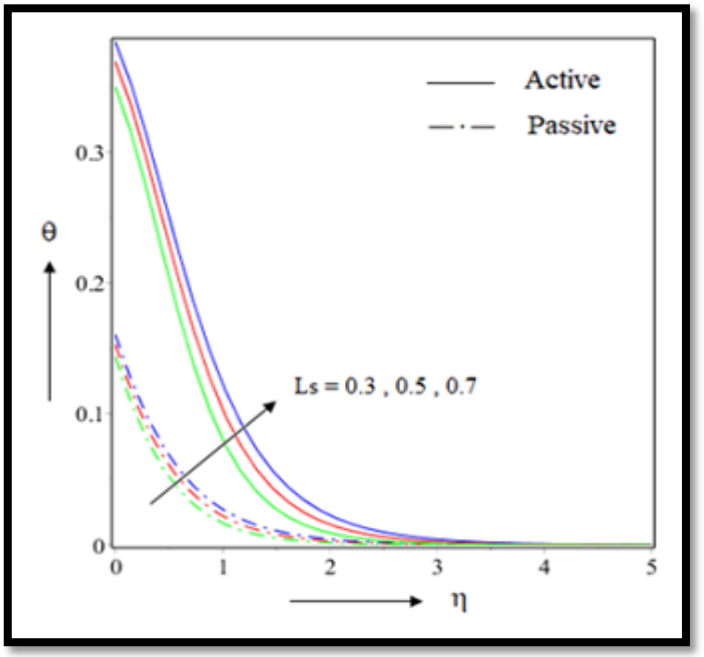

Figure 11.13: Effect of Ls on $\theta(\eta)$

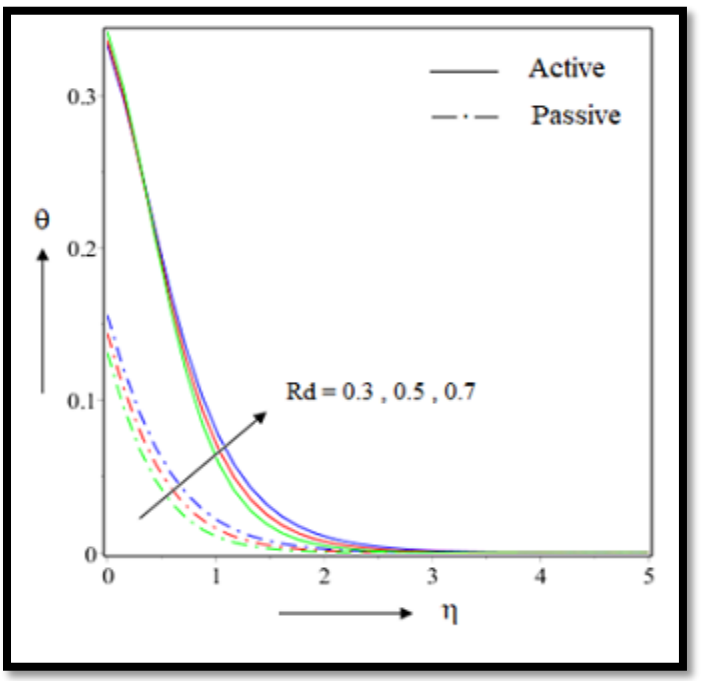

Figure 11.14: Effect of Rd on $\theta(\eta)$

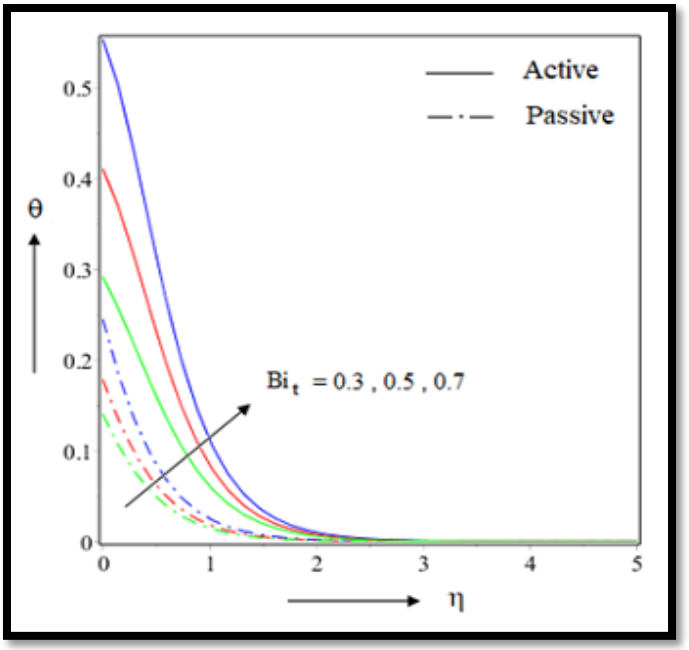

Figure 11.15: Effect of Bi_t on $\theta(\eta)$.

11.4.3. Concentration Profile

Influence over concentration profile for several parameters are described in this section. Magnetic parameter increase the mass lines and it clearly shown in the Figure 11.16 in interval $0 \le \eta \le 3$ beyond that it converges asymptotically. Both actively and passively controlled flow escalate concentration but low value of mass transfer found for passively controlled flow. Upshots of curvature parameter and suction/injection parameter is pictorially presented in Figure 11.17 and 11.18. For both parameter concentration profile get reduced. Shrewood number analysis is given in Table 4. In Figure 11.19 and 11.20 influence Brownian motion ant thermophoresis for differently controlled nanofliud flow is compared. We found that Brownian motion reduce the mass lines but thermophoresis parameter inflated the mass curves. From Table 11.4 increment in Sherwood number is found 7.69% for actively controlled flow under influence of Brownian motion parameter. Declined concentration profile is observed for upraised Schmidt number. Prominent pictorial view is seen in the interval $0 \le \eta \le 2$ (Figure 11.21 referred) beyond that it goes to zero asymptotically. Velocity slip parameter also affect concentration profile which is given by Figure 11.22. The graph shows little inflation in mass lines for higher slip value. Passively controlled flow gives lower magnitude than actively controlled flow in the system. From Table 11.4 it is found

that Sherwood number is reduced by 3.57% for actively controlled flow. Lastly the influence of chemical reaction parameter is depicted by Figure 11.23. Concentration is reduced for higher chemical reaction parameter. Inflated parameter value include more nanoparticle into the chemical reaction which is the main reason behind the result. Change in Sherwood number is given in Table 11.4.

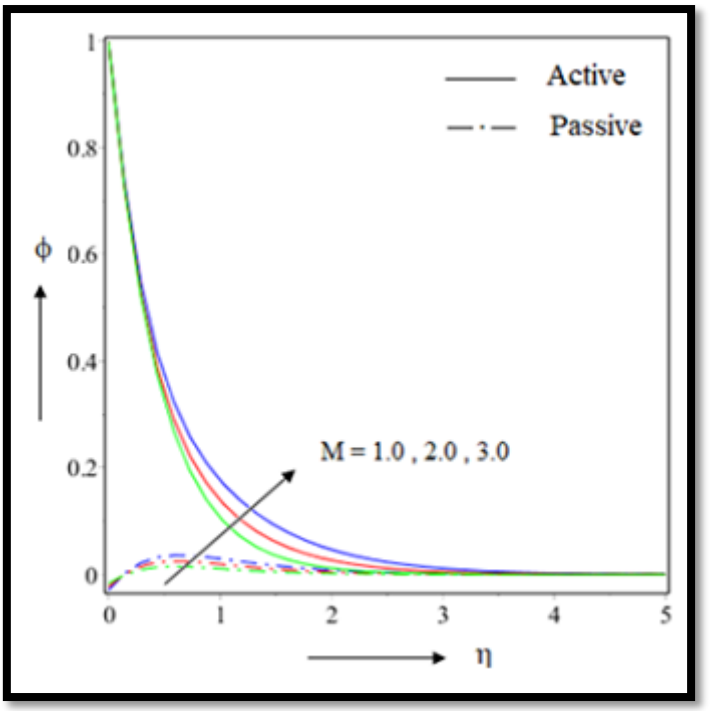

Figure 11.16: Effect of M on $\phi(\eta)$.

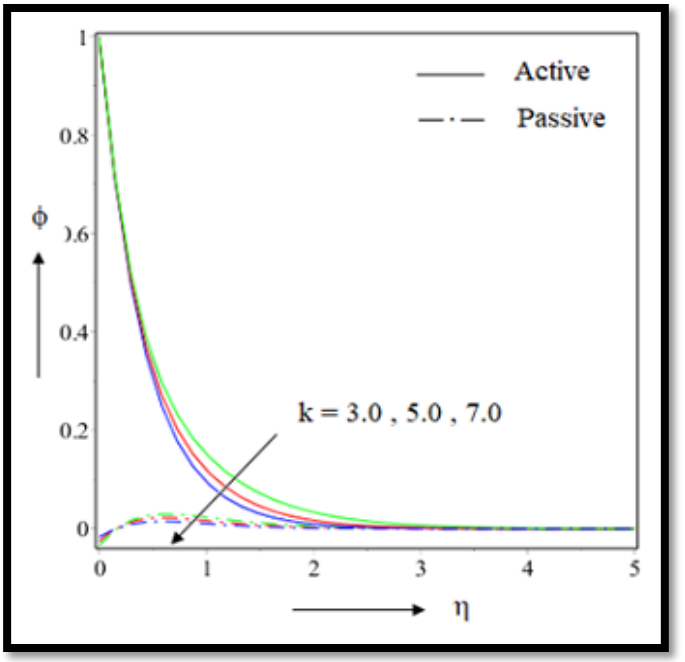

Figure 11.17: Effect of k on $\phi(\eta)$.

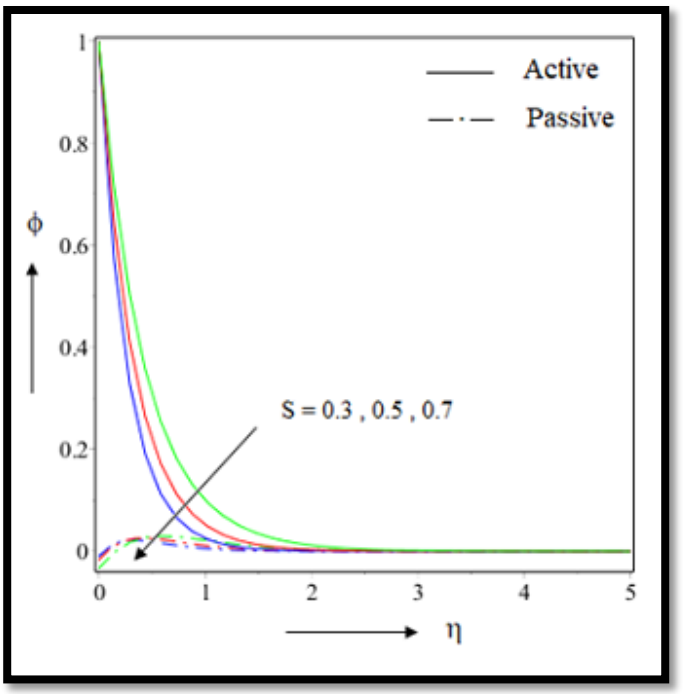

Figure 11.18: Effect of S on $\phi(\eta)$

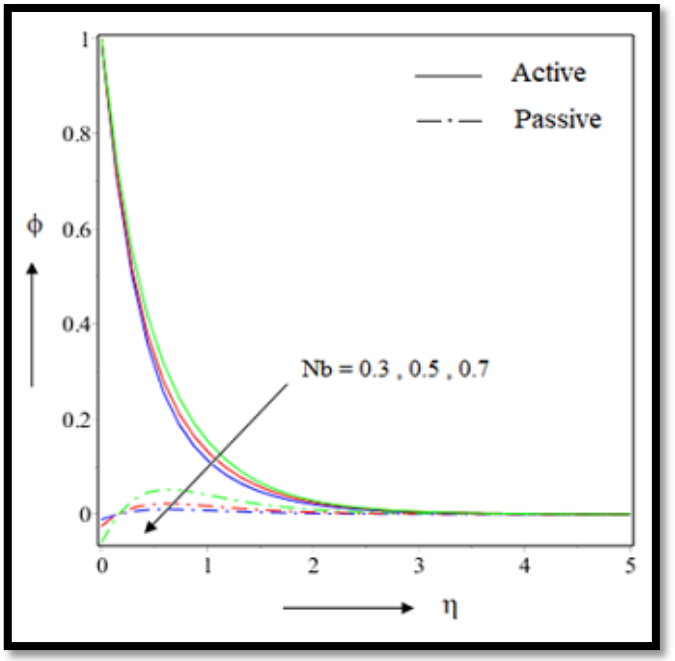

Figure 11.19: Effect of Nb on $\phi(\eta)$.

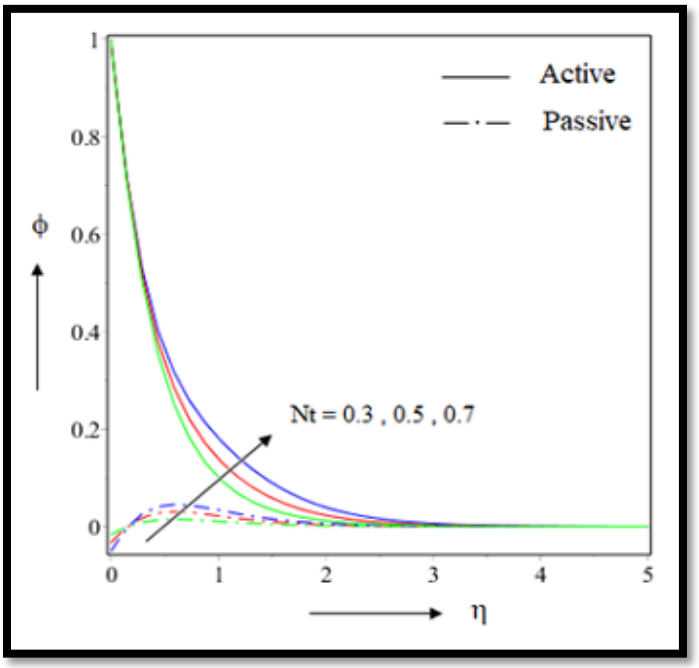

Figure 11.20: Effect of Nt on $\phi(\eta)$.

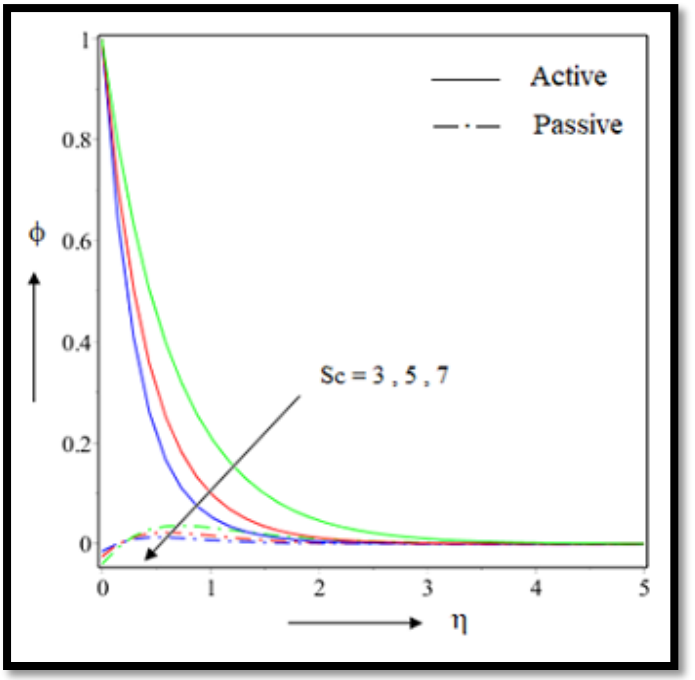

Figure 11.21: Effect of Sc on $\phi(\eta)$.

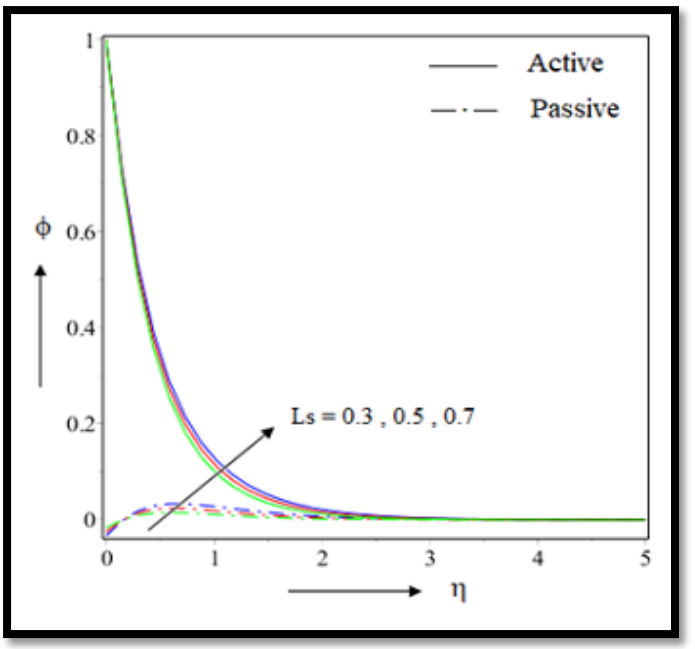

Figure 11.22: Effect of Ls on $\phi(\eta)$

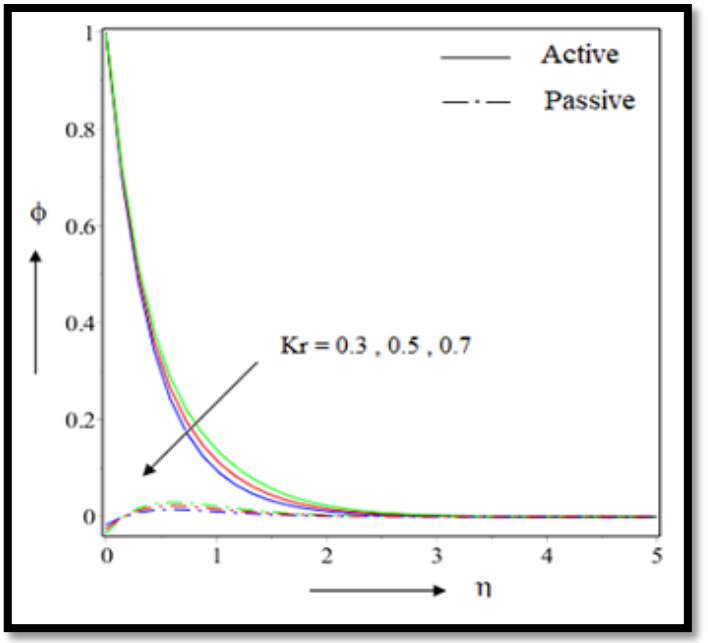

Figure 11.23: Effect of Kr on $\phi(\eta)$.

11.5. Conclusions

Chemically reactive nanofluid through stretching surface with curved nature is investigated in our research. We have imported radiation, convective condition, and velocity slip and suction/injection effect in the system. After analyzing the flow equations following important results are revealed. Graphs and tables are included to make the outcomes more precise.

- Magnetic field decline the velocity profile but it increase heat lines. Nanofluid concentration also increased due to higher magnetic profile. Sherwood number is increased by 2.34% for passively controlled flow.
- Velocity is inflated by curvature parameter so more flat surface gives higher velocity of flow. Temperature and concentration detained for higher value of curvature parameter.
- Radiation is important for thermal profile. It increase the thermal value for both actively and passively controlled flow but for passive control of nanoparticles we get lower thermal value.
- Thermal Biot number influence thermal profile by escalating the temperature of the system. For both active and passively controlled flow.
- Velocity slip parameter decrease the velocity framework but it increase the mass lines. Sherwood number is reduced by 3.57% for actively controlled flow.

- ❖ Brownian migration and thermophoresis parameter increase the thermal value of the system. In both cases passively controlled flow gives lower magnitude.
- ❖ Inflated chemical reaction parameter decrease the concentration of the system for actively and passively controlled nanofluid flow.

This research can be extended for different types of geometry like cylinder, cone, flat surface, disk and many more. Different boundary conditions can also be imported to make the system more realistic. Inclusion of Joule heating, Hall current effect and mixing of carbon nanotubes, microorganisms are encouraged.

Table 11.2: Effect of suitable parameters on skin friction

M	k	Ls	Sc	Cf_r			
				$S = 0.3$	CPU time (Second)	$S = -0.3$	CPU time (Second)
1.0	5	0.5	5	-1.451754	1.65	-1.331350	1.63
2.0				-1.697825	1.61	-1.574433	1.65
3.0				-1.886104	1.66	-1.766810	1.65
2.0	3			-0.944213	1.59	-0.945642	1.61
	5			-1.102275	1.64	-1.087162	1.64
	7			-1.406075	1.66	-1.312504	1.58
	5	0.3		-1.457694	1.64	-1.331350	1.59
		0.5		-1.102275	1.62	-1.025709	1.62
		0.7		-0.891593	1.58	-0.839277	1.66
		0.5	3	-1.457694	1.67	-1.331350	1.60
			5	-1.253486	1.61	-1.157087	1.59
			7	-1.102275	1.63	-1.025709	1.61

Table 11.3: Effect of suitable parameters on heat transfer

M	k	S	Nb	Nt	Ls	Rd	Bi_t	Nu_r			
								Active control	CPU time (Second)	Passive control	CPU time (Second)
1.0	5	0.5	0.5	0.5	0.5	0.5	0.5	0.342565	1.95	0.430966	1.92
2.0								0.318598	1.94	0.427552	1.92
3.0								0.306477	1.89	0.424413	1.95
2.0	3							0.328915	1.96	0.434198	1.90
	5							0.331863	1.95	0.427838	1.89
	7							0.331033	1.88	0.421860	1.89
	5	0.3						0.330660	1.92	0.421622	1.88
		0.5						0.366673	1.93	0.447665	1.94
		0.7						0.391421	1.95	0.458441	1.96
		0.5	0.3					0.386518	1.89	0.439443	1.92
			0.5					0.324185	1.90	0.427342	1.91
			0.7					0.258116	1.96	0.418948	1.90
			0.5	0.3				0.330662	1.97	0.430967	1.94
				0.5				0.317165	1.92	0.426578	1.90
				0.7				0.301297	1.94	0.422202	1.93
				0.5	0.3			0.324741	1.91	0.428081	1.92
					0.5			0.315167	1.95	0.423342	1.96
					0.7			0.307562	1.88	0.419521	1.94
					0.5	0.3		0.328915	1.91	0.434211	1.89
						0.5		0.331863	1.90	0.427838	1.88
						0.7		0.333103	1.92	0.418231	1.92
						0.5	0.3	0.353987	1.95	0.429603	1.96
							0.5	0.392603	1.94	0.547330	1.94
							0.7	0.446028	1.95	0.614212	1.91

Table 11.4: Effect of suitable parameters on mass transfer

M	k	S	Nb	Nt	Sc	Ls	Kr	Sh_r			
								Active control	CPU time (Second)	Passive control	CPU time (Second)
1.0	5	0.5	0.5	0.5	5	0.5	0.5	2.152331	1.37	4.706383	1.35
2.0								2.161225	1.32	4.812245	1.36
3.0								2.173660	1.36	4.922178	1.32
2.0	3							2.243651	1.34	4.548561	1.35
	5							2.232116	1.36	4.652201	1.36
	7							2.222198	1.37	4.741841	1.31
	5	0.3						2.245412	1.32	5.011289	1.30
		0.5						2.982520	1.35	5.488745	1.36
		0.7						3.484547	1.30	5.912326	1.32
		0.5	0.3					2.081112	1.34	4.722136	1.34
			0.5					2.248874	1.32	4.602136	1.35
			0.7					2.296459	1.33	4.512297	1.34
			0.5	0.3				2.245712	1.36	5.213163	1.36
				0.5				2.239945	1.35	4.980123	1.30
				0.7				2.226478	1.35	4.744821	1.37
				0.5	3			1.546213	1.36	4.012247	1.35
					5			2.240002	1.30	5.100272	1.35
					7			2.877405	1.34	6.213328	1.36
					5	0.3		2.240281	1.35	5.848123	1.34
						0.5		2.166419	1.31	5.465428	1.32
						0.7		2.090897	1.35	5.011287	1.34
						0.5	0.3	2.232495	1.32	5.102187	1.38
							0.5	2.336194	1.33	5.212284	1.36
							0.7	2.427745	1.36	5.300281	1.35

Final remarks based on the investigation presented in the thesis

This section represents final outcomes of the whole study. Chapter 2 to chapter 11 leads to different published research work. The most important outcomes from all this chapters are summarized here. The following remarks are the main outcomes of our research. Other outcomes are also discussed in each chapters.

- The radial velocity reduces for the magnetic parameter, but the slip and unsteadiness parameters exhibit the dual outcomes. The tangential velocity declines for magnetic and slips parameters, whereas unsteadiness reveals the dual impact. The axial velocity increases for every parameter. Hybrid nanofluid illustrates the low-velocity profile except for the case of axial velocity.
- Existence of double additive amplify the thermal conductivity of hybrid nanofluid and this conductivity value is higher than the usual nanoliquid.
- External heat source increase the temperature and for active control it is higher in magnitude. Temperature jump decrease both heat and concentration lines.
- Brownian motion and thermophoresis parameter play an important role here. Concentration profile is dropped as we increase the value of Brownian motion and thermophoresis parameter. When it comes to temperature profile Brownian motion and thermophoresis parameter give different result. Brownian motion increases the temperature and thermophoresis drops it down.
- Nonlinear radiation gives higher heat transfer rate and for linear radiation parameter it is almost double. This result is very significant for comparison between linear and nonlinear radiation.
- Higher value of velocity slip parameter reduce the velocity lines but it escalates heat lines and concentration lines. Reduced skin friction increased by 5.40% for injection effect in presence of second order slip parameter.
- Mass Biot number and thermal Biot number both increase the concentration of boundary layer and temperature of the system.

- Mass lines are reduced for higher value of Lewis number. Both actively and passively controlled nanofluid flow have same nature but the magnitude of concentration is lower for passive control of nanofluid flow.
- Reynolds number and Magnetic influence reduced the velocity profile but presence of slip parameter reduce the magnitude of velocity than no slip condition.
- Radiation is an important parameter for thermal profile. It increase the thermal value for both actively and passively controlled flow but for passive control of nanoparticles we get lower thermal value.

Future research scopes

This section leads to some future direction of our research work. One can be reached to some different and attracting results which may introduce some new aspect of heat and mass transfer. Many geometrical changes and also parametrical changes can be introduced into the systems to get different aspects.

The problem considered in chapter 2 can be modified by considering various combinations of nanoparticle. Different hybrid base fluid, viscous dissipation, joule heating, and some novel geometry along with physically reliable conditions can be further introduced to extend the investigation.

The problem of chapter 3 can be modified by (i) including different types of nanoparticles of metals, (ii) considering different geometrical figures like cone and cylinder, (iii) different parameters can be examined for higher volume fraction, and (iv) the flow parameters can be observed in presence and absence of suction/injection parameter.

The problem of chapter 4 can be extended by taking more geometrical structure like sphere, cone. Several conditions like radiation joule heating to inspect the comparison between active and passive control of nanoparticles can included in the problem. Proper boundary conditions can be introduced for further investigations.

The research work of chapter 5 can be solved by other analytical methods like ADM and HPM. The accuracy of analytical work and simulation work may compared. Chemical reaction in the system may be increased to higher order to reveal the thermal aspects.

The investigation of chapter 6 has diversified scopes to advance the results by introducing different metallic particles with higher heat trandfer rate. One can analyzed the results under inclined magnetic field also. Volume fraction of different particles with different numerical values may leads to some new aspects of hydrothermal behavior.

Extension of research work of chapter 7 can be done by taking other geometrical structures like sphere, wedge, and cone with different suitable conditions like Joule heating active and passive control of nanofluid. Moreover several nanofluid and hybrid nanofluid can also be taken to extend the investigation.

The analysis of the problem taken in chapter 8 can be extended by replacing other non newtonian fluid like Williamson nanofluid. Other geometrical models like cone, cylinder and stretching sheet can be taken to explore diversified hydrothermal features.

The problem of chapter 9 can be extended by taking other geometry like sphere , cylinder, cone , stretching sheet. Different parameters can be taken like multiple slip, multiple convection etcetera.

The research work of chapter 10 can be modified by taking some other geometrical structure with radiation and joule heating effect. Reliable geometric conditions and boundary provisions are to be included. Further investigation can be done under above noted circumstances.

The problem considered in chapter 11 can be extended by considering different boundary conditions to make system more realistic. Inclusion of Joule heating, Hall current effect and mixing of carbon nanotubes, microorganisms are encouraged.

BIBLIOGRAPHY

[1] S.U.S. Choi, "Enhancing thermal conductivity of fluids with nanoparticles, in Developments and Applications of Non-Newtonian Flows", American Society of Mechanical Engineers, New York, 66 (1995), 99-105.

[2] L. L. Schramm, E. N. Stasiuk, D. G. Marangoni, "Surfactants and their applications", Annual Report Section C, 99 (2003), 3-48.

[3] H. J. Kim, I. C. Bang, J. Onoe, "Characteristic stability of bare Au-water nanofluidsfabricated by pulsed laser ablation in liquids", Optics and Lasers in Engineering, 47 (5) (2009), 532–538.

[4] H. Chang, C. S. Jwo, P. S. Fan, S.H. Pai, "Process optimization and material properties for nanoflud manufacturing", The International Journal of Advanced Manufacturing Technology, 34(3.4) (2007), 300-306.

[5] Y. Hwang, J.K. Lee, Y. Jeong, S. Cheong, Y.C. Ahn, S.H. Kim, "Production and dispersion stability of nanoparticles in nanofluids", Powder Technology, 186 (2) (2008), 145-153.

[6] Y. Hwang, J.K. Lee, C.H. Lee, Y.M. Jung, S.I. Cheong, C.G. Lee, B.C. Ku, S.P. Jang, "Stability and thermal conductivity characteristics of nanofluids", Thermocimica Acta, 455 (2007), 70-74.

[7] A. K. Singh, V. S. Raykar, "Microwave synthesis of silver nanofluids with polyvinylpyrrolidone (PVP) and their transport properties", Colloid and Polymer Science, 286 (2008), 1667–1673.

[8] L. Prandtl, "On the motion of fluids with very little friction, Über Flüssigkeitsbewegung bei sehr kleiner Reibung", Int. Mathe.-Kong. Heidel, 8(13) (1904).

[9] A. Fick, "Ueber Diffusion", Annalen der Physik (in German), 94 (1855), 59–86.

[10] H. Alfvén, "Existence of electromagnetic-hydrodynamic waves", Nature, 150 (1942), 405-406.

[11] J. Maxwell, "A treatise on electricity and magnetism", second ed., Oxford University Press, 1904, Cambridge.

[12] J. C. Maxwell "A Treatise on Electricity and Magnetism", second ed., Clarendon Press, Oxford, UK, (1881).

[13] S.M.S. Murshed, K.C. Leong, C. Yang, "Enhanced thermal conductivity of TiO_2 -water based nanofluids", International Journal of Thermal Science, 44 (2005), 367-373.

[14] G.S. Mc. Nab, A. Meisen, "Thermophoresis in liquids", Journal of Colloid and Interface Science, 44 (1973), 339-346.

[15] X. Wang, X. Xu, S. U. S. Choi, "Thermal conductivity of nanoparticle-fluid mixture",Journal of Thermophysics Heat Transfer, 13 (1999), 474 – 480.

[16] D. Zhu, X. Li, N. Wang, X. Wang, J. Gao, H. Li, "Dispersion behavior and thermalconductivity characteristics of Al2O3-H2O nanofluids", Current Applied Physics, 9 (2009), 131-139.

[17] G. Xia, H. Jiang, R. Liu, Y. Zhai, "Effects of surfactant on the stability and thermalconductivity of Al2O3/de-ionized water nanofluids", International Journal of Thermal Science, 84 (2014), 118-124.

[18] H. Chang, C. S. Jwo, P. S. Fan, S. H. Pai, "Process optimization and material properties for nanofluid manufacturing", The International Journal of Advanced Manufacturing Technology, 34(3-4) (2007),300–306.

[19] T. Sharma, M. Reddy, T. S. Chandra, S. Ramaprabhu, "Development of carbon nanotubes and nanofluid based microbial fuel cell", International Journal of Hydrogen Energy, 33 (2008), 6749-6754.

[20] H. Xie, J. Wang, T. Xi, Y. Liu, F. Ai, Q. Wu, "Thermal conductivity enhancement of suspensions containing nanosized alumina particles", The Journal of Applied Physics, 91(7) (2002), 4568.

[21] A. Einstein, "Eine neue bestimmung der molekuldimensionen", Annalen der Physik., 324 (1906), 289–306.

[22] H.C. Brinkman, "The viscosity of concentrated suspensions and solutions", The Journal of Chemical Physics, 20 (1952), 571-571.

[23] R. L. Hamilton, O. K. Crosser, "Thermal Conductivity of Heterogeneous Two Component Systems", Industrial & Engineering Chemistry Fundamentals,1(3) (1962), 182-191.

[24] K. V. Wong, O. de Leon, "Applications of nanofluids: current and future", Advances in Mechanical Engineering, 519659 (2010), 1 – 11.

[25] J. Routbort, Argonne National Lab, Michellin North America, Saint Gobain Corporation, (2009).

[26] J. Boungiorno, L.W. Hu, S.J. Kim, R. Hannink, B. Truong, E. Forrest, "Nanofluids for enhanced economics and safety of nuclear reactors: an evaluation of the potential features issues, and research gaps", Nuclear Technology, 162 (2008), 80–91.

[27] S.J. Kim, I.C. Bang, J. Buongiorno, L.W. Hu, "Surface wettability change during pool boiling of nanofluids and its effect on critical heat flux", International Journal of Heat and Mass Transfer, 50 (2007), 4105–4116.

[28] H. Xie, L. Chen, "Adjustable thermal conductivity in carbon nanotube nanofluids", Physics Letters Section A, 373 (2009), 1861–1864.

[29] H. Xie, W. Yu, and Y. Li, "Thermal performance enhancement in nanofluids containing diamond nanoparticles", Journal of Physics D, 42(2009), Article ID 095413.

[30] S. C. Tzeng, C. W. Lin, K. D. Huang, "Heat transfer enhancement of nanofluids in rotary blade coupling of four wheel-drive vehicles", Acta Mechanica, 179 (2005), 11–23.

[31] H.B. Ma, C. Wilson, B. Borgmeyer, K. Park, Q. Yu, S.U.S. Choi, M. Tirumala. "Effect of nanofluid on the heat transport capability in an oscillating heat pipe", Applied Physics Letters, 88 (2006), 143116.

[32] H. B. Ma, C. Wilson, Q. Yu, K. Park, U. S. Choi, M. Tirumala, "An experimental investigation of heat transport capability in a nanofluid oscillating heat pipe", Journal of Heat Transfer, 128 (2006), 1213–1216.

[33] Z. H. Liu, R. L. Hu, L. Lu, F. Zhao, H. S. Xiao, "Thermal performance of an open thermosyphon using nanofluid for evacuated tubular high temperature air solar collector", Energy Conversion and Management, 73 (2013), 135-142.

[34] X. Sun, Z. Liu, J. T. Robinson,A. Goodwin, S. Zaric, H. Dai, "Nano-graphene oxide for cellular imaging and drug delivery", Nano Research, 1(2008) 203.

[35] J. F. Yan, J. Liu, "Nanocryosurgery and its mechanisms for enhancing freezing efficiency of tumor tissues", Nanomedicine: Nanotechnology, Biology, and Medicine, 4 (2008), 79–87.

[36] J. Li, X. Jhang, Bin Xu and M. Yuan, "Nanofluid research and applications: A review", International Communications in Heat and Mass Transfer, 127 (2021), 105543.

[37] A. J. Crane, “Flow past a stretching plate”, Journal of Applied Mathe,matics and Physics, 21 (1970), 645-647.

[38] P. S. Gupta, A. S. Gupta, “Heat and mass transfer on a stretching sheet with suction or blowing”, The Canadian Journal of Chemcal Engineering, 55 (1977), 744-746.

[39] H. I. Andersson, J. B. Aarseth, N. Braud, B. S. Dandapat, “Flow of a power-law fluid film on an unsteady stretching surface”, The Journal of Non-Newtonian Fluid Mechanics, 62 (1996), 1.

[40] O. D. Makinde, A. Aziz, “Boundary layer flow of a nanofluid past a stretching sheet with a convective boundary condition”, International Journal of Thermal Sciences, 50 (2011), 1326–1332.

[41] F. Mabood, S. M. Ibrahim, W. A. Khan, “Framing the features of Brownian motion and thermophoresis on radiative nanofluid flow past a rotating stretching sheet with Magnetohydrodynamics”, Results in Physics, 6 (2015) 1015-1023.

[42] J. V. R. Reddy, V. Sugunamma, N. Sandeep, “Thermophoresis and Brownian motion effects on unsteady MHD nanofluid flow over a slandering stretching surface with slip effects”, Alexandria Engineering Journal, 57 (4) (2018), 2465-2473.

[43] J. K. Zhou, “Differential Transformation and Its Application for Electrical Circuits”, Huazhong University Press, China, (1986).

[44] F. Ayaz, “On the two-dimensional differential transformation method”, Journal of Applied Mathematics and Computing, 143 (2–3) (2003), 361–374.

[45] M. Sheikholeslami, D. D. Ganji, “Nanofluid flow and heat transfer between parallel plates considering Brownian motion using DTM”, Computer Methods in Applied Mechanics and Engineering, 283 (2015), 651– 663.

[46] N. Acharya, K. Das, P. K. Kundu, “The squeezing flow of Cu-water and Cu-kerosene nanofluids between two parallel plates”, Alexandria Engineering Journal, 55 (2016), 1177-1186.

[47] M. A. Noor, S. T. Mohyud-Din, A. Waheed, “Variation of parameter method for solving fifth-order boundary”, Applied Mathematics & Information Sciences, 2(2) (2008), 135–141.

[48] S. T. Mohyud-Din, A. Yildirim, “Variation of parameter method for Fishers equation”, Journal of Advances in Applied Mathematics and Mechanics, 2 (2010) 379–388.

[49] N. Acharya, K. Das, P. K. Kundu, “On the Heat Transport Mechanism and Entropy Generation in a Nozzle of Liquid Rocket Engine using Ferrofluid (CoFe2O4): A Computational Framework”, Journal of Computational Design and Engineering, 6 (4) (2019), 739-750.

[50] M. Sheikholeslami, D. D. Ganji, H. R. Ashorynejad, H. B. Rokni, “Analytical investigation of jeffery hamel flow with high magnetic field and nanoparticle by Adomian decomposition method”, Applied Mathematics and Mechanics, 33 (2012), 1553–1564.

[51] M. Sheikholeslami, D. D. Ganji, H. R. Ashorynejad, “Investigation of squeezing unsteady nanofluid flow using ADM”, Powder Technology, 239 (2013), 259–265.

[52] N. Acharya, K. Das, P. K. Kundu, “Fabrication of active and passive controls of nanoparticles of unsteady nanofluid flow from a spinning body using HPM”, The European Physical Journal Plus, 132 (2017), 323.

[53] R. Ellahi, M. Raza, K. Vafai, “Series solutions of non-Newtonian nanofluids with Reynolds’ model and Vogel’s model by means of the homotopy analysis method”, Mathematical and Computer Modelling, 55 (2012), 1876–1891.

[54] M. Sheikholeslami, R. Ellahi, H. R. Ashorynejad, T. Hayat, “Effects of heat transfer in flow of nanofluids over a permeable stretching wall in a porous medium”, Journal of Computational and Theoretical Nanoscience, 11 (2014), 486–496.

[55] N. Acharya, K. Das, P. K. Kundu, “Ramification of variable thickness on MHD TiO2 and Ag nanofluid flow over a slandering stretching sheet using NDM”, The European Physical Journal Plus, 131 (2016),303.

[56] K. Thriveni and B. Mahanthesh, “Sensitivity analysis of nonlinear radiated heat transport of hybrid nanoliquid in an annulus subjected to the nonlinear Boussinesq approximation”, Journal of Thermal Analysis and Calorimetry, 143, (2021), 2729–2748.

[57] B. Mahanthesh, S.U. Khan, S.A. Shehzad, T. Ambreen, “Significance of Joule heating and viscous heating on heat transport of MoS_2–Ag hybrid nanofluid past an isothermal wedge”, Journal of Thermal Analysis and Calorimetry, 143 (2021), 1221–1229.

[58] A. Ahmadian, M. Bilal, M.A. Khan, M.I. Asjad, “Numerical analysis of thermal conductive hybrid nanofluid flow over the surface of a wavy spinning disk”, Scientific Reports, 10 (2020),18776.

[59] A. Tassaddiq, S. Khan, M. Bilal, T. Gul, S. Mukjtar, J. Shah, E Bonyah, “Heat and mass transfer together with hybrid nanofluid flow over a rotating disk” AIP Advances, 10 (2020), 055317.

[60] T. Hayat, S. Qayyum, M.I. Khan , A. Alsaedi, “Entropy generation in magnetohydrodynamic radiative flow due to rotating disk in presence of viscous dissipation and Joule heating”, Physics of Fluids, 30 (2018), 017101.

[61] M. Iiaz, M. Ayub and H. Khan, “Entropy generation and activation energy mechanism in nonlinear radiative flow of Sisko nanofluid: rotating disk”, Heliyon, 5(6) (2019), e01863.

[62] A. Zeeshan, M. Hassan, R. Ellahi, M. Nawaj, “Shape effect of nanosize particles in unsteady mixed convection flow of nanofluid over disk with entropy generation”, Proceedings of the Institution of Mechanical Engineers, Part E, 231(4) (2017), 871-879.

[63] S. Nadeem, M. Ijaz and M. Ayub, “Darcy–Forchheimer flow under rotating disk and entropy generation with thermal radiation and heat source/sink”, Journal of Thermal Analysis and Calorimetry, 143 (2021), 2313–2328.

[64] M. Ahmad, F. Jalil, M.Taj, S.A. Shehzad, “Lubrication aspects in an axisymmetric magneto nanofluid flow with radiated chemical reaction”, Heat Transfer 49(6) (2020), 3489-3502.

[65] N. Sandeep, M.G. Reddy, “MHD Oldroyd-B fluid flow across a melting surface with cross diffusion and double stratification”, The European Physical Journal Plus, 132 (2017), 147.

[66] M.G. Reddy and K.G. Kumar, “Cattaneo-Christov heat flux feature on carbon nanotubes filled with micropolar liquid over a melting surface: A stream line study”, International Communications in Heat and Mass Transfer, 122(1-3) (2021), 105142

[67] M.G. Reddy, “Cattaneo-Christov heat flux effect on hydromagnetic radiative Oldroyd-B liquid flow across a cone/wedge in the presence of cross-diffusion”, The European Physical Journal Plus, 133 (24) (2018), 24.

[68] M. Khan, A. Shahid, M.Y. Malik, T. Salahuddin, “Chemical reaction for Carreau-Yasuda nanofluid flow past a nonlinear stretching foil considering Joule heating”, Results in Physics, 8 (2018),1124-1130.

[69] B. J. Gireesha, M. R. Krishnamurthy, B. C. Prasannakumara, R. S. R. Gorla, “Mhd flow and nonlinear radiative heat transfer of a Casson nanofluid past a nonlinearly stretching sheet in the presence of chemical reaction”, Nanoscience and Technology, 9(3) (2018) 227-229.

[70] M.R. Eid, F. Mabood, K.L. Mahny, “On 3D Prandtl nanofluid flow with higher-order chemical reaction”, Journal of Mechanical Engineering Sciences, 235(19) (2020), DOI: 10.1177/0954406220975429

[71] A. Yasmin, K. Ali, M. Ashraf, “Study of Heat and Mass Transfer in MHD Flow of Micropolar Fluid over a Curved Stretching Sheet”, Scientific Reports , 10(1) (2020), 4581.

[72] P.T. Manjunatha, A.J. Chamka, R.J.P. Gowda, S.M. Naik, “Significance of Stefan Blowing and Convective Heat Transfer in Nanofluid Flow Over a Curved Stretching Sheet with Chemical Reaction, Journal of Nanofluids” , 10(2) (2021), 285-291.

[73] D.A. Nield, A.V. Kuznetsov, “The Cheng–Minkowycz problem for natural convective boundary-layer flow in a porous medium saturated by a nanofluid”, International Journal of Heat and Mass Transfer.52 (2009), 5792-5795.

[74] A.V. Kuznetsov and D.A. Nield, “The Cheng–Minkowycz problem for natural convective boundary layer flow in a porous medium saturated by a nanofluid: a revised model”, International Journal of Heat and Mass Transfer, 65 (2013), 682-685.

[75] D.A. Nield and A.V. Kuznetsov, “Thermal instability in a porous medium layer saturated by a nanofluid: a revised model”, International Journal of Heat and Mass Transfer, 68 (2014), 211-214.

[76] A.V. Kuznetsov and D.A. Nield, “Natural convective boundary-layer flow of a nanofluid past a vertical plate: A revised model”, International Journal of Heat and Mass Transfer. 77(2014), 126-129.

[77] N.A. Halim, S. Sivasankaran and N.F.M. Noor, “Active and passive controls of the Williamson stagnation nanofluid flow over a stretching/shrinking surface”, Neural Computing & Applications, 28 (2016), 1023-1033.

[78] N.A.Halim, R.U. Haq and N.F.M. Noor, “Analysis of zero and nonzero normal mass fluxes of a Newtonian nanofluid flow”, Meccanica 52 (2017), 1527-1533.

[79] M. Atlas, R.U. Haq and T. Mekkaoui, “Active and zero flux of nanoparticles between a squeezing channel with thermal radiation effects, Journal of molecular liquids, 223 (2016), 289-298.

[80] C.L.M.H. Navier, “Memoire sur les lois du mouvement des fluids”, Mem. Acad. R. Sci.Inst. Fr., 6 (1823), 389–440.

[81] S. Nandi, B. Kumbhakar, S. Sarkar, “MHD stagnation point flow of Fe_3O_4/Cu/Ag-CH_3OH nanofluid along a convectively heated stretching sheet with partial slip and activation energy: Numerical and statistical approach”, International Communications in Heat and Mass Transfer,130 (2022), 105791.

[82] G.S. Seth, R. Sharma, B. Kumbhakar, “Hydromagnetic flow of heat absorbing and radiating fluid over exponentially stretching sheet with partial slip and viscous and joule dissipation”, Engineering with Computers, 33(3) 2016, 907-925.

[83] T. Hayat, S. Asghar, A. Tanveer, A. Alsaedi, “Outcome of slip features on the peristaltic flow of a Prandtl nanofluid with inclined magnetic field and chemical reaction”, European physical journal plus, 5(132),(2017),1-16.

[84] H. Upreti , A.K. Pandey, M. Kumar, “Assessment of entropy generation and heat transfer in three-dimensional hybrid nanofluids flow due to convective surface and base fluids”, Journal of porous materials, 24(3) 2021, 35-50.

[85] L. Wu, “A slip model for rarefied gas flows at arbitrary Knudsen number”, Applied Physics Letters, 93 (2008), 253103.

[86] T. Turkyilmazoglu, “Heat and mass transfer of MHD second order slip flow”, Computer and Fluids, 71 (2013), 426-434.

[87] F. Mabood and K. Das, “Melting heat transfer on hydromagnetic flow of a nanofluid over a stretching sheet with radiation and second-order slip”, European physical journal plus, 131(3) (2016), 3.

[88] T. Fang, S. Yao, J. Zhang, A. Aziz, “Viscous flow over a shrinking sheet with a second order slip flow model”, Communications in Nonlinear Science and Numerical Simulation, 15 (2010), 1831-1842.

[89] T. Watanabe, “Thermal boundary layers over a wedge with uniform suction or injection in forced flow”. Acta Mechanica, 83 (1990), 119–126

[90] A.J. Chamkha, M. Mujtaba, A. Quadri, C. Issa, “Thermal radiation effects on MHD forced convection flow adjacent to a non-isothermal wedge in presence of a heat source and sink”, Heat and Mass Transfer, 39 (2003), 305–312.

[91] A. Asaithambi, “A finite difference method for the Falkner and Skan equation”, Journal of Applied Mathematics and Computing, 92 (1998), 135–141.

[92] R.S.R. Gorla, A.J. Chamkha, A.M. Rashad, “Mixed convective boundary layer flow over a vertical wedge embedded in a porous medium saturated with a nanofluid natural convection dominated regime”, Nanoscale research letters, 6 (2011),1–9.

[93] W.A. Khan, I. Pop, “Boundary layer flow past a wedge moving in a nanofluid”, Mathematical Problems in Engineering, 3 (2013), 1–7.

[94] R. Kandasamy, I. Muhaimin, A.B. Khamis, R.B. Roslan, “Unsteady Hiemenz flow of Cu–water nanofluid over a porous wedge in presence of thermal stratification due to solar energy radiation”, International Journal of Thermal Sciences, 65 (2012), 196–205.

[95] M.M. Rahman, I.A. Eltayeb, “Convective slip flow of rarefied fluids over a wedge with thermal jump and variable transport properties”, International Journal of Thermal Sciences, 50 (2011), 468e479.

[96] M.V. Krishna and A.J. Chamkha, “Hall effects on mhd squeezing flow of a water-based nanofluid between two parallel disks”, Journal of porous media, 22(2) (2019), 209-223

[97] M.M. Rahman, M.K. Amira, Al-Hadhrami, “Nonlinear Slip Flow with Variable Transport Properties Over a Wedge with Convective Surface”, Proceeding CCS Antalia, (2013), 167-181. Conference Paper.

[98] A. Arshad, M. Jabbal, Y. Yan, D. Reay, “A review on graphene based nanofluids: Preparation, characterization and applications”. Journal of molecular liquids. 279 (2019), 444-484.

[99] N.S. Khan, S. Zuhra, Z. Shah, E. Bonyah, W. Khan, S. Islam, “Slip flow of Eyring-Powell nanoliquid film containing graphene nanoparticles”, AIP Advances 8(11) (2018) 115302.

[100] M. Turkyilmazoglu, “Purely analytical solution of magnetohydrodynamic swirling boundary layer flow over a porous rotating disk”, Computers and Fluids, 39(5) (2010), 793-799.

[101] N. Bachok, A. Ishak and I. Pop, “Flow and heat transfer over a rotating porous disk in a nanofluid”, Physica B, 406 (2011), 1767-1772.

[102] M.M. Rashidi, S.A.M. Pour, T. Hayat, S. Obaidat, “Analytic approximate solutions for steady flow over a rotating disk in porous medium with heat transfer by homotopy analysis method”, Computers and Fluids, 54 (2012), 1–9.

[103] I. Ullah, T. Hayat, A. Alsaedi, S. Asghar, “Dissipative flow of hybrid nanoliquid (H_2O-aluminum alloy nanoparticles) with thermal radiation”, Physica Scripta, 94 (2019), 125708.

[104] N.S. Anuar, N. Bachok and I. Pop, “Radiative hybrid nanofluid flow past a rotating permeable stretching/shrinking sheet”, International Journal of Numerical Methods for Heat and Fluid Flow, 8 (2020) 115302.

[105] B. Takabi, A.M. Gheitaghy and M. Tazraei, “Hybrid water-based suspension of Al2O3 and Cu nanoparticles on laminar convection effectiveness”, Journal of Thermophysics and Heat Transfer, 30(3) (2016), 523-532.

[106] A.J. Chamkha, A.S. Dogonchi and D.D. Ganji, “Magneto-hydrodynamic flow and heat transfer of a hybrid nanofluid in a rotating system among two surfaces in the presence of thermal radiation and Joule heating”, AIP Advances. 9 (2019),025103

[107] H.F. Oztop and E. Abu-Nada, “Numerical study of natural convection in partially heated rectangular enclosures with nanofluids”, International Journal of Heat and Fluid Flow, 29 (2008), 1326–1336.

[108] N. Acharya and F. Mabood, “On the hydrothermal features of radiative Fe_3O_4–graphene hybrid nanofluid flow over a slippery bended surface with heat source/sink”, Journal of Thermal Analysis and Calorimetry, 143 (2021), 1273–1289.

[109] T. Fang and C.F. Lee, “A moving wall boundary layer flow of slightly rarefied gas free stream over a moving flat plate”, Applied mathematics letters, 18 (2005), 487–495.

[110] M.M. Rahaman and I.A. Eltayeb, “Convective slip flow of rarefied fluids over a wedge with thermal jump and variable fluid properties”, International Journal of Thermal Sciences, 50 (2011), 468–479.

[111] M. Rashidi, S. Abelman and N.F. Mehr, “Entropy generation in steady MHD flow due to a rotating porous disk in a nanofluid”, International Journal of Heat and Mass Transfer, 62 (2013), 515-525.

[112] T. Fang and H. Tao, “Unsteady viscous flow over a rotating stretchable disk with deceleration”, Communications in Nonlinear Science and Numerical Simulation, 17(12) (2012), 5064-5072.

[113] B. Mahanthesh, S.U. Khan, S.A. Shehzad, T. Ambreen, “Significance of Joule heating and viscous heating on heat transport of MoS_2–Ag hybrid nanofluid past an isothermal wedge”, Journal of Thermal Analysis and Calorimetry, 143 (2021), 1221–1229.

[114] S. Mukhopadhyay, “Slip effects on MHD boundary layer flow over an exponentially stretching sheet with suction/blowing and thermal radiation”, Ain Shams Engineering Journal, 4 (4) (2013), 85–91.

[115] R. U. Haq, S. Nadeem, Z. H. Khan, N. S. Akbar, “Thermal radiation and slip effects on MHD stagnation point flow of nanofluid over a stretching sheet”, Physica E, 65 (2015), 17–23.

[116] S. P. A. Devi, S. S. U. Devi, “Numerical investigation of hydromagnetic hybrid Cu – Al_2O_3/Water nanofluid flow over a permeable stretching sheet with suction”, International Journal of Nonlinear Science and Numerical Simulation, 17 (5) (2016), 249–257.

[117] C. Y. Wang, “Free convection on a vertical stretching surface”, Journal of Applied Mathematics and Mechanics, 69 (1989), 418–420.

[118] B. Nagaraja, B.J. Gireesha and S. Sindhu, “Chemically reactive and radiative flow of ferro-aluminum (AA7075) hybrid nanofluid past a stretching cylinder”, Heat Transfer, 50(7) (2021), 7406-7424.

[119] I. Khan, Shafquatullah, M.Y. Malik, A. Hussain, M. Khan, “Magnetohydrodynamics Carreau nanofluid flow over an inclined convective heated stretching cylinder with Joule heating”, Results in Physics, 3797(17) (2017), 31461-4.

[120] H.R. Ashorynejad, M. Sheikholeslami, I. Pop, D.D. Ganji “Nanofluid flow and heat transfer due to a stretching cylinder in the presence of magnetic field”, Heat Mass Transfer, 49 (2013), 427-436.

[121] C.Y. Wang “Fluid flow due to a stretching cylinder”, Physics of Fluids, 31 (1988), 466.

[122] S.S. Giri, K. Das and P.K. Kundu, “Stefan blowing effects on MHD bioconvection flow of a nanofluid in the presence of gyrotactic microorganisms with active and passive nanoparticles flux”, European physical journal plus, 132 (2017), 1-14.

[123] S. A. Shehzad, A. Alsaedi, T. Hayat, "Hydromagnetic steady flow of Maxwell fluid over a bidirectional stretching surface with prescribed surface temperature and prescribed surface heat flux", PLOS one, 8 (2013), e68139.

[124] A. Munir, A. Shahzad, M. Khan, "Convective Flow of Sisko Fluid over a Bidirectional Stretching Surface", PLoS One, 10(6) (2015), e0130342.

[125] B. Mahanthesh, B. J. Gireesha, R. S. R. Gorla, F. M. Abbasi, S. A. Shehzad," Numerical solutions for magnetohydrodynamic flow of nanofluid over a bidirectional non-linear stretching surface with prescribed surface heat flux boundary", Journal of Magnetism and Magnetic Materials, 417 (2016), 189–196.

[126] C. Y. Wang, "The three-dimensional flow due to a stretching surface", Physics of Fluids, 27 (1984), 1915–1917.

[127] J. K. Zhou, "Differential Transformation and Its Application for Electrical Circuits", Huazhong University Press, China, (1986).

[128] F. Ayaz, "On the two-dimensional differential transformation method", Journal of Applied Mathematics and Computing, 143 (2–3) (2003), 361–374.

[129] M. Sheikholeslami, D. D. Ganji, "Nanofluid flow and heat transfer between parallel plates considering Brownian motion using DTM", *Computer Methods* in *Applied Mechanics* and *Engineering*, 283 (2015), 651– 663.

[130] N. Acharya, K. Das, P. K. Kundu, "The squeezing flow of Cu-water and Cu-kerosene nanofluids between two parallel plates", Alexandria Engineering Journal, 55 (2016), 1177-1186.

[131] I. C. Liu, A. I. Helge, "Heat transfer over a bidirectional stretching sheet with variable thermal conditions", International Journal of Heat and Mass Transfer, 51 (2008), 4018–4024.

[132] T. Hayat, T. anzila , S. Nadeem, "Heat transfer enhancement with Ag-CuO/water hybrid nanofluid", Results in Physics, 7 (2017), 2317-2324.

[133] M. H. Esfe, S. Wongwises, A. Naderi, A. Asadi, M. R. Safaei, H. Rostamian, M. Dahari, A. Karimipour, "Thermal conductivity of Cu/TiO2–water/EG hybrid nanofluid: Experimental data and modeling using artificial neural network and correlation", International Communications in Heat and Mass Transfer, 66 (2015), 100–104.

[134] B. Takabi and S. Salehi, “Augmentation of the heat transfer performance of a sinusoidal corrugated enclosure by employing hybrid nanofluid”, Advances in Mechanical Engineering, 6 (2014), 147059.

[135] A. J. Chamkha, V. I. Miroshnichenko, M. A. Sheremet, “Numerical analysis of unsteady conjugate natural convection of hybrid water-based nanofluid in a semicircular cavity”, Journal of Thermal Science and Engineering Applications, 9 (2017), 041004.

[136] H. F. Oztop, E.Abu-Nada, “Numerical study of natural convection in partially heated rectangular enclosures with nanofluids”, International Journal of Heat and Fluid Flow, 29 (2008), 1326–1336.

[137] J. A. Maxwell, “Treatise on Electricity and Magnetism”, second ed., Oxford University Press, Cambridge (1904).

[138] N. Bachok, A. Ishak, I. Pop, “Flow and heat transfer over a rotating porous disk in a nanofluid”, Physica B, 406 (2011), 1767-1772.

[139] B. Kumbhakar, S. Nandi, A.J. Chamkha, Unsteady hybrid nanofluid flow over a convectively heated cylinder with inclined magnetic field and viscous dissipation: A multiple regression analysis”, Chinese Journal of Physics 79 (2022), 38-56.

[140] N. Acharya, K. Das and P.K Kundu, “Outlining the impact of second order slip and multiple convective condition on nanofluid flow: A new statistical layout”, Canadian Journal of Physics, 96(1) (2017), 104-111.

[141] K. Gangadhar, K. Keziya and B.R. Kumar, “Effect of thermal radiation on heat transfer of ferrofluid over a stretching cylinder with convective heating”, International journal of engineering science technologies, 4(10) (2018), 261-268.

[142] A.K. Pandey, M. Kumar, “Natural convection and thermal radiation influence on nanofluid flow over a stretching cylinder in a porous medium with viscous dissipation”, Alexandria Engineering Journal, 56(1) (2017), 55-62.

[143] A.K. Pandey and M. Kumar, “Boundary layer flow and heat transfer analysis on Cu-water nanofluid flow over a stretching cylinder with slip”, Alexandria Engineering Journal, 56(4) (2017), 671-677.

[144] A. Mishra, A.K. Pandey and M. Kumar, “Ohmic-viscous dissipation and slip effects on nanofluid flow over a stretching cylinder with suction/injection”, Journal for Nanoscience and Nanotechnology, 9(2) (2018), 99-115.

[145] M.M. Nandeppanavar, “Second order slip flow and heat transfer due to shrinking sheet: An analytical Solution. Mathematical Theory and Modeling”, Mathematical theory and modelling, 6(2) (2016).

[146] L. Wu, “A slip model for rarefied gas flows at arbitrary Knudsen number”, Applied Physics Letters, 93 (2008), 253103.

[147] H.R. Ashorynejad, M. Sheikholeslami, I. Pop, D.D. Ganji, “Nanofluid flow and heat transfer due to a stretching cylinder in the presence of magnetic field”, Heat and Mass Transfer, 49 (2013), 427-436.

[148] A. Mishra and M. Kumar, “Ohmic–viscous dissipation and heat generation/absorption effects on MHD nanofluid flow over a stretching cylinder with suction/injection”, Advances in Intelligent Systems and Computing, 702 (2018), 45-55.

[149] N. Acharya, K. Das, P. K. Kundu, “Influence of multiple slips and chemical reaction on radiative MHD Williamson nanofluid flow in porous medium: A computational framework”, Multidiscipline Modeling in Materials and Structures, 15 (3) (2019), 630-658.

[150] R. Raza, F. Mabood, R. Naz, “Entropy analysis of non-linear radiative flow of Carreau Liquid over curved stretching sheet”, International Communications in Heat and Mass Transfer, 119(5) (2020), 104975.

[151] T. Hayat, A. Alsaedi, Q.M.Z. Zai, “Computational analysis of heat transfer in mixed convective flow of CNTs with entropy optimization by a curved stretching sheet”, International Communications in Heat and Mass Transfer, 118 (2020), 104881.

[152] S. Qayyum, T. Hayat, A. Alsaedi, “Optimization of entropy generation in motion of magnetite-Fe_3O_4 nanoparticles due to curved stretching sheet of variable thickness”, International Journal of Numerical Methods for Heat and Fluid Flow , 29(9) (2019), 3347-3365.

[153] Z. Abbas, M. Naveed, M. Sajid, “Heat transfer analysis for stretching flow over a curved surface with magnetic field”, Journal of Engineering Thermophysics , 22(4) (2013),337-345

[154] I.S. Oyelakin, S. Mondal, P. Sibanda, “Unsteady Casson nanofluid flow over a stretching sheet with thermal radiation, convective and slip boundary conditions”, Alexandria Engineering Journal, 55(2) (2016), 1025-1035.

[155] T. Hayat, A. Aziz, T. Muhammad, A. Alsaedi, "Numerical study for nanofluid flow due to a nonlinear curved stretching surface with convective heat and mass conditions", Results in Physics , 7 (2017), 3100–3106

[156] V.M. Falkner, S.W. Skan, "Some approximate solution of the boundary layer equations", Philosophical magazine letters, 12 (1931), 865-896.

[157] K. Stewartson, "Further solution of Falkner and Skan equation", Mathematical Proceedings of the Cambridge Philosophical Society, 50 (1954), 454-465.

[158] S.P. Hastings, ". Reversed flow solutions of Falkner and Skan equation", Society for Industrial and Applied Mathematics, 22 (1972), 329-334.

[159] M.M. Rahman and I.A. Eltayeb, "Convective slip flow of rarefied fluids over a wedge with thermal jump and variable transport properties", International Journal of Thermal Sciences, 50 (2011), 468e479.

[160] M.M. Rahman and Amira M.K. Al-Hadhrami, "Nonlinear Slip Flow with Variable Transport Properties Over a Wedge with Convective Surface", Proceeding CCS Antalia (2013), 167-181.

[161] M.J. Martin and I.D. Boyd, "Momentum and heat transfer in a laminar boundary layer with slip flow", Journal of Thermophysics and Heat Transfer, 20 (2006), 710-719.

[162] M.J. Martin and I.D. Boyd, ". Falkner Skan flow over a wedge with slip boundary condition", Journal of Thermophysics and Heat Transfer, 24 (2010), 263-270.

[163] O.D. Makinde, "Laminar falling liquid film with variable viscosity along an inclined heated plate" Applied Mathematics and Computation, 175 (2006), 80-88.

[164] T. Fang, C.F. Lee, "A moving layer boundary layer flow of a slightly rarefied gas free stream over a moving flat plate" Applied mathematics letters, 18 (2005), 487-495.

[165] B. Nagaraja, B.J. Gireesha and S. Sindhu, "Chemically reactive and radiative flow of ferro-aluminum (AA7075) hybrid nanofluid past a stretching cylinder", Heat Transfer, 50(7) (2021), 7406-7424.

[166] I. Khan, Shafquatullah, M.Y. Malik, A. Hussain, M. Khan, "Magnetohydrodynamics Carreau nanofluid flow over an inclined convective heated stretching cylinder with Joule heating", Results in Physics, 7 (2017), 4001-4012.

[167] H.R. Ashorynejad, M. Sheikholeslami, I. Pop, D.D. Ganji, "Nanofluid flow and heat transfer due to a stretching cylinder in the presence of magnetic field", Heat and Mass Transfer, 49 (2013), 427-436.

[168] S. Mukhopadhyay, "MHD boundary layer slip flow along a stretching cylinder", Ain Shams Engineering Journal, 4 (2013), 317-324.

[169] A.K. Pandey and H. Upreti, "Mixed convective flow of Ag–H_2O magnetic nanofluid over a curved surface with volumetric heat generation and temperature-dependent viscosity", Heat Transfer, 50(7) (2021), 7251-7270.

[170] A. Mishra, A.K. Pandey and M. Kumar, "Thermal performance of Ag–water nanofluid flow over a curved surface due to chemical reaction using Buongiorno's model", Heat Transfer, 50(1) (2021), 257-278.

[171] A.A. Afify, "The influence of slip boundary condition on Casson nanofluid flow over a stretching sheet in the presence of viscous dissipation and chemical reaction", Mathematical Problems in Engineering, Hindawi, (2017), 3804751.

Supratosh Maity
12.09.2024